Search for light dark matter with DAMIC-M experiment

Claudia de Dominicis

THÈSE DE DOCTORAT DE

L'ÉCOLE NATIONALE SUPÉRIEURE
MINES-TÉLÉCOM ATLANTIQUE BRETAGNE
PAYS-DE-LA-LOIRE - IMT ATLANTIQUE

ÉCOLE DOCTORALE N° 596
Matière, Molécules, Matériaux
Spécialité : *Subatomic Physics and Instrumentation*

Par

Claudia DE DOMINICIS

Search for Light Dark Matter with the DAMIC-M experiment

Thèse présentée et soutenue à Nantes, le 18 Octobre 2022
Unité de recherche : SUBATECH, Nantes Université, IMT Atlantique, CNRS-IN2P3
Thèse Nº : 2022IMTA0313

Rapporteurs avant soutenance :

Jules GASCON   Professeur, Université de Lyon
Luca SCOTTO LAVINA   Directeur de recherche, Sorbonne Université

Composition du Jury :

Président :	Antoine LETESSIER-SELVON	Directeur de recherche, LPNHE
Examinateurs :	Muriel FALLOT	Maître de conférences HDR, SUBATECH – IMT Atlantique
	Jules GASCON	Professeur, Université de Lyon
	Luca SCOTTO LAVINA	Directeur de recherche, LPNHE
	Rocio VILAR CORTABITARTE	Maître assistant, University of Cantabria
Dir. de thèse :	Mariangela SETTIMO	Chargée de recherche HDR, SUBATECH - CNRS
Co-encadrant de thèse :	Paolo PRIVITERA	Professeur, University of Chicago

ACKNOWLEDGEMENT

I am extremely grateful to my supervisors, Paolo and Mariangela, who trusted me and guided me throughout this thesis, making me a better researcher. I couldn't have asked for better guidance.

I also want to thank all the members of the DAMIC-M collaboration who helped me along the way.

Thanks to all my colleagues and friends with whom I shared this PhD adventure and who made me feel at home even in another country.

More generally, I thank all my friends who stayed by my side during these three years, even if only virtually.

Thanks so much to Nicola, who has been my rock during these years.

Ultima ma non meno importante, vorrei ringraziare la mia famiglia che mi ha sempre supportata e senza la quale non sarei potuta arrivare fin qui.

TABLE OF CONTENTS

INTRODUCTION

Ordinary matter constitutes only a small fraction (5%) of the Universe, while 27% of it is composed of an elusive type of matter known as Dark Matter (DM). Even if DM is five times more abundant than ordinary matter, its nature remains a mystery. The evidence collected so far indicates that DM interacts with ordinary matter predominantly via gravity, has a life-time compatible with the age of the Universe, is invisible, non-relativistic, and collisionless.

Many candidates have been proposed in the years. Among the most popular ones, there are the so-called Weakly Interacting Massive Particles (WIMPs), with mass in the few GeV-TeV range. These particles are supposed to be in thermal equilibrium with the radiation and baryon plasma in the early Universe. When the expansion of the Universe made impossible the DM particle interaction and annihilation, a freeze-out mechanism occurred. Thus, the DM decoupled from the plasma and its abundance remained fixed to the current observed value. In order to reproduce the latter, an annihilation cross-section of the weak interaction scale is needed. This coincidence is referred as the "WIMP miracle".

Exploring and confirming the DM composition would require it to interact with the ordinary matter in an alternative way other than gravitationally. Based on the assumption that this is possible, even if extremely rare, different approaches have been developed in the past decades to catch a DM signal. The direct detection method looks for scattering events of DM particles with underground ordinary matter targets. The indirect approach, instead, assumes the DM particles to decay in ordinary matter ones. Finally, DM searches at colliders look for hints of the production of DM particles in ordinary matter collisions.

Given the lack of an observation of a WIMP signal, whose parameter space is getting more and more constrained, the scientific community drove their interests towards other candidates, e.g., the hidden sector ones. The hidden sector would be "parallel" to the ordinary one and the communication between the two would be possible through a portal. For example, the existence of an extra U(1) symmetry has been theorized together with the corresponding gauge boson, the dark (or hidden) photon. The latter, having a kinetic mixing with the ordinary photon, would allow a link between the two parallel sectors.

DAMIC-M (Dark Matter In CCD at Modane) is a near future direct detection experiment that will reach unmatched sensitivity to hidden sector DM particles, while also continuing the search for WIMPs at low masses. The experiment will be installed in 2024 at the Underground Laboratory of Modane and will have a target constituted by Charge Coupled Devices (CCDs). These are silicon-based pixelized sensors, commonly employed in the astronomical field. CCDs are able to collect the charges created by particle interactions that take place in their silicon bulk. Due to the low level of dark current and of readout noise introduced on the single charge measurements, these devices can detect small ionization signals (only a few electrons) from recoiling nuclei or electrons following the scattering of low-mass dark matter particles. The silicon small nucleus mass ensures a good sensitivity to nuclear recoils of WIMPs with masses in the range 1-10 GeV, while silicon small band gap ($\sim$1.1 eV) provides sensitivity to the hidden sector DM-electron interactions. Furthermore, the excellent spatial resolution of CCDs results in the unique capability to characterize and reject background events from radiogenic sources. The use of these instruments in the DM search was pioneered by DAMIC at SNOLAB. The experiment consisted of 7 CCDs (4k pixels $\times$ 4k pixels, 6 cm $\times$ 6 cm) and featured an active mass of about 42 g. The CCDs were cooled down to a temperature of about 140 K to ensure a low level of dark current. The minimum dark current level that has been measured is about 10^{-3} e^{-}/pixel/day. The readout noise on a single pixel charge measurement was 1.6 e^{-}. DAMIC-M will introduce several novelties with respect to its predecessor. The detector mass will be increased by about a factor 17, using $\sim$200 CCDs, each with an area of 1.5k $\times$ 6k pixels (2.25 cm $\times$ 9 cm). The background level will reach a fraction of d.r.u (events/keV/kg/day) against the about 10 d.r.u reached by DAMIC. Furthermore, a novel CCD technology, based on skipper amplifiers, will allow for sub-electron readout noise. Standard CCDs are limited by low frequency noise components that don't permit to further improve the readout noise to the sub-electron level. Thanks to the skipper readout, the same pixel charge can be read multiple times in a non-destructive way. Averaging over the N different measurements allows to dump by a factor $1/\sqrt{N}$ the readout noise.

This thesis is inserted in this context of DM search with DAMIC-M. It focuses mainly on the background estimation via simulations and its characterization via specific experimental measurements.

To lower the DAMIC-M background rate to the foreseen goal, an extensive campaign of innovation of the detector technology and design is ongoing. Simulations are being ex-

ploited to optimize the detector design and to drive the material selection and handling. The author of this thesis was mostly involved in this task. The simulation chain relies on a Geant4 and a Python based codes. These have been developed by the DAMIC-M collaboration and part of this thesis was committed to their improvement and optimization. The Geant4 based code is used to simulate the interactions of the particles that pass through the experimental setup. The Python based code is called WADERS (softWAre for Dark matter ExpeRiments with Skippers) and has been developed to mimic the CCD response. For each assessed detector design, a full simulation of the setup is performed. Isotopes are generated in the bulk or surface of the detector components and the corresponding background level is predicted, based on the expected isotope activities. The simulations presented in this work helped to identify the major contributors to the background and to derive a limit for the exposure time to cosmic rays of the detector components.

Having a complete knowledge of the possible background sources is fundamental for the DM search. Compton scattered electrons by environmental gamma rays represent a major source of background for DAMIC-M, since their spectra extend down to the energy region of interest (eV - keV range). Therefore, a precision measurement of the Compton spectrum was carried out with a DAMIC-M pre-production CCD, exposed to 60 keV gamma rays from an ^{241}Am source. Thanks to the skipper readout, the spectrum was measured down to 23 eV. The excellent energy resolution of the skipper CCD allowed to probe characteristic spectral features that could not be resolved in a previous measurement using a DAMIC standard CCD. The author of this manuscript contributed to the analysis of the data collected in this new measurement. A parametrization of the Compton spectrum was also derived in this thesis work context.

This thesis is structured as outlined in the following. Chapter 1 introduces dark matter, the main evidence of its existence and the most popular candidates. Chapter 2 describes the operation of CCDs with a focus on their application in DM experiments like DAMIC and DAMIC-M. Chapter 3 summarizes the most relevant types of background for DAMIC-M and the main strategies for their mitigation. Chapter 4 describes the simulation codes and their features. Chapter 5 offers an overview of all the assessed detector designs and the main simulation outcomes. Lastly, Chapter 6 focuses on the Compton scattering measurement carried out by the DAMIC-M collaboration.

Dark matter

The name Dark Matter (DM) refers to the unknown and invisible mass component of the Universe that so far has been observed interacting only gravitationally with Standard Model (SM) particles. The word "dark" reflects the lack of knowledge about its composition or type of interactions, while the word "matter" refers to its gravitational influence on the standard matter. Despite overwhelming astrophysical and cosmological evidence exists for DM, it still continues to elude detection strategies. Many different candidates have been proposed and currently several experiments all around the world are looking for a trace in their experimental setups to reveal DM elusive nature.

The direct detection is one of the approaches adopted for the DM search. It relies on the possibility of having a signal from a DM colliding with ordinary matter targets. Among the experiments that exploit this strategy there are the DAMIC and DAMIC-M ones, on which this thesis is focused. The two experiments feature a silicon-based target, which ensures a good sensitivity to low mass DM candidates. DAMIC and DAMIC-M will be further described in Chapter 2.

This chapter summarizes the many observations that largely support the existence of such a mysterious type of matter. The main detection strategies and the most popular DM candidates will be outlined, the latter focusing on those to which both DAMIC and DAMIC-M detectors are sensitive.

1.1 Evidence of Dark Matter existence

Since the beginning of the 20th century, evidence started to come out suggesting that luminous stars may not comprise most of the mass of the galaxies, as it was initially thought. The first mention of "dark matter" came from the French mathematician and physicist Henri Poincaré. In 1906, he used the term "matière obscure" [1] referring to the work of the physicist Lord Kelvin, who first pointed out that many of the starts of the Milky Way, "perhaps the majority of them", may be "dark bodies" [2]. The Swiss-

American astronomer Fritz Zwicky is often considered as the first to have inferred the existence of dark matter. In the 1930s, he applied the virial theorem to the Coma galaxy cluster to relate its potential and kinetic energies [3, 4]. He found evidence of unseen mass that he called "dunkle Materie" (dark matter). The astronomy community responded to these results with skepticism and struggled for decades to find a unified solution for this non-luminous unexplained mass problem. A huge leap forward in the acceptance of the dark matter existence was made in the 1970s by Vera Rubin and her collaborators [5, 6]. They observed an inconsistency between the measured velocity distributions of stars and gas orbiting the galactic centre and the expected ones. This can be explained assuming that the mass of a galaxy has a significant non-luminous dark matter component. Later on, cosmological and astrophysical measurements related to the large scale structure of the Universe provided further compelling evidence for the existence of dark matter. In this context, the precision measurements of the small fluctuations in the Cosmic Microwave Background (CMB) are particularly relevant. These provided a solid experimental basis for what today is considered to be the standard model of cosmology, the ΛCDM model [7]. Within this model, the ordinary baryonic matter constitutes only 5% of the energy–matter density of the Universe, $\Omega_B \simeq 0.05$, while the cold dark matter (CDM), accounts for 27% of it, $\Omega_C \simeq 0.27$ [1]. Finally, gravitational lensing effects also allowed to reveal the presence in galaxies of a important dark matter mass component.

The most relevant dark matter evidence will be further explored in the following sections.

1.1.1   Rotation curves of galaxies

One of the most direct evidence of dark matter comes from the rotation curves of galaxies, i.e., the circular velocity profile of the stars and gas in a galaxy as a function of their distance from the galactic center. Under some reasonable simple assumptions, it is possible to derive the mass distribution of galaxies from their rotation curves. In a spiral galaxy like the Milky Way, the majority of the luminous mass is located in the central bulge. Outside this region, the tangential velocity v of a star of mass m can be derived

---

1. Most of the energy–matter density of the Universe is in the form of dark energy, $\Omega_\Lambda \simeq 0.68$. The dark energy is attributed to a non-zero cosmological constant (Λ) of Einstein's general relativity equations and is considered to be the cause of the acceleration of the Universe expansion [7].

considering the centripetal force in a gravitational field [7]:

$$\frac{mv^2}{r} \approx \frac{Gm}{r^2}M(r),\qquad(1.1)$$

where $M(r)$ is the total mass within a radius r. Since most of this mass is concentrated in the central bulge, the tangential velocities of the stars should decrease as $r^{-1/2}$. However, in the 1970s, Vera Rubin and Kent Ford found this assumption to be false for the Andromeda nebula and other spiral galaxies [5, 6]. In fact, they observed the rotation curves to be flat at very large galactocentric distances, implying the mass distribution in the galaxy to be approximately proportional to r, as shown in Figure 1.1. Historically, it was
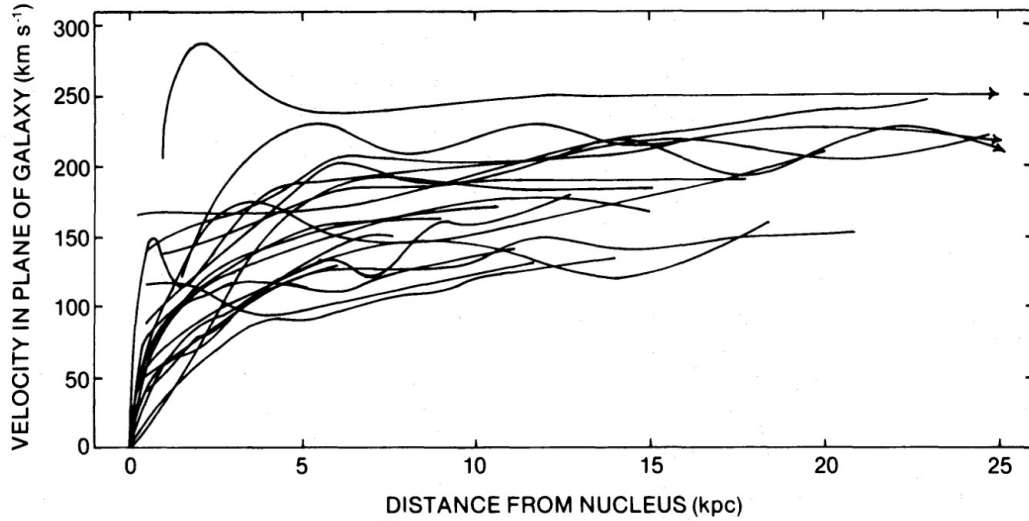
Figure 1.1 – Rotation curves for 21 spiral galaxies measured in [6]. © AAS. Reproduced with permission.

this observation that did the most to convince the scientific community of the presence of a significant non-luminous component, known as dark matter, in the outer regions of galaxies.

1.1.2 Cosmic Microwave background

Measurements related to the large scale structure of the Universe and precision measurements of the small fluctuations in the Cosmic Microwave Background (CMB) provided other evidence for the existence of dark matter.

The Cosmic Microwave Background represents the relic sea of photons originated in
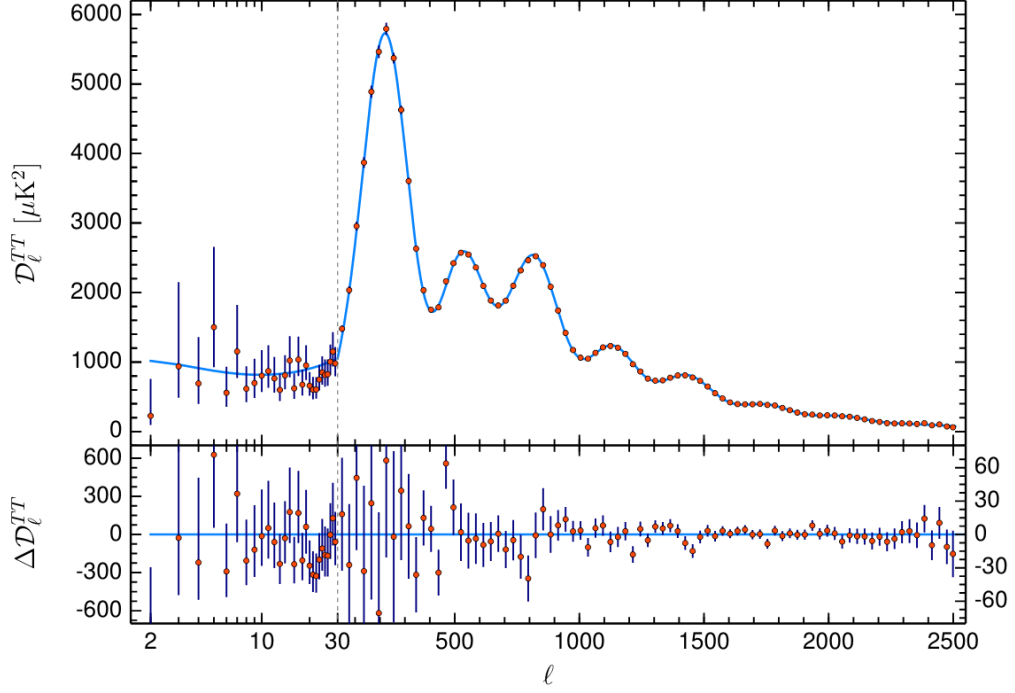
Figure 1.2 – Planck 2018 temperature power spectrum [8]. The parameter *l* indicate the multiple moment (linked to the angular scale as $\theta \sim 1/l$). The best ΛCDM fit is plotted in light blue in the upper panel. Residuals with respect to this model are shown in the lower panel. The position of first peak, related to the curvature of the universe, is consistent with a flat universe. Credit: [8], reproduced with permission © ESO.

the early Universe when electrons started to be bounded in atoms. This epoch is referred by cosmologists as *recombination*, and establish the moment when the Universe, initially hot and fully ionized, became "transparent", allowing photons to travel undisturbed without scattering off free electrons [9]. The CMB provides important information about the temperature fluctuations experienced by the baryon-radiation plasma (baryon[2] and radiation are in thermal equilibrium) at *recombination*. In fact, although the CMB has an almost constant temperature of ~2.73 K, it features very small anisotropies of the order of μK [10]. These temperature fluctuations are directly correlated to the density anisotropies, that then growing gave rise to the current large scale structure of the Universe. A huge hint for the dark matter existence comes from the CMB temperature fluctuations. These are measured to be $\frac{\delta T}{T} \sim 10^{-5}$ [8, 10, 11]. However, assuming a universe composed by only baryons and photons, fluctuations $\frac{\delta T}{T} \sim 10^{-3} - 10^{-4}$ are required at *recombination*

---

2. In cosmology, this word refer to protons, neutrons ed electrons.

to reproduce the current large scale structure [9]. The presence of DM allows to solve this discrepancy. In fact, DM doesn't decouple from radiation at *recombination* like ordinary baryonic matter, but before, allowing the fluctuations to grow enough until the CMB creation. In particular, the dark matter decouples from the baryon-radiation plasma before the so-called *equivalence* (prior to *recombination*) [9]. The name *equivalence* derives from the fact that the matter density equals radiation density, establishing the transition from a radiation dominated era to a matter dominated era. From the *equivalence* on, dark matter density perturbations are allowed to grow, since gravitational interactions are no more damped by radiation. On the contrary, ordinary matter and radiation are strictly coupled until the *recombination*, and density perturbation cannot grow, due to radiation pressure.

By decomposing $\frac{\delta T}{T}$ in spherical harmonics, the CMB power spectrum can be derived (Figure 1.2). Its distinctive oscillation pattern (acoustic peaks) is due to the oscillations of the baryon-photon fluid in the gravitational potential dominated by dark matter density perturbations [9]. From the relative height of these acoustic peaks, the amount of baryonic and dark matter can be estimated. The Planck satellite provided the most accurate measurement of temperature anisotropies in the CMB [8]. Planck results affirm that about 27% of the energy-matter density is in the form of dark matter, while only the 5% in the form of ordinary matter. This measurement was, and still is, one of the most compelling evidence supporting the existence of DM and the validity of the ΛCDM model.

1.1.3 Gravitational lensing

Gravitational lensing is an effect that lays its foundation on the theory of General Relativity, for which the light path can be bent by mass. The massive body inducing this deviation is accordingly called a gravitational lens. This phenomenon can cause far away objects to be observed distorted, elongated or duplicated around a gravitational lens. While a strong lensing phenomenon leads to easily visible distortions, this is not the case for weak lensing effects, which rely more on statistical analysis and a proper characterization of the systematic uncertainties [13]. By observing distortions in a large number of galaxies, the dark matter distribution in the area can be inferred. Weak lensing analysis applied to the Bullet Cluster revealed the signature of DM [12]. The Bullet Cluster was formed in the merger of two sub-clusters, each composed by galaxies, X-ray emitting hot gas plasma, and potentially dark matter. During the merger, galaxies behave like collision-less particles, while the fluid-like X-ray emitting plasma experiences
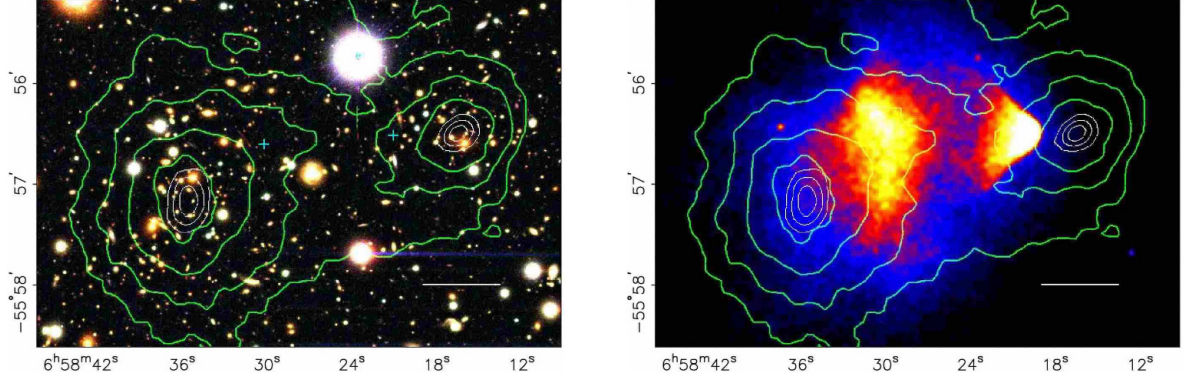
Figure 1.3 – Images of the Bullet cluster merging with the mass distribution reconstructed using weak gravitational lensing (green contours) [12]. The peaks of the mass distribution are indicated by the white contours (68.3%, 95.5%, and 99.7% confidence level). On the right the X-ray image of the bullet cluster (colored regions: blue least dense to white most dense), taken by the Chandra telescope [12]. © AAS. Reproduced with permission.

ram pressure. By deriving the map of the gravitational potential, it was possible to test the presence of a component of dark matter. In fact, in its absence, the gravitational potential is expected to trace the dominant visible matter component, which is the X-ray plasma. However, the opposite situation was observed, with the mass distribution deviating significantly from the X-ray one, as shown in Figure 1.3 [12]. This indicated the presence of a collision-less, non luminous dark matter component.

1.2   Dark matter candidates

Dark matter is one of the most important Universe ingredients for the ΛCDM model. However, another condition is required, that is the necessity for the dark matter to be cold. From this the acronym "CDM". This requirement comes from cosmological simulations that demonstrated the influence of a cold or hot dark matter candidate on the evolution of the large scale structure [14]. Being cold means to be non-relativistic during the epoch of structure formation, in contrast with a hot candidate. Neutrinos represent an example of hot dark matter, as they remain relativistic throughout the expansion and cooling of the Universe [7]. Massive particles instead became non-relativistic during the first few years after the Big Bang [7]. Simulations have shown that hot dark matter particles would tend to collapse and form very large structures first, and only later would form smaller (i.e., galaxy-sized) halos through the fragmentation of larger halos ("top-down"

scenario). This is because, at smaller scales, density fluctuations would be washed out by the random thermal motion of dark matter if relativistic [14]. On the contrary, cold dark matter particles form structures through a "bottom-up" scenario, beginning with the smallest halos, which then proceed to form larger halos through a succession of mergers [14]. By comparing results of simulations with those of galaxy surveys, it was possible to deduce that the majority of the energy-mass density associated with the non-baryonic dark matter is due to cold (non-relativistic) matter [14]. Warm dark matter candidates (WDM) are possible as well, with a mass $\gtrsim$ keV to not damp the growth of density perturbations [15]. An example of warm candidate is the sterile neutrino, much heavier and with much weaker interactions than ordinary neutrinos [16]. This particle was never in equilibrium with the SM thermal bath and could have been produced by oscillations due to its mixing with the SM neutrinos [15, 16].
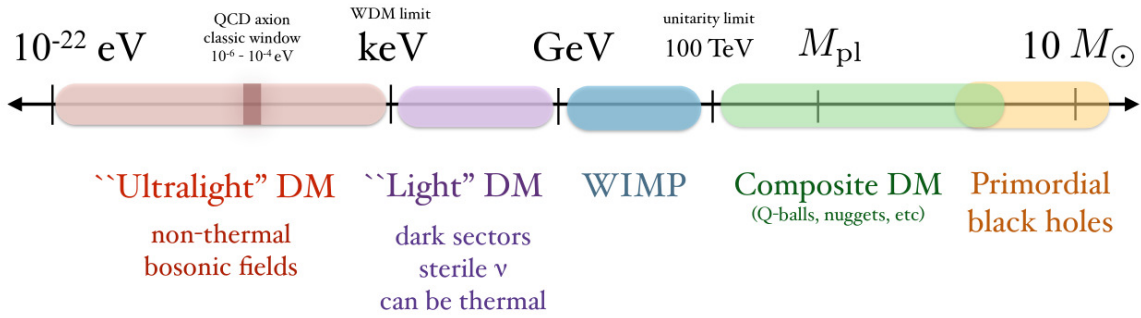
Figure 1.4 – The mass range of allowed DM candidates (not to scale), including both particle candidates and primordial black holes [15]. M_{pl} indicates the Planck mass.

Each dark matter candidate must be consistent with a broad range of observations on astrophysical and cosmological scales, while also satisfying laboratory bounds. The requirements for a dark matter candidate can be summarized as follows [15, 17]:

— DM has gravitational interactions with normal matter. Non-gravitational interactions of DM must be very rare;

— DM is very stable, with a life-time comparable to that of the Universe;

— DM is cold (non-relativistic). Warm candidates are also allowed in particular scenarios;

— DM is collisionless, otherwise non-gravitational interactions within the dark matter sector would affect the growth of density perturbations.

In the past decades, many candidates have been proposed, which span a wide range of masses. Figure 1.4 gives a taste of the current DM landscape. The main candidates

are described in following sections.

It is worth mentioning that a modified gravity theory (MOdified Newtonian Dynamics, MOND) framework has also been proposed as an alternative to the dark matter hypothesis [18]. The MOND paradigm assumes a departure from the Newtonian theory on the galactic scale and does not require any additional matter content. However, even the most popular MOND theory, TeVeS [19], gives a notably worse fit to CMB and large scale structure data compared to ΛCDM [15].

1.2.1   Weakly Interacting Massive Particles
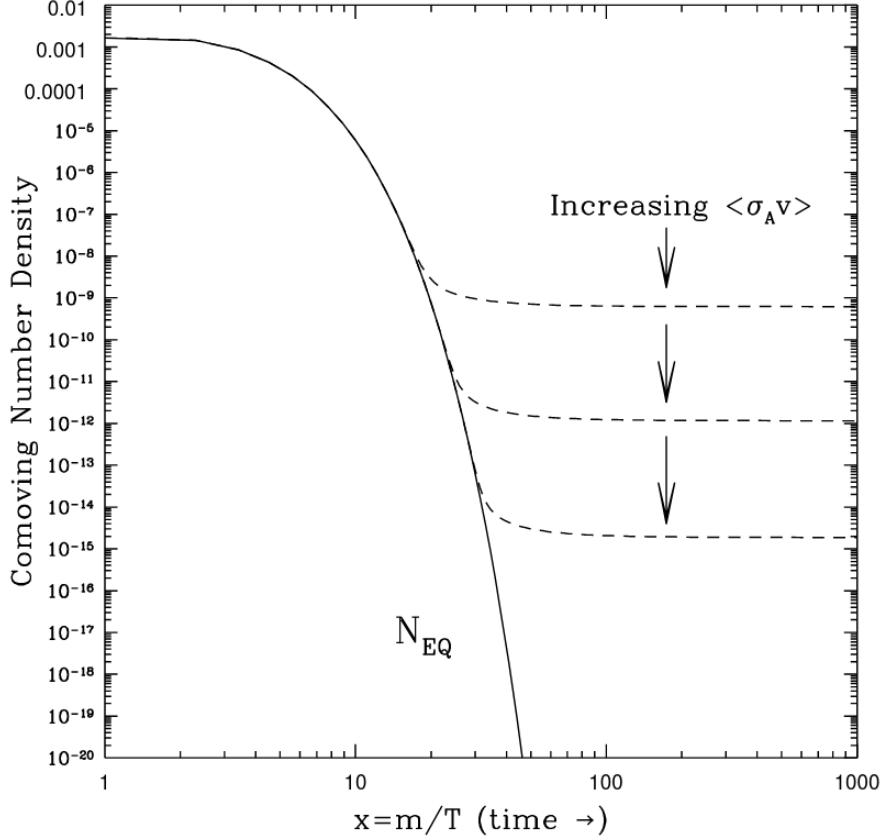
Figure 1.5 – Comoving number density of a WIMP in the early Universe [20]. The x parameter indicates the ratio between the mass of the WIMP (m) and the temperature of the universe (T). The solid curve is the equilibrium abundance. The dashed curves indicate the relic abundance for different values of the velocity averaged annihilation cross-section $\langle\sigma v\rangle$. To reproduce the current dark matter abundance, $\langle\sigma v\rangle \sim 3 \cdot 10^{-26}\mathrm{cm}^3\mathrm{s}^{-1}$.

19

The ΛCDM standard model of cosmology suggests that a significant fraction of the cold dark matter in the Universe may be in the form of a new type of Weakly Interacting Massive Particle (WIMP), with a mass in the few GeV-TeV range. WIMPs are assumed to have been produced in the early Universe when they were in equilibrium with the thermal plasma. At that stage, dark matter annihilation into lighter particles and the inverse process (production) were equally efficient. However, as the Universe expanded, the temperature of the plasma became lower than the WIMP mass, making impossible the production processes. The dark matter number density started to drop exponentially, until the annihilation rate Γ became smaller than the Hubble expansion rate (H). Dark matter thus decoupled from the plasma and reached its relic density. The moment when Γ = H is referred as "freeze-out". Figure 1.5 shows the evolution in time of the comoving [3] number density of a stable particle as the WIMP in the early Universe. The dark matter relic density is inverse proportional to the velocity averaged annihilation cross section $\langle \sigma v \rangle$. In order to reproduce the current dark matter density, $\langle \sigma v \rangle$ is of the order of the weak interaction scale, $\sim 3{\cdot}10^{-26}$ cm^3 s^{-1} . This coincidence is usually referred as "WIMP miracle" [20]. By expressing the cross section as a function of the dark matter mass, this result is compatible with a mass in the range between $\mathcal{O}(10 - 1000\text{GeV})$.

WIMPs represent one of the most popular DM candidates, especially in the direct detection field. Section 1.3.3 focuses on the WIMP searches in direct detection experiments.

1.2.2 Hidden sector particles

The interest in the hidden, dark sector is growing more and more, due to the lack of experimental observations of WIMPs. Dark sector particles populate the sub-GeV range of the dark matter landscape. Considering the simple thermal relic framework, with abundance fixed by freeze-out in the early Universe, DM in the MeV-GeV mass range are allowed if there are light (below the weak scale) dark mediators that control the annihilation rate [15]. In this way, the annihilation cross section would be large enough to make the DM mass density not too high with respect to the observed one. This motivated the assumption of the existence of a dark sector, parallel to the ordinary one described by the standard model. Such dark sector can contain few or many states, like fermions or scalars or both, depending on the model, and dark matter can be found among them

---

3. The comoving coordinate system is used in cosmology to factor out the expansion of the universe. Therefore, in a comoving coordinate system, particles that don't move through space have fixed coordinates, even is that space is expanding.

[21]. The interaction between the two parallel worlds would take place through a portal, which may take various forms depending on the type of involved mediator [21]. One of the best motivated and most studied cases is the portal involving the so-called dark photon, a spin-1 vector mediator. The latter would be the gauge boson of an extra U(1) symmetry, in an analogy with the electro-magnetism case. However, unlike the visible one, the dark photon can be massive. The dark photon mediates the interactions among the dark sector particles but (if massive[4]) is also coupled to standard model because of its kinetic mixing with the ordinary, visible photon [21]. This would lead to detectable signals and it is therefore of major interest for direct detection experiments (see Section 1.3.3). Of course, the coupling with the SM particles has to be sufficiently small, otherwise numerous laboratory experiments would have already detected a DM signal. Furthemore, in case of an ultra-light mediator (mass $\ll$ keV), the couplings are so small that the DM would never have thermalized with the SM sector. The DM abundance would be therefore set by a "freeze-in" mechanism, via SM particle annihilation or decay into DM particles [22].

Even if in most scenarios dark matter is considered to be one of the fermion or scalar states of the hidden sector, it is also possible for a massive light dark photon itself to be a DM candidate [21]. In this scenario, the dark photon would be produced non-thermally in the early Universe, via a mechanism similar to that of the axion [21] (see Section 1.2.3). A dark matter dark photon could also have been produced gravitationally, during inflation [21]. A dark photon can have a mass in the MeV–GeV range, but also sub-eV masses are possible [23]. The existence of a dark photon dark matter candidate can be probed by direct detection experiments via its interaction with electrons in the target material. This is discussed in Section 1.3.3.

1.2.3   Axions

One of the unresolved puzzles in the Standard Model is the lack of any observed CP (Charge conjugation Parity) violation in the strong interactions described by Quantum Chromodynamics. This is usually referred as "strong CP problem". In fact, as in the case of the weak interactions, which are known to violate CP, the strong interactions also

---

4. If massless, the dark photon does not couple directly to any of the SM currents and interacts with ordinary matter in a different way than the massive case [21]. The massive dark photon has been receiving so far most of the attention because it couples directly to ordinary matter and therefore is more readily accessible in the experimental searches [21].

contain a CP-violating term in the Lagrangian. For non-zero quark masses, this term leads to (unobserved) CP-violating effects of the strong interactions. Peccei and Quinn [24] proposed the introduction of a pseudoscalar field, the axion field, as a solution for the strong CP problem. The axion particle features a very low mass, below 10^{-3} eV, but can still act as a non relativistic (cold) particle, due to the misalignment mechanism [25, 26]. In this scenario, the axion field is assumed to have a constant initial value in the early Universe that is away from the minima of the strong interaction potential. The expansion rate of the Universe H, being much larger than the axion mass, did not allow the field to relax to one of the potential minima. However, when H became comparable to the axion mass (H $\sim \frac{m_a}{3}$), the field started to oscillate. These oscillations behave like non-relativistic matter [21, 25, 26]. Although in a small mass range $\sim 10^{-6}$-10^{-4}eV, axions can account for all the dark matter density observed [14].

1.2.4 Superheavy dark matter and primordial black holes

Very heavy DM candidates can be consistent with observations of galactic dynamics, up to a mass $\sim 10^4 - 10^5$ M$_\odot$ [5] [15].

Super heavy particle candidates have been proposed and are typically called WIMPzillas [15]. For masses larger than the Planck mass M$_{pl}$, DM candidates include composite objects, such as bound states or nuggets of lighter fundamental particles [15].

The dark matter is usually assumed to be made up of some form of elementary particle. However, primordial black holes (PBHs) could also provide a fraction of it. These must have formed well before the *recombination* epoch in the early Universe, and therefore they differ from the standard black holes, made up of baryons and formed at the present epoch. Various constraints restrict the possible PBH mass windows to 10^{16}–10^{17} g, 10^{20}–10^{24} g, and 10–10^3 M$_\odot$ [15, 27].

1.3 Dark matter search strategies

Scientists have adopted three different strategies to detect DM particles. Direct detection (DD) experiments look for Galactic DM colliding with underground targets made of ordinary matter. Indirect detection (ID) experiments, instead, search for SM particles produced by the annihilation of DM particles localized within the gravitational potential

---

5. 1 M$_\odot$ is equal to $\sim 2 \times 10^{30}$ kg.

wells of the Milky Way and elsewhere. DM is also searched for at colliders between the products of SM particle collisions (collider production). All these search types are based on the assumption that the DM interacts with ordinary matter not only gravitationally, but also in an alternative way: DM-nucleon or DM-electron interactions in DD searches, DM annihilation to SM particles in ID searches, DM production from SM particles in searches at colliders. Figure 1.6 shows a schematic representation of the possible dark matter ($\mathcal{X}$) couplings to an ordinary matter particle (P) on which each detection method is based. It is worth noting that the various detection strategies provide different and complementary information about the nature of DM [17, 28]. This will be especially relevant in presence of a signal. Making a comparison between the outcomes of DM searches at colliders, DD, and ID experiments requires to assume a specific particle physics model. For example, collider results can be interpreted in terms of fundamental parameters of a simplified model (e.g., masses, couplings) [17]. Note, however, that collider searches cannot directly measure a dark matter particle or test its lifetime. Therefore, the definitive confirmation of a discovery would require a combination with DD and ID results. Making a link between the outcomes of the DD and ID experiments can be also demanding. In fact, the ID approach is sensitive only to the annihilation cross section of dark matter and not to the scattering one. However, there are some exceptions, for example considering the case of DM captured by the Sun via elastic scattering. The DM can in turn decay into SM particles, making possible to link the elastic scattering cross section to the annihilation one [28].

In the next sections, collider, ID, and ID searches are described in more details, with a focus on the DD approach and the corresponding detection channels.

1.3.1   Indirect detection

In regions of high DM density, an enhanced DM self-annihilation, scattering or decay into Standard Model particles, could produce a measurable particle flux. The prime goal of dark matter indirect detection is to recognize these products of dark matter origin and distinguish them from the astrophysical background. DM particles can gravitationally accumulate in astrophysical objects such as stars and galaxies. The most favoured sources to search for indirect signals are the galactic centre and halo and close galaxy clusters or dwarf galaxies. Milky Way dwarf spheroidals galaxies are ideal targets for an indirect detection of DM [29]: they are located not too far from Earth (20–200 kpc), they have a large measured mass to light ratio, which indicates the presence of a large amount of
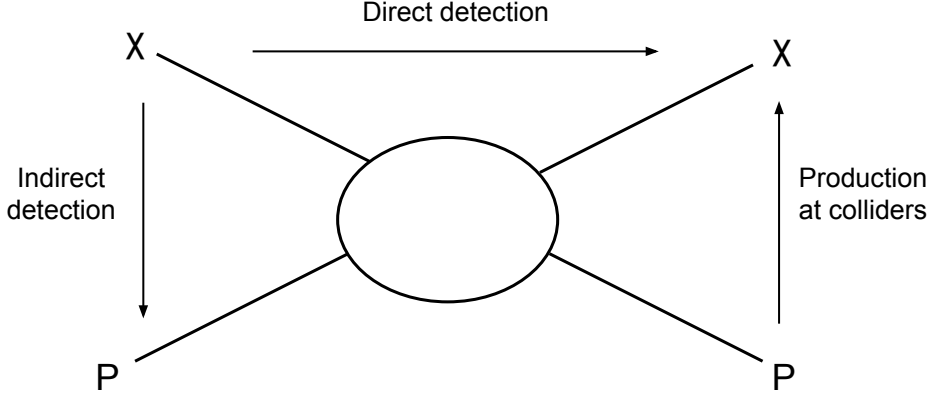
Figure 1.6 – Schematics showing the possible dark matter detection strategies. $\mathcal{X}$ represents a dark matter particle interacting with an ordinary matter one (P).

DM, and they are characterized by a small astrophysical background. Possible examples of dark matter ($\mathcal{X}$) annihilation channels are [28]:

$$\mathcal{X}\bar{\mathcal{X}} \to \quad \gamma\gamma, \gamma Z, \gamma H \tag{1.2}$$

$$\mathcal{X}\bar{\mathcal{X}} \to \quad q\bar{q}, ZZ, W^+W^-. \tag{1.3}$$

Some of the products decay further into e^+e^-, $p\bar{p}$, γ-rays, and neutrinos. Standard model particles can also be produced via DM decay. However, while the annihilation cross section depends quadratically from the DM density, decay processes depend only linearly. Furthermore, DM particles might be gravitationally captured inside the Sun due to the elastic scattering with its nuclei. The annihilation of captured DM particles can produce neutrinos that can propagate then out of the Sun and might be detectable with Earth-based neutrino telescopes. In general, the most convenient SM products to look at are γ-rays and neutrinos, since, being neutral, they point to the source where they were produced[6]. On the contrary, produced charged particles are deflected in the interstellar magnetic fields. Examples of telescopes, satellites, and detectors looking for DM interaction products are: the MAGIC [30], HESS [31] and VERITAS [32] Cherenkov telescopes, the XMM-Newton [33] and Chandra [34] X-ray satellites, the Ice Cube [35], ANTARES

---

6. While neutrinos travel unaffected from the production source, γ-rays can be affected by absorption in the interstellar medium.

[36], and Super-Kamiokande [37] large neutrino detectors, the AMS [38] and PAMELA [39] satellites, the Large Area Telescope (LAT) [40]. So far no significant DM signal has been observed in a indirect detection search.

1.3.2 Production at colliders

Colliders have revealed much about ordinary matter and could play an important role also for learning more about DM, assuming that it can be produced in SM particle collisions [17]. DM-SM matter interactions may be feeble because mediated by a heavy mediator or by a mediator with small couplings to the Standard Model. Therefore, many high-energy collisions are required to extensively search for these interactions. This makes the LHC (Large Hadron Collider), the highest-energy collider currently in operation, and its successors suitable means to look for a DM signature [17]. In 2015-2018, the LHC achieved a recorded luminosity of $140\,\mathrm{fb}^{-1}$ for proton-proton collisions but its upgrade, high-luminosity LHC (HL-LHC), is planned to reach an integrated luminosity of $3000\,\mathrm{fb}^{-1}$ [17].

Collider experiments alone cannot discover DM, but they can indirectly prove the existence of invisible particles, potential DM candidates. Like neutrinos, DM produced at colliders would almost always pass invisibly through the detector. Consequently, the presence of a DM particle would only be inferred by observing events with missing momentum and energy [7] [17]. Collider can probe reactions of the type:

$$pp \rightarrow \mathcal{X}\overline{\mathcal{X}} + x \tag{1.4}$$

where p is the proton, $\mathcal{X}$ a dark matter particle, and x can be a hadronic jet, a photon or a leptonically decaying Z or W boson. Dark interactions at colliders can also be probed by looking for resonances (e.g, dilepton, dijet), due to a dark mediator decay in SM particles (e.g., leptons or quarks). The results obtained so far at LHC are consistent with the Standard Model expectations but further searches will be performed in the next years [17].

---

7. In hadron colliders, the quantity of interest for a DM search is the missing transverse momentum and energy. The transverse plane is the one perpendicular to the colliding beam direction. The missing energy and moment can only be measured in the transverse plane since the initial momentum of colliding partons is not known a priori.

1.3.3 Direct detection

The aim of direct detection experiments is to identify nuclear or electron recoils produced by dark matter particles in the detector target. The type of recoil depends on the dark matter candidate. WIMPs are expected to induce nuclear recoils, while hidden sector particles are explored via their interaction with the electrons in target materials. The phenomenology linked to each of these candidates is described in the following sections.

A dark matter interaction can induce three types of signals, depending on the detector technology in use: the production of heat (phonons in a crystal), the release of scintillation photons following the excitation/de-excitation of a target nucleus, and the direct ionization of the target atoms. Detection strategies focus either on one of the three, or on a combination of two of these signals. Having two detection channels can be very useful to discriminate between different particle signals and to reject background events. Figure 1.7 shows a scheme of the possible types of signals, as well as the associated most common detector technologies.
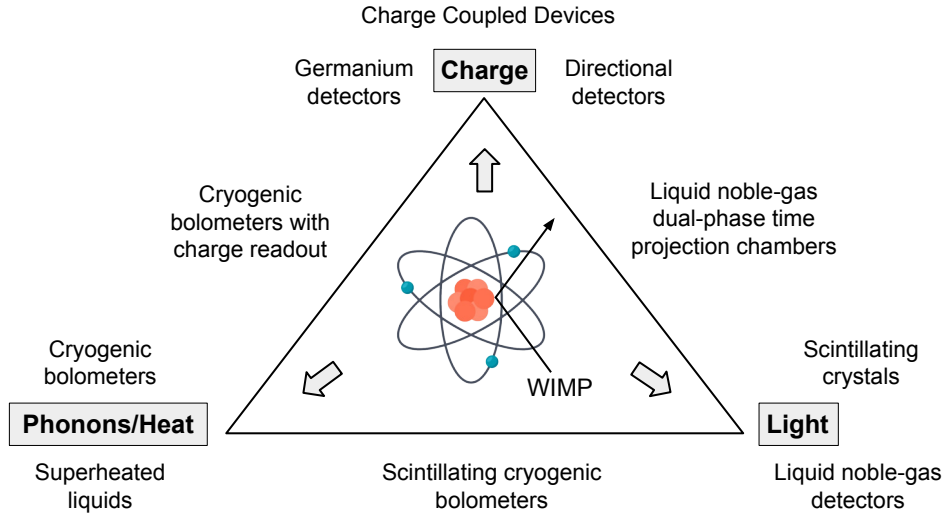
Figure 1.7 – Possible DM detection channels associated with the corresponding most common detector technologies. In the image, a WIMP interacting with a nucleus is represented but the same is valid for a general (DM) particle which releases energy in a target material.

The signal energy threshold depends on the type of detector in use. For example, the typical energy scale to create phonons in crystals is of the order of a few meV [28]. To create an electron-hole pair in semiconductors an energy of a few eV is necessary [28].

Instead, for liquid noble gases the ionisation energy is of the order of (10-20) eV [28]. In the case of scintillators (solid or liquids), only a small fraction (1-10 %) of the total recoil energy is transferred to scintillation processes [28]. The lower is the threshold, the smaller are the recoil energies that can be probed.

Examples of dark matter experiments using scintillator targets are DAMA [41], Anais [42], and COSINE [43] which employ low radioactivity NaI(Tl) crystals.

To collect the phonons induced by a particle interaction, crystal bolometers are used, cooled down to a temperature of about 10-100 mK. The ionization or scintillation charge signal can be recorded as well. The SuperCDMS experiment [44] uses germanium and silicon bolometers to search for dark matter. It measures both the phonon as well as the charge signal. A similar technique is used by the EDELWEISS experiment [45] constituted by germanium bolometers. The CRESST-II experiment [46] exploits, in addition to the phonon signal, also the scintillation light emitted by recoils in CaWO4 crystals.

Liquid noble-gas (argon or xenon) detectors feature high scintillation and ionisation yields. To exploit both these two detection channels, dual phase (liquid/gas) Time Projection Chambers (TPCs) are tipically used. This strategy is adopted by the XENON [47], LUX-ZEPLIN (LZ) [48], and PANDA-X [49] collaborations (using xenon) and by the DarkSide-50 experiment (using argon). Another technique to detect DM signals consists in using a Spherical Proportional Counter (SPC) filled with light noble gases (H, He and N), able to collect the ionization charges created in its inside. This strategy is at the base of the NEWS-G experiment [50].

Other types of detectors exploited in the DM search are the so-called directional ones. This name derives from the aim to study the direction of the recoils induced by DM interactions. To do so, they make use of nuclear emulsions or low pressure gas targets in TPCs with different electron amplification devices and track readouts, like Multi-Wire Proportional Chambers (MWPC). DRIFT (Directional Recoil Identification From Tracks) [51] was the pioneer experiment of this class of detectors, using MWPCs attached to a TPC filled with electronegative gas.

Superheated liquids are also used as DM target materials in bubble chambers. The liquids are kept at a temperature mildly below their boiling point such that a local phase transition will create a bubble (if the energy deposited in the medium is above some threshold). The PICO experiment [52] is based on this technology.

The DAMIC [53], DAMIC-M, and SENSEI [54] experiments exploit the capability of Charge Coupled Devices (CCDs) to collect the ionization charges created in their

silicon bulk. Like SuperCDMS and EDELWEISS, they feature a semiconductor target but they cannot measure the phonon signal. However, particles can be identified exploiting the excellent spatial resolution of CCDs. The DAMIC and DAMIC-M experiments are extensively described in the next chapter, being at the core of this thesis work.

WIMPs scattering off nuclei

The WIMPs are expected to interact with the target material of a direct detection experiment scattering off nuclei. The elastic scattering of a WIMP with mass between 10-1000 GeV would produce a nuclear recoil with energy in the range of 1-100 keV [28]. Due to the low interaction strength expected for a dark matter particle, only single scattering events are expected. The identification of such interaction events requires a detailed knowledge of the signal signature, the particle and nuclear physics aspects, as well of astrophysical parameters such as the dark matter density and the halo velocity distribution in the Milky Way. The differential recoil spectrum resulting from WIMP interactions can be written as [28]:

$$\frac{\mathrm{dR}}{\mathrm{dE}}(E,t) = \frac{\rho_0}{m_\chi m_A} \int v \cdot f(\mathbf{v},t) \cdot \frac{\mathrm{d}\sigma}{\mathrm{dE}}(E,v)\, d^3v, \tag{1.5}$$

where m_χ is the dark matter mass, m_A is the nucleus mass, ρ_0 is the local dark matter density, v is the dark matter velocity defined in the rest frame of the detector, $f(\mathbf{v},t)$ accounts for the WIMP velocity distribution in the detector reference frame, and $\frac{\mathrm{d}\sigma}{\mathrm{dE}}(E,v)$ is the scattering differential cross section.

Considering the astrophysical aspect, it is common to assume a local DM density of 0.3 GeV/cm^3, derived from the mass modelling of the Milky Way, using parameters in agreement with observational data [28, 55]. However, depending on the profile model used for the halo, the density can vary from 0.2 to 0.6 GeV/cm^3 [28]. Given the constant DM density, the heavier is a particle, the less particles are available for scattering [28]. The dark matter velocity profile $f(v)$ is commonly described by an isotropic Maxwell-Boltzmann distribution which is truncated at velocities exceeding the galactic escape velocity (v_{esc}), usually set to 544 km/s [28, 55]. In the rest frame of a DD experiment, this velocity distribution is time dependent due to the revolution of the Earth around the Sun.

On the base of equation 1.5, direct detection experiments can exploit the energy, time or direction dependencies of the signal. The most common approach consists in

measuring the energy dependence of dark matter interactions. Another strategy is based on the study of the temporal variation of the differential event rate, looking for the so-called "annual modulation" signature: as a consequence of the Earth rotation around the Sun, the speed of the dark matter particles in the Milky Way halo relative to the Earth reaches his maximum around June 2nd and his minimum in December. Consequently, the amount of particles able to produce nuclear recoils above the detector energy threshold is also maximized in June [56]. This is the approach used by the DAMA experiment, which is the only one to have claimed the detection of a DM signal. This result is in conflict with the negative ones of all the other experiments, which even using the same detection technique and target didn't succeed in confirming the DAMA observation [57]. Directionality is another dark-matter signature which can be exploited for detection, since the direction of the nuclear recoils resulting from WIMP interactions has a strong angular dependence. The rate of events scattering in the forward direction is expected to exceed the rate for backwards scattering events by an order of magnitude. An oscillation of the mean direction of recoils over a sidereal day is also expected due to the rotation of the Earth (if the detector is placed at an appropriate latitude) [28].

To interpret the data of DM experiments, further assumptions on the specific particle-physics model as well as on the involved nuclear-physics processes have to be made. In general, the differential WIMP-nucleus cross section, $\frac{d\sigma}{dE}(E, v)$, can be written as the sum of a spin-independent (SI) contribution and a spin-dependent (SD) one. For WIMP spin-independent interactions, it is assumed that neutrons and protons contribute equally to the scattering process (isospin conservation), while for spin-dependent interactions, only unpaired nucleons contribute. In the case of a spin-independent and isospin-conserving dark matter interaction, the differential recoil spectrum takes the following form [28]:

$$\frac{\mathrm{dR}}{\mathrm{dE}}(E, t) = \frac{\rho_0}{2\mu_A^2 m_\chi} \cdot (\sigma_0 \cdot F^2(E) \cdot A^2) \int_{v_{min}}^{v_{esc}} \frac{f(\mathbf{v}, t)}{v} \, d^3v, \qquad (1.6)$$

where A is the number of nucleons, μ_A is the WIMP-nucleus reduced mass, σ_0 is the dark matter-nucleon cross-section at zero moment transfer, and F is a form factor taking into the dependence of the cross-section from the momentum transfer. The v_{min} parameter is the minimum WIMP velocity that can produce a nuclear recoil with energy equal to the threshold of the detector (E_{thr}):

$$v_{min} = \sqrt{\frac{m_A \cdot E_{thr}}{2\mu_A^2}}. \qquad (1.7)$$

A useful figure of merit is the maximum energy transferred at the nucleus during the scattering:

$$E_{nr}^{max} = \frac{2(v\mu_A)^2}{m_A} = \begin{cases} 2v^2 m_A & \text{if } m_\chi \gg m_A \\ 2v^2 \frac{m_\chi^2}{m_A} & \text{if } m_\chi \ll m_A. \end{cases} \qquad (1.8)$$

Considering the maximum v equal to 764 km/s (the galactic escape velocity plus the Earth velocity), the silicon nucleus mass of $\sim$28 GeV, and a DM mass of 1 GeV, the resulting recoil energy is of about 0.5 keV. This gives a sense of the importance of having a light nucleus as a target and a low energy threshold to probe light DM particles. Silicon, which constitutes the target material for the DAMIC and DAMIC-M experiments, does not only feature a relatively small nucleus mass, but also a low ionization threshold ($\sim$1.2 eV). This makes the silicon-based detectors suitable for the low mass WIMP search.

On the base of equation 1.6, usually DD experiments, in absence of any WIMP signal, set constraints on the DM-nucleon cross-section as a function of the WIMP mass. The lower is the minimum cross-section that an experiment is able to exclude, the higher is the sensitivity. As already mentioned before, having a lighter nucleus target allows to probe less massive WIMP candidates, even if a smaller A value reduces the overall sensitivity. Lowering the energy threshold instead would allow not only to extend the sensitivity to lighter WIMP masses but also to probe smaller cross-sections. The overall sensitivity of an experiment can be increased by lowering the background level and by increasing the exposure, i.e, the product of the size of the target and the duration of the experiment.

The parameter space of the WIMP-nuclei interactions is getting more and more constrained by DD experiments, as shown in Figure 1.8 for the spin-independent case. Furthermore, experiments are likely to hit the neutrino floor in the next decade, wherein neutrinos, coherently scattering off nuclei, will become an irreducible background for WIMP searches. New low mass candidates (sub-GeV), such as the hidden sector ones (see Section 1.2.2), are being explored. Referring to equation 1.8, it is clear that it would be very hard to detect such low mass particles via their scattering with nuclei. Therefore, alternative detection channels, which are discussed in the next section, are being probed. It is also worth mentioning that a possible solution that has been proposed to extend in the MeV regime the sensitivity to DM-nucleus interactions is to profit of the so-called Midgal effect [64, 65]. As a consequence of the latter, a low mass DM interaction with a nucleus would lead to an additional electronic recoil. This is because the electron cloud does not follow the recoiling nucleus instantaneously. The electronic recoil could in turn induce a detectable excitation/ionisation signal above threshold. However, this effect has
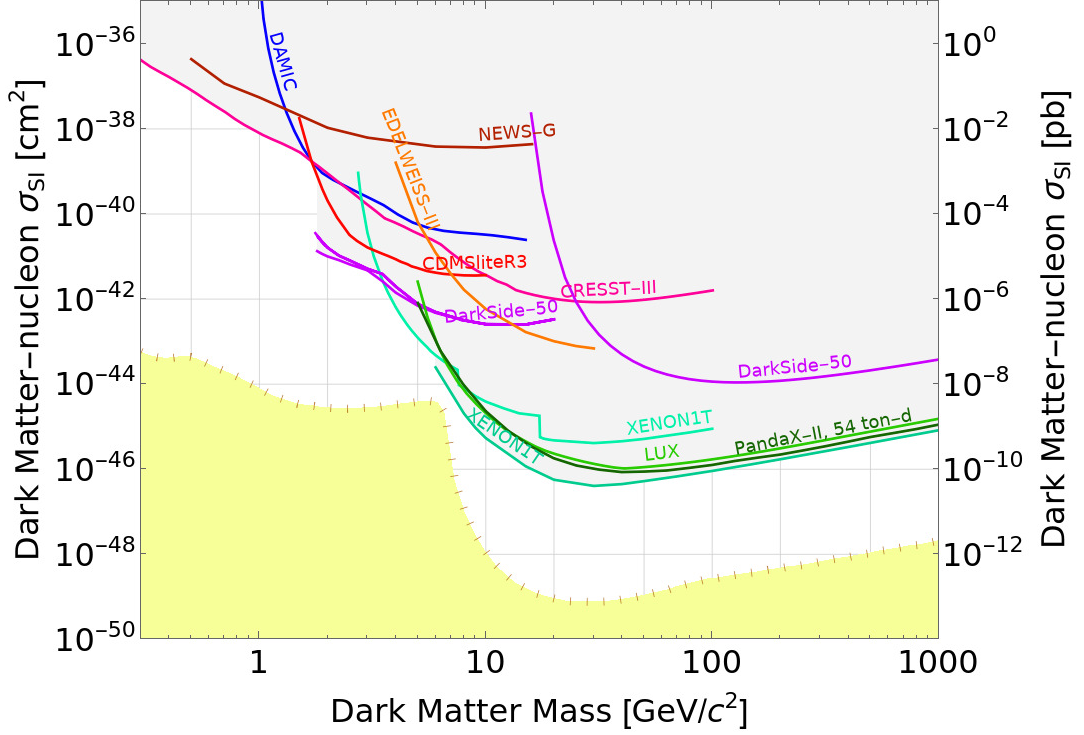
Figure 1.8 – Dominant current exclusion limits of spin-independent WIMP-nucleon cross-section as a function of the WIMP mass. All nuclear recoil limits are scaled to a local dark matter density of 0.3 GeV/c³. This plot was produced using the Dark Matter Limit Plotter application (https://supercdms.slac.stanford.edu/dark-matter-limit-plotter). The neutrino floor (dashed line) is also shown for a Xenon target [58]. The source of each experimental limit: DAMIC (blue) [53], NEWS-G (brown) [50], CDMSliteR3 (red) [44], EDELWEISS-III (orange) [59], CRESST-III (pink) [46], DarkSide-50 (purple) [60, 61], XENON1T (light aquamarine, dark aquamarine) [47, 62], LUX (light green) [63], PandaX-II (dark green) [49]. Note that this plot does not included the recent results (July 2022) from the LZ experiment, which placed the most stringent exclusion limits for WIMP masses above 9 GeV [48].

yet to be observed experimentally in nuclear scattering.

DM interactions with electrons

As already mentioned, sub-GeV DM candidates, as the hidden sector ones, are gaining more and more attention in the scientific community. Current DD experiments cannot look for these particles via their elastic scattering with nuclei. In fact, due to the DM low mass, the resulting nuclear recoil energy would be too low to be detected. Therefore, it

is necessary to pursue alternative interaction channels. One of this is the inelastic DM-electron scattering, which would lead to sufficiently large energy transfers to be detectable down to DM masses of $\mathcal{O}(\text{MeV})$ [22, 66]. Semiconductors are particularly promising target materials due to their $\mathcal{O}(1\,\text{eV})$ band gaps which allow for the detection of small ionization signals. Furthermore, semiconductors benefit also of an increased event rate for all DM masses with respect to targets with higher energy thresholds [66]. In fact, given the characteristic velocities of DM particles and electrons, $\sim$1 eV recoil energies are typical. Instead, energy recoils of the same order of the ionization threshold in liquid noble gases, 10-20 eV, require velocities that are only found on the tails of the DM and electron velocity distributions [66].
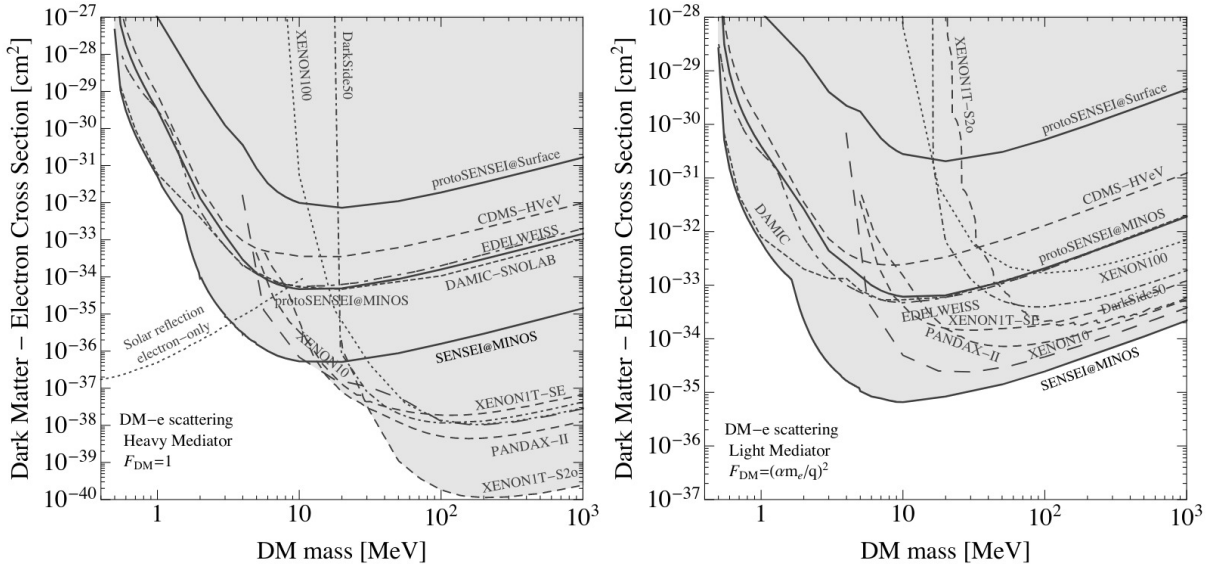
Figure 1.9 – Current 90% C.L. limits on DM-electron scattering through a heavy mediator (left) or an ultralight mediator (right) [67].

In order to model DM-electron interactions, it is necessary to take into account the bound nature of the electrons, as well as the crystalline band structure. In the following the differential event rate is discussed considering a crystal target, as it is the case for the DAMIC and DAMIC-M experiments. The differential event rate for a DM with mass m_χ interacting with electrons is [66]:

$$\frac{dR}{dE_e} \propto \overline{\sigma_e} \int \frac{dq}{q^2} \eta(m_\chi, q, E_e) |F_{DM}(q)|^2 |f_c(q, E_e)|^2, \tag{1.9}$$

where E_e and q are the transferred energy and momentum, respectively, $\overline{\sigma_e}$ is a reference

cross section for free electron scattering, η includes properties of the incident flux of galactic DM particles, F_{DM} is the dark matter form factor, and the crystal form factor $f_c(q, E_e)$ quantifies the atomic transitions of bound-state electrons. The DM form factor, $F_{DM}(q)$, encodes the momentum-transfer dependence of the interaction. It can take different values, depending on the type of mediator and coupling: $F_{DM}(q) = 1$ in case of a point-like interaction induced by the exchange of a heavy vector mediator or magnetic dipole moment coupling, $F_{DM}(q) = (\alpha m_e/q)$ for an electric dipole moment coupling, and $F_{DM}(q) = (\alpha m_e/q)^2$ for exchange of a massless or ultra-light vector mediator [66]. The exclusion limits derived by several DD experiments for a DM-electron scattering interaction are shown in Figure 1.9.
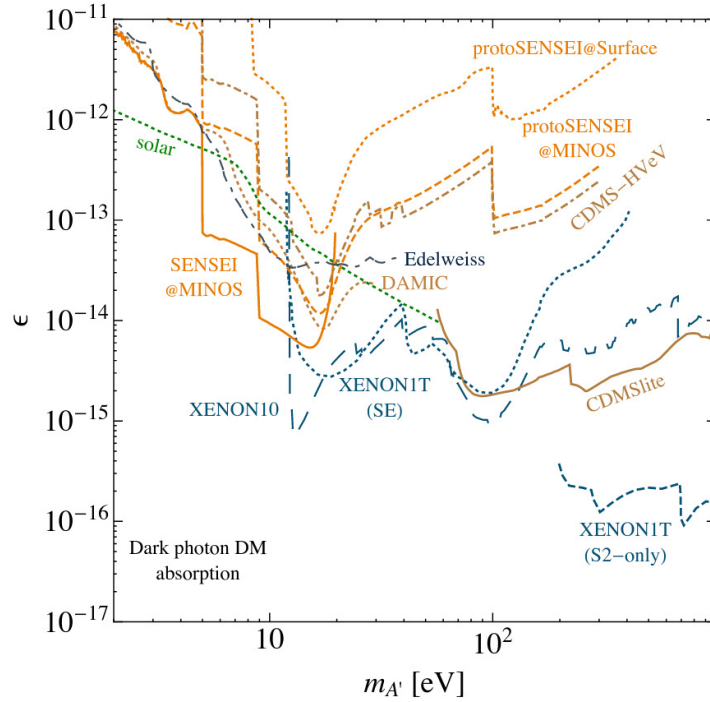
Figure 1.10 – Constraints on dark photon dark matter absorption. The parameter ϵ indicates the kinetic mixing between the hidden photon and the ordinary one [67].

Another possible DM detection channel consists in looking for a dark photon absorption by electrons. This results in a sort of photoelectric effect, leading to the creation of ionization charges in a target material. Considering the case of a silicon detector, a non relativistic hidden photon, depositing its rest energy in the target, would be able to produce charge carriers for masses above the band gap of silicon. The hidden photon absorption cross section (σ_V) can be related to that of the photoelectric cross section (σ_γ)

[68, 69]:

$$\sigma_V(E = m_V)v_V \simeq \kappa^2 \sigma_\gamma(E = m_V)c, \tag{1.10}$$

where E is the energy of the ordinary photon, m_V is the hidden photon mass, v_V the velocity of the incoming DM, and κ is the kinetic mixing between the hidden photon with its visible, ordinary counterpart (in literature also referred as ϵ). However to take into account the in-medium dispersion effects of the target material, it is necessary to substitute κ with an effective mixing parameter κ_{eff} [68–70]:

$$\kappa_{\text{eff}} = \frac{\kappa^2 m_V^4}{(m_V^2 - Re[\Pi(E)])^2 + (Im[\Pi(E)])^2}, \tag{1.11}$$

where $\Pi(E)$ is the polarization tensor which is related to the complex conductivity of the medium $\hat{\sigma}(E) = \sigma_1 + i\sigma_2$, which is in turn related to the complex index of refraction of the medium $\hat{n}^2 = 1 + i\hat{\sigma}E$. Finally the absorption rate of hidden photons can be written as [68–70]:

$$\Gamma = \frac{\rho_0}{m_V}\kappa_{\text{eff}}^2\sigma_\gamma(E = m_V)c, \tag{1.12}$$

where ρ_0 is the local dark matter density. Note the lack of dependence of Γ on the local DM velocity, in contrast to regular WIMPs, implying no potential annual modulation in detection. The current DD constraints on the dark photon dark matter absorption as a function of the dark photon mass are shown in Figure 1.10.

$$* * *$$

Nowadays, the Dark Matter search is a very active field. Direct detection experiments play an essential role in determining the DM particle nature. Impressive improvements have been done in the last decades in terms of sensitivity to DM interactions. WIMPs, which once were the most popular candidates, are being more and more constrained. This drove the interest of the scientific community towards lighter sub-GeV DM particles, whose parameter space is still relatively poorly constrained. DAMIC-M is a near future direct detection experiment that aims to explore this un-probed region. The following chapters describe the operation principle of this experiment and report the improvements in its conception and characterization.

DARK MATTER IN CHARGE COUPLED DEVICES

The Charge Coupled Devices (CCDs) are light sensors commonly used in digital cameras and telescopes for astronomical applications. These instruments can collect and store the charges produced inside them by particle interactions. Their applicability in the search for dark matter (DM) was successfully demonstrated by DAMIC at SNOLAB, which looks for DM particle interactions in the silicon CCD bulk. The silicon low nucleus mass ensures a good sensitivity to WIMPs with masses in the range 1-10 GeV, while its small band gap (~ 1.1 eV) provides sensitivity to the hidden sector DM-electron interactions. A near future experiment called DAMIC-M is under development. It will be installed at the Laboratoire Souterrain de Modane (LSM) in France and will increase by 17 times the mass of its detector with respect to its predecessor. It will employ the so-called skipper CCDs to achieve sub-electron resolution on the charge measurements [71]. Furthermore, the radiogenic background rate will be lowered by about 100 times with respect to DAMIC, achieving a fraction of events per keV per kg-day of target exposure. Due to these features and to a low level of dark current, DAMIC-M will be extremely sensitive to very feeble ionization signals down to few eV which are expected from DM interactions with nuclei or electrons in the silicon bulk.

In the following sections, the CCDs are described and presented together with the DAMIC and DAMIC-M experiments.

2.1 Charge Coupled Devices

Charge Coupled Devices are pixelized ionization collection devices. They were invented in 1969 by Willard Boyle and George E. Smith who in 2009 were awarded the Nobel Prize for Physics for the invention of the CCD concept. In [72], Boyle and Smith described the CCDs as a "new semiconductor device concept" able to store and move charges across an

array of conductor-insulator-semiconductor capacitors by applying appropriate voltages to the conductors [72]. Different types of applications were also listed, e.g., memory storage or imaging. Only in the latter sector the CCDs found their major development. The first verification of the CCD concept arrived in 1970 with G. F. Amelio, M. F. Tompsett, and G. E. Smith, which used closely spaced MOS (Metal Oxide Semiconductor) capacitors on an n-type silicon substrate [73]. Later on, in 1971, M. F. Tompsett submitted a patent for charge transfer imaging devices, marking the beginning of the CCD application in the imaging field. In 1975, Kodak created the first digital camera using a CCD, made of 100×100 capacitors (also called pixels). In 1976, B. A. Smith demonstrates the capability of using CCDs in the astronomical telescopic imaging domain. Nowadays, CCDs are still largely used in this field due to their efficiency and low noise, as well as their size. In fact, CCDs can reach $\sim$0.7 mm of thicknesses and feature large array of pixels, achieving also linear dimensions of several cm. The first DAMIC-M CCD prototypes are among the biggest CCDs ever built, with a length of 9 cm. CCDs can also be exploited to detect particles, as in the case of the DAMIC and DAMIC-M experiments which are described in Sections 2.2 and 2.3. In the following, a brief introduction about semiconductor materials, with a focus on silicon, is reported. The structure and operation of a CCD are then described, in particular, referring to those of a DAMIC and DAMIC-M device.

2.1.1 Semiconductor materials: Silicon

Semiconductors are at the base of the modern technologies, with silicon being one of the most common type of employed materials. What first gained the attention of physicists in the early nineteenth century, is the particular feature of semiconductors to have a declining electrical resistance with raising temperature, unlike metals [74]. This is due to the energy band structure[1] of semiconductors characterized by a conduction band and a valence band separated by a relatively small[2] forbidden energy gap (E_g). In the case of intrisic semiconductors at T= 0 K, the valence band can be seen as the ensemble of the highest occupied energy levels. The conduction band is just above the valence one, consisting of the lowest unoccupied energy levels. Figure 2.1 (left) schematizes the band structure of a pure (intrinsic) semiconductor. In the case of silicon, $E_g = 1.12$ eV

---

1. A band structure arises in crystalline materials, due to the overlap of the wave functions of electrons of neighbouring atoms. Due to the Pauli exclusion principle, this results in collections of closely spaced energy levels, called bands [74, 75].
2. In most important semiconductors, the energy gap is less than 2 eV [74].
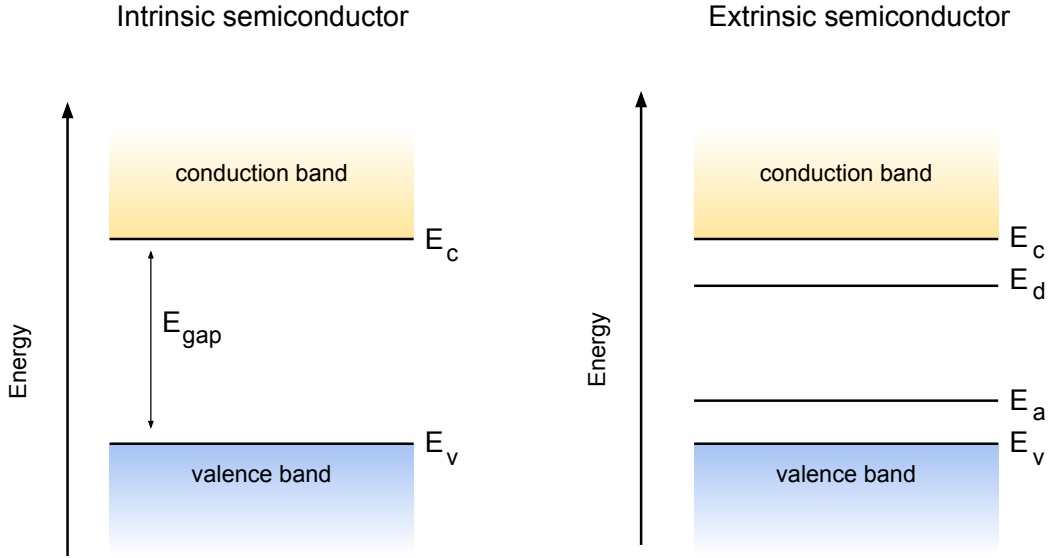
Figure 2.1 – Left: band structure in the case of an intrinsic semiconductor. The conduction and valence band are shown. Right: band structure in the case of an extrinsic semiconductor, with additional impurity energy levels (E_a for acceptors, E_d for donors).

at T=300 K [74]. Note that the energy gap depends on the temperature and varies by about 10% between 0 K and room temperature [74]. Its variation with temperature can be modeled as [76]:

$$E_g(T) = E_g(0) - aT^2/(T + b), \tag{2.1}$$

with $E_g(0)$ the energy gap at 0 K, and a and b positive constants for silicon. Given the small energy gap, an electron can be easily promoted by thermal excitation from the valence band to the conduction band, becoming able to carry current. In particular, the fraction of excited electrons are of the order of $e^{-E_g/2k_BT}$ [74]. An electron promoted to the conduction band leaves an hole in the valence band, which also contributes to the conductivity (σ) of the material [74]:

$$\sigma[(\Omega\text{cm})^{-1}] = e(\mu_n n_c + \mu_p p_v), \tag{2.2}$$

where e is the electric charge, n_c (p_v) the electron (hole) concentration in the conduction (valence) band[3], μ_n (μ_p) the electron (hole) mobility. The latter is defined as the ratio between the drifting velocity of a charge in an electric field (v_D) and the electric field it self (E) [74]:

$$\mu = v_D/E. \tag{2.3}$$

The reciprocal of the conductivity is the resistivity (ρ):

$$\rho[\Omega\text{cm}] = 1/\sigma. \tag{2.4}$$

Impurities in the crystal can substantially affect the electrical properties of a semiconductor, increasing the charge carrier concentrations and thus the conductivity of the material. Therefore, artificially introducing impurities in the material allows to modify ad hoc its electrical properties. This procedure takes the name of "doping" and it's at the base of the success of semiconductors in the electronic field. A semiconductor is called extrinsic (in contrast with a perfectly pure intrinsic semiconductor) if impurities contribute in a significant way to the carrier density (conduction band electrons or valence band holes). Two types of impurities (dopant) exist, donors and acceptors. The first supplies additional electrons to the conduction band, the second additional holes to the valence band. Donors and acceptors are essentially atoms which feature an higher or lower chemical valence than the pure semiconductor atoms. A common donor (acceptor) for silicon is phosphorus (boron), which has 1 more (less) valence electron than silicon. By replacing in the lattice a silicon atom with a donor one would result in 1 electron which is not involved in the 4 covalent bonds with the neighbouring atoms. An additional energy level is thus introduced just below the conduction band, with a distance which is far smaller than the E_{gap} of silicon (Figure 2.1, right). It is thus necessary to provide a very small amount of energy to promote the electron in the impurity level to the conduction band. In case of a silicon lattice with phosphorus impurities, the difference between the conduction level and the donor level is of 0.044 eV [74]. In a similar way, when an acceptor is introduced in the lattice, a lack of 1 electron involved in the 4 covalent bonds is created. An energy level is thus introduced just above the valence band, which can be later filled by valence electrons (Figure 2.1, right). In case of a silicon lattice with boron impurities, the difference between the valence level and the donor level is of 0.046 eV [74]. Silicon doped with

---

3. In a perfect pure intrinsic semiconductor the concentrations of holes and electrons are the same. This is not the case if impurities are present in the lattice, leading to a difference in the number of electrons and holes [74].

donor (acceptor) impurities is called n-type (p-type) silicon.

The p-n junction
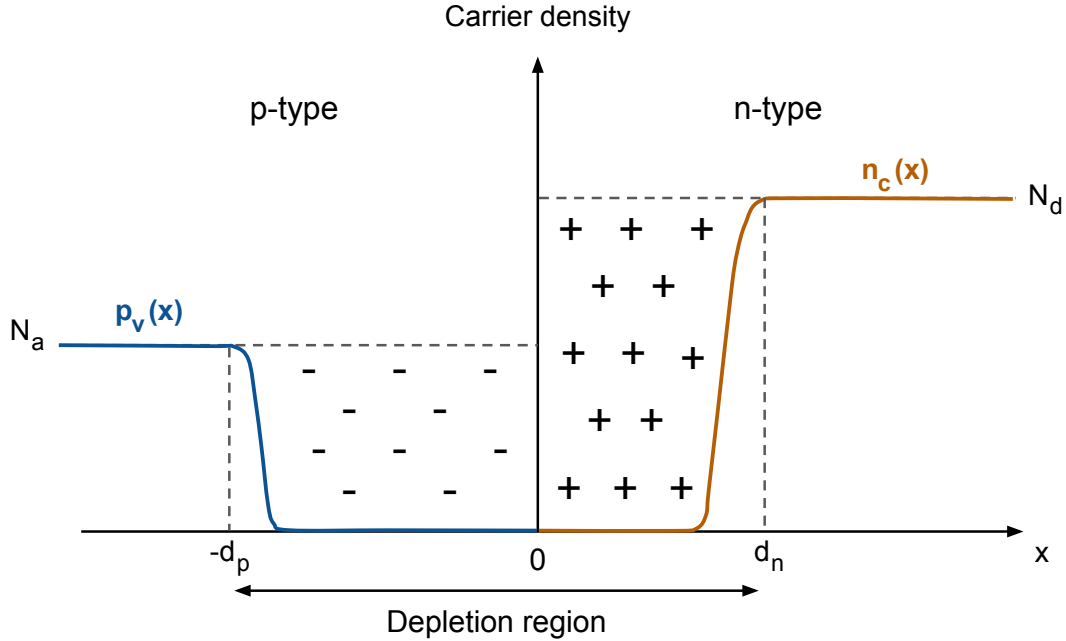
Figure 2.2 – Representation of a p-n junction assuming that the impurity concentration varies along the x direction. The junction is at x=0. The carrier densities (p_v and n_c) as a function of x are shown. d_p and d_n define the extent of the depletion layer. The + and − signs indicate the donor and acceptor ions, respectively.

A p-n junction consists of a semiconducting crystal in which the donor and acceptor concentrations vary across a given direction (Figure 2.2). On one side there is a preponderance of acceptors (the majority carriers are holes), on the other of donors (the majority carriers are electrons). This causes the diffusion of carries towards the zone where their concentration is lower. Electrons diffuse from the n-side to the p-side and holes from the p-side to the n-side. However, electrons diffusing towards the p-side leave behind positively charged donors. The same happens for holes that leave behind negative charged acceptors. This causes the creation of an electric field which points in the opposite direction with respect to the diffusion flow. These two opposite effects finally compensate each other at thermal equilibrium. The positively and negatively charged regions at the junction are depleted of any mobile charge and therefore are referred as "depletion region".

Any electron or hole entering in this region would be swept out by the electric field. The extent of the depletion region (d) depends on the acceptor and donor densities (N_a, N_d), as well as on the potential difference between the two extremes of the junction ($\Delta\phi$) [74]:

$$
\begin{aligned}
d = d_n + d_p &= \left(\frac{\epsilon\Delta\phi(N_a + N_d)}{2\pi e(N_a N_d)} \right)^{1/2} , \\
d_{n,p} &= \left(\frac{(N_a/N_d)^{\pm 1}\epsilon\Delta\phi}{2\pi e(N_d + N_a)} \right)^{1/2} ,
\end{aligned}
\tag{2.5}
$$

where ϵ is the static dielectric constant of the semiconductor, and e the electron charge. The depletion region can be narrowed or extended by applying an external electric field. If the direction is the same of the built-in junction electric field ("reverse bias"), then the depletion region becomes wider. In the opposite situation ("forward bias"), the depleted region narrows. In the case of an external potential applied (V), the extension of the depletion region can be calculated as [74]:

$$
d(V) = d(0) \left[1 - \frac{V}{\Delta\phi} \right]^{1/2} ,
\tag{2.6}
$$

with $d(0)$ is obtained from equation 2.5, $\Delta\phi$ is the potential difference in absence of any external voltage bias, and V>0 (V<0) in case of forward (reverse) bias.

The p-n junction is at the base of a CCD structure, described in details in the next section. CCDs in fact are composed by a p-n junction to which a reverse bias is applied. The depletion region represents the active volume of a CCD where particles, interacting with the medium, can free electron and hole pairs, which are immediately driven out by the electric field.

2.1.2 CCD structure and operation

CCD structure

A DAMIC (or DAMIC-M) CCD consists of a 2D array of coupled MOS capacitors, commonly called pixels, each of them with an area (x-y plane) of 15 μm $\times$ 15 μm. A DAMIC-M CCD prototype is shown in Figure 2.3 (a). Each pixel features a 3 polysilicon-metal gates (3-phase CCD structure) on top of an insulator layer [4], positioned above a p-n

---

4. Commonly used insulting materials are Si_3N_4 or SiO_2.

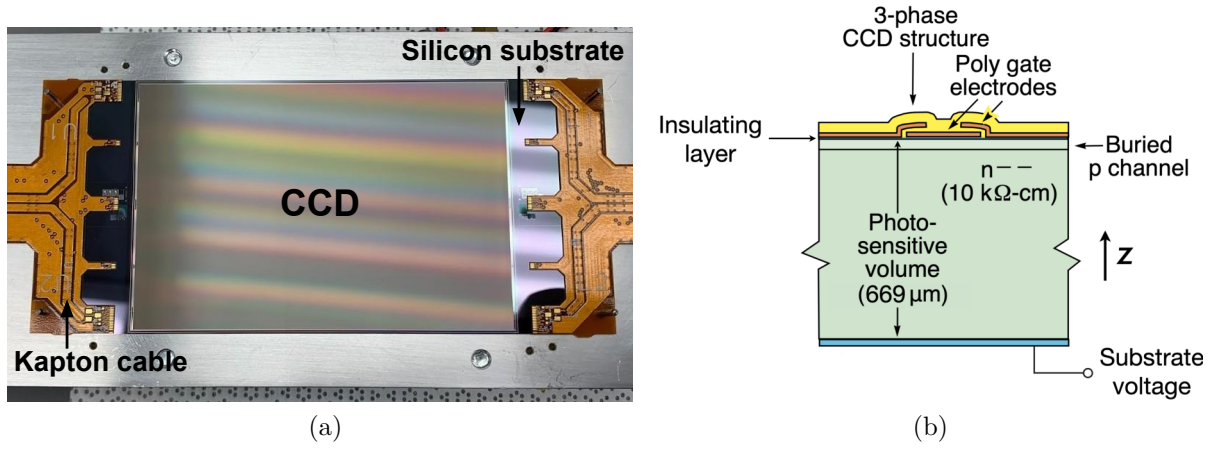Figure 2.3 – (a): DAMIC-M prototype featuring 4k pixels × 6k pixels. The CCD is mounted on a silicon substrate and wire-bonded to kapton cables that carry signals to and from the CCD. (b): MOS capacitor (pixel) structure consisting of 3 polysilicon metal gates, an insulating layer (0.1 μm thick, made of silicon nitride, Si_3N_4), and a p-type silicon buried channel fabricated over a n-type silicon substrate. The polysilicon gates are insulated from each other by means of silicon dioxide (SiO_2), shown in yellow. The direction of the electric field on z-axis is also indicated.

junction (Figure 2.3, b). The latter is composed by a thin buried p-channel (1 μm thick) of boron doped, p-type silicon and by a very thick substrate ($\sim$668 μm thick) made of phosphorus doped, high resistivity, n-type silicon. The high resistivity ($\sim$10 kΩcm) of the substrate makes for a low donor density ($\sim$10^{11} cm^{-3}), allowing to deplete the junction over its whole volume (full depletion) at reasonably low values of bias voltages (> 40 V)[5]. This substrate potential V_{sub} is applied via a contact placed at the backside of the CCD, generating an electric field across the device and fully depleting it. The depletion region represents the active region of the CCD where the signal charge from ionization events is produced. Its substantial thickness allows for high quantum efficiency and mass exposure, required for a DM search. The backside contact is constituted by a 1 μm thick in-situ doped polysilicon (ISDP) layer, having also a gettering function, i.e., absorbing heavy metals and other impurities from the silicon substrate during manufacturing [77]. These gettering properties are due to the presence of both the polysilicon and phosphorus[6], with

---

5. For p-buried CCDs, the depletion extent can be calculated via equation 2.6, assuming $N_a \gg N_d$.
6. As it will be also discussed later on in this thesis, the DAMIC collaboration found that phosphorus, diffused into the CCD during fabrication, is the cause of ionization charge losses by recombination in the CCD backside [78].

which the layer is heavily doped. The gettering layer is then capped by polysilicon and silicon dioxide layers.

Figure 2.4 shows the cross-section view of a pixel, together with the voltage profile.
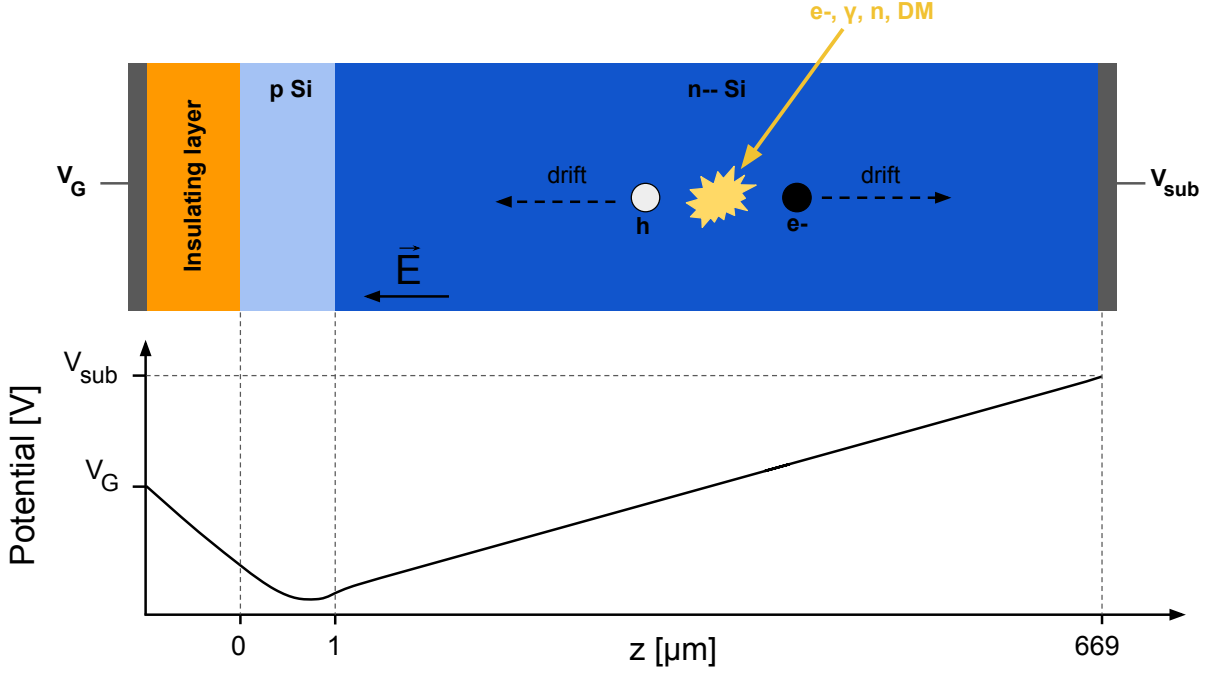
Figure 2.4 – Top: Pixel cross section diagram showing its internal structure. The z coordinate runs along the thickness of the CCD and indicates the depth of the interaction. A bias voltage V_{sub} is applied to the backside contact of the CCD, generating an electric field that fully depletes the device. The basic working principle of a CCD following a particle interaction is also shown: an incident particle releases energy in the depletion region, creating electron-hole pairs. These charges then drift following the electric field. The holes are then collected at the minimum of the potential (see bottom panel). Bottom: The voltage profile as a function of depth. The minimum of the potential lies close to the p-n junction location (z = 1 μm), in the p-doped region.

CCD charge creation

Charges can be created in the CCD by the interaction of an incident particle with the silicon substrate or bulk (see Figure 2.4). A particle, releasing energy in the depletion region, can promote an electron to the conduction band, assuming that the energy deposit is greater than the silicon band gap. This leaves an electron vacancy (hole) which acts in an electric field like a physically charged particle.
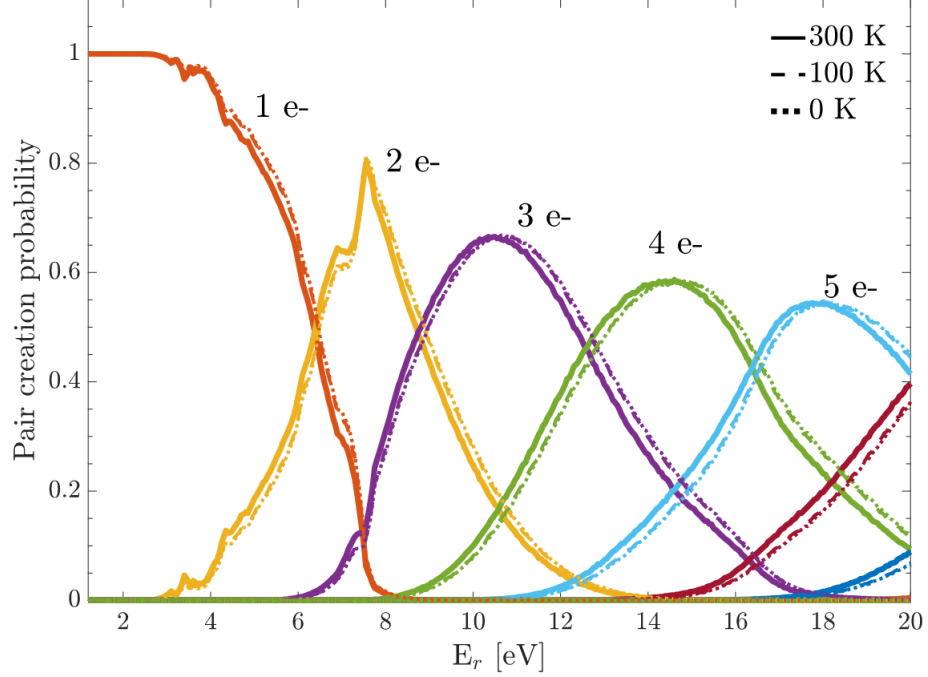
Figure 2.5 – Pair-creation probability distributions 0 K, 100 K and 300 K (former curves effectively overlap). These lines indicate the probability to ionize the labeled number of charge pairs for a given deposited energy [79]. Reprinted figure with permission from [79]. Copyright (2017) by the American Physical Society.

The number of electron-hole pairs n_{eh} created for a given interaction can be inferred by dividing the deposited energy E by the mean energy per pair ϵ_{eh}:

$$n_{eh} = \frac{E}{\epsilon_{eh}}, \tag{2.7}$$

where $\epsilon_{eh} > E_{gap}$ due to the concurrent emissions of phonons during the ionization process [80]. Like the energy gap, the ϵ_{eh} value depends as well on the temperature. In particular, ϵ_{eh} was measured to be 3.66 eV in silicon at T=300 K [80]. For T=123 K, its measured value increases to 3.74 eV [81]. Another important parameter quantifying the dispersion of n_{eh} for a given E is the Fano factor (F). F is less than 1, indicating a sub-poissonian dispersion. In [82] F was found to be 0.128 for silicon (T= 130 K). Due to the statistical nature of the ionization process, for energy deposits $\gg 50$ eV, F and ϵ_{eh} have an almost constant behaviour. Therefore, the probability to create n_{eh} for a given energy deposit can be assumed to follow a gaussian distribution with a standard deviation

43

equal to $\sqrt{n_{eh}F}\epsilon_{eh}$ and mean value derived from equation 2.7. However, this is not the case in the low energy regime. Uncertainties lie especially in the energy range between $E = 2E_{gap}$ and the high energy limit. In fact, for $E < 2E_{gap}$, F= 0 and $\epsilon_{eh} = E$, being only one electron-hole pair allowed to be produced [82]. In [79], the probability to ionize n_{eh} charge-pairs as a function of the deposited energy is computed in the low energy regime, employing a phenomenological model. The resulting pair-creation probability distributions are shown in Figure 2.5.

CCD charge collection
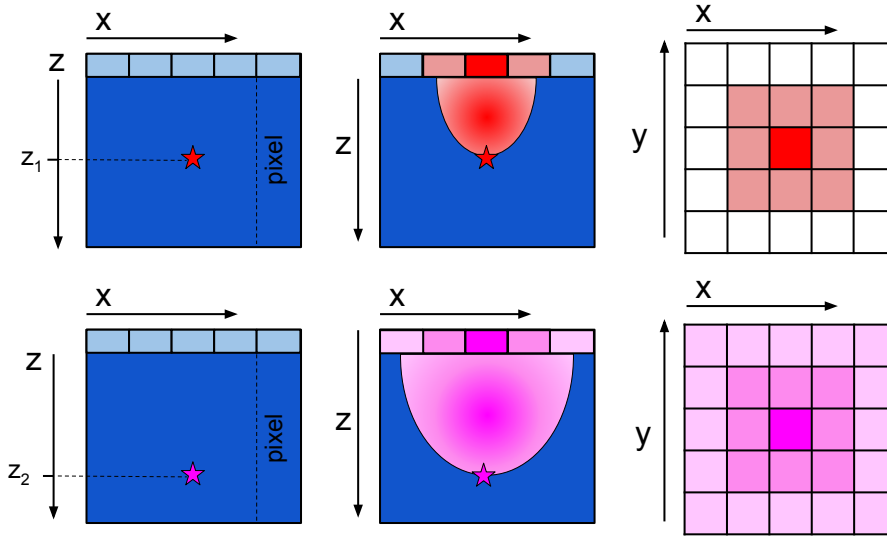
Figure 2.6 – Cross-sectional representation of the charge produced by a point-like ionization event (star) in the CCD bulk as it is drifted towards the polysilicon gates. The top and bottom panels represent two different situations in which the interaction takes place at different depths (z coordinate), referred as z_1 (top) and z_2 (bottom). In particular, $z_1 < z_2$. The x-y distributions of charge on the pixel array following the ionization event are also shown at the right of the two panels. Because of diffusion, the charge is collected in multiple pixels, with the lateral spread being positively correlated with the depth of the interaction.

Once the charges have been produced in the depletion region, the electric field sweeps the electrons to the backside while pushing the holes towards the top gate structure. The holes are therefore the signal charges collected and read by DAMIC and DAMIC-M CCDs. During the drifting (z-axis), charges undergo lateral (x-y axis) thermal diffusion.

In this way, depending on the strength of the diffusion, they can reach pixels that are horizontally far away from the one in which they were initially produced. Charge diffuse following a gaussian distribution with $\sigma = \sqrt{2Dt_r}$, where t_r is the carrier transit time and D is the diffusion coefficient, linked to the carrier mobility via the Einstein relation[7] [83]. Considering the electric field profile within the CCD substrate, σ can be expressed as (for point-like interactions) [84]:

$$\sigma = \sqrt{-A\ln|1 - Bz|},\tag{2.8}$$

where A and B are related to the physical properties and operating parameters of the device and z is the depth of the ionization event. In particular, A and B are given by [84]:

$$
\begin{aligned}
A &= \frac{\epsilon}{\rho_n}\frac{2k_B T}{e},\\
B &= \left(\frac{\epsilon V_b}{z_D \rho_n} + \frac{z_D}{2}\right)^{-1},
\end{aligned}
\tag{2.9}
$$

where ϵ is the permittivity of silicon, ρ_n the donor charge density in the substrate, T the operating temperature, e the electron charge, z_D the thickness of the device, V_b the bias applied across the substrate (the potential difference between the charge-collection well and the CCD backside). These parameters can be also be derived experimentally as explained in the Section 2.2.3. An important consequence of the relation 2.8 is that it is possible to retrieve the depth of an interaction by looking at the diffusion spread of charges. This allows to have a 3D reconstruction of energy deposits, whose x-y coordinates are already provided by the pixel positions. The diffusion process is schematized in Figure 2.6.

Once the holes have reached the buried p-channel region (see Figure 2.4), where the minimum of the potential profile lies, they are held in place until the beginning of the readout process. The time period when the charge is accumulated in the individual pixels is commonly called "exposure" and its length is decided by the user.

Readout process: standard and skipper

The exposure phase is then followed by the readout one. By applying to the 3 metal gates appropriate voltages with the proper sequencing, charges are transferred across

---

7. The Einsten relation describes the relation between the diffusion coefficient (D) and the carrier mobility (μ): $D/\mu = k_B T/e$, with k_B the Boltzmann constant, T the absolute temperature and e the electrical charge.

different pixels. Clocks (alternating signals) are used to switch the 3 gate voltages independently from low to high or vice-versa, modifying the potential well below the gates. A voltage is lowered to accumulate charges below the corresponding gate. On the contrary, it is raised to drift the charge out. This procedure is called "clocking". Its basic principles are summarized in Figure 2.7.
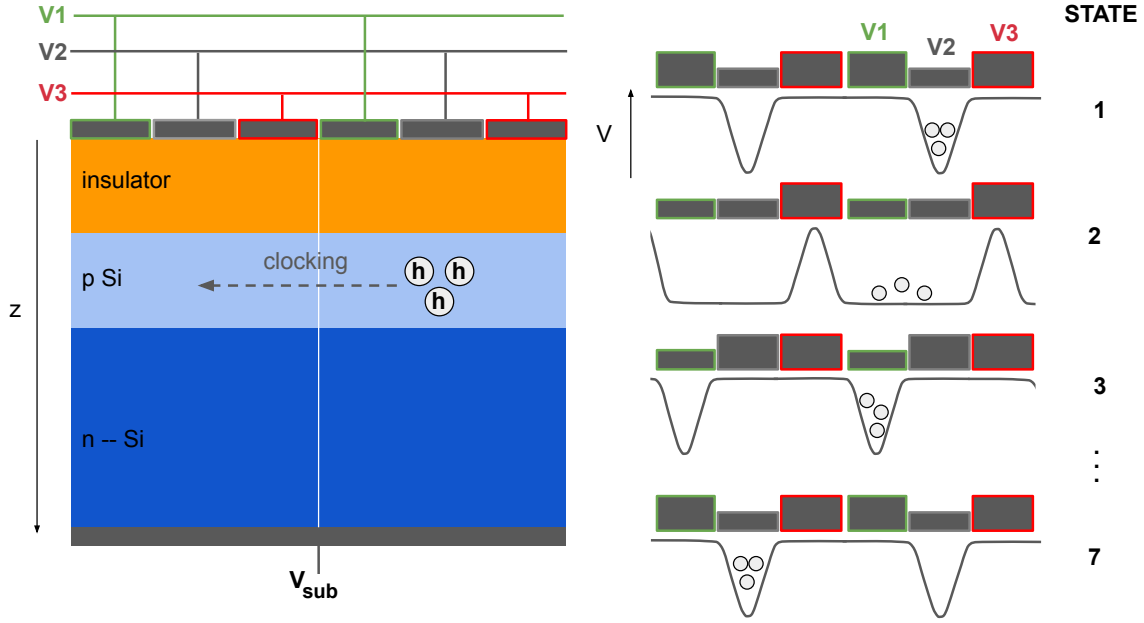
Figure 2.7 – Left: Cross section of two adjacent pixels. The clocking direction is indicated. To each polysilicon gate a different voltage value (V1, V2, V3) is applied. Right: In order to trasfer charges between pixels, the 3 gate voltages are changed over time. The voltage sequence is reported and divided in states. In state 1, the charges are held in the pontential well created below the gate 2 (to which the potential V2 is applied). In state 2, the potential V1 is lowered, allowing the charges to spread below the gate 1. In state 3, charges reach the gate 1. At this point the charges are transferred to the adjacent pixel, by switching from high to low and vice-versa the gate voltages, as just explained. Finally, in state 7, the charges have reached the gate 2 of the second pixel.

The clocks that transfer charge across one column (i.e., in the y direction) are called parallel (vertical) clocks, while the clocks that transfer charge across one row (i.e., in the x direction) are called serial (horizontal) clocks. Vertical pixels are connected with each other, allowing charge to be transferred along a column. On the contrary, channels stops,

consisting of n-type implants between columns[8], prevent charge from moving horizontally. During the readout phase, the entire rows (y-axis) are shifted simultaneously in the parallel direction towards a horizontal "serial register" (basically the first row of the CCD array). A "transfer gate" (TG) regulates the flow of charges into the serial register thanks to the creation of a potential barrier[9]. Only when the TG is open, charges can enter into the serial resister. Once in the serial register, the charge is moved in horizontal direction (x-axis) towards the readout amplifier thanks to horizontal clocks. Also in this case the charge transfer is based on a 3-phases clocking procedure. Horizontal clocks are about 100 times faster than the vertical ones. In particular, the widths of the parallel and serial clocks are in the order of 10 μs and 0.1 μs, respectively. This ensures that an entire row is emptied (read out) before the next one flows through the TG. The 2D pixel array, together with its principal elements, is sketched in Figure 2.8.

The CCD 3-phase structure allows to maximize the efficiency of the charge transfer between pixels. However, due to potentially non-optimized clock voltage potentials and lattice traps and impurities, a small fraction of holes can be lost. The quantity measuring the fraction of charge lost over a single transfer is called "Charge Transfer Inefficiency" (CTI) and is of the order of 10^{-6} for scientific-grade CCDs, like DAMIC ones [83].

When the charge exits the serial register, before reaching the readout amplifier, it passes through a series of successive gates, the Summing Well (SW), the Output Gate (OG), and the Sense Node (SN). Figure 2.9 (inset) shows all the relevant components in a conventional CCD.

In the SW, the charge of multiple pixels can be collected. For example, it may be necessary, in order to increase the signal to noise ratio, to measure in one time the charge accumulated in different pixels of the serial register. This operating mode is called "serial binning". Performing a "parallel binning" is possible as well. In this case the charge of multiple rows is accumulated in the serial register before the activation of the horizontal clocks. The OG controls the flow of charge between the SW and the SN, where pixel charge is measured. Raising the SW voltage level above that of the OG allows the charge to transit into the SN. The latter basically consists in a capacitor with capacitance equal to C_S, whose potential is set to a bias voltage reference V_R. When the charge flows into

---

8. Channel stops are implanted deeper than the buried-channel, reaching the substrate silicon.

9. If the potential well state is set to low, then the gate is open and thus charges can enter into the serial register. On the contrary, if the potential well state is set to high, then the gate is closed, not allowing any charge to pass through.
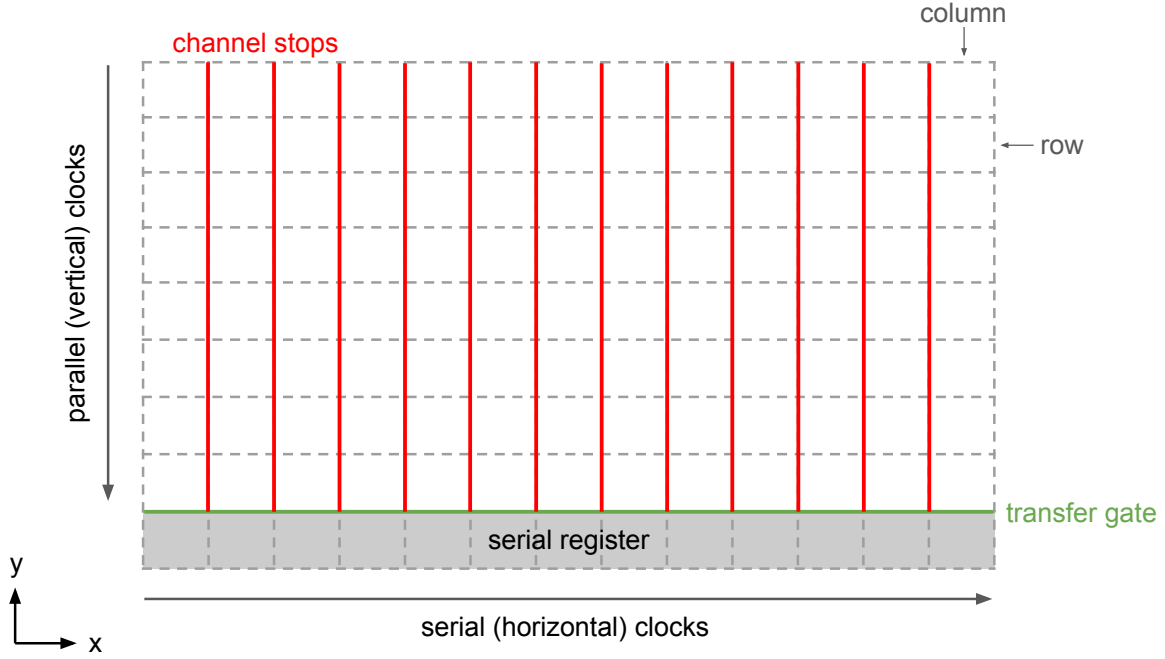
Figure 2.8 – View of the 2D pixel array, showing its principal elements. Channel stops prevent charge to move horizontally (x axis) between pixels of the same row. Charges are instead allowed to move vertically (y axis), between pixels belonging to the same column. A transfer gate regulates the flow of holes into the serial register, the first row of the CCD array. Once in the serial register charges are moved horizontally towards the readout amplifier.

it, it causes a change in the SN potential equal to:

$$\Delta V_S = \frac{Q}{C_S} \sim \mathcal{O}(1\mu\text{V}). \tag{2.10}$$

This small μV signal is then amplified by an output transistor and constitutes the Video signal which is sent out of the CCD. Before performing the next measurement, the charge in the SN is drained via a reset pulse, which is also detected by the output amplifier and which resets the SN potential to V_R [10]. However, this process can inject spurious charge into the SN. To solve this issue, the charge in the SN is measured two times:

— right after the reset pulse, when a charge packet is still in the SW, over an integration time equal to τ_{int}. A pedestal value is thus obtained;

---

10. The SN potential is reset to V_R via a transistor (called also reset switch) which is connected to a reset gate (RG). If the state of the RG is set to high a reset pulse is produced.
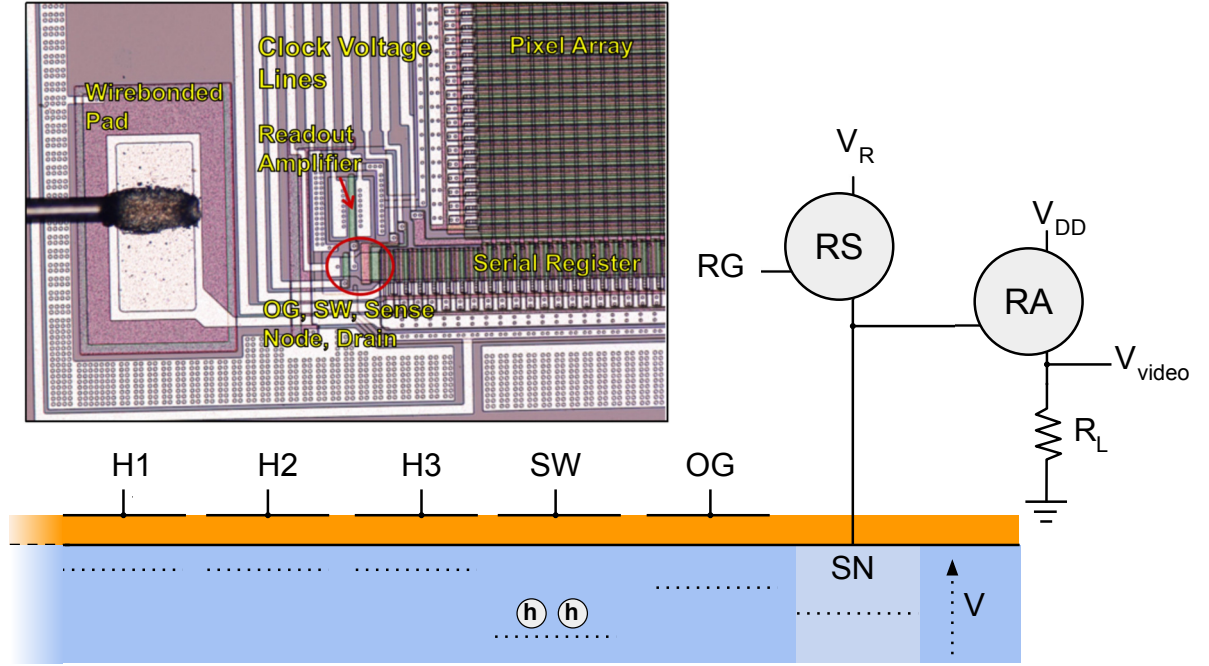
Figure 2.9 – Simplified circuit diagram of a DAMIC CCD readout stage. The key components are shown and labelled: the pixel array, the serial register, the summing well (SW) and the output gate (OG), the sense node (SN), the reset switch (RS), the reset gate (RG), and the readout amplifier (RA). H1, H2, H3 are the serial horizontal clocks which drive the charges into the SW. The holes are then transferred via the output gate to the SN. The inset shows a micrograph of a conventional CCD Courtesy of the Pacific Northwest National Laboratory (PNNL).

— after the charge trasfer through the OG into the SN, over an integration time equal to τ_{int}. A signal value is measured.

Subtracting the pedestal value to the signal one significantly suppresses the reset noise. This technique is called "Correlated Double Sampling" (CDS) [85] and has also the advantage to reduce the contribution of high-frequency noise components (unrelated to the reset noise). In fact, the high frequency ($f \gg \tau_{int}^{-1}$) variation of the Video signal amplitude can be compensated for by the CDS integration [11]. On the contrary, the CDS is not effective in suppressing low frequency noise components. Figure 2.10 shows the CDS method applied on Video signals, obtained in an ideal case and in presence of high- and low-frequency noise components.

---

11. The optimal τ_{int} can be found experimentally, by selecting the one ensuring the lowest noise (noise of the entire electronics chain).

49

(a)   (b)
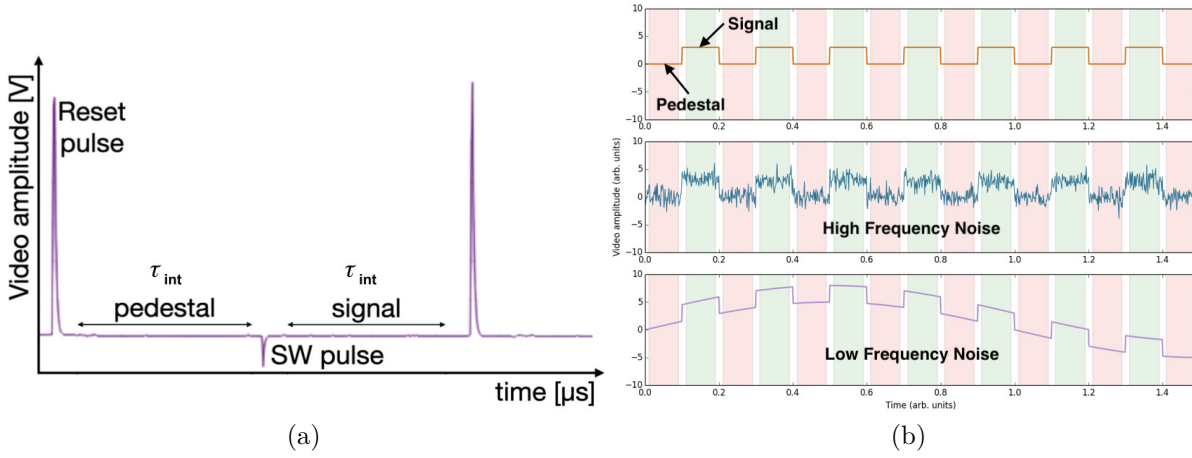
Figure 2.10 – (a): CCD Video signal, during the readout of a single pixel charge. The reset pulse is visible, indicating the end of a pixel measurement. The summing well pulse denotes the moment when the charges flow into the SN. The video signal is integrated over a time equal to τ_{int} before and after the SW pulse, obtaining a pedestal and signal value. By subtracting them, the final signal is retrieved. The time needed to readout a pixel is usually of the order of 10 μs. DAMIC at SNOLAB used a τ_{int}= 40 μs. (b): Examples of video signal in 3 different regimes [86]: no noise (top), high frequency noise (middle), and low frequency noise (bottom). The correlated double sampling strongly suppress high-frequency noise components, but it is not effective in removing low-frequency ones.

The readout procedure described so far is referred as standard or conventional readout. However, DAMIC-M CCDs, unlike DAMIC ones, will be equipped with skipper amplifiers, conceptually devised by Janesick et al. in the early '90s [87]. The skipper amplifiers allow to perform multiple non-destructive measurements of the same pixel charge (NDCMs, also called "skips"), in contrast with the destructive nature of standard readout. This is achieved by using a floating gate as SN, instead of a floating diffusion gate. In this way, the charge accumulated in the node doesn't make contact with the measurement apparatus, unlike in the standard case[12]. The charge still induces (electrostatically) a voltage measured by the output amplifier, but there is no contact that forces the charge to be flushed (destructively) when the floating gate potential is set back to V_R. The charge can therefore be moved back and forth from the sense node and the SW, by transforming the OG from a fixed bias to a clock (see Figure 2.11). For example, by changing the bias voltage of the latter to be higher than the SW one and lower than the SN one, the charge

––––––––––––––––––––––––––––––––

12. In the standard case, the SN is directly connected, usually via a metal contact, to the readout amplifier and the reset switch.

can be driven back from the SN to the SW. The charge is then moved again into the SN for a new measurement. This cycle is repeated as many times as the desired number of skips. Then, thanks to the introduction of a new Dump Gate (DG) and a new Drain potential V_{drain}, the charge is cleared out.
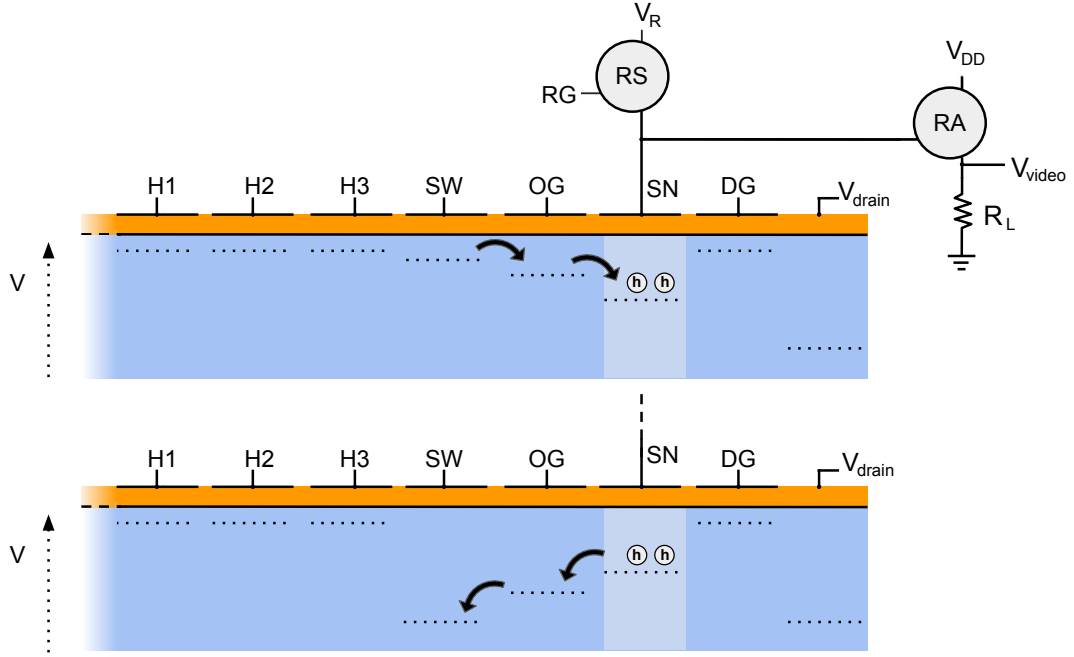
Figure 2.11 – Simplified circuit diagram of a skipper CCD readout stage. H1, H2, H3 are the serial horizontal clocks which drive the charges into the SW. RA indicates the readout amplifier and RS the reset switch. Charges are moved back and forth from the SN to the SW by raising or lowering the OG potential. This cycle is repeated as many times as the desired number of non-destructive measurements. Charge is then cleared out via the Dump Gate (DG).

The main advantage of using skipper amplifiers is the reduction of the readout noise, in particular, of the low frequency noise components that constitute the main limitation for standard CCDs. In fact, the pixel charge (Q_{pix}) can be thought to be distributed following a gaussian distribution centered in the charge value (μ_Q) and spread with a standard deviation equal to the readout noise (σ_{pix}):

$$Q_{pix} = Gaus(\mu_Q, \sigma_{pix}). \tag{2.11}$$

Assuming to read the same pixel multiple times (N_{skips}) and in independent ways, the

final charge can be retrieved by averaging over all the measurements:

$$\overline{Q}_{pix} = \frac{1}{\text{N}_{\text{skips}}} \sum_{i=1}^{\text{N}_{\text{skips}}} (Q_{pix})_i, \tag{2.12}$$

with $\overline{Q}_{pix}$ having a standard deviation equal to $\sigma_{pix}/\sqrt{\text{N}_{\text{skips}}}$. Since standard CCDs feature a readout noise of about 2 electrons, skipper amplifiers can potentially achieve sub-electron noise levels by choosing the proper number of skips. The low frequency noise components are reduced by employing a shorter integration time to measure the pedestal and the signal levels, as shown in Figure 2.12. However, the main drawback of using skipper amplifiers
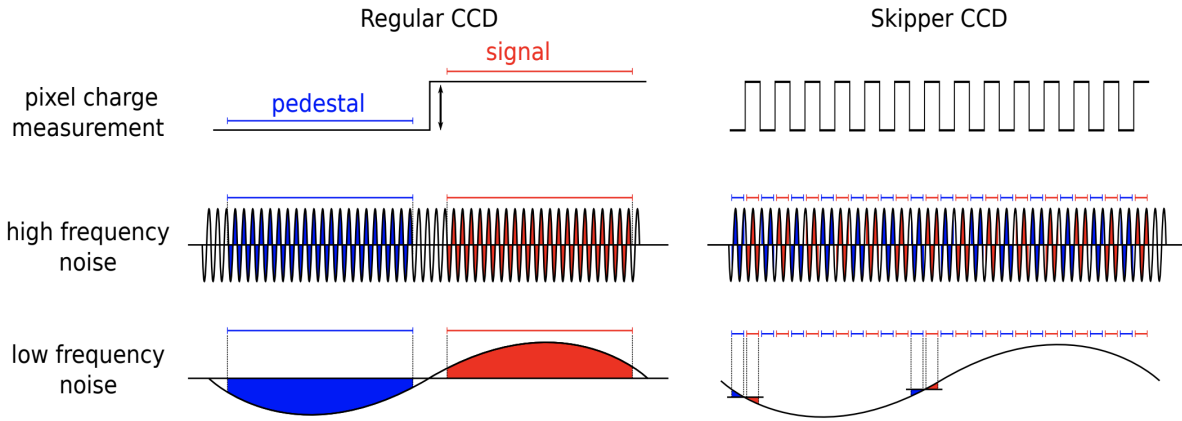
Figure 2.12 – Comparison between the measurement of a pixel charge in case of a standard (left) or skipper (right) readout procedure [86]. For a skipper CCD, the contribution of the low frequency noise is visibly smaller than for a standard CCD.

is that the time needed to read a whole CCD significantly increases with respect to the standard case. For example, a DAMIC CCD (4k pixels ×4k pixels) can be efficiently read in 12 minutes with a ∼2 electrons noise level. To reduce it by 10 times, to 0.2 electrons, 100 skips are needed. This would imply 1200 minutes to read out the CCD.

2.1.3 CCD images

The Video signal from the output amplifier is digitized by a 16-bit Analog to Digital Converter (ADC), with dynamic range values between 0 and 65535 ADU. This digital information is then transmitted via optical fibers to the DAQ machine, where it is stored in the form of a FITS (Flexible Image Transport System) file. The latter thus contains the

final CCD image, which consists of a 2D stacked history (projected on the x-y plane) of all the ionization events taking place in the device, with each pixel value being proportional to the number of collected carriers. An example of CCD image is shown in Figure 2.13 (a). Note that each pixel is 15 μm wide in the x and y directions. Given the excellent spatial resolution of CCDs, particles interacting in the device can be distinguished by the shape of their tracks, as shown in Figure 2.13 (b). A track is also referred as cluster, consisting in a set of contiguous pixels. Low energy electrons and nuclear recoils, whose physical

(a)

(b)
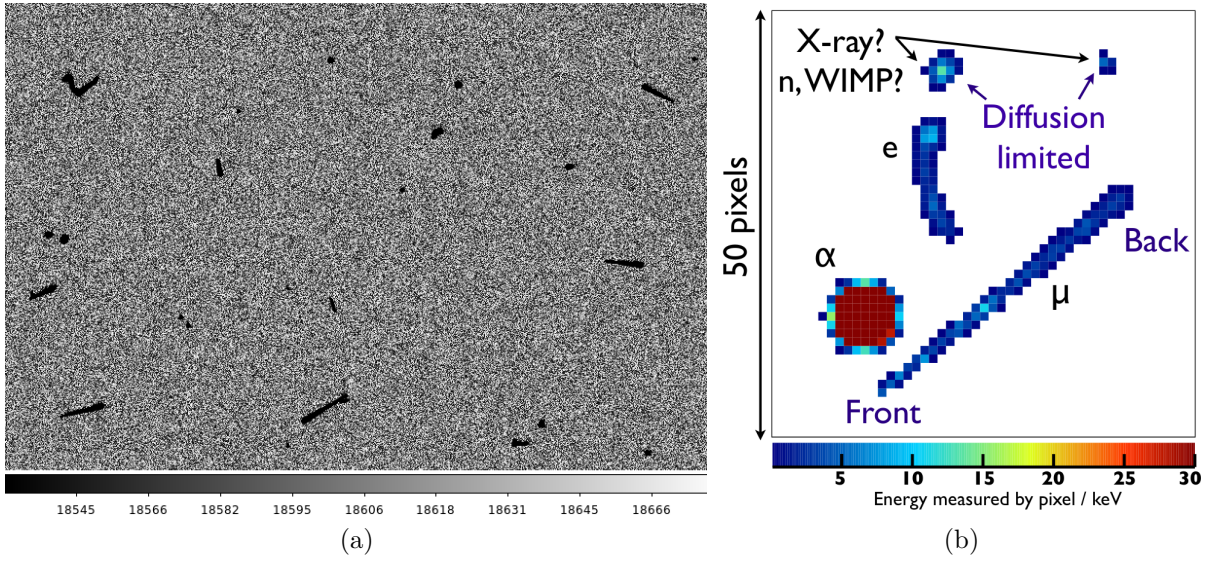
Figure 2.13 – (a): A raw CCD image visualized via the SAOImageDS9 tool. Image acquired at the LPNHE laboratory in Paris [86]. The gray-scale indicates the pixel charge values in ADU. (b): Reconstructed particle tracks observed in CCD images, including electrons, muons, α particles, and diffusion-limited clusters [86].

track length is <15 μm, produce the so-called "diffusion limited" clusters, since their spatial extension is dominated by charge diffusion. Higher energy electrons, instead, lead to extended tracks, featuring a worm like shape. Alpha particles in the bulk or from the back of the CCD produce large round structures due to the plasma effect [88]. The local electric field within the plasma is greater than the electric field applied across the substrate. Therefore, for interactions deep in the substrate, where the electric field is only along z, the charge carriers diffuse laterally toward regions of lower charge concentration until the substrate electric field becomes dominant. This brings to highly-diffuse, round clusters. Alpha particles can also feature "bloomed" tracks, elongated in the y direction

53

(not shown in Figure 2.13, b) [89]. This happens when particles strike the front of the CCD and deposit their energy less than 20 μm below the gate. In this case, the high-density charge cloud created by the alpha particles can easily overcome and spillover the potential barriers between vertical pixels, while it is harder for it to overcome the potential barrier of the vertical channel stops between columns. Cosmic muons passing through the CCD leave a straight track with a wider width where the particle crossed the back of the CCD, due to diffusion.

The size of an image depends on the user desire. It is possible to readout all the pixels of the CCD or only a fraction[13]. Furthermore, an image can also exceed the physical dimension of a CCD. The extra pixels are called "overscan" pixels and consist of additional measurements performed by the device beyond its physical length (in x or in y). Overscan pixels on the x-axis, having almost no charge due to the short exposure time, can be used to retrieve information about the baseline (or image pedestal), the ADU value corresponding to no charge, as described in Chapter 6. The image visual inspection is a fundamental step during the characterizing or testing of a CCD, and allow to identify the presence of anomalies like hot regions, glowing, CTI, and pedestal fluctuations.

Furthermore, CCDs can be equipped with up to 4 amplifiers, one in each corner of the device. These can be used simultaneously or not, depending on the user necessity. Further details on the procedures followed to acquire, analyze and inspect CCD images will be provided in Chapter 6, for the specific case of Compton scattering measurement carried out by the DAMIC-M collaboration.

2.1.4   Sources of noise for a CCD

Several source of noises exists, which can affect a CCD charge measurement. These are summarized in the following.

Output amplifier noise (or readout noise): to this group belongs the reset noise, which, as already mentioned before (Section 2.1.2), is introduced with the creation of the so-called reset pulse and can be suppressed via the correlated double sampling technique. Furthermore, it shows a temperature dependence of the type $\propto \sqrt{T}$ [85]. Other types of amplifier noise are the thermal white noise and flicker noise (or 1/f noise). The former dominates at high frequency and is described by the Johnson white noise equation,

---

13. For example, it might be useful in terms of noise, to acquire smaller images than the CCD size (see Chapter 6).

showing as well a $\propto \sqrt{T}$ dependence [85]. The flicker noise is the main limitation for the noise improvement in standard readout CCDs. It is due to random trapping and emission of charge carriers near CCD interfaces, like the silicon - silicon oxide ones, and it is the dominant type of noise at low readout frequency [85]. It can be significantly suppressed with the skipper readout.

Charge Transfer Inefficiency (CTI): it quantifies the fraction of the charge lost while being transferred across different pixels, as already mentioned in Section 2.1.2. Theoretically, the amount of charge lost can be calculated according to a Poisson distribution:

$$S_{N_P+n} = \frac{S_i (N_P \mathrm{CTI})^{\mathrm{n}}}{n!} \exp\{(-N_P \mathrm{CTI})\}, \qquad (2.13)$$

where S_i is the charge in the initial target pixel, n the trailing pixel number following the target one (the target pixel has n=0), and N_P the number of pixel transfers [85]. CTI can induce a deformation in the topology of a cluster (ensemble of contiguous pixels), which would feature a tail of deferred charges in the opposite direction with respect the one of the charge transfer. Furthermore, a charge can be detached from the original packet and be reconstructed as a distinct cluster. CTI can be caused by defects, impurities in the CCD, as well as not proper clock settings (e.g., the difference between the low and high clock rail voltages).

Dark current (DC): this includes processes of thermal (intrinsic dark current), environmental (extrinsic dark current) and operational origins which cause the creation of spurious charges in the pixels. Intrinsic dark current can be classified into bulk and surface contributions, the former occurring in the silicon bulk and the latter at the interfaces between the CCD layers. Both are strongly temperature dependent. The bulk component is expected to be the dominant one and it is also refferred as "depletion dark current" [80]. This is driven by imperfections and impurities, which add energy levels into the band gap of silicon [80, 90]. The temperature (T) dependence of the depletion dark current rate is found proportional to $T^{3/2}e^{-E_{gap}(T)/2k_B T}$, where E_{gap} is the band gap of silicon and k_B the Boltzmann constant [80, 85, 90]. In order to reduce this noise source, DAMIC CCDs (and the future DAMIC-M ones) are cooled down to temperatures ≤ 140 K [14]. The bulk

---

14. Note that there is a low temperature limit (around $\sim$70 K) under which the CCD ceases to work. At this temperature the dopant atoms do not ionize and form potential wells. Therefore, the structure of the crystal is frozen and any created electron-hole pairs will recombine [85].

DC depends also linearly on the depletion region width and on the pixel area [85, 90]. Extrinsic dark current is instead due to external sources of few-electron signals, as the Cherenkov radiation. The emission of infrared light by the output amplifier causes the so-called glowing dark current, visible in the CCD images as an excess of charge near the amplifier. Clock Induced Charge (CIC) can be also be considered a type of dark current, due to spurious carriers generated by clocks during charge transfer [80, 85].

Pick-up Noise: this is caused by external sources of electronic noise, for example due to electromagnetic interference or improper electrical grounding [85]. Possible strategies to reduce these types of noise include the use of EM shielding and the optimization of the grounding system [85].

2.2 DAMIC at SNOLAB

The Dark Matter In CCDs (DAMIC) experiment is the first dark matter detector to employ a multi-CCD array [78].

DAMIC story starts in 2012, when the detector was deployed at the SNOLAB laboratory in Canada in the Creighton active mine [91]. The overburden of the site (2 km, 6010 meters water equivalent) efficiently shields the experiment from cosmic ray muons, reducing their flux to a negligible level of <0.27 m^{-2} d^{-1} (about a factor 5×10^7 lower than the flux at sea level) [84]. Throughout 2014–2016, an active R&D program was carried out to demonstrate DAMIC capabilities consisting of radioactive background studies, calibration measurements, and first dark matter searches (WIMPs, hidden sector) [70, 84, 89]. Such studies demonstrated the stable, low-noise and low-background operation of DAMIC in a deep underground laboratory and therefore the feasibility of the use of CCDs for the dark matter search. Furthermore, these studies proved DAMIC sensitivity to energy depositions as small as the band gap of silicon from dark matter interactions. In the years, DAMIC deployment was modified and upgraded for lower backgrounds, more CCD detectors, and longer exposure. The final detector configuration was installed in January 2017. The results of the latest setup include the search for hidden-sector dark matter particles from its interactions with electrons [92] and the most sensitive search for silicon nuclear recoils from the scattering of light-mass WIMPs (1-10 GeV) [53].

All the results obtained by DAMIC laid the foundations for the DAMIC-M experiment, later described in Section 2.3. This section summarizes all the results obtained by the

experiment at SNOLAB.

2.2.1 DAMIC detector
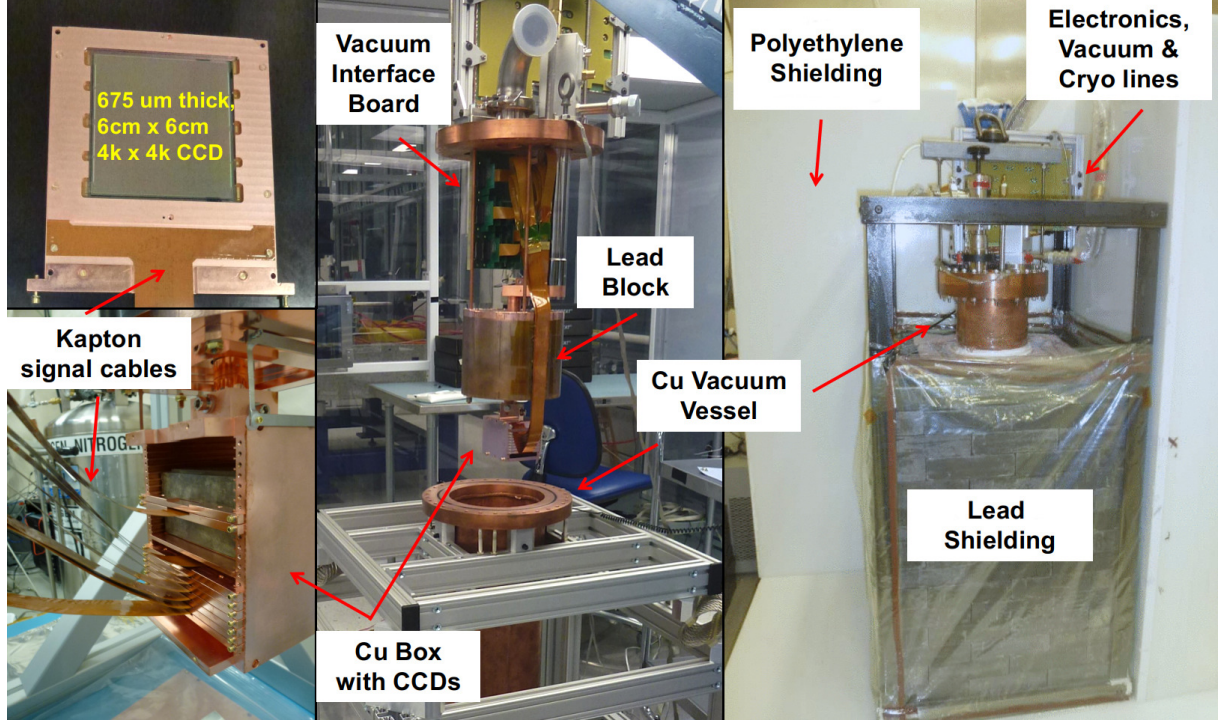
Figure 2.14 – Final DAMIC at SNOLAB detector configuration, with labelled components [80].

DAMIC final configuration consists of an array of 7 CCD modules in a tower-like configuration [15] [78]. Modules are inserted into slots of a copper box with wall thickness of 6.35 mm. The box acts as mechanical support but also as a cold IR (infrared radiation) shield during operation. A CCD module is composed by a CCD package installed in a copper support frame. The Fermi National Accelerator Laboratory (Fermilab) took care of the CCD packaging. A CCD sensor is glued, together with a kapton flex cable, onto a silicon support made from high-resistivity silicon wafers (of the same origin as those used for CCD fabrication). The CCDs are then wire-bonded to the cables that deliver signals from (CCD output signal) and to (clocks and bias voltages) the devices.

---

15. The array initially consisted of 8 CCDs. However, one of them was disconnected soon after installation due to luminescence from one of the amplifiers, which was producing unwanted charge throughout the CCD array.

The CCDs were developed by the Lawrence Berkeley National Laboratory (LBNL) MicroSystems Lab [83]. Each CCD features an array of 4116×4128 pixels (62×62 mm^2), a thickness of about 0.675 mm (only 0.669 mm active), and a mass of 5.9 g. Fully depletion is achieved with a substrate bias of 70 V. The readout noise achieved by DAMIC CCDs is of about 1.6 electrons, by using the CDS technique with optimized integration time (40 μs) to suppress high-frequency noise. DAMIC CCDs have the lowest dark current ever measured in a silicon detector, $\leq 2 \times 10^{-22}$ A/cm^2 at an operating temperature of 140 K. More details about the specific CCD structure and operation are reported in Section 2.1.2.

The topmost CCD module (CCD 1) was fabricated with ultra-low radioactivity copper, electro-formed by PNNL [93]. Furthermore, it is shielded on top and on bottom by two 2.5 cm thick ancient lead bricks. The latter come from an ancient Spanish galleon, sunken more than 300 years ago. Therefore, these bricks feature negligible ^{210}Pb content as well as low contamination from cosmic activation and radon deposition, having been protected from them in the deep sea for centuries and having been later stored underground. More details about low background materials, like electro-formed copper and ancient lead, are reported in Section 3.3.5. An additional ∼1 mm thick electro-formed copper plate is placed on top of the lower ancient lead brick. CCD1 thus features a lower background environment with respect to the other devices. Profiting of this, its data was used to cross-check the radioactive background model for the dark matter search, constructed using the other CCD events (see Section 2.2.5).

All the other copper components of the CCD modules and box, not made of electro-formed copper, were machined from oxygen-free high conductivity (OFHC) copper. These parts were cleaned and passivated with ultra-pure water and acids in order to reduce the radiogenic contamination on their surfaces.

An 18 cm thick cylindrical ancient lead block shields the copper box from the Vacuum Interface Board (VIB), to which the kapton cables are attached. The cylindrical lead block has a central hole to let through a copper cold finger, needed to cool down the copper box to temperatures in the 120-150 K range.

All the components are contained in a copper cryostat held at pressures of 10^{-6} mbar. CCDs have to be cooled down in vacuum, since an open-air environment would bring to thermal losses and humidity in the air would condensate and freeze on the device surfaces, causing a short-circuit.

The vacuum vessel is surrounded by a lead castle about 20 cm thick, with the innermost

5 cm being ancient lead and the outer lead being low-radioactivity. In this way, the CCDs are shielded in all the directions from high energy environmental photons by at least 18 cm of lead. Furthermore, all ancient lead surfaces were cleaned in an ultra-pure dilute nitric acid bath, to further reduce their background contribution. Finally, a 42 cm of polyethylene shield is placed around the lead one and above the cryostat flange to shield against external neutrons.

The apparatus is then enclosed in an hermetic box and flushed with pure nitrogen to free its volume from radon.

The VIB is then connected to the CCD controller located outside the shielding. The controller transmits the clock and bias voltages to the CCDs and processes the CCD output signal. Finally, the CCD controller is programmed by a DAQ computer.

Figure 2.14 shows the DAMIC setup at SNOLAB.

2.2.2   Energy calibrations

A series of measurements were carried out by using radioactive and optical sources to calibrate the detector response to electron and nuclear recoils.

DAMIC CCDs energy response was initially evaluated on surface using X-ray fluorescence light from Al, Cr, Fe, Mn, O and Si for energies >0.5 keV [84]. Figure 2.15 (a) shows the energy spectrum measured by a DAMIC CCD exposed to a ^{55}Fe source. The low-energy response was instead investigated later at SNOLAB using visible photons from a red light-emitting diode (LED) [84]. These measurements demonstrated the linearity of the CCD to be within 5% down to detector threshold (~ 40 eV) [84] and are summarized in Figure 2.15 (b). Additional investigations were carried out by measuring on-site the copper (8 keV) and lead (10.8, 12.7, and 13.0 keV) fluorescence lines from parts of the apparatus. Further insight on CCD response to electron recoils was provided by studying the spectrum of Compton scattered electrons using ^{241}Am and ^{57}Co sources [82]. The same measurement was carried out by the DAMIC-M collaboration with a skipper CCD and it is the topic of Chapter 6.

The DAMIC CCD response to α particles was also calibrated using an ^{241}Am source. The energy scales from α-induced and electron-induced ionization were found to be within 3%, with an α energy resolution of 50 keV at 5.5 MeV [89].

A recoiling silicon nucleus in the CCD bulk deposits only a fraction of its energy through ionization, producing a significantly smaller signal than a recoiling electron of the same energy. Therefore the knowledge of the nuclear recoil ionization efficiency, which
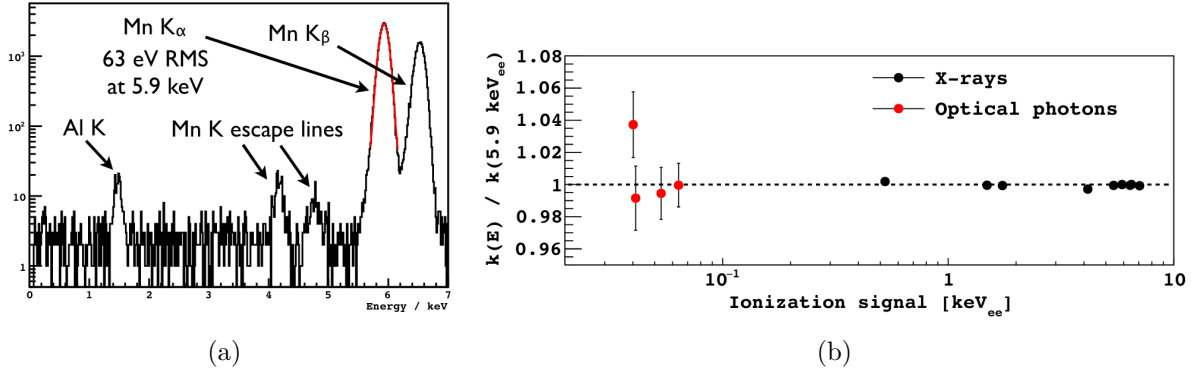
(a)   (b)

Figure 2.15 – (a): Spectrum obtained with a ^{55}Fe source illuminating a CCD from the back [91]. The two main X-rays from the source are the Kα and Kβ from the daughter Mn nucleus. The source holder is made of aluminum, which is the origin of the fluorescence Al K X-ray observed. While the main Kα and Kβ peaks are formed by X-rays that deposit their full energy in the CCD, the Mn escape lines are due to partial energy deposits. In fact, if a Si fluorescence X-ray is produced (1.7 keV), it will likely "escape" from the original point of interaction. The silicon X-ray can be then absorbed by the CCD at some other pixel location or escape from the sensor entirely. (b): Linear constant k(E) relating the CCD output signal to the ionization generated in the substrate [84]. Values are given relative to the k value measured at 5.9 keV. The linearity of the CCD energy response is demonstrated down to 40 eVee. The average energy needed to generate an e-h pair is assumed equal to 3.77 eV. Reprinted figure with permission from [84]. Copyright (2016) by the American Physical Society.

relates the ionization signal in the detector (in units of eVee) to the kinetic energy of the recoiling nucleus (in units of eVnr), is fundamental to properly interpret the measured ionization spectrum in terms of nuclear recoils induced by WIMPs. Dedicated measurements were carried out by exposing a CCD (developed in the R&D efforts of DAMIC) to neutrons from an ^{124}Sb-^{9}Be photoneutron source [94]. The nuclear recoil ionization efficiency in silicon was thus obtained for nuclear recoils between 0.7 keVnr (0.06 keVee) and 2.3 keVnr (0.4 keVee), a range previously unexplored and relevant for the direct detection of low-mass WIMPs (Figure 2.16). Therefore, this measurement allowed to have a complete understanding of the response of the detector to a potential WIMP signal interacting with silicon nuclei. A similar measurement is being performed by the DAMIC-M collaboration to characterize the nuclear recoils in a skipper CCD.
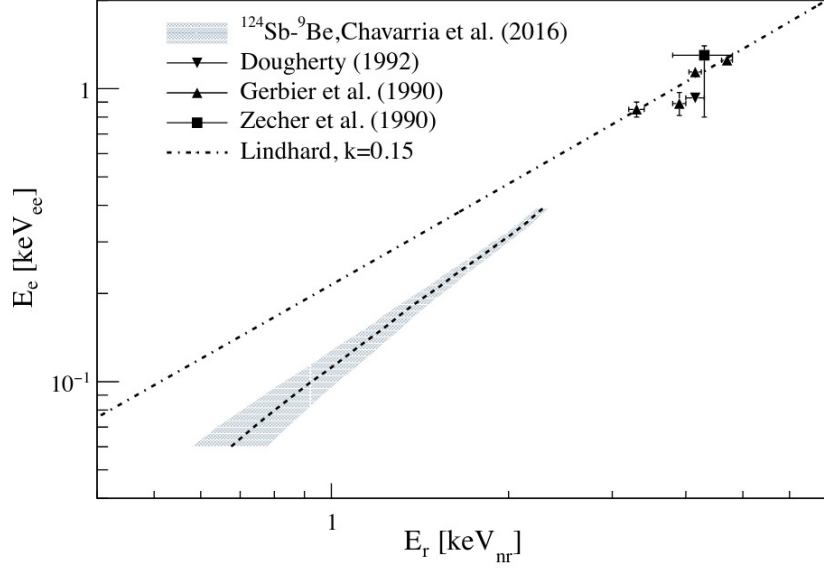
Figure 2.16 – Ionization signal (E_e) as a function of nuclear recoil energy (E_r) in silicon obtained in [94]. The gray band represents the 1σ uncertainty on the measurement. Results from previous experiments are also shown, together with the prediction from the Lindhard model [95, 96]. A deviation is observed between the theoretical model and the experimental measurement. Reprinted figure with permission from [94]. Copyright (2016) by the American Physical Society.

2.2.3 Depth calibration

As already mentioned in Section 2.1.2, by looking at the diffusion spread of charges, it's possible to reconstruct the z coordinate (depht) of the energy deposits. In order to do so, it is necessary to determine the diffusion parameters of equation 2.8, describing the relation between the diffusion spread and the interaction depth. DAMIC retrieved these parameters experimentally by fitting muons tracks [78, 84]. In fact, cosmic muons passing through the CCD leave a straight track of minimum ionizing energy. The orientation of the track is immediately evident by looking at its width variation: the end-point of the track on the back of the CCD is much wider than the end point at the front due to charge diffusion (see Figures 2.13 (b) and 2.17). By using surface laboratory images, a fit to the charge distribution of the observed muons was performed, convolving the cosmic ray trajectory with a gaussian spread using equation 2.8. A percent-level deviation from the theoretical diffusion spread was found in data, proportional to the event energy (E). To take this into account a multiplicative linear correction was applied to the spread (σ) of
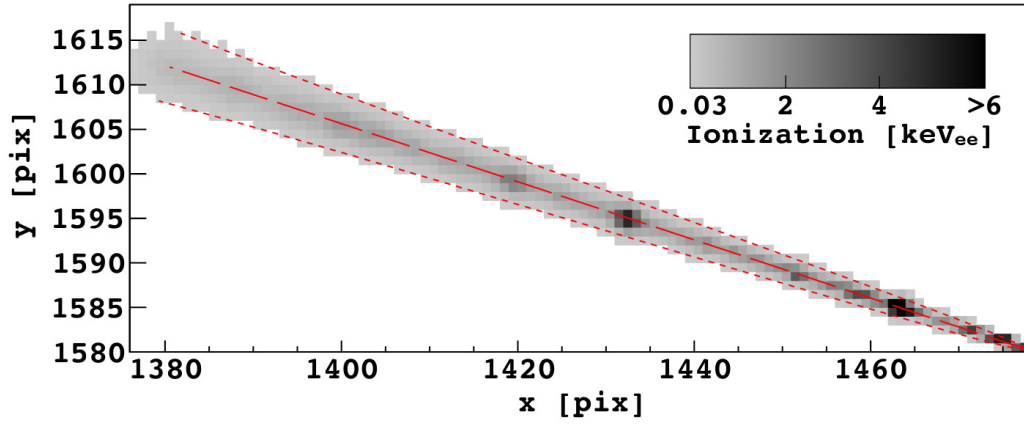
Figure 2.17 – Muon track observed in cosmic ray background data acquired on the surface [84]. The large area of diffusion on the top left corner of the image is where the muon crossed the back of the CCD. Conversely, the narrow end on the bottom right corner is where the muon crossed the front of the device. The reconstructed trajectory is shown by the long-dashed line. The short-dashed lines show the 3σ band of the charge distribution according to the best-fit diffusion model. Reprinted figure with permission from [84]. Copyright (2016) by the American Physical Society.

equation 2.8:

$$\sigma = \sqrt{-A \ln |1 - Bz|}(\alpha + \beta E). \tag{2.14}$$

An example of fitted muon track is shown in Figure 2.17. This procedure was also used to obtain the diffusion parameters related to the skipper CCD used for the Compton scattering measurement, described in Chapter 6.

2.2.4 Dark matter search

The initial goal of the DAMIC experiment was to look for the interaction of light WIMPs with silicon nuclei in the bulk of scientific-grade charge-coupled devices. In fact the relatively low mass of the silicon nucleus, as well as the low read-out noise of the detector, make the CCDs ideal instruments for the identification of the nuclear recoils with keV-scale energies from WIMPs with masses <10 GeV [53]. The DAMIC scientific program was then extended to the search of hidden sector particles, which couple weakly with ordinary matter through, for example, the mixing of a hidden-photon with an ordinary photon. Therefore, unlike WIMPs candidates, hidden sector candidates also interact with electrons in the target material, with sufficiently large energy transfers to be detectable

down to DM masses of $\approx$MeV [92]. In addition, hidden photon DM particles with masses above the band gap of silicon, $\sim$1.2 eV, can be probed through absorption by electrons in detection targets.
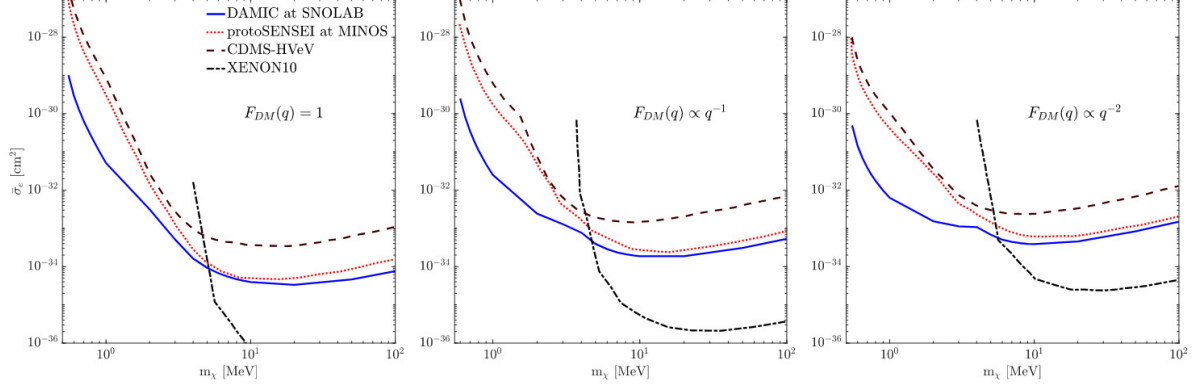
Figure 2.18 – 90% C.L. upper limits on the DM-electron free scattering cross section as a function of the DM mass m_χ for a dark matter form factor $F_{DM} \propto q^{-n}$ (n = 0, 1, 2), with q indicating the momentum transfer between the DM and the electron [92]. DAMIC at SNOLAB results [92] are shown as a solid blue line. Limits from protoSENSEI at MINOS [97, 98] (dotted line), CDMS-HVeV surface run [99] (dashed line), and an analysis of the XENON10 data [100] (dashed-dotted line) are also shown for comparison. Reprinted figure with permission from [92]. Copyright (2019) by the American Physical Society.

By exploiting its extremely low levels of leakage current (2–6×10^{-22}A cm^{-2}), DAMIC was able to place constraints on a so-far unexplored parameter space for hidden sector dark matter masses between 0.6 and 100 MeV (Figure 2.18) [92]. Furthermore, it reported the best direct-detection constraints on hidden-photon dark matter with masses in the range 1.2–30 eV (Figure 2.19) [92].

DAMIC data excluded spin-independent WIMP-nucleon scattering cross sections as low as 3×10^{-41} cm^2 for WIMPs with masses from 7 to 10 GeV, placing the strongest constraints from a silicon target on the existence of WIMPs with mass $<$9 GeV (Figure 2.20) [53]. These results provided further insights for the interpretation of the excess of nuclear-recoil events observed by the CDMS silicon experiment in 2013 and which could be attributed to the scattering of WIMPs with mass $\sim$9 GeV [104]. In fact, DAMIC limits excluded with the same nuclear target a significant fraction of the parameter space corresponding to a dark matter interpretation of the CDMS excess.

As can be observed from Figure 2.20, there is a discrepancy between the placed ex-
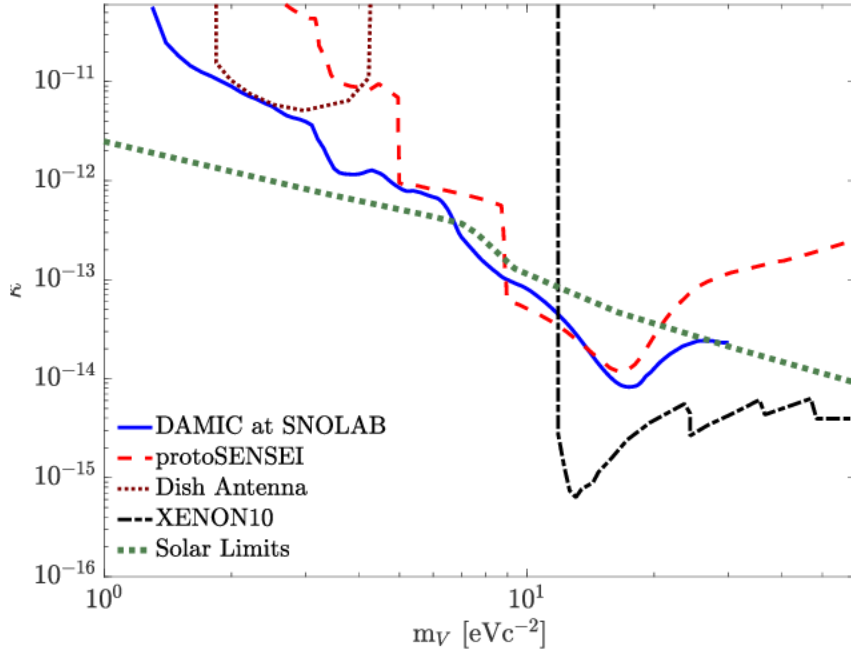
Figure 2.19 – 90% C.L. constraints upper limits on the hidden-photon DM kinetic mixing parameter κ (mixing of a hidden-photon with an ordinary photon) as a function of the hidden-photon mass m_V [92]. DAMIC results are shown as a solid blue line [92]. Direct-detection limits from protoSENSEI at MINOS [97], an analysis of the XENON10 [101] data, a dish antenna [102], and astrophysical solar limits [101, 103] are also shown for comparison. Reprinted figure with permission from [92]. Copyright (2019) by the American Physical Society.

clusion limit and the expected sensitivity. This is due to a statistically significant (3.7 σ) excess of ionization events over the background model (see Section 2.2.5) measured above the analysis threshold of 50 eVee and below 0.20 keVee (Figure 2.21). The excess is populated by events produced in a uniform way in the bulk of the CCDs. Note that the depth was determined by looking at the diffusion spread of clusters. The statistical significance of the excess is driven by events with diffusion spread $\sigma \sim 0.2$ pixels. Events from the CCD backside are thus excluded as origin of this signal. An analysis showed that these events were unlikely to have originated on the surface of the CCD [53]. The excess amplitude (s) is of 17.1 ± 7.6 events, leading to a rate of a few events per kg-day. Although many systematic checks and many hypothesis were explored, the origin of these events (e.g., whether they are electronic or nuclear recoils, or some unexpected instrumental effect) remains unknown. An R&D program is currently ongoing to explore the causes of this excess using skipper CCDs, deployed in the DAMIC cryostat at SNOLAB. Skipper
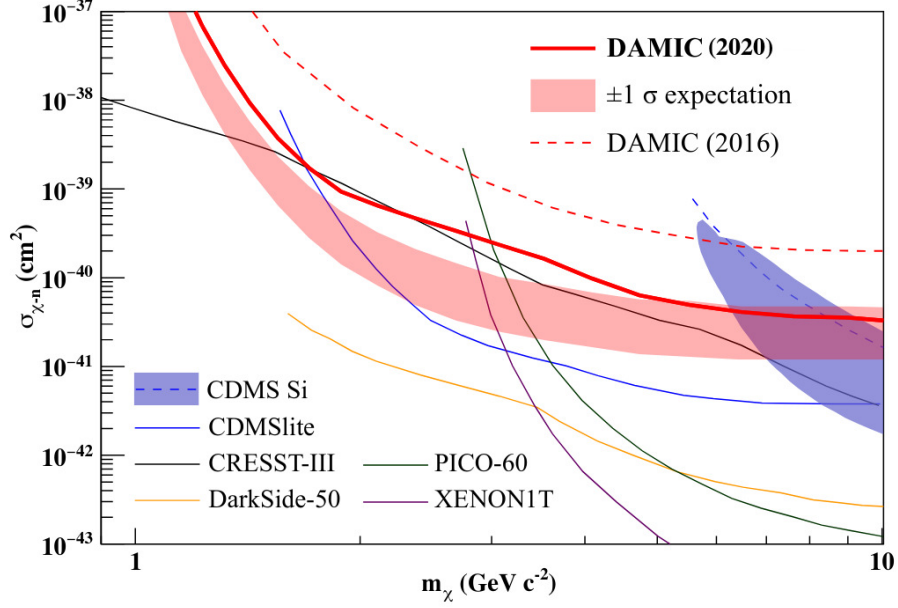
Figure 2.20 – Upper limit (90% C.L.) on the WIMP-nucleon cross section obtained by DAMIC in [53] with a 11 kg-day exposure (solid red line). The expectation $\pm 1\sigma$ band, if only known backgrounds are present in DAMIC data set, is shown by the red band. For comparison, 90% C.L. exclusion limits from a previous result with a 0.6 kg-day exposure is included, together with results from other experiments and the 90% C.L. contours for the WIMP-signal interpretation of the CDMS silicon result [104]. Reprinted figure with permission from [53]. Copyright (2020) by the American Physical Society.

CCDs in fact will allow to push down the detector energy threshold and thus will be able to probe the excess spectrum down to lower energies. DAMIC-M, with its ~200 CCDs, will provide further insight into this low energy range in a completely new location and setup.

2.2.5 Background characterization

A comprehensive radioactive background model for the dark matter search was constructed for DAMIC, by taking advantage of the the well-characterized depth and energy resolution of the detector and using detailed Geant4 based particle-transport simulations. Both bulk and surface backgrounds from natural radioactivity were modelled down to 50 eVee [78]. This laid the foundation for the background characterization for the DAMIC-M experiment.
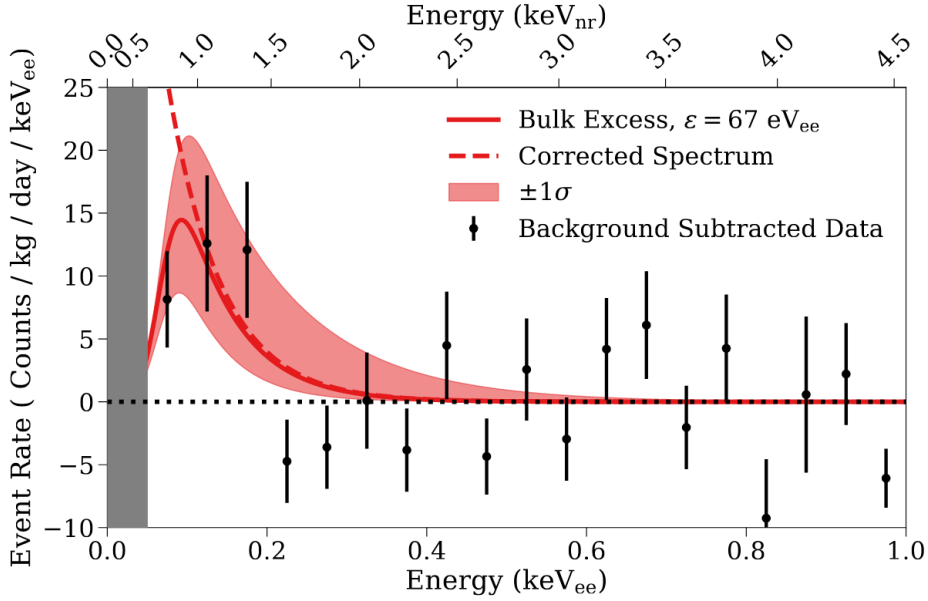
Figure 2.21 – Energy spectrum of the best-fit generic signal (red lines) overlaid on the background-subtracted data (markers), obtained with DAMIC data (11 kg-day exposure) [78]. The fit spectrum including the detector response is shown (solid line), together with the spectrum corrected for the detection efficiency (dashed line). The red shaded region represents the 1σ uncertainty from the likelihood-ratio tests. For reference, the equivalent nuclear recoil energy (keVnr) is also shown on the top axis. The signal is assumed to have an exponentially decreasing spectrum with decay energy ϵ and amplitude s.

The current background level of DAMIC is of 12.28 d.r.u (events/kg/keV/day) for CCDs 2-7 and 8.28 d.r.u for CCD 1, measured between 1-6 keVee. DAMIC determined the relative contributions of various radioactive background sources, indicating cosmogenic tritium in the bulk of CCDs and ^{210}Pb deposited on the surfaces of the CCDs as the dominant ones. Cosmogenic isotopes and ^{210}Pb in the OFHC components are also found to be major contributors. This highlighted the necessity for future experiments like DAMIC-M to limit the cosmogenic activation of the silicon and copper components as well as the exposure of the detector surfaces to radon, including those of wafers prior to CCD fabrication. Furthermore, DAMIC analysis revealed the presence of a partial charge collection (PCC) region on the backside of the CCDs, which causes a significant distortion of the spectrum at low energy (especially affecting the spectrum from ^{210}Pb decays on the backside of the CCDs). As anticipate in Section 2.1.2, this is due to the diffusion of phosphorous from the backside ISDP layer into the high-resistivity bulk silicon. In fact, the

concentration of phosphorus (P) donors changes the mobility and lifetime of the minority charge carriers (holes) and the electric field profile near the back of the CCD, as shown in Figure 2.22. High phosphorus concentration, as it is the case at the CCD backside, brings to a short carrier lifetime and charge recombination. At intermediate concentrations, however, charges, having longer lifetime, only partially recombine and can be collected at the CCD gates. Therefore, phosphorus, diffusing in the CCD active region, can induce partial collection of charges created by ionization events in the back of the CCD [78]. Note that the PCC effect was also taken into account in the DAMIC analysis. A possible
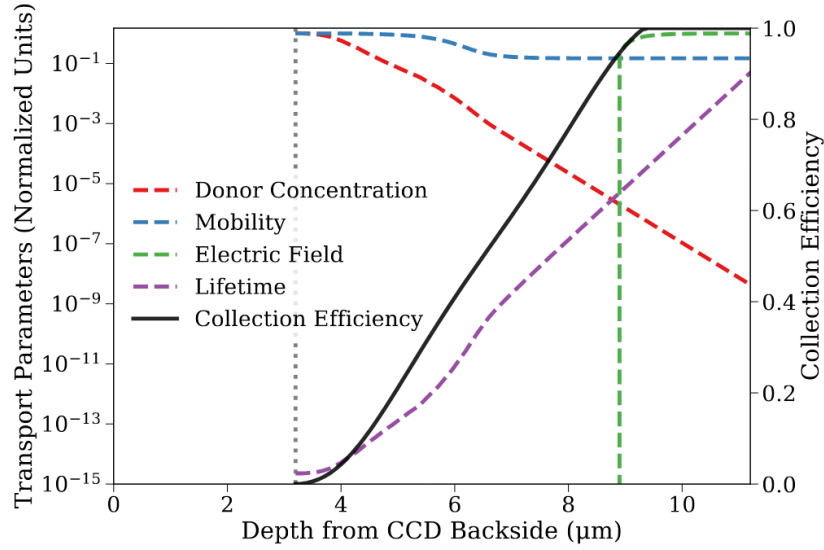
Figure 2.22 – Properties determining the charge transport and recombination in silicon (dashed lines) in normalized units of 10^{20} cm^{-3} (donor P concentration), 55×10^9 μm^2/V/s (mobility), 0.1 V/μm (electric field), and 1.2×10^5 s (lifetime) as a function of depth from the CCD backside (z") [78]. The calculated charge collection efficiency is shown by the solid black line. The position of the original wafer surface is denoted by the vertical dotted grey line. For z" < 8.8 μm, there is a field-free region where diffusion is the only mechanism that allows charges to reach the fully depleted active region. If the carrier life time is short, as it is in the case of high P concentration, charges immediately recombine. At intermediate P concentration, the carrier lifetime is sufficiently long. Therefore, some of the charge diffuses into the active region before recombining, creating the PCC region.

solution for DAMIC-M would be to remove $\sim$10 μm from the backside of the CCDs after fabrication. Further details about the relevant sources of background for a dark matter experiment like DAMIC or DAMIC-M are extensively discussed in Chapter 3.

2.3 DAMIC-M

DAMIC-M is the successor of DAMIC and will be installed in 2024 at the Laboratoire Souterrain de Modane (LSM) in France, under 1800 m of rock. DAMIC-M will feature ∼200 CCDs, reaching a mass of about 700 g. A first conceptual design of the detector is shown in Figure 2.23. A vacuum copper cryostat will host the CCD stack, which will be cooled down to a temperature of about 100 K to decrease the level of dark current. The setup will be screened from external gamma rays and neutrons using a lead and a polyethylene shields. In the conceptual design, the DAMIC shield is taken as reference but the exact size and thickness will be optimized for LSM conditions and stricter DAMIC-M background requirements.
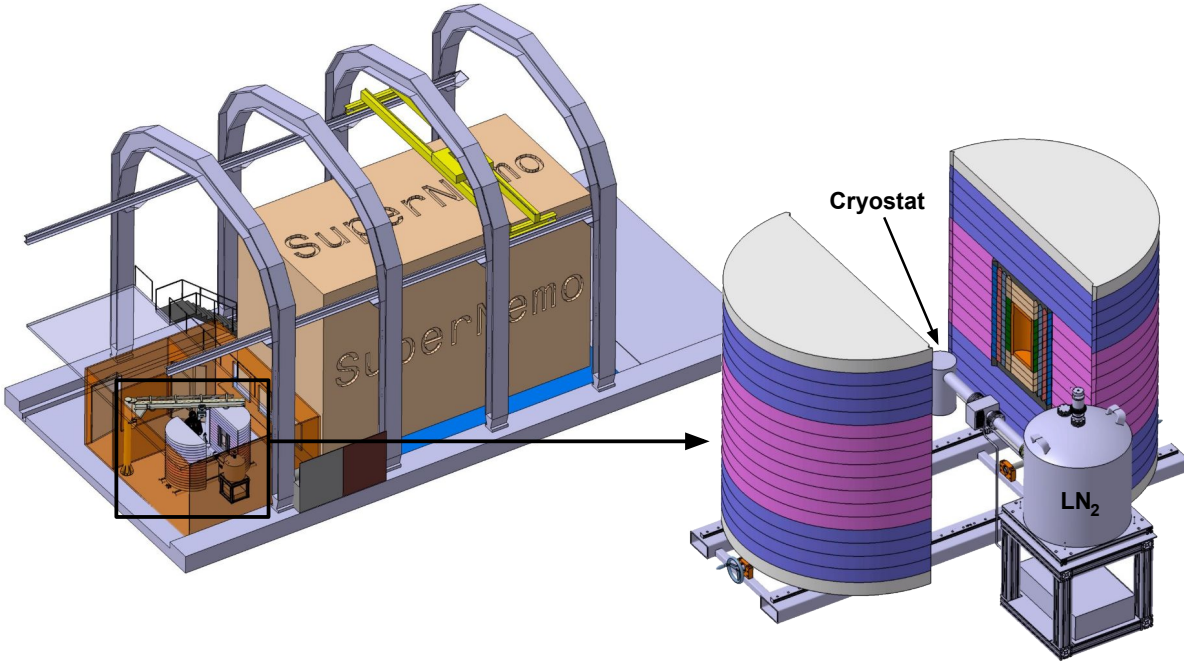
Figure 2.23 – First conceptual design of DAMIC-M in its clean room at LSM, next to the SuperNEMO experiment [105]. The external shielding consist of about 40 cm of polyethylene (outermost part, in white, violet, and pink) and 20 cm of lead (with the innermost part in ancient lead shown in orange). A cylindrical cryostat contains the CCD stack. Its cooling is provided by a copper cold finger connected to a liquid nitrogen dewar located outside the shielding.

While capitalizing on DAMIC experience, DAMIC-M will take a huge leap forward in the sensitivity to dark matter by innovating the detector technology. Conventional

CCDs will be replaced by skipper CCDs, allowing to break the sub-electron noise barrier (see Section 2.1.2). A new custom acquisition system is being developed in order to reduce the noise introduced by the external electronics. This consists of a control board, providing the signals necessary for the CCD to work (bias voltages and clocks), a front-end amplifier improving the signal-to-noise ratio of the CCD output signal, an analog-to-digital converter, performing the signal transition from the analog to the digital domain, and finally a motherboard, allowing the communication of the user with the electronics. Although not finalized yet, many advancements have been done concerning the electronics and the acquisition system and promising results have been obtained [106].

As already mentioned, the background goal for DAMIC-M is of a fraction of d.r.u (events/kg/day/keV), a factor $\sim$100 lower than the one achieved by DAMIC. The accomplishment of this challenging goal requires an accurate background control and optimization of the detector design. The components nearest to the detector will be made of low background materials like ancient lead and electro-formed copper. New low radioactivity flex cables will be used, produced using radiopure copper-polyimide laminates and by mitigating background contributions during fabrication. Geant4 simulations are being exploited to drive the detector conception and the material selection and handling. The author of this thesis was principally involved in this task to which Chapter 5 is devoted. There, all the explored detector designs and the associated background budgets will be discussed. It worth noting that, at the time of writing, the possibility of using the external shielding of the Edelweiss experiment [107] was being investigated. Edelweiss is a direct detection dark matter experiment using germanium bolometers which operated at LSM. The use of the Edelweiss shield will imply further modifications in the detector design and related simulations. As presented later in this thesis, to limit the cosmogenic isotope contribution to the background, simulations results restrict to 10 days the exposure time to cosmic rays of the electro-formed components and to 3 months the one of the OFHC copper ones. All the detector materials will be shipped avoiding airplane trasportation and will be shielded against cosmogenic activation. To this purpose, a custom-made shielded container was designed for transatlantic journeys [16]. As also highlighted by the DAMIC results, controlling the exposure time of silicon is pivotal. A great effort has been done by the DAMIC-M collaboration in reducing the cosmogenic activation of the silicon wafers that will be later on used for the CCD production. The silicon ingot was produced

---

16. The container consist of a 20' standard dry container with inside a $\sim$15 t iron shielding. In the latter, a cavity 50 cm $\times$ 40 cm $\times$ 110 cm will host the CCD packages and the electro-formed components.

at TOPSIL (Denmark), stored underground at the Boulby laboratory, and then cut into wafers by Shin-Etsu Handotai Europe (Scotland). Wafers were finally shipped to Canada and they are currently stored at SNOLAB. CCDs will be fabricated by Teledyne DALSA (Canada). So far, the DAMIC-M collaboration succeeded in reducing the exposure time to cosmic rays of the wafers from the initially foreseen 3 months to 15 days. A dedicated shielding will be also used during the production of CCDs to further reduce their activation. Furthermore, a radon-free clean room at LSM will host the CCD packaging and test facilities to reduce surface contamination. Background mitigation techniques will be described in more details in Chapter 3.
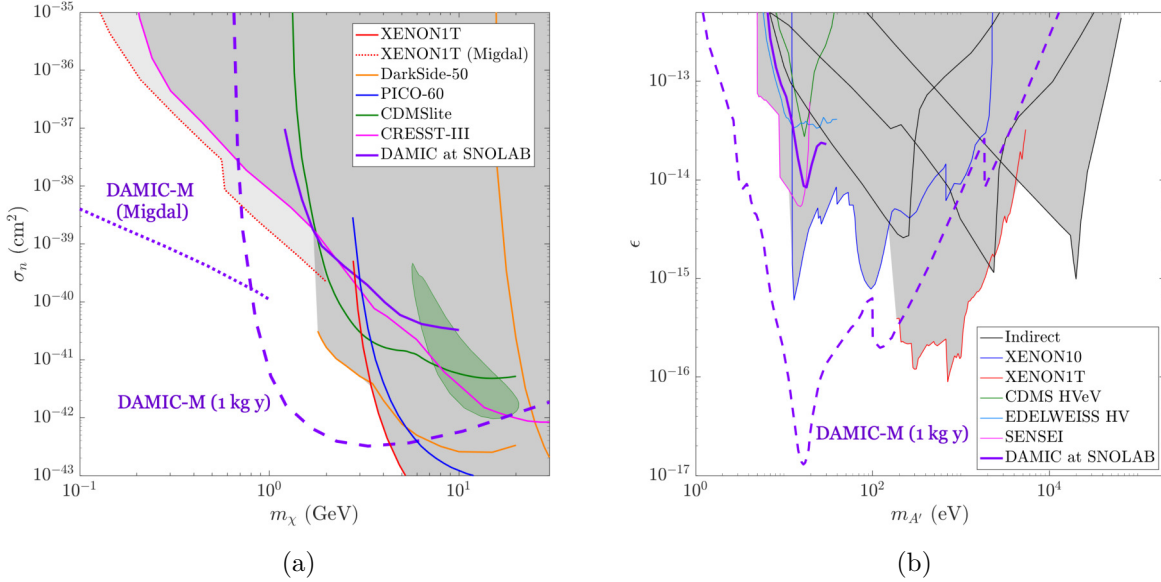
Figure 2.24 – (a): Sensitivity (90% C.L.) on the WIMP-nucleon spin-independent scattering cross section obtained for DAMIC-M compared to other dark matter experiments exclusion limits. The Midgal projection comes from [65]. (b): Kinetic mixing parameter ϵ as a function of the dark photon mass $m_{A'}$, assuming the dark photon constituting all of the dark matter.

The DAMIC-M pre-production CCDs demonstrated to have single electron resolution and low dark current level in the testing procedures. They are currently being exploited in calibration measurements (like the Compton scattering measurement, see Chapter 6) and in the DAMIC-M prototype installed at LSM, called Low Background Chamber. The latter will allow to open the way for DAMIC-M and is described in the following section
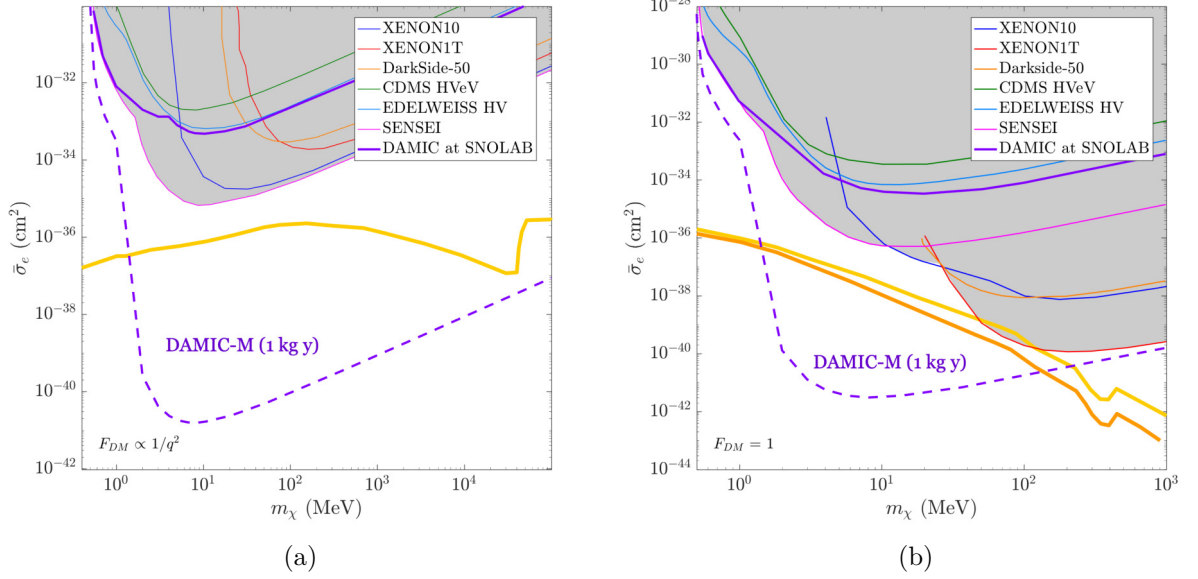
Figure 2.25 – (a): DAMIC-M sensitivity (90% C.L.) for a DM-electron interaction via a light dark photon mediator. The yellow curve corresponds to a freeze-in scenario. (b): DAMIC-M sensitivity (90% C.L.) for a DM-electron interaction via a heavy dark photon mediator. The orange and yellow curves correspond to a freeze-out scenario for a fermion DM (orange) and for a scalar DM (yellow). Exclusion limits from other dark matter experiment are shown for comparison.

(Section 2.3.1). To push down the level of dark current, DAMIC-M CCDs will employ the continuous readout mode. Images will be acquired continuously, lowering basically to 0 s the exposure phase.

The DAMIC-M scientific program covers a broad range of dark matter masses from 1 eV to 10 GeV, progressing in the search for GeV-scale WIMP dark matter and hidden-sector particles (eV-scale hidden photons and MeV-scale hidden sector particles). Strengthened by the increased mass and the lowered background and noise levels, DAMIC-M will reach unmatched sensitivity to the dark matter candidates of the so-called hidden sector with masses 1 MeV to 1 GeV. The expected sensitivity of DAMIC-M to WIMPs and hidden-sector particles is shown in Figures 2.24 and 2.25 for an expected exposure of 1 kg-y.

2.3.1 The Low Background Chamber

The Low Background Chamber (LBC) is the DAMIC-M prototype, installed at the end of 2021 at the LSM. Figure 2.26 shows the setup inside the DAMIC-M cleanroom at LSM. The Low Background Chamber is meant to help to define the background mitigation techniques and the logistics for DAMIC-M. Another important objective of the prototype is to probe the electronics chain, for example by performing grounding checks. A first dark matter search will be carried out with the LBC data which will then leave the floor to DAMIC-M.
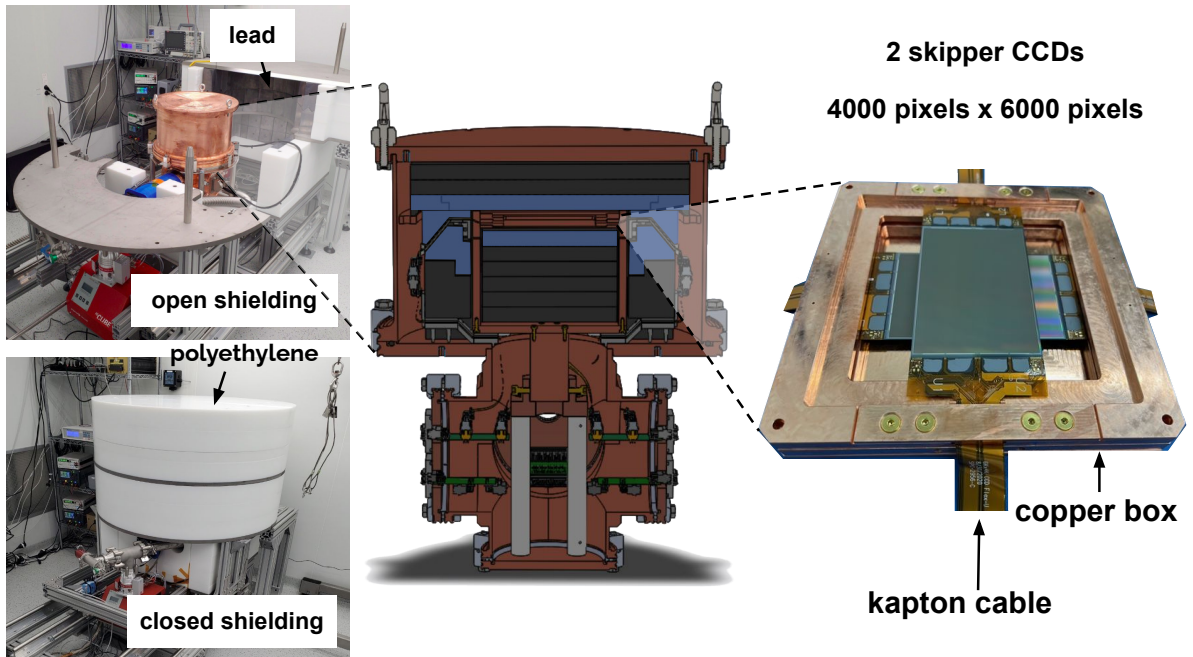
Figure 2.26 – Low Background Chamber installed at the LSM with labelled components. The external shielding is made of polyethylene and lead and it is shown in the open and closed configuration on the left. 20 cm of polyethylene and 15 cm of lead screen from the above and laterally the upper cylindrical part of the cryostat (housing the CCD box). The vacuum pump is visible in red, as well as the cryocooler in blue. The cryostat is made of oxygen-free high thermal conductivity (OFHC) copper. Inside it, the lead layers (∼2 cm thick) are shown in black, shielding the CCD box. The parts in ancient lead are highlighted in blue. The latter contains the two skipper CCDs and is made of OFHC. It will later on be substituted with a one in electro-formed copper. The entire setup is sustained by a stainless steel structure.

The detector features two high-quality 4k×6k skipper CCDs and is expected to achieve

a background rate similar to that of DAMIC ($\sim$10 d.r.u) in an initial phase. The background level will be then further improved to $\mathcal{O}(1$ d.r.u) in a second phase. A CCD controller (referred also as "Leach") produced by Astronomical Research Cameras Inc. [108], provides all CCD control signals, biases, and clocks, necessary for the exposure and readout phases. The "Leach" system will be then substituted by the DAMIC-M custom electronics. The CCDs are enclosed in a box made of oxygen-free high thermal conductivity (OFHC) copper, which supports the devices while acting as a cold IR shield. This will be later on changed with one made of electro-formed copper. CCDs are cooled down to a temperature of about $\sim$120 K with the use of a cryocooler. The CCD box is then surrounded by lead bricks, with the innermost ones made of ancient lead. The internal shields and the CCD box are enclosed in a OFHC vacuum copper cryostat. Finally, the setup is protected from external gammas and neutrons by a shield made of lead (most internal part) and polyethylene (most external part). CCDs, DAQ, and instrumentation can be all run remotely and are constantly monitored with a slow control system. All LBC components were chemically cleaned to remove any surface contamination from the radon progeny. Assays were carried out to measure the material radioactive contamination. The design was optimized via simulations performed by using the software described in Chapter 4, the same employed to assess the DAMIC-M detector design (Chapter 5). Therefore, LBC data will help to provide a first validation of the background model down to a few electrons threshold.

Since its installation, LBC went across two different phases, commissioning and science. In the first case, images were acquired with the open shielding configuration, reaching a background rate of about $\sim$300 d.r.u. This data will help to characterize the external background. Furthermore, the performances of the detector were verified and the CCD parameters were optimized. The external shield was then closed and a new commissioning run was acquired. Dark current reduction tests (thermal tests by cooling-down and warming-up the setup by 0.1 K/min) were performed and analysis procedures were developed. A science phase then started, whose data will be subject to advanced analysis and will be used for a first dark matter search. Images are acquired using the continuous readout mode and 2 amplifiers simultaneously, each of them reading half of the CCD. A dark current level as low as $\sim$3 $\cdot$ 10^{-3} e$^-$/pixel/day, a readout noise of 0.2 e^- (650 skips), and a background rate compatible with the one of DAMIC were achieved. The latter will be further reduced with the installation of the new EF copper CCD box. Furthermore, new data will be acquired with a reduced (at least by factor of 3) dark current level.

Following a preliminary analysis, the LBC placed very competitive exclusion limits on the interaction of hidden sector candidates with electrons with only 115 g-days exposure (about 1 week of data). The world-leading DM limits were placed for a dark matter mass above a few MeV as shown in Figure 2.27. These preliminary results give confidence in the forthcoming search for dark matter particles with the DAMIC-M experiment. The analysis is currently being extended with higher quality data and increased statistics. New results are expected soon.
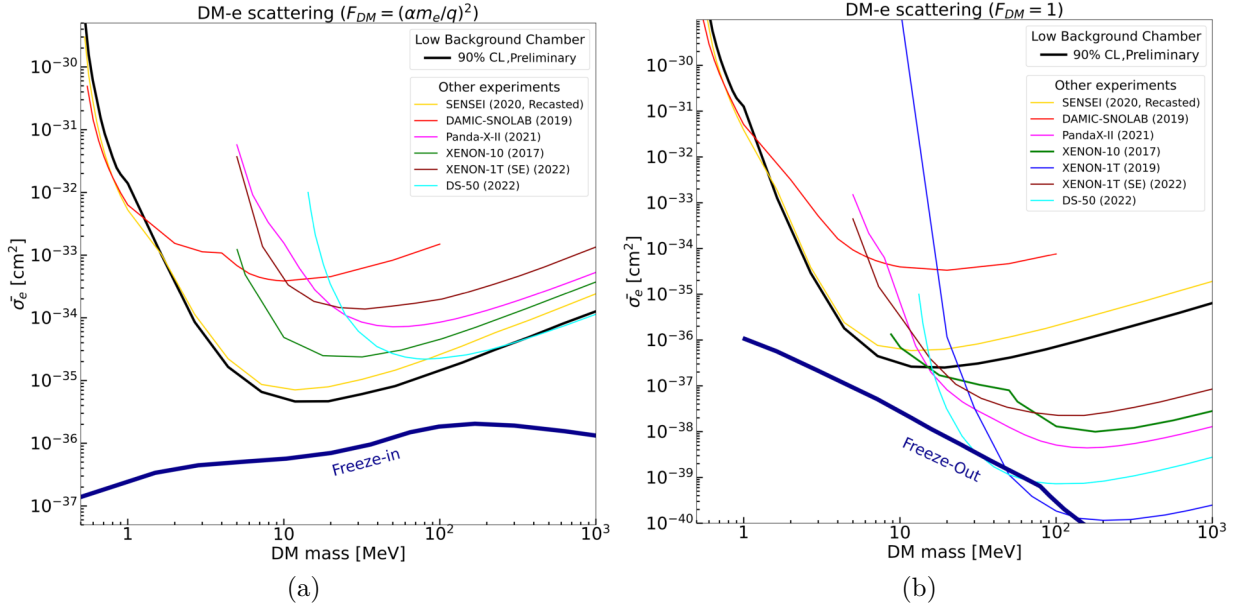
Figure 2.27 – Preliminary results from the first LBC science run with 115 g-days exposure [109]. (a): 90% C.L. exclusion limit for a DM-electron interaction via a light dark photon mediator. (b) 90% C.L. exclusion limit for a DM-electron interaction via a heavy dark photon mediator. Exclusion limits from other dark matter experiment are shown for comparison. The Sensei limit was recasted to use the low energy ionization model of [79] and agree upon DM halo parameters as suggested in [55]. This figure will be updated soon with new data.

BACKGROUND SOURCES FOR THE DARK MATTER SEARCH

In order to be sufficiently sensitive to the feeble interaction cross-section of dark matter with ordinary matter, experiments must be able to tag and discriminate the background events that could otherwise hide a potential dark matter signal. A major challenge is the control of the background that for DAMIC-M is expected to be at the level of a fraction of decay/kg/day [d.r.u]. Main background sources are γ-rays, electrons and neutrons of both radiogenic or cosmogenic origins, from materials surrounding the detector or in the silicon bulk and surface.

This chapter describes the relevant types of background for DAMIC-M.

3.1 Muon induced background

Rare event physics experiments are typically installed in underground laboratories to provide the overburden necessary to shield them from cosmic-ray muons and their progenies. In the lower half of the atmosphere, muons are the most numerous among all the charged cosmic ray secondary particles, with a mean energy of 4 GeV and an intensity of about 1 cm^{-2} min^{-1} for planar detectors [110]. Muons are highly penetrating particles and can reach significant depths underground. For a dark matter experiment, muons traversing the detector and its surrounding materials are a source of background by themselves, but so are also the secondary particles induced in the shielding materials, in particular fast neutrons and cosmogenic radioactivity [111]. The induced background is the major concern since muons traversing the detectors are typically easy to identify and track.

The muon rate depends on the traversed depth of the rock, given in km of water equivalent (km.w.e.), where 10^5 g/cm^2 = 1 km.w.e. With a depht of few km.w.e., the muon flux is reduced by a factor of 10^5-10^7 with respect to surface [112]. If a laboratory is

situated underneath a mountain, as in the case of the Laboratoire Souterrain de Modane (LSM) situated under the Fréjus peak, the total muon flux is influenced by the mountain shape [111]:

$$I_{tot} = \int sin(\theta)d\theta \int I(h(\theta,\phi))G(h,\theta)\,d\phi, \tag{3.1}$$

where $h(\theta,\phi)$ is the mountain shape, also known as elevation map, $G(h,\theta) = sec(\theta)$, θ is the zenith angle, and ϕ is the azimuthal angle. $I(h)$ is the differential muon intensity corresponding to the slant-depht h and can be calculated by using the Depth-Intensity-Relation (DIR) [111]:

$$I(h) = I_1 e^{-h/\lambda_1} + I_2 e^{-h/\lambda_2}, \tag{3.2}$$

where the I_1, I_2, λ_1 and λ_2 values can be obtained by fitting experimental data, as reported in [111]. By using equation 3.1 and the information provided in [113], a total muon flux of $(4.83\pm0.5)\cdot10^{-9}$ cm^{-2}s^{-1} is obtained for the LSM laboratory [111], which is consistent with the Frejus collaboration result within 12% [113]. The equivalent vertical depth relative to a flat overburden corresponding to the calculated flux is equal to 4.2 ± 0.2 km.w.e. Figure 3.1 shows the total muon flux measured for various underground sites as a function
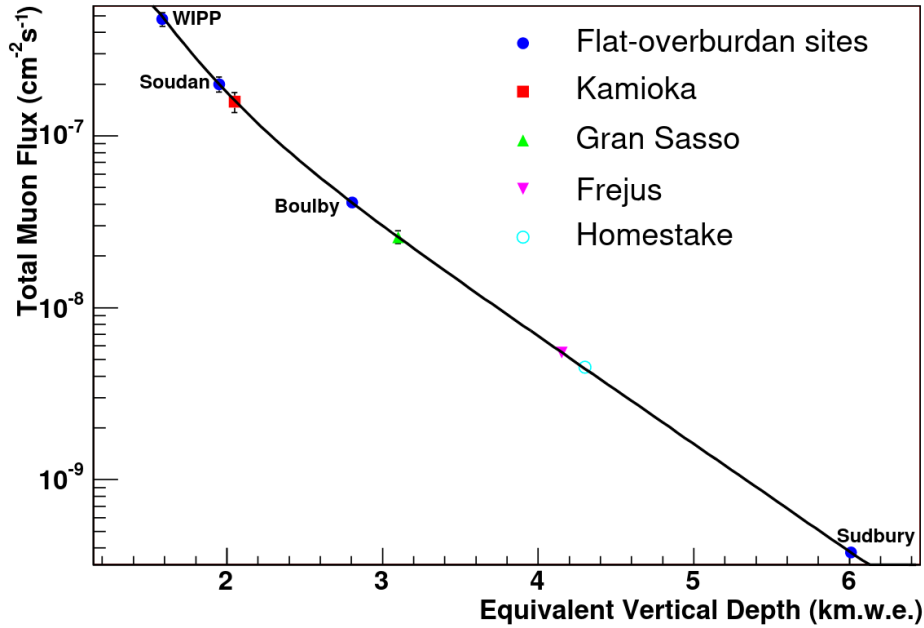

Figure 3.1 – Total muon flux measured for various underground sites as a function of the equivalent vertical depth relative to a flat overburden [111]. Reprinted figure with permission from [111]. Copyright (2006) by the American Physical Society.

of the equivalent flat overburden.

For the LSM site, the local muon spectrum as a function of azimuthal and zenith angles is obtained in [114] (Figures 3.2 and 3.3), showing the effect of the montain shape on the muon flux. The spectra are derived analytically by considering the Gaisser parametrization for the cosmic-ray muon flux at sea-level and the energy loss for muons as a function of the amount of traversed matter. The former is equal to [115]:

$$\frac{dN_{\mu,0}}{d\Omega_{\mu,0}dE_{\mu,0}} = \frac{0.14}{\text{cm}^2\text{s}\cdot\text{sr}}\cdot\left(\frac{E_{\mu,0}}{\text{GeV}}\right)^{-2.7}\left(\frac{1.0}{1+\frac{1.1\cdot E_{\mu,0}\cos\theta_{\mu,0}}{115\text{GeV}}}+\frac{0.054}{1+\frac{1.1\cdot E_{\mu,0}\cos\theta_{\mu,0}}{850\text{GeV}}}\right), \quad (3.3)$$

where the index 0 indicates quantities at sea level. The latter is derived as [110]:

$$\frac{dE}{dX} = a + b\cdot E, \tag{3.4}$$

where b is the fractional energy loss of the muon by radiation processes (bremsstrahlung, e^+e^- pair production, nuclear scattering) and a is the ionization loss. By using equation 3.4 and considering an initial energy at sea level $E(X=0) = E_{\mu,0}$, the muon energy $E(X=t) = E_\mu$ at a given laboratory depth (t) can be calculated as:

$$E_\mu = (E_{\mu,0} + \epsilon_\mu)e^{-bt} - \epsilon_\mu, \tag{3.5}$$

where ϵ_μ is the ratio of the ionization loss a to b. Note that equation 3.5 is derived assuming a continuous energy loss for muons propagating through rock and neglecting fluctuations due to radiation processes.

The distribution $\frac{dN}{d\Omega dE_\mu}$ for muons at depth t is then obtained as:

$$\frac{dN}{d\Omega dE_\mu} = \left.\frac{dN_{\mu,0}}{d\Omega_{\mu,0}dE_{\mu,0}}\right|_{E_{\mu,0}(E_\mu)}\frac{dE_{\mu,0}}{dE_\mu}. \tag{3.6}$$

The ϕ and θ distributions derived from equation 3.6 are then used in [114] as input for Geant4 simulations and compared to the measurements by the Fréjus experiment, as shown in Figures 3.2 and 3.3.

The underground muon energy distribution can be parametrized as [111]:

$$\frac{dN}{dE_\mu} = Ae^{-bh(\gamma_\mu-1)}\cdot(E_\mu + \epsilon_\mu(1-e^{-bh}))^{-\gamma_\mu}, \tag{3.7}$$
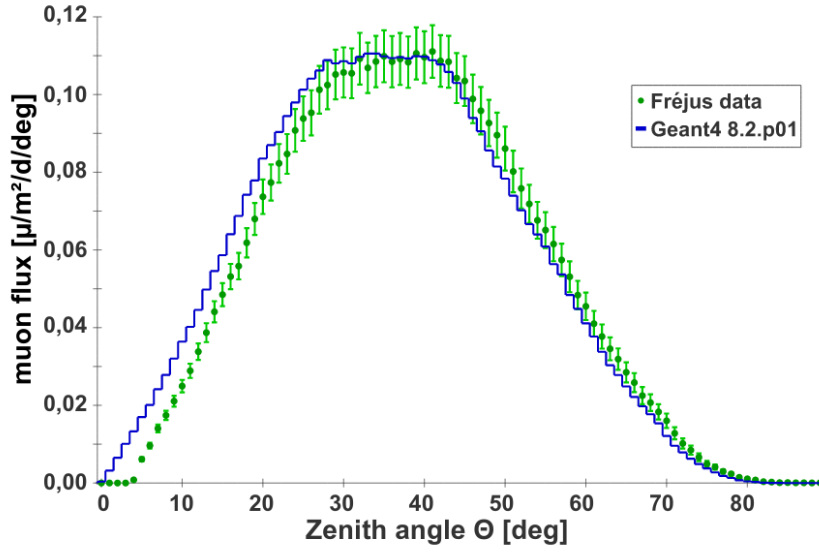
Figure 3.2 – The local muon spectrum as a function of zenith angle θ for the LSM underground laboratory compared with experimental data obtained by the Fréjus experiment [113, 114]. The simulations are not corrected to the detector efficiency. The detector acceptance was limited to $\theta > 4°$.
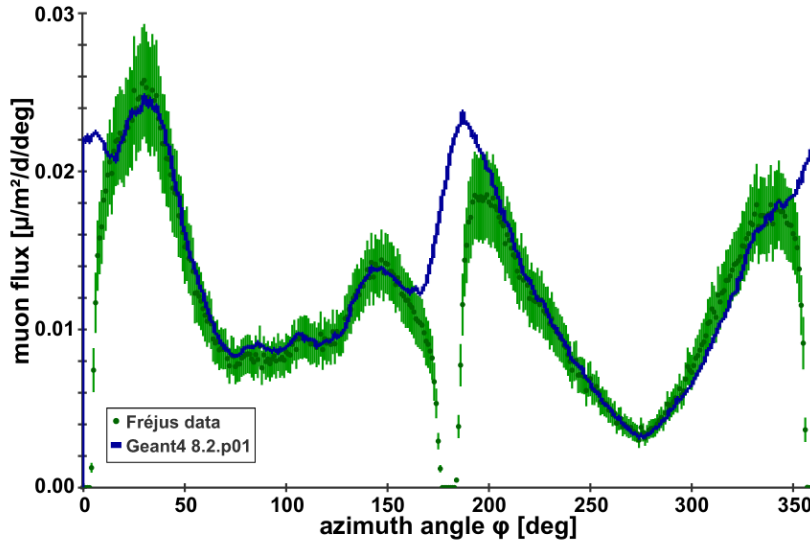
Figure 3.3 – The local muon spectrum as a function of azimuth angle ϕ for the LSM underground laboratory integrated over all zenith angles. The experimental data is obtained by the Fréjus experiment [113, 114]. In the coordinate system of the laboratory, the geographical north direction corresponds to $\phi= 16$ degrees. The detector was characterized by two blind angles in the azimuthal direction, namely $\phi= 0°$ and $\phi= 180°$ (in the LSM coordinate system).
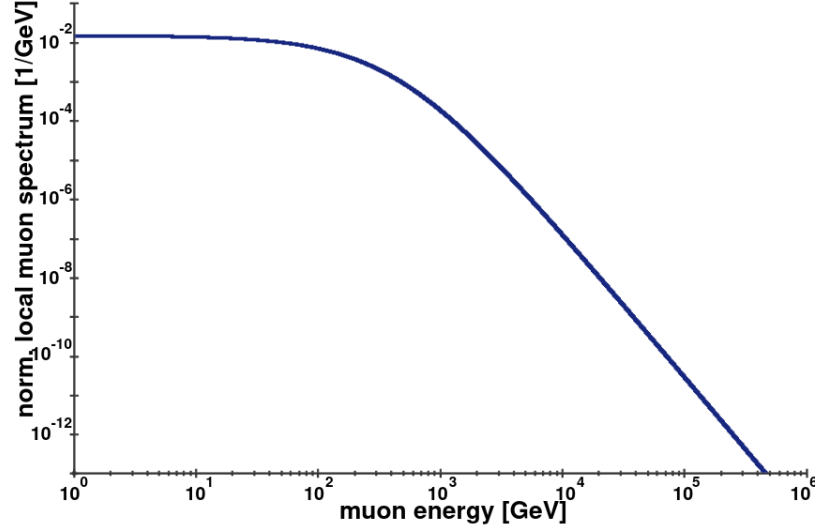
Figure 3.4 – The local muon energy spectrum for the LSM laboratory, normalized to unity [114]. This distribution does not differ significantly from the one expected for a flat overburden and an effective depth as modeled in [111].

where A is a normalization constant, E_μ is the muon energy after crossing the rock slant depth h, $\gamma_\mu = 3.7$ is the spectral index of the muon beam [110, 111]. From equation 3.7, the average muon energy at depth h can be derived:

$$\langle E_\mu \rangle = \frac{\epsilon_\mu (1 - e^{-bh})}{\gamma_\mu - 2}. \tag{3.8}$$

For the LSM, considering an average depht of 4600 m.w.e., $b = 4.38 \cdot 10^{-4}$m.w.e^{-1}, and $\epsilon_\mu = 495$ GeV [114], an average muon energy of about 252 GeV is obtained. Variations in this value can be observed due to the uncertainties in the muon energy spectrum in the atmosphere, details of muon energy loss in media, and the local rock density and composition used to calculate the ϵ_μ, b, and γ_μ parameters [111].

The local muon energy spectrum for the LSM laboratory is shown in Figure 3.4. The spectrum is derived by taking into account the elevation map of the Fréjus mountain and by integrating over all θ and ϕ [114].

Muons traversing the detector itself or the external rock can produce fast neutrons, depending strongly on the depth and composition of an underground site. Neutron background contribution is discussed in more detail in the Section 3.2.

Muons can also induce the creation of radioactive isotopes in the crossed materials.

This process is described in Section 3.1.1.
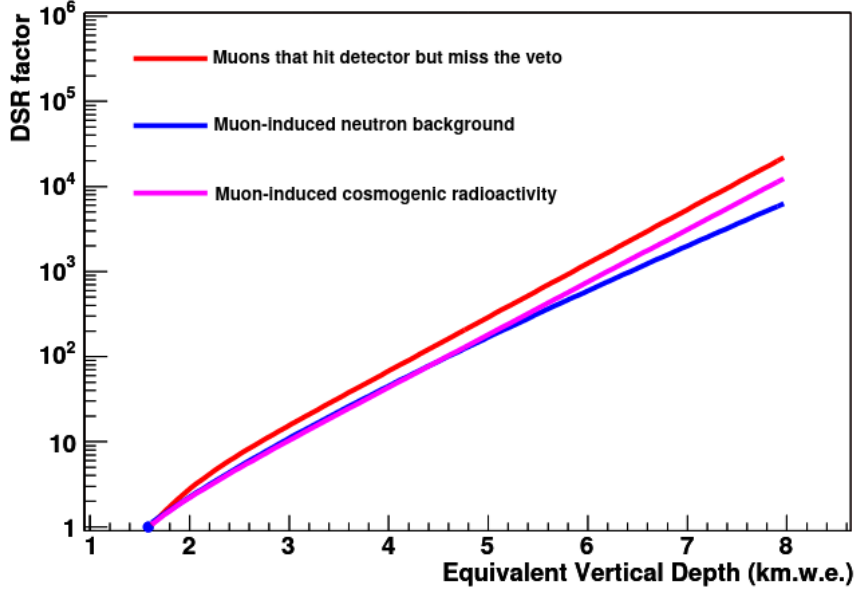
Figure 3.5 – Global view of the relative attenuation factors for the muon and muon-induced activities as a function of overburden. The curves are normalized, arbitrarily, to unity for the shallower depth defined by the WIPP site at 1.585 km.w.e [111]. The muon veto refers to a possible system installed around the detector to tag cosmogenic muons, which is used in some dark matter experiments. DAMIC-M will not be equipped with an external veto since muons can be identify by the shape of their tracks in CCDs. Reprinted figure with permission from [111]. Copyright (2006) by the American Physical Society.

The Depth-Sensitivity-Relation (DSR) for the major components of the muon-induced background, namely the cosmic-ray muons themselves, the induced neutron background, and cosmogenic radioactivity, is derived in [111] and is shown in Figure 3.5. The DSR curves are indicative of the relative muon flux and muon-induced activity for a given laboratory site at its characteristic depth. The effect of the activity will depend on the specific details of a given detector geometry, including shielding, and the goals of a particular experiment. An attenuation factor of about one order of magnitude is achieved for every 1.5 km.w.e. increase in depth.

3.1.1 Muon-induced activation

An important muon-induced process that dark matter experiments must consider is the cosmic activation of detector materials. Spallation of nuclei by high energy protons and neutrons (MeV-GeV range), photonuclear interactions, and muon capture processes cause the creation of radioactive isotopes. Their production rate R can be written as [116, 117]:

$$R = N \int \Phi(E) \cdot \sigma(E) dE, \tag{3.9}$$

where $\Phi(E)$ is the cosmic ray flux, σ the cross section of the isotope production, E is the particle energy, and N is the number of target nuclei. At sea level, the neutrons and protons fluxes are about the same at energies of a few GeV. However, at lower energies the proton to neutron ratio decreases significantly because of the absorption of charged particles in the atmosphere. Therefore the typical contribution from protons to isotope production is quoted as about 10% of the total [116]. The contribution from other cosmic particles like muons or gammas is even smaller [116]. The fluxes of cosmogenic protons, neutrons, and gammas at sea level are shown in Figure 3.6.

The exposure time, height above the sea, and latitude affect the isotope production [28, 116]. The cosmogenic activity is dominated by activation of detector materials at the surface and prior to underground storage, given the reduced flux of muons at higher depths [28, 111]. The isotope production rate underground $R(underground)$ can be estimated from the following Depth-Sensitivity-Relation (DSR) factor F [111]:

$$F = \frac{R(surface)}{R(underground)} = \left(\frac{4GeV}{\langle E_\mu \rangle}\right)^\alpha \frac{\phi_\mu(surface)}{\phi_\mu(underground)}, \tag{3.10}$$

where ϕ_μ is the muon flux at the experimental site, $\langle E_\mu \rangle$ the average muon energy underground, and α is a constant which varies from 0.50 and 0.93 with a mean value of 0.73 ± 0.10 for liquid scintillators [111]. Thus, the DSR factor describes the reduction in muon-induced activity as one moves to deeper and deeper sites.

Cosmogenic isotopes decay producing βs and γs, which are a major source of background for dark matter experiments. More details about these types of background are provided in Section 3.3.
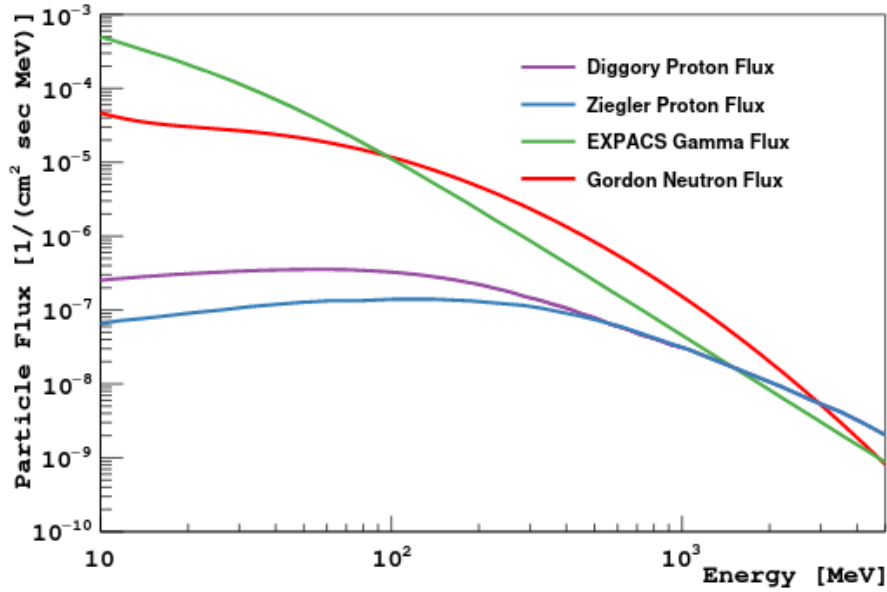
Figure 3.6 – Comparison between the sea-level cosmic-ray fluxes of protons, gamma rays, and neutrons [116]. The reported neutron flux, the so-called "Gordon spectrum" [118], is the most commonly used reference spectrum for sea-level cosmic-ray neutrons. The proton fluxes are derived from the spectra obtained by Diggory [119] and Ziegler [120, 121]. The gamma flux is obtained with the EXPACS software program [122]. New York City is used as reference location for the spectra. The intensity of the fluxes varies with altitude, location in the geomagnetic field, and solar magnetic activity. However, the spectral shapes don't vary as significantly and correction factors can be applied to calculate the appropriate fluxes [116]. Reprinted figure with permission from [116]. Copyright (2020) by the American Physical Society.

3.2 Neutron background

Neutrons can be created by cosmic ray muon interactions in the materials around an experiment (prompt cosmogenic neutrons, as discussed in the previous section) or via radioactive processes, i.e., (α, n) and spontaneous fission reactions [28]. Neutrons can then induce nuclear recoils and produce signals resembling those due to a dark matter interaction. Generally, the neutron production rate at a deep underground laboratory is two to three orders of magnitude smaller than the one from local radioactivity via (α, n) reactions. However, whereas the latter process produces low energy neutrons (typically <8 MeV) which are relatively easy to shield, the muon-induced neutrons (also called fast neutrons) have a very hard energy spectrum, which reaches several GeV. Therefore,

they can penetrate a significant depth in both the surrounding rock and detector shielding materials [111]. Cosmogenic and radiogenic neutrons are discussed in the following sections.

3.2.1 Cosmogenic neutrons

The flux of prompt cosmogenic neutrons in an underground site is the convolution of the local muon flux (see Section 3.1) and the neutron production yield in the different traversed materials.
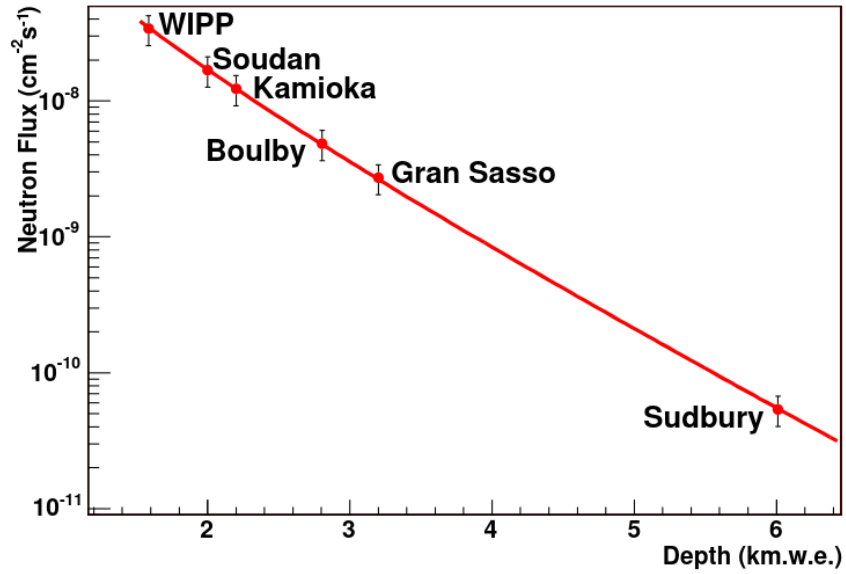
Figure 3.7 – Total muon-induced neutron flux for various underground sites obtained via simulations [111]. The error bars on each point reflect the uncertainties in the knowledge of the absolute muon fluxes and neutron production rates. The neutron flux at the LSM laboratory can be extrapolated to be about $6 \cdot 10^{-10} \mathrm{cm}^{-2} \mathrm{s}^{-1}$. Reprinted figure with permission from [111]. Copyright (2006) by the American Physical Society.

Figure 3.7 shows the total muon-induced neutron flux (Φ_n) for different underground sites as a function of the equivalent vertical depth (h) [111]:

$$\Phi_n = P_0 \frac{P_1}{h} e^{-h/P_1}, \tag{3.11}$$

with $P_0 = (4.0 \pm 1.1) \cdot 10^{-7} \mathrm{cm}^{-2} \mathrm{s}^{-1}$ and $P_1 = 0.86 \pm 0.05$ km.w.e. Considering $h = 4.2$ km.w.e

for the LSM, a neutron flux of about $6{\cdot}10^{-10}$cm^{-2}s^{-1} is obtained.

Cosmogenic neutrons can be divided into two groups: the directly generated neutrons that are immediately produced by muons interacting with nuclei (e.g., negative muon capture, quasi-elastic scattering, muon spallation) and the secondary neutrons generated in hadronic and electromagnetic showers initiated by muons [123]. In muon interactions with nuclei in rock, the secondary neutrons are the dominant component [123].
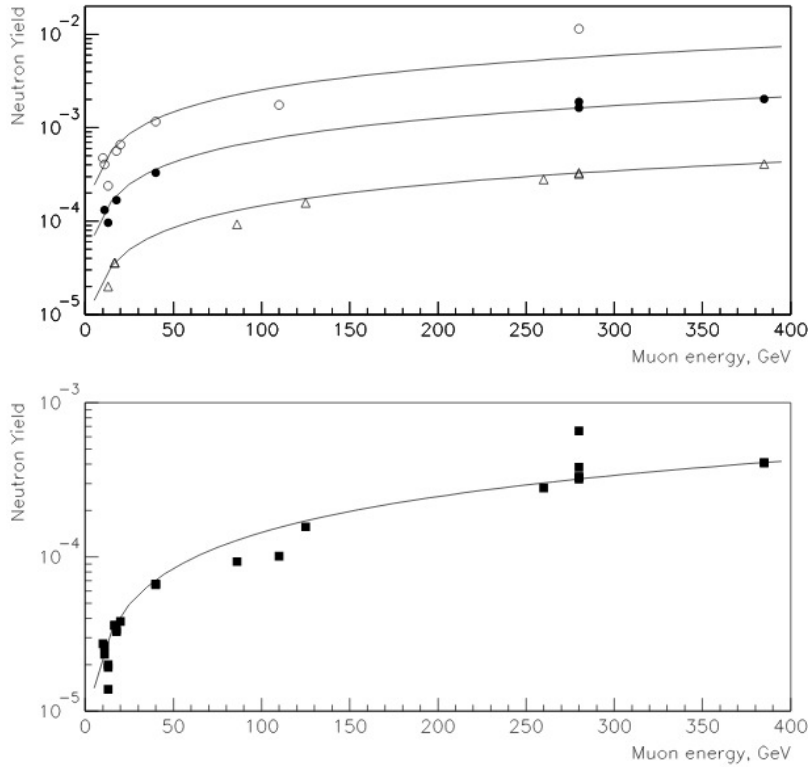
Figure 3.8 – Dependence of the neutron yield on A and $\overline{E_\mu}$ [124]. The Neutron Yield is expressed in n/μ/(g·cm^{-2}). Upper panel: experimental points for lead (A=207, open circles), iron (A=56, filled circles) and scintillator (A=10.3, open triangles). The curves are functions $Y_n(A, \overline{E_\mu}) = cA^\beta \overline{E_\mu}^\alpha$ at different A and $c = 4.4 \cdot 10^{-7}$, $\beta = 0.95$, $\alpha = 0.78$. Lower panel: neutron yield for scintillator; the experimental data for iron and lead are reduced to scintillator; the curve is a function $Y_n = 4.4 \cdot 10^{-7} 10.3^{0.95} \overline{E_\mu}^{0.78}$. Reprinted figure with permission from [124]. Copyright (2013) by the American Physical Society.

The muon-induced neutron yield[1] (Y_n) depends on both the mean muon energy $\overline{E_\mu}$ and atomic weight A of medium. In [124], a universal formula which takes into account

---

1. The neutron yield is defined as the number of neutrons produced by a muon over the path length of 1 g/cm^2

the two dependencies is proposed:

$$Y_n(A, \overline{E_\mu}) = cA^\beta \overline{E_\mu}^{-\alpha},\qquad(3.12)$$

where c, β, and α are constants. Their values are obtained by fitting experimental data. The best fit function is shown in Figure 3.8.

Fast neutrons can also be created by muons passing through the materials commonly used to shield a detector from natural radioactivity. Figure 3.9 shows the neutron yield
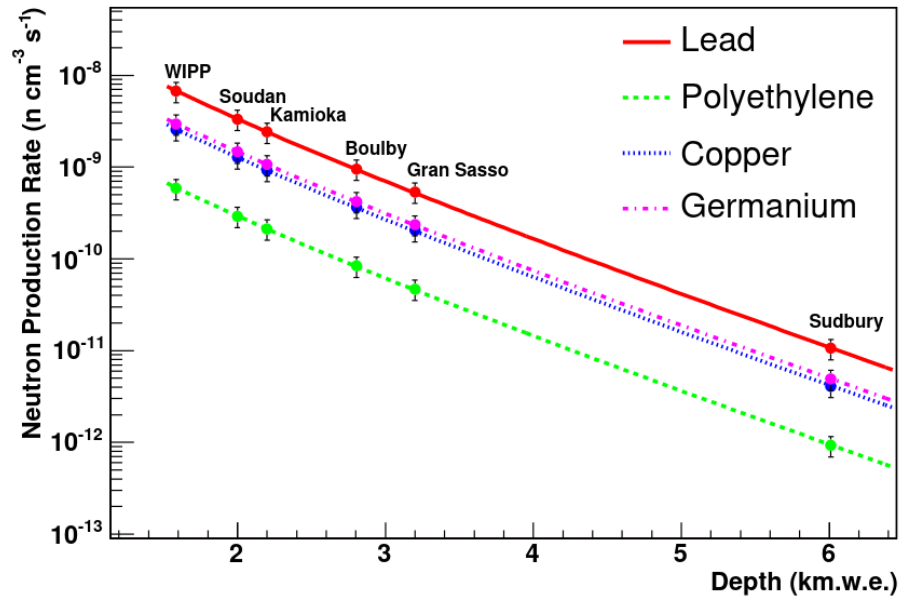
Figure 3.9 – The muon-induced neutron production rate predicted via simulations for some common detector shielding materials. The colored lines indicate the fitting functions which have the same form of equation 3.11. The resulting P_0 and P_1 values for each material are reported in [111]. Minor variations due to neutron back-scattering have been neglected in these calculations [111]. Reprinted figure with permission from [111]. Copyright (2006) by the American Physical Society.

in some usual shielding materials as a function of the vertical depth of the underground site. Polyethylene (CH_2), which is known to be an excellent neutron moderator, is one of the materials listed in the figure. Direct dark matter experiments are usually surrounded by a high density polyethylene shield to reduce the background from external neutrons (both prompt and radiogenic ones) [28]. A shielding thickness of about 55-60 g/cm^2 of polyethylene is able to suppress the external neutron flux by six orders of magnitude [112].

A similar result can be achieved by using 45-50 g/cm^2 of CH$_2$ together with 20-30 cm of lead placed between the rock and CH$_2$ [112]. The DAMIC-M detector will use a polyethylene shield of about 40 cm.

As also showed in Figure 3.9, lead is characterized by a high neutron yield due to its high A value. Since this material is often used for γ-ray shielding (as explained in Section 3.3), sometimes it is convenient to include an internal low-A shielding (e.g., polyethylene or water) between the lead shielding and the sensitive detector, in order to reduce the muon-induced neutron background [112]. An optimization of the shielding design is thus required, paying particular attention to the mass and position of high-A materials since they may behave as neutron sources under muon irradiation [112]. The final shielding configuration should be the compromise between the suppression of external radiation, the reduction of muon-induced background produced within the setup, and the overall cost and dimension of the setup (if the available space is limited) [112].

3.2.2 Radiogenic neutrons

The radiogenic neutrons arise from (α, n) and spontaneous fission reactions. The most important sources are ^{238}U, which undergoes spontaneous fission, and the α-emitters from the uranium (^{238}U) and thorium (^{232}Th) chains (Figure 3.10) [112]. It is thus necessary to select materials with a poor content of uranium and thorium in order to reduce the flux of radiogenic neutrons. Figure 3.11 shows the energy spectrum of neutrons in the rock around the LSM cavern together with the single contributions from uranium and thorium (α, n) reactions and ^{238}U spontaneous fission [112]. The total energy spectrum has a mean value of about 1.95 MeV and extends up to about 8 MeV. By using as input spectrum the one in Figure 3.11, the energy distribution of neutrons emerging from the LSM rock into the laboratory was derived in [112] via Geant4 simulations (Figure 3.12). Both the total yield and the spectral shape depend strongly on the chemical composition of the traversed medium and in particular on the abundance of light elements and hydrogen. The latter, in fact, affects the thermalization and absorption of neutrons and hence suppresses the total flux. Only 1% of hydrogen reduces the neutron flux above 100 keV (1 MeV) by a factor of 4.7 (1.8) [112].

A study was carried out between 2008 and 2009 to measure and continuously monitor the thermal neutron flux at LSM [126]. The measurements took place especially in the proximity of the EDELWEISS-II experiment but also at various other locations in the laboratory with less exposure time. The resulting thermal neutron flux was (3.57 $\pm$
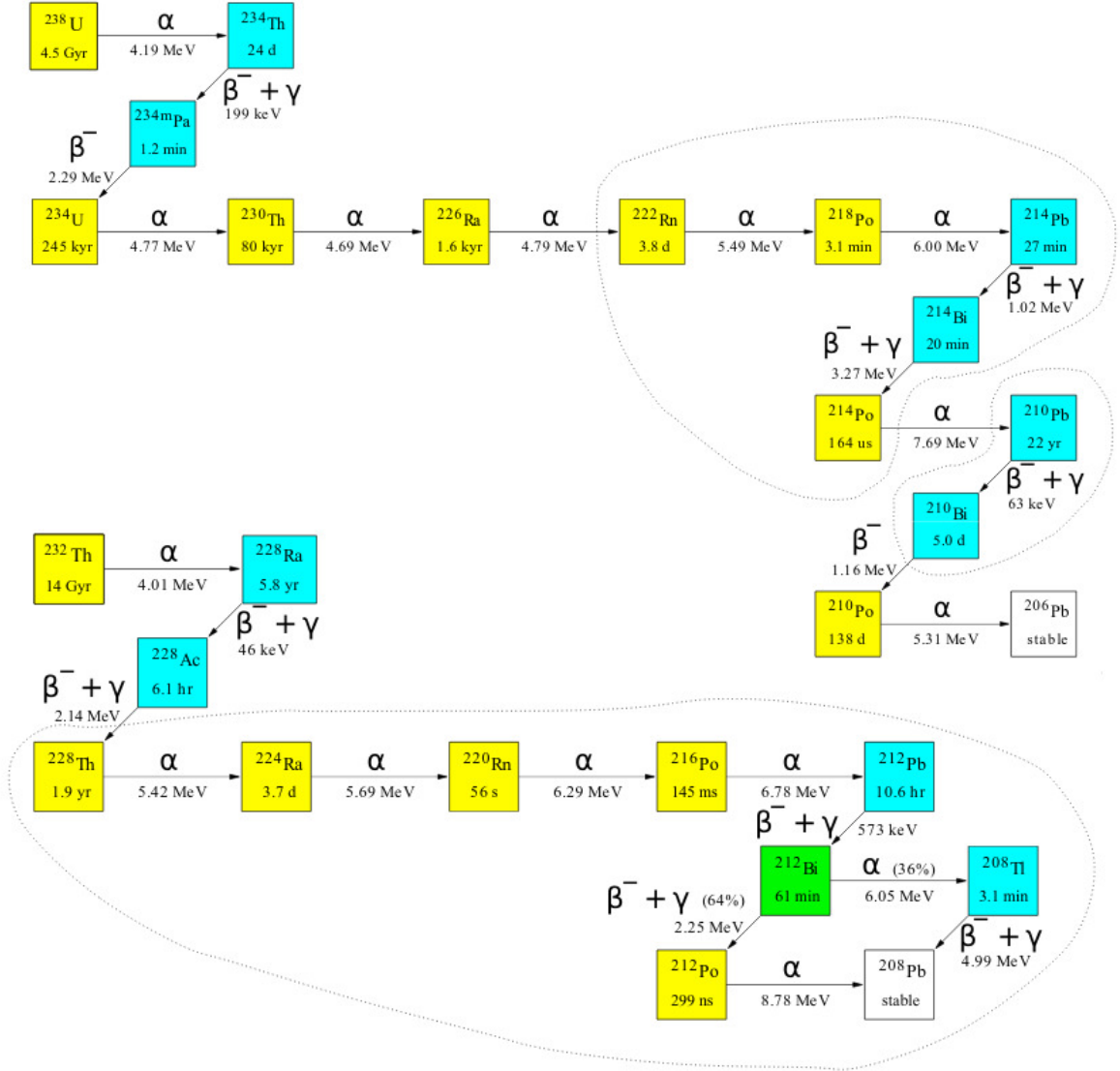
Figure 3.10 – ^{238}U and ^{232}Th decay chains [89]. Alpha (β) emitters are colored in yellow (teal). For each isotope, α energies, β Q-values and half-lives are given. Isotope sequences expected to be in secular equilibrium are grouped by dashed lines. Secular equilibrium is reached when the half-life of the parent nuclide is much longer than the one of the daughter nuclide. © IOP Publishing. Reproduced with permission. All rights reserved.

$0.05^{\text{stat}} \pm 0.27^{\text{syst}}) \cdot 10^{-6}$ neutrons/cm^2/s in the vicinity of the EDELWEISS-II setup [126]. The flux measured at the position which seems to be the closest to the one that DAMIC-M will occupy [2] is instead $(3.9 \pm 0.4^{stat}) \cdot 10^{-6}$ neutrons/cm^2/s [126].

---

2. In [126], the position which seems to be the closest to the current location of the DAMIC-M clean
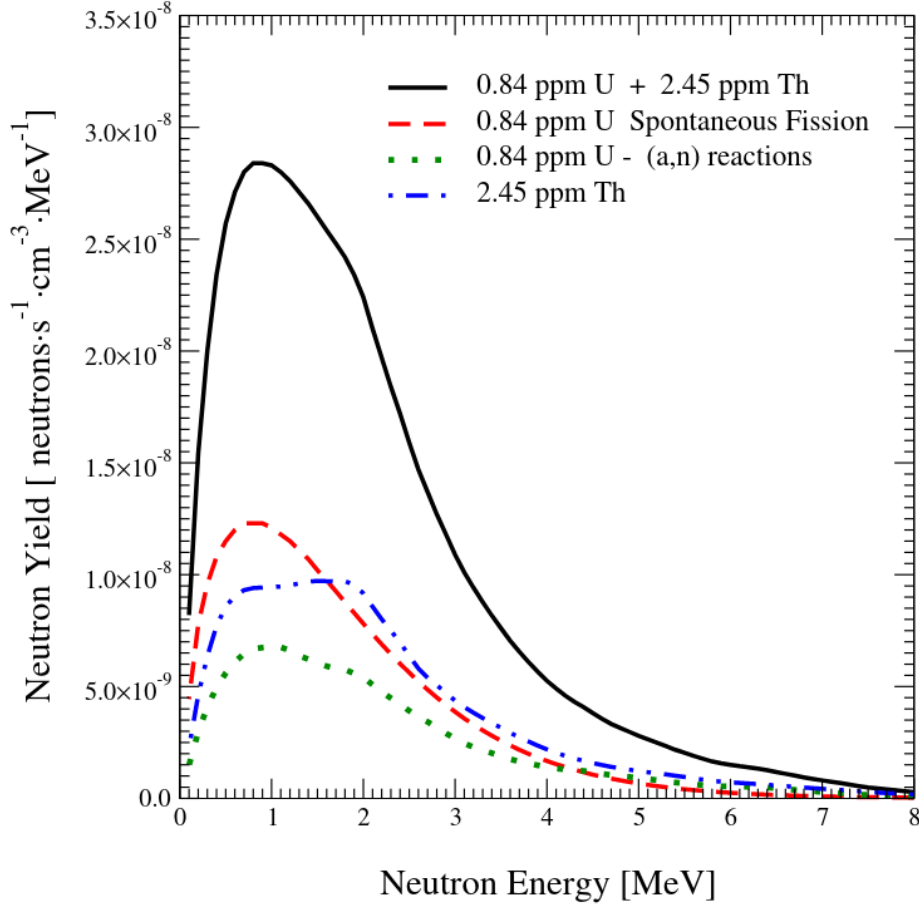
Figure 3.11 – Neutron energy spectra from uranium and thorium (α, n) reactions, and ^{238}U spontaneous fission in the LSM rock. The sum spectrum is shown by the solid curve. The spectra were calculated in [112] by assuming the rock composition and U/Th concentrations reported in [125]. Reprinted by permission from Springer Nature: Spinger Nature The European Physical Journal A [112], © (2008).

As already mentioned before, a dedicated thick shield made of polyethylene or water is commonly used in low-background experiments to reduce the neutron flux from the rock. With an external neutron shielding, the dominant sources of radiogenic neutrons are the detector components [112]. Therefore, special care has to be taken for the radiopurity of the internal detector parts, as well as for the optimization of the shielding.

---

room is labelled with the number 6.
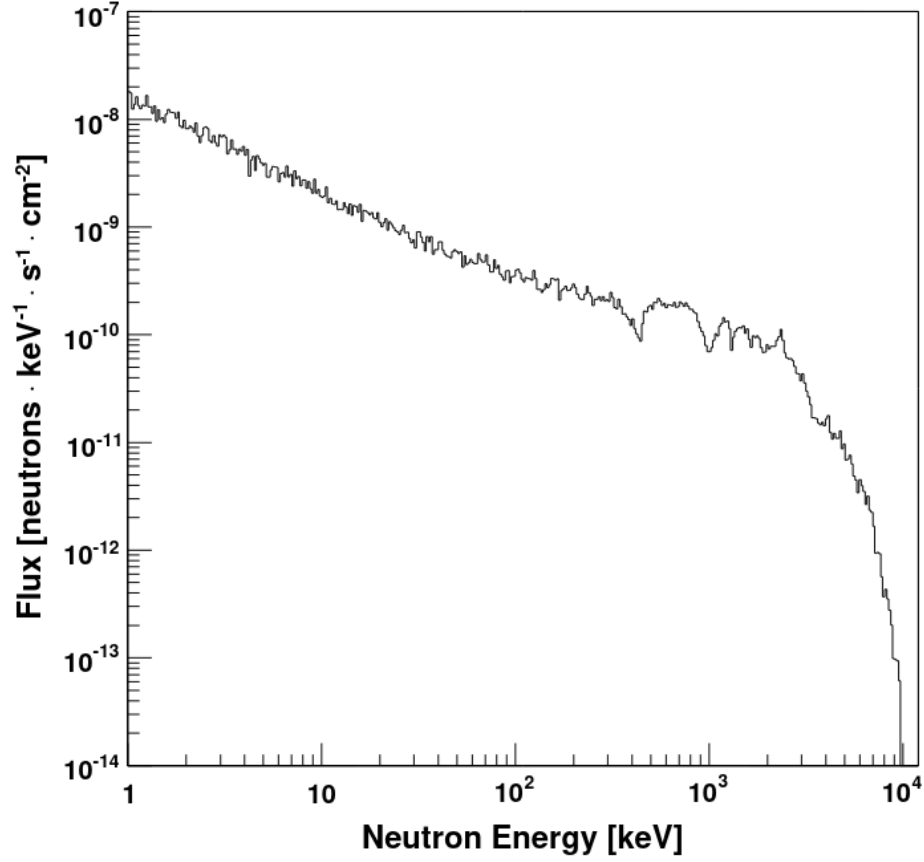
Figure 3.12 – Neutron energy spectrum from U and Th traces in the LSM rock [112]. The spectrum is obtained by propagating neutrons from evenly distributed sources through rock to the laboratory walls using Geant4. The peaks and dips on the neutron spectrum are not of statistical origin but reflect the shape of the cross-section of neutron interaction with rock. Reprinted by permission from Springer Nature: Spinger Nature The European Physical Journal A [112], © (2008).

3.3 Electron and γ-ray background

Electrons and γ-rays are produced by nuclear decays in the materials around and inside an experimental setup. γ-rays can generate electrons via photoelectric effect, Compton scattering and e^+/e^- pair production. Low energy electrons from Compton scattering are particularly critical at the energies of interest of DAMIC-M. A detailed measurement of the spectrum of Compton scattered electrons in the bulk of a skipper CCD was carried out at the University of Chicago by the DAMIC-M collaboration [127]. The Compton scattering process and the measurement results will be discussed in Chapter 6. The principal sources

of electrons and γ-rays are the ^{238}U and ^{232}Th chains, ^{40}K, and the cosmogenic isotopes. The most critical isotopes for DAMIC-M are listed in Table 3.1 with their life time, decay modes and Q-energy. In the following, a more detailed description will be provided for the isotopes reported in the Table 3.1, together with the strategies used to control and reduced their contamination.

Parent chain	Isotope	Half life	Q-value	Decay mode
^{238}U	^{234}Th	24.1 d	272 keV	$\beta-$
	^{234m}Pa	1.159 min	2.27 MeV	$\beta-$
^{226}Ra	^{214}Pb	26.916 min	1.02 MeV	$\beta-$
	^{214}Bi	19.8 min	3.27 MeV	$\beta-$
^{210}Pb	^{210}Pb	22.23 y	63.5 keV	$\beta-$
	^{210}Bi	5.011 d	1.16 MeV	$\beta-$
^{232}Th	^{228}Ra	5.75 y	45.5 keV	$\beta-$
	^{228}Ac	6.15 h	2.12 MeV	$\beta-$
	^{212}Pb	10.64 h	569 keV	$\beta-$
	^{212}Bi	60.54 min	2.25 MeV($\beta-$)	$\beta-(64\%)$
			6.2 MeV (α)	$\alpha(36\%)$
	^{208}Tl	3.058 min	5 MeV	$\beta-$
^{40}K	^{40}K	1.2504 10^9 y	1.31 MeV ($\beta-$)	$\beta-(90\%)$
			1.50 MeV ($\beta+$)	$\beta+(10\%)$
Copper activation	^{60}Co	5.2711 y	2.82 MeV	$\beta-$
	^{59}Fe	44.494 d	1.56 MeV	$\beta-$
	^{58}Co	70.85 d	2.31 MeV	$\beta+$
	^{57}Co	271.81 d	836 keV	$\beta+$
	^{56}Co	77.236 d	4.57 MeV	$\beta+$
	^{54}Mn	312.19 d	1.38 MeV	$\beta+$
	^{46}Sc	83.787 d	2.37 MeV	$\beta-$
^{32}Si	^{32}Si	150 y	227 keV	$\beta-$
	^{32}P	14.284 d	1.71 MeV	$\beta-$
Silicon activation	^{22}Na	2.6029 y	2.84 MeV	$\beta+$
	^{3}H	12.312 y	18.6 keV	$\beta-$

Table 3.1 – Isotopes source of background for DAMIC-M grouped by parent decay chain. Half lives, Q-values and decay mode are also provided. Data are provided from the Nucléide-Lara library.

3.3.1 Material assays

Assays are usually carried out to measure the ^{238}U, ^{232}Th, and ^{40}K activities. Parent and daughter nuclei have the same activity if secular equilibrium is reached. This situation occurs when the half-life of a nuclide is considerably shorter than the parent's one. Chemical and physical processes can break this equilibrium by causing the removal of one or more components from the chain [128]. For example, radium is a chemically highly-reactive element, which may be either removed or enriched in the material processing [129]. Concerning the ^{238}U chain, it is thus useful to measure the contamination of ^{210}Pb and ^{226}Ra, which delimit the three different segments of the chain out of equilibrium.

The assays techniques can be divided in two different methods: mass spectroscopy and γ-ray counting. The former measures the elemental composition of a sample and estimates the activity of a specific isotope from its natural abundance [78]. The most popular mass spectroscopy technique is the inductively coupled plasma mass spectrometry (ICP-MS) which can achieve part-per-trillion (ppt) g/g level sensitivity to ^{238}U and ^{232}Th. It requires the digestion of the sample in a liquid solution and it is therefore considered as a destructive technique [130]. A flow of gas (usually argon) then converts the liquid sample into a fine aerosol which is atomized and ionized before entering the final mass filter (often a quadrupole) [131]. Measurements can be performed at room temperature and assays from small samples can typically be delivered with turnaround times of the order of 1–2 days [130]. However, stringent cleanliness protocols have to be followed during the preparation of the sample, in order to limit possible contamination [130]. Furthermore, it is not possible to assay the whole ^{238}U and ^{232}Th decay chains since daughter nuclei have a too low concentration to be detected by mass spectroscopy.

The γ-ray counting method instead uses the intensity of specific γ lines from radioactive decays in the sample to measure in a non-destructive way the isotopic abundance [78]. Important gamma emitters are for example ^{40}K (1.46 MeV gamma line) and ^{208}Tl (2.6 MeV gamma line). High-purity germanium detectors allow to detect ^{238}U, ^{232}Th and ^{40}K at mBq·kg^{-1} levels and lower, corresponding to 10^{-10} g/g for U and Th, and to 10^{-8} g/g for K [128]. Cryogenic operating temperatures are needed in order to ensure a low level of dark current, due to the thermal generation of charges in the semiconductor. The γ-ray counting techniques, unlike in the ICP-MS, are able to probe also the lower part of the ^{238}U and ^{232}Th decay chains (e.g, ^{214}Pb, ^{210}Pb, ^{208}Tl) and study any deviation from equilibrium of the progeny [129]. Furthermore, it allows to measure the activities of cosmogenic isotopes like ^{60}Co. However, the actual sensitivity strongly depends on the

mass of the sample and several weeks are typically necessary to assay clean components [129, 130].

The two different approaches provide complementary information and therefore are both needed to obtain a complete understanding of the sample contamination.

Assays are important to control isotope contamination and to proper characterize their energy spectra. Activities are a fundamental input for simulations, which are used to optimize the detector design prior to its fabrication and to model the background. DAMIC-M design simulations are discussed in Chapter 5.

3.3.2   Surface backgrounds

Uranium, thorium and their decay products are ubiquitous in nature. They can be found in the bulk of the detector components, including the CCDs, but also in particulates on their surfaces, e.g., dust, or as absorbed radon daughters [89]. The uranium, thorium decay chains are shown in Figure 3.10.

^{210}Pb and its daughter ^{210}Bi on the surface of the CCDs or of the components surrounding them are a dominant source of background. ^{210}Pb is a member of the ^{238}U decay chain and is often found out of secular equilibrium since chemical processes in the manufacture of materials separate it from other ^{238}U daughters. The ^{210}Pb nucleus decays 84% of the time into an excited state of ^{210}Bi. The latter promptly releases its energy (46.5 keV) by internal conversion (IC) in 80% of the decays or by γ-ray emission in 4% of the time [89].

When a material is exposed to air, ^{218}Po from ^{222}Rn decay sticks to nearby surfaces. The following sequence of α decays further embeds the long-lived ^{210}Pb ($\tau_{1/2} = 22.3$ years) daughter up to 100 nm into a surface, where it remains until decaying [78]. The recoiling ^{206}Pb nucleus, following the decay chain of ^{210}Pb on the surface of a CCD, could also be a dangerous low energy background, given its kinetic energy of 103 keV. The DAMIC collaboration obtained an upper limit of 35 eV on the energy deposited in the sensitive region of a CCD due to a recoiling ^{206}Pb nucleus [78]. Since this would result in a signal with an energy below DAMIC threshold (50 eVee), this kind of background was not considered in their analysis [78]. However, the contribution of ^{206}Pb will be reconsidered for DAMIC-M, since it will feature a lower energy threshold with respect to DAMIC.

In order to reduce ^{210}Pb surface contamination of CCDs is important to control their exposure to air and thus to ^{222}Rn. Particular attention must be paid also to silicon wafers prior the CCD fabrication. To this end, wafers are usually stored in containers purged

with nitrogen. The exposure to radon during fabrication is negligible. Furthermore, part of ^{210}Pb nuclei deposited on wafer surfaces is eliminated during CCD fabrication via polishing procedures. To further reduce radon contamination, the DAMIC-M collaboration is planning to perform the CCD packaging in a radon-free cleanroom. The possibility to remove about 10 μm from the backside surface of the device has been also proposed. This technique would allow not only to eliminate surface ^{210}Pb, but also to remove the partial charge collection region (PCC) in the back of CCDs, which may lead to distortions in the low part of the energy spectrum [132] (see Section 2.2.5).

In order to reduce the surface contamination of the components surrounding the CCDs, cleaning procedures, like the wet etching, can be adopted [133]. These would remove few μm of material from the surfaces of the volumes, like copper or lead ones, and effectively eliminate surface ^{210}Pb [78].

Finally, surface background rejection can also be done at analysis level, e.g., by selecting a fiducial volume where there is a high signal to noise ratio. In fact, events coming from low-energy electrons and photons radiated by surfaces surrounding the CCDs and from electrons produced in the silicon that exit the device after depositing only a small fraction of their energy occur tens of μm or less from the surface of the CCD [84]. Therefore, they can be rejected by appropriate requirements on the depth of the interaction. This approach was used by the DAMIC collaboration in [84]. Figure 3.13 shows the fiducial selection (horizontal dashed lines) applied in DAMIC for the low-mass WIMP search [84], compared to simulated surface events (gray) and real data (red and black markers). Events are represented as a function of their energy and their lateral spread (σ_{xy}) which is positively correlated with the depth of an interaction. The possibility of applying fiducial cuts also on the x and y position of the events is being explored for DAMIC-M. Another analysis technique developed by the DAMIC collaboration to identify and reject CCD surface ^{210}Pb decay chains is described in Section 3.3.4.

3.3.3 Bulk background

Silicon and copper activation

Cosmogenic isotopes, especially those present in the copper components surrounding the CCDs or in the CCD bulk it self, are another problematic source of background for DAMIC-M. As already discussed in Section 3.1, they are produced by spallation of cosmic rays in the detector components. The activity (A) of the cosmogenic isotopes in a material
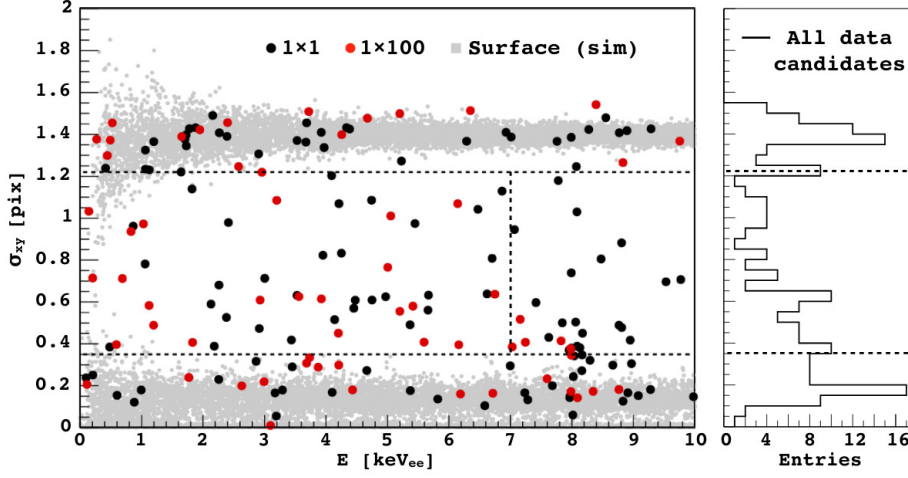
Figure 3.13 – Lateral spread (σ_{xy}) versus measured energy (E) of the clusters that passed DAMIC selection criteria for the WIMP search [84]. The lateral spread is positively correlated with the depth of the interaction. Black and red markers correspond to candidates in two different data set. Grey dots show the simulated distribution of energy deposits near the front and back surfaces of the CCD. The projection on the σ_{xy} axis of the identified clusters is shown on the right. The horizontal dashed lines represent the fiducial selection of events with $0.35 < \sigma_{xy} < 1.22$, corresponding to interactions that occur more than 90 μm and 75 μm from the front and back surfaces, respectively. The vertical dashed line indicates the upper bound of the WIMP search energy range. Reprinted figure with permission from [84]. Copyright (2016) by the American Physical Society.

depends on the time of exposure to cosmic rays (T_{exp}), the time spent underground before data collection (T_{cool}), and the running time of the experiment (T_{run}):

$$A = R \cdot (1 - e^{-\lambda T_{exp}}) \cdot e^{-\lambda T_{cool}} \cdot (1 - e^{-\lambda T_{run}})/(\lambda T_{run}) \tag{3.13}$$

where $\lambda = \ln(2)/t_{1/2}$, $t_{1/2}$ is the half life of the isotope and R is the cosmogenic production rate (Equation 3.9) [78, 117].

^{60}Co is one of the most dangerous cosmogenic isotopes in copper. It is produced by ^{63}Cu(n,α)^{60}Co reactions and is characterized by a long half life (about 5.3 y) and high production rate (about 2100 μBq/kg, as measured in [134]). Figure 3.14 shows the ^{60}Co activity as a function of T_{cool} and T_{exp}, with fixed $T_{run} = 1$ y. The plot emphasizes the importance of limiting the exposure time to cosmic rays of the copper components in order to ensure a low activity for the long-lived isotopes. In fact, their activity cannot be
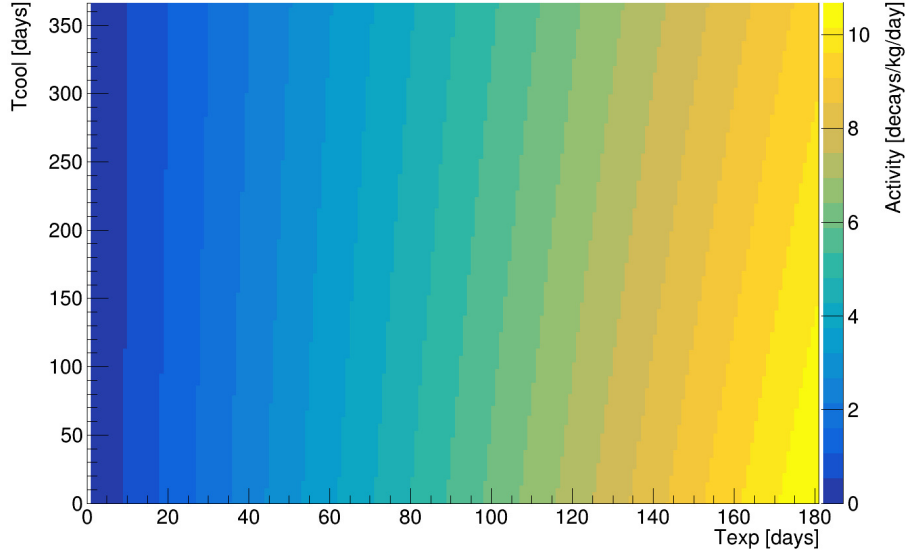
Figure 3.14 – ^{60}Co activity as a function of T_{cool} and T_{exp}, with fixed T_{run}= 1 y. The activity is calculated using equation 3.13 with R = 2100 μBq/kg, as measured in [134].

adequately reduced by a reasonable amount of cooling time.

The cosmogenic isotopes in the silicon bulk of CCDs are mostly produced by cosmic-ray interactions with the silicon crystals prior the storage underground. Only radioisotopes with half-lives less than 100 years are considered, assuming that the silicon crystal growth drives out all non-silicon atoms and that the period of time from the crystal production to the underground storage of CCDs is less than 10 years. Otherwise not sufficient activity is built up to produce significant backgrounds. The most critical cosmogenic isotopes for DAMIC-M are tritium and ^{22}Na [116]. Tritium in silicon at sea-level is mostly produced by spallation of high-energy cosmogenic neutrons with Si nuclei. ^{22}Na is instead produced as a residual nucleus following cosmogenic (neutron or proton) interactions with silicon. ^{22}Na can also be created indirectly following the production and decay of short-lived isotopes like ^{22}Mg, ^{22}Al, and ^{22}Si. However, the total contribution from these isotopes is less than 1% [116]. Tritium decays by pure beta emission and its low Q-value (18.6 keV) results in a large fraction of low-energy events in the expected dark matter signal region. The ^{3}H production rate at energies below 5 keV corresponds to an activity of roughly 0.002 decays/(keV·kg·day) per day of sea-level exposure [116]. A smaller fraction of events in the energy range of interest for dark matter searches is instead expected from ^{22}Na emissions. ^{22}Na decays by positron emission (90.3%) or electroncapture (9.6%)

to the 1275 keV level of ^{22}Ne. For thin silicon detectors like DAMIC-M CCDs, ^{22}Na can be an important source of background as it is likely that both the 1275 keV γ-ray and the 511 keV positron-annihilation photons escape undetected. Therefore, only the emitted positron (before annihilation) or the atomic de-excitation following electron capture deposit energy in the detector.

In order to reduce cosmogenic isotope contamination, it is pivotal to strictly control the exposure time of detector components to cosmic rays, for example by shielding them during the transportation and subsequently storing them underground. Furthermore, tritium can be baked out from silicon wafers at high temperatures (about 900 °C), prior CCD fabrication [135]. The possibility of using low-temperature baking to remove implanted tritium from fabricated silicon devices has also been proposed and is being investigated [116, 135].

^{32}Si background

The ^{32}Si isotope is also an irriducible source of background. It is produced by spallation, or nuclear fragmentation, of atmospheric argon impacted by cosmic rays. It is then trasported to the surface by precipitation and is therefore present in natural silica from which detector-grade silicon is manufactured. The nucleus undergoes sequential beta decays whose β spectra extend to the low-energy region considered for the DM search [89]:

$$
\begin{aligned}
^{32}\text{Si} &\to {}^{32}\text{P} + \beta^- \\
^{32}\text{P} &\to {}^{32}\text{S} + \beta^-.
\end{aligned}
\tag{3.14}
$$

The half lives of the isotopes and the Q-values of the decays are reported in Table 3.1. Spectral measurements of radioactive background in silicon detectors suggest a rate of ^{32}Si at the level of hundreds of decays/kg/day. Thus, the understanding and reduction of such contamination source plays a crucial role in the sensitivity of next-generation, large-exposure, solid state silicon experiments. An analysis technique developed by the DAMIC collaboration allows to identify and reject ^{32}Si decay chains taking place in the CCD bulk [89, 136]. ^{32}Si activities were also derived following this method, described in Section 3.3.4.

3.3.4   Decay chain identification

Due to the unique spatial resolution of DAMIC-M, it is possible to identify ^{32}Si and ^{210}Pb decay chains and measure their activities by exploiting analysis techniques which look for spatial correlated events in the CCD silicon bulk [89, 136]. Both ^{32}Si and ^{210}Pb undergo sequential beta decays and the deriving intermediate nuclei, ^{32}P and ^{210}Bi, are expected to remain in the same lattice site as their parent nuclei. Therefore, a search for electron-like tracks starting from the same spatial position and compatible in time distance and energy with the considered decay sequence, allows to select ^{32}Si and ^{210}Pb chains with high efficiency.

The activity of ^{210}Pb is notoriously difficult to measure by standard assay techniques. In fact, its abundance is too low to be detected by mass spectroscopy because of its relatively short half-life, and its decay products are too low in energy to be efficiently detected by γ-ray counters [78]. However, capitalizing on the superior spatial resolution of CCDs, the DAMIC collaboration was able to place a strong upper limit on ^{210}Pb contributions of $< 160 \mu$Bq/kg (95%CL) [136]. This upper limit is orders of magnitude better than the Bq/kg sensitivity obtained by direct assay techniques that measure bulk ^{210}Pb in materials. The ^{32}Si activity in the CCDs was also measured and was found to be $140 \pm 30 \mu$Bq/kg [136].
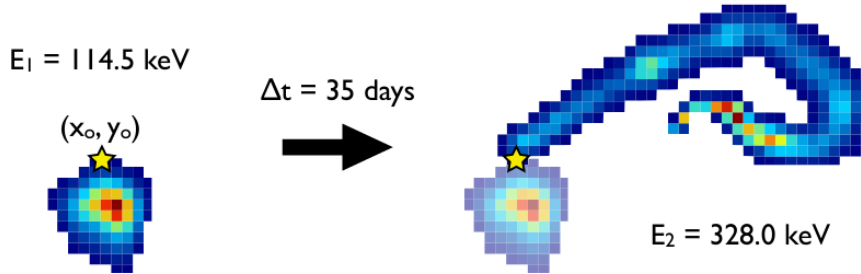
Figure 3.15 – A spatially-correlated $\beta \rightarrow \beta$ candidate decay in the reconstructed data from the ^{32}Si-^{32}P search [89]. The first cluster deposited 114.5 keV of energy. A second cluster, with energy 328.0 keV, was observed in an image taken 35 days later. Both tracks appear to originate from the same point (yellow star) in the CCD x-y plane. © IOP Publishing. Reproduced with permission. All rights reserved.

Figure 3.15 shows an example of a spatially-correlated candidate decay from the DAMIC ^{32}Si search. A similar approach can also be applied to look for spatially-correlated α and β decays and measure ^{238}U and ^{232}Th contamination in the CCD bulk [136].

3.3.5 Low background materials

To reduce the radioactive isotope contamination of the detector components, the DAMIC-M collaboration will employ high purity materials, e.g., ancient lead and electro-formed copper (EFC).

The latter is constructed by electroplating in a $H_2SO_4/CuSO_4$ bath under the influence of a low-voltage. A filtration cartridge for particulates is also seeded with $BaSO_4$ for the purpose of scavenging Ra from the solution. A close control of the background level is needed to ensure a very low contamination of ^{238}U and ^{232}Th in the electro-formed copper samples [93]. Furthermore, electroforming and machining the copper underground prevents the ingrowth of cosmogenically produced isotopes. For DAMIC-M, EFC will be employed to build the nearest components to the CCDs. Instead, the farther volumes will be made of oxygen-free high thermal conductivity copper (OFHC), a commercial product which is widely used in cryogenics and is characterized by high chemical purity. The OFHC shows higher levels of uranium and thorium contamination than EFC and its exposure time to cosmic rays on surface is difficult to control [131].

Archeological lead can be used to shield the detector from γ-rays, given its high density and low level of contamination of ^{238}U and ^{232}Th. In fact, due to the age of this material, coming for example from the Roman era, most of the isotopes have decayed. The most abundant contaminant measurable in lead samples is ^{210}Pb. The reduction of its concentration in lead is problematic due to their affinity. In fact, during refining processes, while other radioactive nuclides that are chemically not affine to lead are segregated from the slag, ^{210}Pb gets concentrated [137]. Therefore, the ^{210}Pb contamination of a lead sample could only be reduced by a cool-down time on the scale of the half-life of the nuclide (about 22 y). Since ancient lead is much older than 22 y, it is characterized by very low levels of ^{210}Pb.

DAMIC-M will employ a lead external shielding to suppress the flux of γ-rays from the environment. The most internal part will be made of Roman archaeological lead. Additional ancient lead shields will be placed inside the cryostat to proper shield the CCDs from γ-rays from the internal components. The activities of the isotopes in the EFC, OFHC and ancient lead components will be provided in Section 5.1.

DAMIC-M SIMULATION SOFTWARE

Simulations play a crucial role in the characterization of the background that limits the experiment sensitivity to dark matter events.

A Geant4 [138] and a Python based codes (WADERS) have been developed by the DAMIC-M collaboration to reproduce the response of the detector to the interactions that take place inside it. The first code simulates the physics processes undergone by a particle passing through the experimental setup. The second mimics the CCD response, e.g., the diffusion process, the dark current, the electronic saturation, and the readout noise.

Part of this thesis work was committed to developing and testing the simulation code, which is described in this chapter. The use of simulations for the optimization of the DAMIC-M detector design is instead discussed in Chapter 5.

4.1 DAMIC-M Geant4 simulations

Geant4 is a software toolkit based on Monte Carlo methods and used to simulate the passage of particles through matter [138]. The toolkit allows to model the geometry and the materials of a given experimental setup and to define the particles of interest along with the associated physical interactions.

Each Geant4 based code is provided of a Physics list where the physics processes, the particles and their production cuts are defined. Given the multi-disciplinary nature of the toolkit, an abundant set of physics processes is supplied to handle diverse interactions of particles with matter over a wide energy range. In many cases, different models are available for the same physics process. More details about the DAMIC-M physics list are provided in Section 4.1.1.

A production cut is the minimum length that a secondary particle has to be able to travel in order to be produced. This particle range cut is set by the user and is then internally converted in an energy value that depends on both the particle type and the

material where the interaction is taking place. Production cuts were introduced to avoid infrared divergences of some electromagnetic processes like ionization and Bremsstrahlung. The range cuts are applied to $e^{\pm}$, γ but also to protons, as production thresholds of nuclei for hadron elastic processes.

A Geant4 run is the largest unit of a simulation and consists of a sequence of events. Within a run, the detector geometry and the physics processes used in the simulation remain unchanged. For each event, the initial conditions have to be provided by the user: the primary particle, its energy, its direction, and its position. Particles can be then tracked in matter. A track is defined in Geant4 as a snapshot of a particle, having the physical quantities only of the current instance and without having a record of the previous quantities. A track is updated by steps, each of them defined as "delta" information of a track. A track object is deleted when it goes out of the implemented geometry, it disappears (e.g, by means of decays, inelastic scattering, or pair production processes), it has zero kinetic energy and no other processes can take place or the user kills it artificially. Figure 4.1 shows a Geant4 run structure.
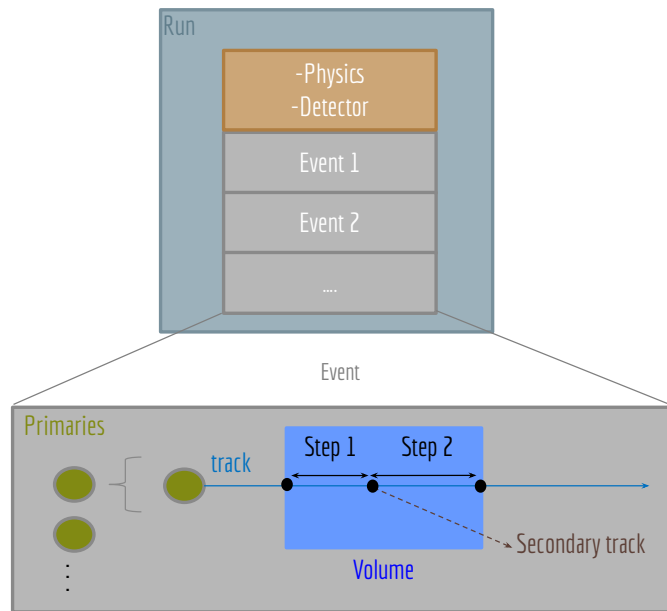
Figure 4.1 – Schematics representing the structure of a run in Geant4. The black points on the track indicate where physics processes occur. The step length depends on the physics processes which the particle is undergoing and also on the geometry of the volume is traversing, e.g. the presence of volume boundaries

The results of a simulation can be then stored in analysis object like histograms, ntuples, or tree[1] as in DAMIC-M code case. DAMIC-M simulation output are discussed in Section 4.1.4.

Being Geant4 based on Monte Carlo methods, the simulation result depends on the used set of pseudo-random numbers identified by an initial seed parameter. This seed number can be provided by the user or automatically set by Geant4 to a default value. To generate two distinct simulations with the same configuration and initial conditions, different seed number values have to be set.

A Geant4 (v.10.04) based code has been developed by the DAMIC-M collaboration. The simulation options are set by the user via a macro. This file contains a list of commands used by the user to define the initial conditions of a simulation (primary particle type, position, energy, and direction), the seed number, the wanted output analysis objects, the number of simulated events, etc. An example of macro used for the DAMIC-M simulations is showed in the following (Listing 4.1).

```
/run/initialize
/random/setSeeds 14744 30482
/damic/gun/particle ion
/damic/gun/ion 82 210 0 0.0
/damic/gun/energy/mono 0 eV
/damic/gun/direction/oned
/damic/gun/direction/onedX 1
/damic/gun/direction/onedY 0
/damic/gun/direction/onedZ 0
/damic/gun/position/dovolume
/damic/gun/position/addvolume CCDSensor_PV 1 false
/analysis/setFileName CCDSensor_PV_210a82z1_10000_s1
/run/beamOn 10000
```

Listing 4.1 – Example of macro used to simulate 10000 ^{210}Pb nuclei in the bulk of the sensitive part of the CCD.

In the following sections a comprehensive description of the code is provided.

---

1. A tree consists of a list of independent branches, each of them containing a single value or an array of values.

4.1.1 DAMIC-M Physics list

The DAMIC-M code uses the Livermore physics list [139] provided with Geant4 and additionally includes hadron (e.g. neutrons and protons) processes and radioactive decays. Some of the most relevant models are summarized in the following and in Table 4.1.

Livermore low-energy electromagnetic models describe the interactions of electrons and photons with matter using interpolated data tables based on the Livermore library (EADL-EEDL-EPDL) [139–142]. The implementation of low energy processes is valid for elements with atomic number between 1 and 99, and for energies up to 100 GeV. The lower energy bound depends on the process. Gamma processes (i.e, photoelectric effect, compton scattering, Rayleigh scattering, conversion) have a recommended low energy applicability limit of 250 GeV. Electron processes (i.e, ionization and Bremsstrahlung) instead have a lower recommended limit of 10 eV. Even if the models are applicable down to the binding energy of corresponding atomic shells (values are taken from the EADL database), accuracy is not guaranteed outside the recommended energy range. In the DAMIC-M code, the Livermore low-energy electromagnetic models are used to describe the interactions with matter of electrons and photons between 20 eV and 100 GeV. In [78], the DAMIC collaboration extended down to 50 eV the use of the Livermore models. Low Background Chamber data could be used to validate them down to 20 eV. Above 100 GeV (up to 100 TeV) standard Geant4 models are used.

Neutrons processes like elastic scattering, thermal scattering, inelastic scattering, and capture are also included in the DAMIC-M physics list. Neutron elastic scattering is simulated according to the CHIPS (CHiral Invariant Phase Space) model [139, 143] (above 19 MeV) and the High Precision neutron model (between 4 eV and 20 MeV) [139]. The latter is also used to describe neutron capture and inelastic scattering processes below 20 MeV and thermal scattering below 4 eV. The higher energy range for inelastic scattering is instead covered by the Fritiof string (FTF) [139, 144] and Bertini (BERT) models [139, 145]. The application energy ranges are 4 GeV - 100 TeV and 19 MeV - 5 GeV, respectively.

Muons processes like ionization, Bremsstrahlung, multiple scattering, pair production, and capture (for μ- only) are considered as well in the DAMIC-M physics list, using Geant4 standard models up to 100 TeV [139].

The radioactive decay process [139] is also included in DAMIC-M simulations. The user can choose (via macro) to simulate the entire decay chain or stop it after the first decay, once the daughter nucleus has reached the ground state. By default, a nucleus

	Model	Energy range
e-	G4eMultipleScattering	0 eV - 100 TeV
	G4LivermoreIonisationModel	20 eV - 100 GeV
	G4eIonisation	100 GeV - 100 TeV
	G4LivermoreBremsstrahlungModel	20 eV - 100 GeV
	G4eBremsstrahlung	100 GeV - 100 TeV
γ	G4LivermoreRayleighModel	0 eV - 100 GeV
	G4RayleighScattering	100 GeV - 100 TeV
	G4LivermorePhotoElectricModel	20 eV - 100 GeV
	G4PhotoElectricEffect	100 GeV - 100 TeV
	G4LivermoreComptonModel	20 eV - 100 GeV
	G4ComptonScattering	100 GeV - 100 TeV
	G4LivermoreGammaConversionModel	20 eV - 100 GeV
	G4GammaConversion	100 GeV - 100 TeV
neutrons	G4ChipsElasticModel	19 MeV - 100 TeV
	G4ParticleHPElastic	4 eV -20 MeV
	G4NeutronHPThermalScattering	0 eV - 4 eV
	G4NeutronInelasticProcess - FTF Model	4 GeV - 100 TeV
	G4NeutronInelasticProcess - BERT Model	19 MeV - 5 GeV
	G4ParticleHPInelastic	0 eV - 20 MeV
	G4NeutronRadCapture	19.9 MeV - 100 TeV
	G4ParticleHPCapture	0 eV - 19.9 MeV
muons	G4eMultipleScattering	0 eV - 100 TeV
	G4MuIonisation	0 eV - 100 TeV
	G4MuBremsstrahlung	0 eV - 100 TeV
	G4MuPairProduction	0 eV - 100 TeV
	G4MuonMinusCapture (only μ-)	0 eV - 100 TeV
ion	G4RadioactiveDecay	
	G4IonParametrisedLossModel	0 eV - 100 TeV
	G4hMultipleScattering	0 eV - 100 TeV
	G4NuclearStopping	
α	G4ionIonisation	0 eV - 100 TeV
	G4hMultipleScattering	0 eV - 100 TeV
	G4NuclearStopping	
	G4HadronElasticProcess	0 eV/n - 100 TeV/n
	G4AlphaInelasticProcess - FTF Model	4 GeV/n - 100 TeV/n
	G4AlphaInelasticProcess - BERT Model	0 eV/n - 5 GeV/n

Table 4.1 – Subset of DAMIC-M physics list for the most relevant type of particles simulated. For each particle are reported both the list of models used to describe its interactions and the corresponding adopted energy range.

(different than ^{4}He) is killed if it is created following another nucleus decay and it has reached the ground state. This helps to optimize the computing time.

4.1.2 Detector construction

The DAMIC-M detector design and the corresponding materials are implemented through a GDML (Geometry Description Markup Language) file, an application-independent geometry description format [138]. GDML is a specialized XML-based language designed for describing the geometries of detectors associated with physics measurements, allowing to identify the position of individual solids, as well as to describe the materials they are made of. A wide range of solids are available. Materials can be defined directly from an element or created as a mixture of previously defined elements or materials, on the base of the number of atoms or the fraction of mass involved for each species.

A sensitive detector is defined in the geometry, which in the case of DAMIC-M is the CCD active part. This allows to collect and store all the information concerning the physical interactions taking place inside the chosen sensitive volume.

In a GDML file is also possible to associate to a given user-defined region productions cut for e$^\pm$, γ, and protons. Production cuts are defined to optimize the computing time without introducing energy spectrum deformations. The CCD sensitive region and all the nearby components have the shortest production cuts to ensure the maximum precision and minimum energy thresholds. The following production cuts were applied for the DAMIC-M design: 10^{-4} mm for the CCD, the cables and copper components nearest to the CCD, 10^{-3} mm for the farthest copper and cable components and 10^{-1} mm for ancient lead.

An example of GDML file is shown in the following (Listing 4.2). Five different blocks can be identified:

— "define" block: it contains the global variable definitions;
— "materials" block: it contains the material definitions;
— "solids" block: it contains the geometrical object definitions, e.g., a box, a tube;
— "structure" block: properties are associated to solids, e.g., material, region, color, position. A hierarchy between volumes is defined. The user can assemble volumes together, put them one inside the other and assign their relative positions. In this way a geometry tree is created;
— "setup" block: the top volume in the geometry tree is specified, i.e., the volume which encloses all the other ones.

```xml
<?xml version="1.0" encoding="UTF-8" standalone="no" ?>
<gdml xmlns:xsi="http://www.w3.org/2001/XMLSchema-instance"
    xsi:noNamespaceSchemaLocation="schema/gdml.xsd">
<define> <!-- definition of global variables-->
    <variable name="Lx_SenCCD" value="90.0"/> <!-- units: mm-->
    <variable name="Ly_SenCCD" value="90.0"/>
    <variable name="Lz_SenCCD" value="0.669"/>
</define>
<materials> <!-- material definition -->
    <element name="G4_Si" formula="Si" Z="14.">
        <atom value="28.0855"/>
    </element>
</materials>
<solids> <!-- solid definition -->
    <box name="CCDBox" lunit="mm" x="Lx_SenCCD" y="Ly_SenCCD" z="
    Lz_SenCCD"/>
</solids>
<structure> <!-- implementation of the geometry tree (hierarchy of
    volumes) and assignment of solids properties (e.g. material) -->
    <volume name="CCDSensor">
        <materialref ref="G4_Si"/>
        <solidref ref="CCDBox"/>
        <auxiliary auxtype="SensDet" auxvalue="CCD"/>
        <auxiliary auxtype="Color" auxvalue="0.453,0.566,0.727"/>
        <auxiliary auxtype="Region" auxvalue="CCDRegion, 0.0001"/>
    </volume>
</structure>
<setup name="Default" version="1.0"> <!--  specify  the  top  volume
    of  the  geometry tree -->
    <world ref="CCDSensor"/>
</setup>
</gdml>
```

Listing 4.2 – Example of implementation in a GDML file of a volume (box) representing the sensitive part of the CCD (9 cm × 9 cm and 669 μm thick). The volume is made of silicon and belongs to a region called "CCDRegion" to which a production cut of 10^{-4} mm is assigned.

A GDML parser, implemented in the DAMIC-M code, ensures the proper conversion between a GDML geometry description and a Geant4 geometry one.

4.1.3   Primary particle generators

The DAMIC-M code offers a discreet variety of already implemented spatial, direction and energy distributions for primary particles. Most of them are inherited from the DAMIC code [146]. Thought Geant4 provides the possibility to set different distributions via macro, in the DAMIC-M code particular command lines were implemented for specific simulation purposes. These distributions are discussed in the following.

An external file can also be used to provide all the necessary primary particle information, like position, momentum, or energy. This option can be exploited to resume simulations from a specific moment and was initially implemented for the external shielding simulations (e.g., simulations of cosmic rays crossing the external shielding). In fact, one may want to test the same shielding configuration for different designs of the detector inside it. However, external shielding simulations are computationally expensive. It is thus convenient to split them in two parts, one dependent and the other independent of the detector design. In a version of the DAMIC-M code dedicated to external shielding simulations, there is a specific command which allows the user to save in a tree the properties of the particles that come out of the most internal layer of the external shielding and enter the cavity that houses the detector. These particles are then artificially killed. The user can then resume the simulation using the information stored in the tree, using another implemented command. Threfore, the same external shielding simulation can be used for different detector designs.

Angular distributions

The direction of the primary particles can be generated with a fixed value or by following a distribution, e.g., an isotropic distribution. Moreover, a special case is that of the cosmogenic primaries. The angle (zenith and azimuthal) distributions of muons at LSM, discussed in Section 3.1, were also implemented in the code during this thesis. The distributions are derived from equation 3.6, following the procedure proposed in [114]. The azimuthal and zenith angle distributions are shown in Figure 4.2.

Energy distributions

The primary particle energy can be generated with a fixed value or following a distribution, e.g., an uniform distribution. The energy distribution of muons at LSM (see Section 3.1) was also implemented in the code and it is defined by equation 3.7 with

(a)   (b)
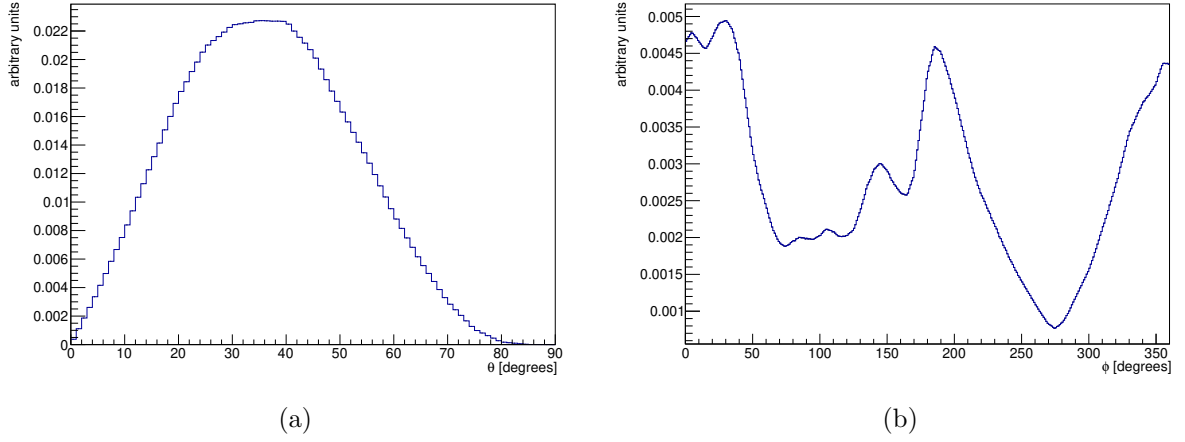
Figure 4.2 – (a): The simulated muon zenith angle (θ) distribution. Since muons are considered to come from the roof of the laboratory, they are generated with an angle equal to $(180 - \theta)$ degrees. The distribution is normalized to the total number of simulated muons (10^8 muons). (b): The simulated muon azimutal angle (ϕ) distribution. The distribution is normalized to the total number of simulated muons (10^8 muons) .

$\gamma_\mu = 3.77$, ϵ_μ=495 GeV, b= 0.438 km.w.e^{-1}, h=4.2 km.w.e, and A equal to the value of the function $\frac{1}{A}\frac{dN}{dE_\mu}$ in E_μ=0. The used h value is the equivalent vertical depth relative to a flat overburden calculated in [111] for the LSM laboratory. The ϵ_μ and b values, describing the muon energy loss in media and depending on the local rock density and composition, are those derived for the LSM laboratory and the Fréjus mountain overburden [114]. The resulting muon energy distribution is shown in Figure 4.3.

Initial position

The primary particle position can be a point as well as be distributed following a particular shape, volume or surface. Particles can be distributed in a uniform way inside a parallelepiped, a sphere or a cylinder. It is also possible to select a component of the implemented geometry and distribute primary particles in its volume or on its surface. Particles are distributed inside the volume in a uniform way. These options were used to simulate radioactive isotopes in the bulk or on the surface of the different detector components, as discussed in Section 5.1. In order to distribute particles on the surface, it is necessary to also select the embedded minimum and maximum depth from the surface. At this point, particles can be distributed in a uniform way between the two depth extremes
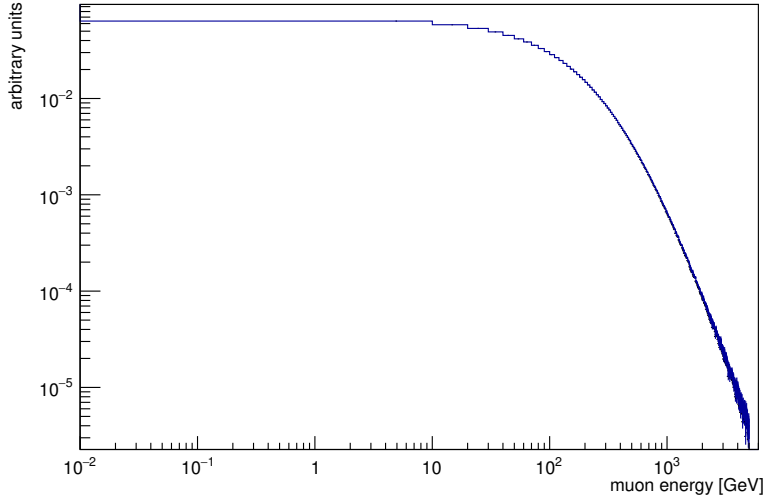
Figure 4.3 – The simulated muon energy distribution. The distribution is normalized to the total number of simulated muons (10^7 muons).

or following a complementary error function:

$$\text{Erfc(z)} = \frac{2}{\sqrt{\pi}} \int_{2z/M_d}^{\infty} e^{-t^2} dt. \tag{4.1}$$

where z is the depth from the surface of the simulated volume and M_d is characteristic maximum depth which is set by the user. This function can be used to simulate the profile of ^{210}Pb penetration distance following a material exposure to air and thus to ^{222}Rn. This process is discussed in Section 3.3.2.

4.1.4   DAMIC-M simulations output

The variables of interest obtained from a DAMIC-M simulation are stored in analysis objects called trees. These are contained in a root file, which is automatically created at the end of a simulation with an user defined name. Three trees are always produced: RunInfo, EventOut, CCDOut. These contain the general information of the simulated setup, of the generated events, and of the energy deposits in a CCD, respectively. The creation of 2 more optional trees can be enabled by the user via macro: TrackOut and PartInfo. TrackOut contains information on all particle steps in a CCD, while PartInfo information on each particle of a given event. Due to the amount of data contained in these two trees, in order to optimize the disk consumption, it is preferable to create them

only if necessary. The output trees are summarized in Table 4.2, while their contents are listed in Tables A.1, A.2, A.3, A.4, A.5 in Appendix A.

Tree name	Information on	Structure	Strategy
RunInfo	simulation setup	1 entry per run	mandatory
EventOut	generated event	1 entry per event	mandatory
CCDOut	energy deposits in the CCD sensitive region	1 entry per event	mandatory
PartInfo	each particle of a given event	1 entry per event	optional
TrackOut	each step of a particle in the sensitive volume	1 entry per event	optional

Table 4.2 – Geant4 output trees.

4.2   WADERS

WADERS (softWAre for Dark matter ExpeRiments with Skippers) is a Python3 based code used to process both simulations and real data. WADERS has been developed starting from the DAMIC at SNOLAB analysis code, with several additional features implemented later on, especially to analyze Compton (see Chapter 6) and Low Background data and to simulate the skipper and continuous readout modes which are specific to DAMIC-M. In this section, the main steps of the simulation processing are described.

Once the energy deposits in the CCD are generated using Geant4, WADERS is used to simulate the detector response and provide the cluster reconstruction. The code uses as input the information contained in the CCDOut output tree (see Section 4.1.4). WADERS is developed in a modular approach through the implementation of different processes that are configurable at runtime by the user via a JSON file. Each process can be either activated or de-activated by the user. The different processes can be divided in two classes: detector response and reconstruction. The former includes all the tools needed to mimic the response of a CCD, e.g., the division in pixels, electron-hole pairs creation, diffusion, dark current, electronic noise, pixel saturation, and continuous readout. The reconstruction class contains all the tools for the reconstruction process, e.g., the minimum energy threshold and the clusterization. The processes are executed in the following order (considering only the ones enabled by the user): pre-processing of the Geant4 energy deposits, electron-hole pairs creation, diffusion, continuous readout, pixelization, dark current, readout noise, pixel saturation, energy threshold, and cluster finder (or clusterization).

4.2.1 Detector response

The detector response processes are used to mimic the CCD operation which is not simulated via Geant4. Data from the CCDOut tree are organized in *hits* which are collections of energy deposits per event per CCD per image. The division in images is done on the base of the time associated to a given energy deposit. The time length of an image is set by the user (via JSON file). The default time length is 10^9 s which ensures that all the energy deposits of a given event belong to the same time image. The *hits* collections are then processed following the instructions provided by the user in the JSON file. All the available processes are described in the following.

Electron-hole pairs creation and diffusion

The electron-hole pairs creation and diffusion processes are discussed in Section 2.1.2. To simulate the former, two different approaches were developed, hereafter called "gauss" and "advanced". The diffusion process is then simulated in the same way for both methods.

(a)   (b)
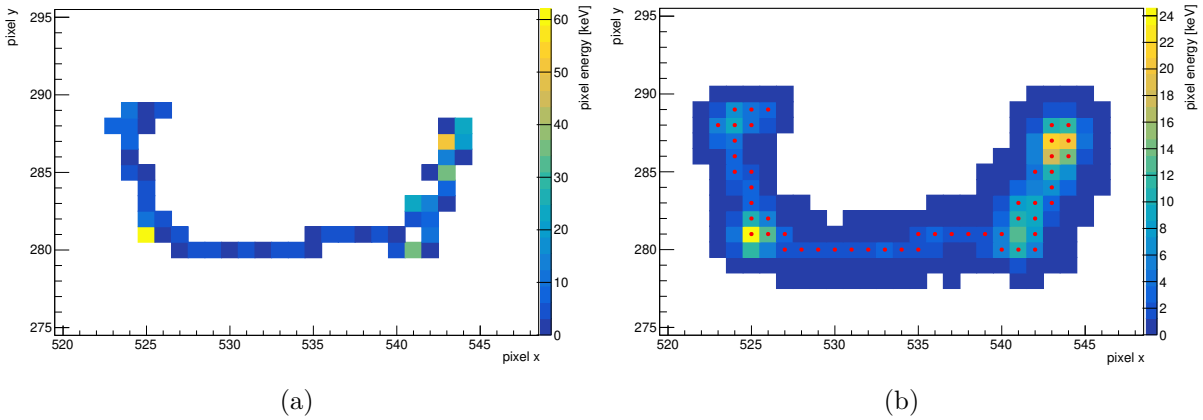
Figure 4.4 – Example of cluster obtained before (a) and after (b) applying the e$^-$/h pair production and diffusion processes. In (a) the reconstructed cluster energy is 457.663 keV. To calculate the number of created pairs associated to a given energy deposit, the "gauss" model was used together with the default parameters. Concerning the diffusion process, A, B, α, and α_0 are set as well to their default values equal to 216.2 μm^2, 8.86$\cdot$10^{-4} μm^{-1}, 5.97$\cdot$10^{-6} pixel/eV, 1, respectively. These values were derived for DAMIC at SNOLAB. In (b), the cluster energy is reconstructed equal to 458.108 keV. The red points indicate the cluster before applying the e$^-$/h pair creation and diffusion processes.

In the "gauss" approach, the number of electron/hole (e$^-$/h) pairs created by an

energy deposit (E_{dep}) is extracted from a Gaussian distribution $\mathcal{G}(\mu, \sigma)$, whose mean and standard deviation are defined in the following way:

$$\mu = E_{dep}/\epsilon_{eh}, \tag{4.2}$$

$$\sigma = \sqrt{(F \cdot \mu)}. \tag{4.3}$$

The Fano factor (F) and the mean energy required to produce an e$^-$/h pair (ϵ_{eh}) are set by the user to constant values via the JSON file (the default values being 0.12 and 3.77 eV, respectively).

As already mentioned in Section 2.1.2, equations 4.2 and 4.3 are known to break down in the low-energy regime (for deposited energies less than 50 eV), where deviations from the asymptotic (constant) behaviour of ϵ_{eh} and F are observed [79]. The "advanced" approach provides a proper description of the diffusion process for low energy deposits and it is based on the phenomenological model proposed in [79]. If the sum of all the E_{dep} in a given *hit* ($E_{sum} = \sum_i E_{dep}^i$, i belonging to the same event, CCD and image) is greater than 50 eV, then the number of e$^-$/h pairs is calculated on the base of the following probability [79]:

$$p_n(E) = \frac{1}{\sqrt{2\pi n F_\infty}} \exp\left[-\frac{1}{2}\left(\frac{n\epsilon_{eh,\infty} - E}{\sqrt{nF_\infty}\epsilon_{eh,\infty}}\right)^2\right], \tag{4.4}$$

where n is the number of e$^-$/h pairs, $\epsilon_{eh,\infty}$ and F_∞ are the asymptotic values (provided by the user) of ϵ_{eh} and F. For a given E_{sum} the algorithm calculates the associated p_n for a reasonable set of n values. The lower (n_{min}) and upper (n_{max}) bounds of the set are evaluated by requiring:

$$p_n(E)/p_{n_{avg}}(E) = 5\%, \tag{4.5}$$

with n_{avg} calculated using equation 4.2. By approximating $\sqrt{\frac{n}{n_{avg}}} \approx 1$, the equality 4.5 results in a quadratic expression in n, whose solutions are equal to n_{min} and n_{max}:

$$n_{min,max}(E) = \frac{1}{2\epsilon_{eh}}\left[2E + F_\infty\epsilon_{eh,\infty}k^2 \pm k\sqrt{(F_\infty\epsilon_{eh}k)^2 + 4EF_\infty\epsilon_{eh,\infty}}\right],$$
$$k = \sqrt{\left(\frac{n_{avg}\epsilon_{eh,\infty} - E}{\sqrt{n_{avg}F_\infty}\epsilon_{eh,\infty}}\right)^2 - 2\ln(0.05)}. \tag{4.6}$$

The probability $p_n(E_{sum})$ is then calculated for each $n \in [n_{min}, n_{max}]$ by normalizing to $\sum_{n=n_{min}}^{n_{max}} p_n(E_{sum})$. If instead $E_{sum} \leq 50$ eV, the p_n values are read from a file provided

in [79] for a temperature of 100 K. The first column of the file contains energies between the energy gap of silicon at 100 K (E_{gap} = 1.1 eV) and 50 eV, in intervals of 0.05 eV. The remaining consecutive columns are the p_n values for n=[1..20]. In case $E_{sum} < E_{gap}$, then E_{sum} is considered to be equal to E_{gap}.

The number of e$^-$/h pairs associated to a given E_{sum} is determined by randomly choosing it from the provided set of $n(E_{sum})$, each value weighted by the corresponding $p_n(E_{sum})$. Once $n(E_{sum})$ is obtained, it is necessary to distribute the number of pairs over all the energy deposits of a given event, CCD, and image. A fraction of pairs proportional to the carried fraction of energy is assigned to each energy deposit:

$$n(E_{dep}) = n(E_{sum}) \cdot \frac{E_{dep}}{E_{sum}}, \tag{4.7}$$

where the result is approximated to the greatest smaller or equal integer. If the sum of all the $n(E_{dep})$ values is less than $n(E_{sum})$, then the remaining number of pairs are redistributed. The number of remaining pairs assigned to each energy deposit is determined on the base of the probability $p_r(E_{dep})$:

$$p_r(E_{dep}) = \frac{n(E_{sum}) \cdot \frac{E_{dep}}{E_{sum}} - n(E_{dep})}{\sum(n(E_{sum}) \cdot \frac{E_{dep}}{E_{sum}} - n(E_{dep}))}. \tag{4.8}$$

Once the number of electron/hole pairs is determined for each energy deposit, the charges are diffused transversely. The implemented procedure, described below, is the same for both the gauss and advanced approaches. To each pair is assigned the same spatial position as the initial energy deposit (x',y',z'). Their x-y position is then spread following a Gaussian distribution centered in (x',y') with a standard deviation σ_{xy} [78]:

$$\sigma_{xy}(z, E_{dep}) = \sigma_{xy}(z, E_{dep} = 0)\left(\alpha_0 + \frac{\alpha E_{dep}}{\sigma_{xy}(z = z_{\mathrm{D}}, \mathrm{E}_{dep} = 0)}\right), \tag{4.9}$$

where α and α_0 are needed to model the dependence of the spread on the deposited energy, z_{D} indicates the back of the CCD, and

$$\sigma_{xy}^2(z, E_{dep} = 0) = -A\ln\left(1 - B(z - z_{\mathrm{offset}})\right). \tag{4.10}$$

A and B are coefficients which depend on the physical parameters of the silicon detector (permittivity of silicon, donor charge density, operating temperature, bias across the CCD,

and thickness of the active region) and which can be measured directly from data (see Sections 2.2.3 and 6.5). To each e$^-$/h pair is then assigned an energy equal to the mean energy-per-pair ϵ_{eh} provided by the user. Figure 4.4 shows the effect of the e$^-$/h pair production and diffusion processes on clusters.

Continuous readout

CCDs can be read in two different modes: standard or continuous readout. The first consists in exposing the CCD for a specific amount of time (called exposure time) and then reading out the accumulated charges. After an image has been read, the CCD is cleaned from all the remaining charges before being exposed again. If continuous readout is used, instead, the CCD is read continuously. This induces a bad reconstruction of the y position of an energy deposit, due to the limited temporal resolution of the CCD.
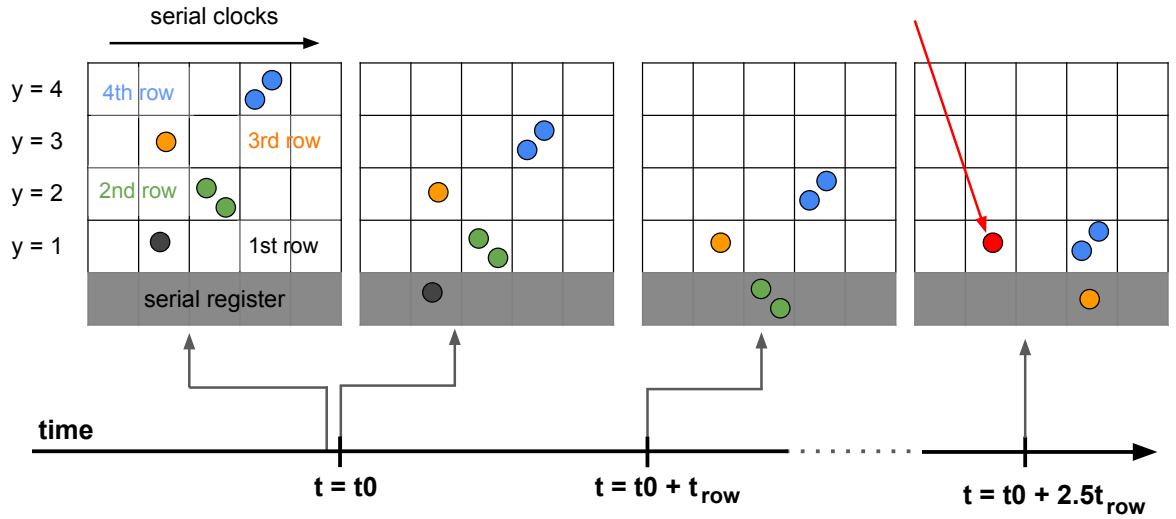
Figure 4.5 – Example showing the continuous readout effect on the reconstruction of y position of the energy deposits. The readout process starts at the time t = t0, when the first row is moved into the serial register. The time needed to read a row is equal to t$_{\mathrm{row}}$. The colored circles indicate the charges collected in each pixel. The color depends on the charges y position before the beginning of the readout process. If after a certain amount of time Δt = 2.5t$_{\mathrm{row}}$, a particle deposits some amount of energy in a pixel with y = 1 (red circle), this energy deposit will be reconstructed with y = 4 (and not with y = 1), since it will be read out together with all the charges which before t = t0 were in the 4th row (blue circles).

A schematic example is shown in Figure 4.5. Let's assume that the readout process

starts at the time t=t0 and the time needed to readout a row is equal to t_{row}. Just before the beginning of the readout process, there are 6 charges already accumulated in the CCD pixels, indicated by different colours depending on their y position. During the readout process, rows are moved one by one into the serial register. If a new energy deposit occurs in the first row at $t = t0 + 2.5t_{row}$, it will be read together with the charges present at $y = 4$ before the beginning of the readout process. Therefore, this new charge will be reconstructed with $y = 4$ (and not with $y = 1$). To simulate this effect, a shift on the y position of a pixel is applied in WADERS, calculated as:

$$\Delta Y = (t_{Edep} - t0)/t_{row} + 1, \tag{4.11}$$

where ΔY is rounded down to the closest integer. It should be noted that this bad y reconstruction is experienced each time the exposure time is much shorter than the readout time (as in the case of the Compton scattering measurement, described in Chapter 6).

Pixelization

The pixelization process is a generalization of a 2-dimensional histogram function. The x and y positions of the energy deposits are converted from mm to pixel units by using the size of a pixel (0.015 mm). The pixels positions are then organized in a 2-D histogram, with a bin width of 1 pixel and the size of a CCD image. For each pixel, different variables are calculated, e.g., the total deposited energy. Pixel properties are listed in Table B.2 of the Appendix section B.

Dark current

The dark current (DC) phenomenon is described in Section 2.1.4. A source of DC is the continuous thermal generation of electron-hole pairs in the depletion region (active region) of a CCD. Its rate largely depends on the CCD active area, on the CCD temperature, on the band gap energy of silicon, and on the operation voltage. Dark currents can also be generated by leakage currents not related to thermal excitation processes. The dark current is assumed to follow a Poisson distribution with a mean proportional to the pixel exposure time. The single pixel exposure time is the sum of the image exposure time and the time needed to move the pixel charge from its position to the serial register. Therefore, farther pixels (in terms of rows[2]) from the serial register have a larger exposure time than

---

2. The row number corresponds to the pixel y coordinate.

those which are closer.

(a)   (b)
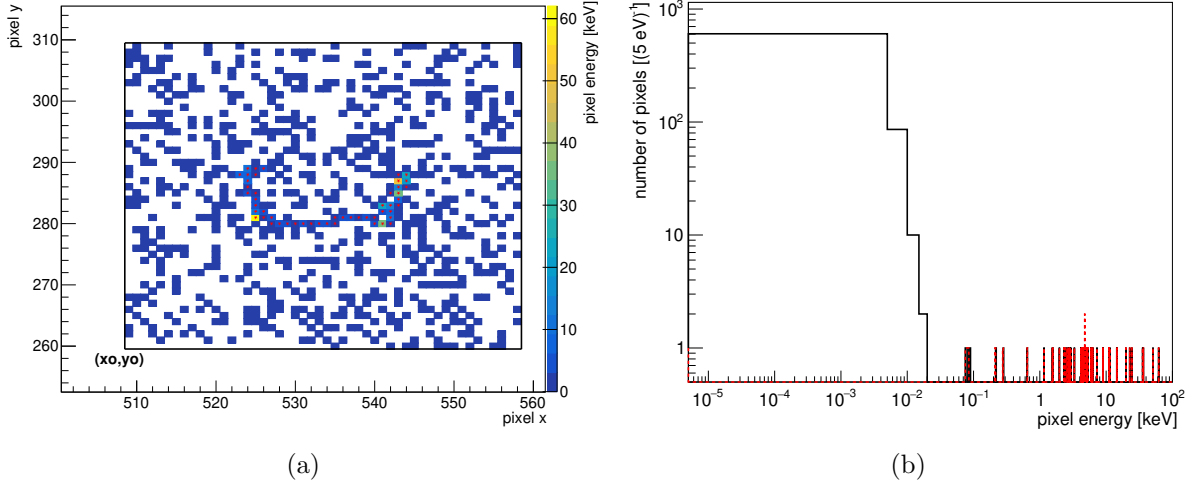
Figure 4.6 – (a): Image obtained by simulating a dark current with a rate of 1 e$^-$/pixel/day and considering an exposure time of 8 hours ("exposure" mode). Among the detector response processes, only the pixelization and the dark current ones are enabled. The "cropped-image" mode was used with $\Delta_{CI} = 50$ pixels. The cropped image was pasted on top of the initial CCD image containing a cluster with a total energy of 457.66 keV (50 pixels). The pixels belonging to the initial simulated track are indicated by red stars. (b): Pixel energy distribution (black line) for the image shown in a). The dark current Poisson distribution is visible at low energy (black). The dashed red histogram indicates the distribution before simulating the dark current.

In order to simulate the process, the user has to provide the DC rate (R_{DC}) in number of electrons per pixel per day, the image exposure time in days (t_{img}) and the time in days needed to read a single CCD row (t_{row}). The mean (λ) of the DC Poisson distribution is then calculated:

$$\lambda = R_{DC} \cdot t_{pixel}, \tag{4.12}$$

where t_{pixel} is the pixel exposure time. The t_{pixel} parameter can be calculated in two different ways:

— "exposure" mode: the same exposure time is assigned to each pixel, i.e, $t_{pixel} = t_{img}$.
— "exposure-per-row" mode: the pixel exposure time depends on the row position, i.e., $t_{pixel} = t_{img} + n_{row} \cdot t_{row}$, where n_{row} indicates the row number (the higher is the number, the farther the row is from the serial register) [3].

---

3. Note that, internally in WADERS, the row number runs from 0 to the total number of rows minus 1.

The two options are needed to mimic the dark current behaviour in case of standard [4] or continuous readout. In fact, in the first case the pixel exposure time and therefore the associated dark current depend on the pixel position. On the contrary, with the continuous readout, all pixels feature the same exposure time (after the first entire CCD image acquisition). The user can select the wanted method via JSON file.

Two running modes are available: the "cropped-image" and the "full-image" modes. The usage of the former is preferable, being the latter computationally inefficient. In the "full-image" mode, a DC image is generated with the same size of the CCD. Each pixel is then filled with values following a Poisson distribution with mean equal to λ. The number of DC charges is then converted in energy, assuming the mean energy per charge set by the user (by default equal to 3.77 eV). In the "cropped-image" mode, instead, a smaller image (squared image) is generated with dimensions provided by the user (Δ_{CI}). A new image is created for each *hit*.

For a given *hit*, the minimum and maximum x and y positions of the charged pixels are considered (x_{min}, x_{max}, y_{min}, y_{max}). The DX and DY variables are then calculated as:

$$DX = x_{max} - x_{min} + 1, \tag{4.13}$$

$$DY = y_{max} - y_{min} + 1. \tag{4.14}$$

The two variables thus define the minimum x and y dimensions of a rectangle enclosing all the charged pixels of a given event, CCD, and image. If the dimensions of the squared cropped image (Δ_{CI}) are smaller than DX or DY, then the image size is increased by a user-defined number of pixels. Exception made for specific cases, the cropped image is placed in such a way that the energy deposits are centered. In particular, the bottom-left corner of the image is placed in $(x_0, y_0) = ([x_{min} + DX/2 - \Delta_{CI}/2], [y_{min} + DY/2 - \Delta_{CI}/2])$. If a charged pixel is placed near one edge of the CCD, the x_0 and y_0 values are calculated in a different way:

$$x_0 = \begin{cases} 0 & \text{if } x_{min} < L_x = \frac{\Delta_{CI}-DX}{2}, \\ X_{CCD} - \Delta_{CI} & \text{if } X_{CCD} - (x_{max} + 1) < L_x = \frac{\Delta_{CI}-DX}{2}, \end{cases} \tag{4.15}$$

---

4. This type of readout was used in DAMIC as well as in the Compton scattering measurement (see Chapter 6). In the case of DAMIC, the exposure time is much longer than the time needed to readout a whole CCD image. Therefore, the dependence of the dark current on the row position is negligible. This is not the case for the Compton measurement, for which the exposure time is much shorter than the readout time.

$$y_0 = \begin{cases} 0 & \text{if } y_{min} < L_y = \frac{\Delta_{CI} - DY}{2}, \\ Y_{CCD} - \Delta_{CI} & \text{if } Y_{CCD} - (y_{max} + 1) < L_x = \frac{\Delta_{CI} - DY}{2}, \end{cases} \quad (4.16)$$

with X_{CCD} (Y_{CCD}) the number of pixels of the CCD on the x-axis (y-axis). Once the cropped image is correctly positioned, the dark current image is "pasted" on the top of the initial CCD image. The energy in each pixel is therefore the sum of the initial simulated charge and the dark current charge in the corresponding pixel. An example of image obtained by simulating the dark current process is shown in Figure 4.6.

Electronic noise

Electronic noise or readout noise is described in Section 2.1.4. It is introduced each time a pixel is read and it is assumed to follow a Gaussian distribution. The readout noise can be reduced via skipper measurements, that are multiple non-destructive measurements (skips) of the same pixel charge. In WADERS, the user-provided input values are the mean

(a)   (b)
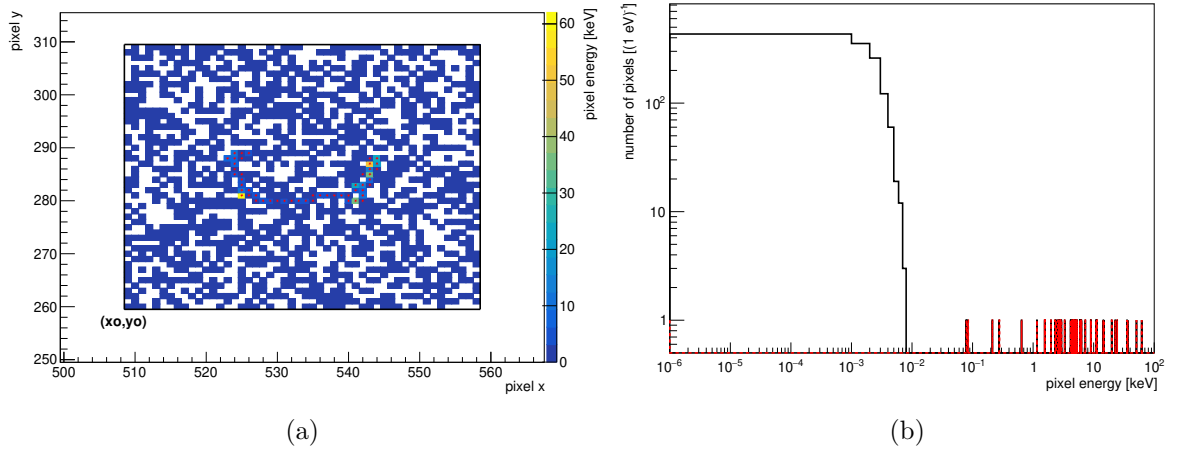
Figure 4.7 – (a): Image obtained by simulating a readout noise with a sigma equal to 0.6 e$^-$ (1$^-$ = 3.77 eV) and $\mu = 0$. Among the detector response processes only the pixelization and the electronic noise processes are enabled. The "cropped-image" mode was used with $\Delta_{CI} = 50$ pixels. The cropped image was pasted on top of the initial CCD image containing a cluster with a total energy of 457.66 keV (50 pixels). The pixels belonging to the initial simulated track are indicated by red stars. After applying the readout noise process, only 1 cluster is found by the clustering algorithm (described in Section 4.2.2, with N=2) with energy equal to 459.905 keV (1313 pixels). (b) Pixel energy distribution (black line) for the image shown in (a). The dashed red histogram indicates the distribution before simulating the readout noise.

(μ, also called pedestal) and standard deviation (σ) of the Gaussian and the number of skips ($nSamples$). For a number of skips greater than 1, the standard deviation is calculated as $\frac{\sigma}{nSamples}$. By default, $nSamples = 1$. As in the case of the dark current process, two running mode are available: the cropped-image and the full-image modes. In the full-image mode, a noise image is generated with the same size of the CCD. Each pixel is then filled with values following a Gaussian distribution with mean μ and standard deviation σ. The number of charges per pixel is then converted in energy, assuming the mean energy per charge set by the user (by default equal to 3.77 eV). In the cropped-image mode, instead, a smaller image (squared image) is generated with dimensions provided by the user. A new image is created for each *hit*, following the same procedure described in Section 4.2.1. After the cropped image has been placed as explained in Section 4.2.1, the readout noise image is "pasted" on the top of the initial CCD image. The energy in each pixel is therefore the sum of the initial simulated charge and the readout noise charge in the corresponding pixel. An example of image obtained by simulating the readout noise process is shown in Figure 4.7.

Pixel saturation

In raw CCD images, the charge in a pixel is given in ADU (analog-to-digital units). The calibration formula needed to convert the charge from electron units to ADU (and vice-versa) can be derived directly from real data (see Section 6.4.4). The ADC (Analog-to-Digital-Converter), having a limited number of bits (N_{bits}), can only return up to $2^{N_{bits}}$ different values. This implies a saturation for charge values exceeding the highest possible N_{bits}-digit binary number (converted in decimal number). For example, considering a 16-bit ADC, the saturation value is equal to 65535 ADU. In WADERS, the saturation effect can be enabled, providing in the JSON file the maximum charge value (in ADU) as well as the conversion factor between eV and ADU.

4.2.2   Reconstruction

This class includes all the processes needed for the cluster reconstruction: the minimum energy threshold and the clusterization. The former is used to select only the pixels with charge above a given energy threshold. These pixels, considering only the contiguous ones, are then grouped in clusters by the clusterization algorithm. If the minimum energy threshold process is not enabled by the user, the clusterization is run over all the charged

pixels, without any minimum energy requirement.

Minimum energy threshold

Through the "minimum energy threshold" process, only pixels with charge above an user-defined threshold are considered for clusterization. This procedure can be used to exclude all the pixel charges that are compatible with the readout noise distribution. The threshold is provided by the user via the JSON file.

Cluster Finder

This process, also called clusterization, is meant to collect all the contiguous charged pixels above a threshold (see Minimum energy threshold process) in a cluster. The contiguity condition is defined via an acceptance radius r:

$$r = N\sqrt{2}, \tag{4.17}$$

where N an interger and is defined by the user via JSON file. By default, N = 2. All pixels with an Euclidean distance less or equal to the radius of acceptance are grouped in the same cluster, as shown in Figure 4.8.
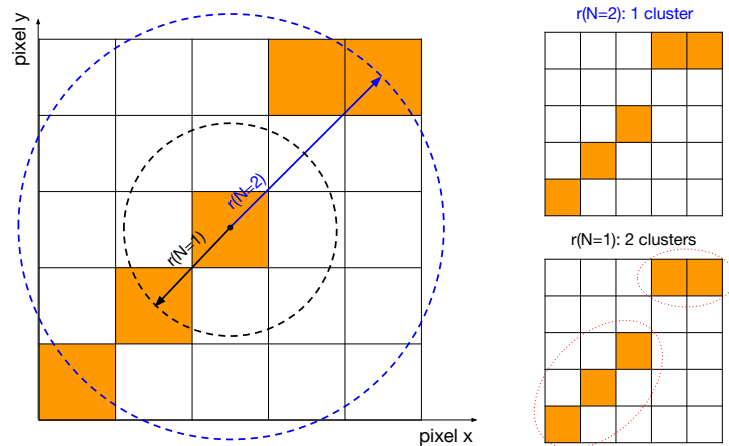

Figure 4.8 – Clusterization algorithm. All charged pixels (orange) with an Euclidean distance less or equal to the radius of acceptance (r) are grouped in the same cluster. If N=2, the charged pixels are grouped in only 1 cluster. If N=1,instead, the clusterization algorithm will reconstruct two separate clusters.

The clusterization takes place once all the other enabled processes have been applied (detector response processes and reconstruction processes).

For each cluster, a set of variables is computed, e.g., the cluster energy, the cluster size, and the cluster spatial position. The full list of these quantities is provided in the Appendix (Table B.1).

4.2.3   WADERS output

As in the DAMIC-M Geant4 code case, WADERS stores the variables of interest in trees contained in root files. Four different trees are created:

— clustersRec: it contains the information relative to a cluster, but also to the primary particle of a given event.

— pixelizedEvent: it contains all the information relative to pixels. The tree is created at the end of the pixelization process.

— geant4_config: it contains the information concerning the Geant4 simulation run, e.g., number of simulated events, seed value, properties of the simulated geometry.

— process_config: it contains all the parameters used to configure the different WADERS processes.

The content of each tree is reported in the Tables B.1, B.2, B.3, B.4 in Appendix B.

* * *

Before concluding this chapter, it is worth mentioning that WADERS can also perform the reconstruction of real data events. For example, it has been used to process the data of the Compton scattering measurements (see Chapter 6) and of the Low Background Chamber. WADERS is meant to be used also in the future for DAMIC-M data.

DAMIC-M BACKGROUND ESTIMATION AND DESIGN OPTIMIZATION

An extensive campaign of innovation of the detector technology and design is ongoing to fulfill DAMIC-M scientific goals. In particular, simulations are exploited to optimize the detector design, drive the material selection and handling, and test background rejection techniques.

Most of this thesis work was devoted to the simulation development, background estimation and optimization. Different detector designs were studied and the obtained results were fundamental for the evolution of the detector conception and to define the material, shape, and position of the different components.

In this chapter, the simulation outcomes are discussed.

5.1   Detector simulations

The DAMIC-M detector design is under continuous development. Each of the proposed designs is fully simulated to predict the corresponding background level and possibly propose further improvements. The simulations are performed by using the Geant4 and WADERS codes described in Chapter 4. The radioactive isotopes are uniformly simulated in the bulk of the detector components, choosing only the proper ones depending on the volume material. The following isotopes from the ^{238}U and ^{232}Th chains are considered: ^{210}Pb, ^{210}Bi, ^{212}Pb, ^{212}Bi, ^{214}Pb, ^{214}Bi, ^{234}Th, ^{234m}Pa, ^{228}Ac, ^{208}Tl. The cosmogenic isotopes from copper activation are included: ^{60}Co, ^{56}Co, ^{57}Co, ^{58}Co, ^{54}Mn, ^{59}Fe, ^{46}Sc. The ^{40}K and the ^{87}Rb isotopes are also considered. As already mentioned in Section 4.1.1, the components of a radioactive chain are simulated separately to speed up simulations. For the purpose of the current studies the detector effects as diffusion, saturation and clustering threshold are not included, being their effect negligible. For the clustering process (Section 4.2.2), N is set to 2 pixels, i.e., all pixels with an Euclidean distance less

or equal to $2\sqrt{2}$, are grouped in the same cluster.

The background rate is obtained for each isotope by scaling the cluster energy spectrum for a proper factor f:

$$f = \frac{n_{bins} \cdot A_{iso} \cdot m_{vol}}{\Delta E \cdot N_{decays} \cdot M_{detector}}, \tag{5.1}$$

where $\Delta E/n_{bins}$ is the bin width, A_{iso} is the activity of the isotope in decays/kg/day, m_{vol} is the mass in kg of the volume of the detector where the radioactive element is simulated, $M_{detector}$ is the mass of the whole sensitive detector in kg, and N_{decays} the number of simulated events. Unless differently specified, the used isotope activities are those measured at SNOLAB for the DAMIC experiment or provided by the material suppliers. The activity values are reported in the following sections. An assay program is planned for all DAMIC-M detector materials. Those measurements will be used to obtain more accurate estimations of the background rates associated with the detector design.

The activity of the cosmogenic isotopes is calculated based on the exposure time to cosmic rays (T_{exp}), the time spent underground before data collection (T_{cool}) and the running time of the experiment (T_{run}) using Equation 3.13 and the production rates reported in Table 5.1. The exposure time, cooling time, and run time of the oxygen-free

Isotope	half life [days]	R [μBq/kg]
^{56}Co	77.236	230
^{57}Co	271	1800
^{58}Co	70.83	1650
^{60}Co	1923	2100
^{54}Mn	312.13	215
^{59}Fe	44.495	455
^{46}Sc	83.788	53

Table 5.1 – Cosmogenic isotopes half lives and production rates (R) [134].

high conductivity copper (OFHC) components are set to the predicted values equal to 3, 6, and 12 months, respectively. In the case of the electro-formed copper (EFC) components, a reference limit for the exposure time and cooling time is retrieved via simulations. In the following, these values are set to 10 days, 6 months, respectively, together with a run time of 12 months. A more detailed description of the contribution of the cosmogenic isotopes in the EFC components is provided for the latest discussed cryostat design.

The rate of background events is estimated by a fit with a constant function in the energy interval between 2-7.5 keV. This energy range is chosen to exclude the silicon and

copper fluorescence Kα emission peaks at 1.7 keV and 8 keV, respectively. The maximum likelihood method is used to perform the fit, being more suited to describe distributions with low-statistics of events. By using this fitting approach, the resulting background rate (r) is compatible with the one obtained using the so-called "counting method". The latter consists in summing up the number of events $n(E)$ (properly rescaled) falling in a given spectrum region and then dividing for the energy range considered ($\Delta E = E_{max} - E_{min}$):

$$r = \frac{1}{\Delta E} \sum_{E=E_{min}}^{E_{max}} n(E) \frac{A_{iso} \cdot m_{vol}}{N_{decays} \cdot M_{detector}}. \tag{5.2}$$

In the following sections, the results obtained during the whole period of time of this thesis work are summarized, following the temporal evolution of the detector conception. The main assessed cryostat designs are described in Section 5.1.1. Cables and external shielding simulations are discussed separately in Sections 5.1.2 and 5.1.3, respectively. The contribution to the background of the surface and bulk contaminants of CCDs and pitch adapters is explored in Section 5.1.4.

5.1.1   Detector design

The cryostat design has to fulfill mechanical, thermal, and background requirements. The structure has to be mechanically stable, sustain vacuum[1], ensure a temperature of about 100 K for the CCD stack[2], as well as feature the lowest background possible. The design is optimized in terms of background via simulations.

Figures 5.1 and 5.2 show the evolution of the cryostat and the CCD stack conception. All the proposed cryostat designs are characterized by a L-shape, in contrast with the I-shape of DAMIC at SNOLAB. This was motivated by the possibility of moving the most radioactive components, like the cable connectors board (not shown in Figure 5.1), in the horizontal arm to avoid a direct line of sight with the CCD stack[3]. Each design is characterized by the presence of a cooling system which is principally made of copper, being it an excellent conductor of heat, and which is connected to an external liquid nitrogen source (not simulated and not shown in Figure 5.1). The system varies across the different cryostat versions. For example, in design A, it is represented by a cold finger

---

1. Usually the pressure is of about 10^{-6} mbar (see Section 2.2).
2. As mentioned in Section 2.1.4, low temperature is required to reduce the dark current.
3. Simulations were run to validate this choice, but are not reported in this thesis for the sake of brevity.
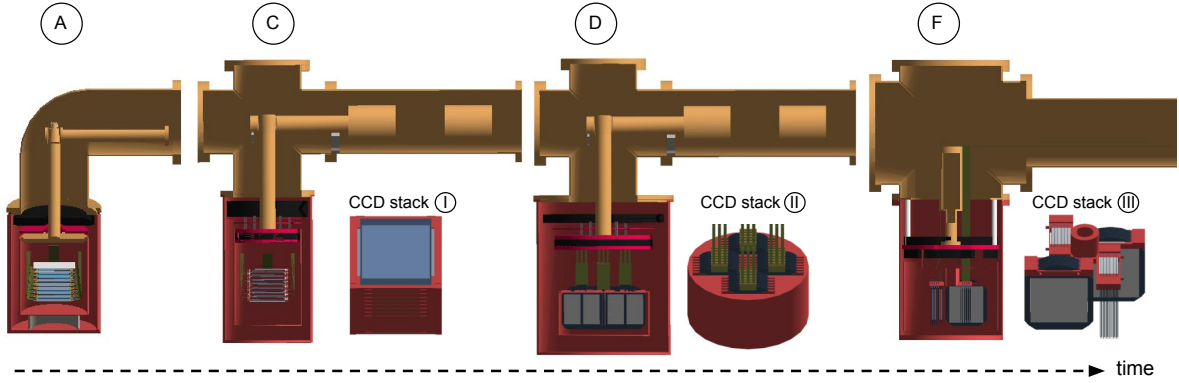
Figure 5.1 – Time evolution of the cryostat designs. The cryostat configurations are labeled by letters, while the CCD stack ones by roman numbers. The missing designs (B,E) are not shown in this figure but the related results are discussed in Chapter 5.1.1. The red components are made of EFC, the yellow ones of OFHC and the black ones of lead. The cables are shown in green. For the CCD, the sensitive part (light blue), the not sensitive part (dark blue), and the top and bottom dead layers (gray) are visible.
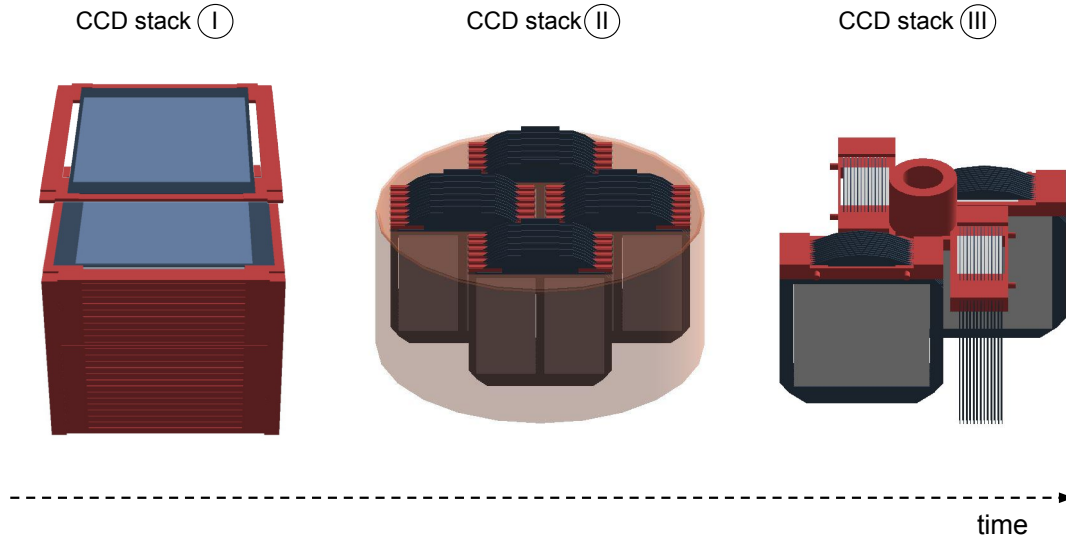
Figure 5.2 – Time evolution of the CCD stack designs. Color code as in Figure 5.1.

connected to a cylindrical cold IR shield (referenced as cold shield in the following) which contains the CCD stack. From design B, a heat exchanger is also introduced to better control the temperature and to optimize the nitrogen consumption. Internal shields, made of ancient lead and EFC disks, are also present in each cryostat configuration in order to screen the CCD stack from the background events coming from the above. The thickness of these disks was optimized with simulations. As already explained in Section 3.3.5, archaeological lead is employed due to its high γ attenuation coefficient and low radioactivity. DAMIC-M will use lead recovered from a Roman ship sunk in Brittany in 400 A.C., which is available at the LSM. However, despite being the most radio-pure, the ancient lead can still add a relevant contribution to the background (considering DAMIC-M background goals), as observed in the following. Therefore, an EFC shield is often placed below the lead shield to reduce the lead-induced background rate.
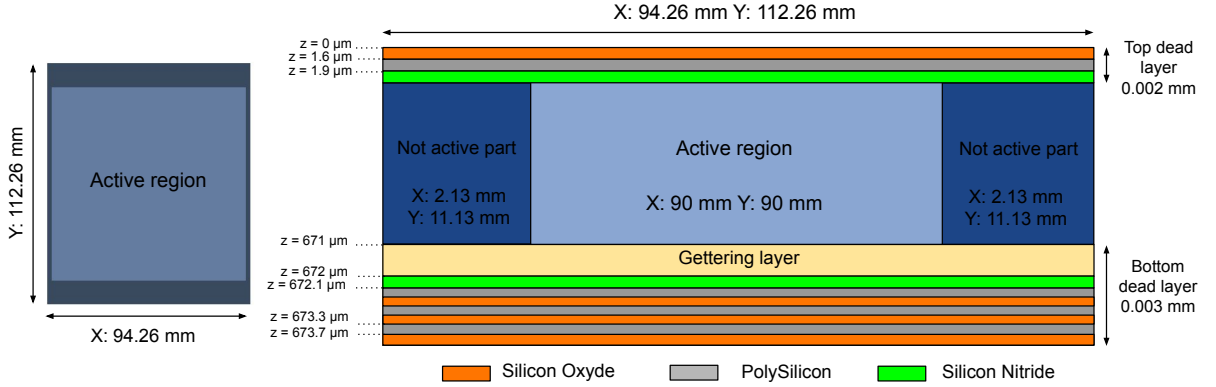
Figure 5.3 – Simulated CCD structure for the CCD stack I (right image not to scale). The top and bottom dead layers are 0.2 and 0.3 μm thick, respectively. The sensitive (active) part of the CCD is instead 0.669 mm thick.

The CCD stack design also evolved over time. Initially, in design I, the CCDs were horizontally stacked one atop the other, each CCD rotated by 90 degrees with respect to the previous one. It was then decided to adopt a vertical orientation of the CCDs (design II and III) to reduce the background contribution of the components above the stack, without limiting the expected rate of the dark matter interactions. The x and y dimensions of the single CCDs also changed with time. Although this modification doesn't have an impact on the active total mass of the detector, it implies a change in

the design and cabling. Each simulated CCD is composed by a sensitive (active) part, a not sensitive part, and two dead layers above and below them, as for DAMIC CCDs. The total thickness is of 0.674 mm, of which only 0.669 mm are active. The sensitive part initially featured an area of 9 cm × 9 cm (6k pixels × 6k pixels). The first simulated CCD structure is shown in Figure 5.3. To ensure better production yields, instead of having a unique 6k pixels x 6k pixels CCD, DALSA proposed a design with each CCD divided in 2 (two 3k pixels × 6k pixels CCDs, as in CCD stack II) or 4 (four 1.5k pixels × 6k pixels CCD, as in CCD stack III). The thickness remained unchanged, while the dimensions of the not sensitive area changed to 49.6 mm x 94.5 mm for the design II, 24.8 mm x 106.5 mm for the design III. Whereas the horizontal CCD stack I is characterized by 50 CCDs (6k pixels × 6k pixels) and a total sensitive detector mass of about 0.64 kg, the vertical CCD stack II (III) is composed by 104 (208) CCDs, 3k pixels × 6k pixels (1.5k pixels × 6k pixels), with a slightly higher sensitive detector mass of about 0.66 kg.

Isotope	OFHC	EFC	Ancient Lead
^{210}Pb	2350 ± 720	$<\mathbf{45.8}$	2850*
^{232}Th	<3.5	<0.0022	0.2*
^{226}Ra	<11.2	$0.018^\dagger$	$<\mathbf{2.0}$
^{238}U	<10.7	<0.018	<2.0
^{40}K	$<2.7^*$	$2.7^\dagger$	<0.5
^{87}Rb	7.4^*	$7.4^\dagger$	-

Table 5.2 – Activities in decays/kg/day per isotope and material used for simulations. The OFHC and ancient lead activities were measured by the DAMIC collaboration [78]. The EFC activities were provided by the material suppliers. The bold activities are decreased by a factor 10 with respect to the measured value at SNOLAB, given the expected reasonable improvement in the material purity. (†): in absence of measurements, the activity of ^{226}Ra was assumed equal to that of ^{238}U, the ones of ^{40}K and ^{87}Rb for EFC equal to that of the OFHC. (*): measurement with unknown precision.

In the next sections, the different detector designs and the corresponding background estimates are discussed, following the temporal evolution. The used activities are reported in Table 5.2. Secular equilibrium is assumed for the ^{232}Th chain and the different segments of the ^{238}U chains (leaded by ^{238}U, ^{226}Ra, and ^{210}Pb). In absence of the measurements of the ^{226}Ra and ^{210}Pb activities, secular equilibrium over the whole ^{238}U chain is assumed.

Design A

Figure 5.4 shows the first proposed design (A), with the horizontal CCD stack configuration I. All the components in this figure are simulated. For each isotope, generally
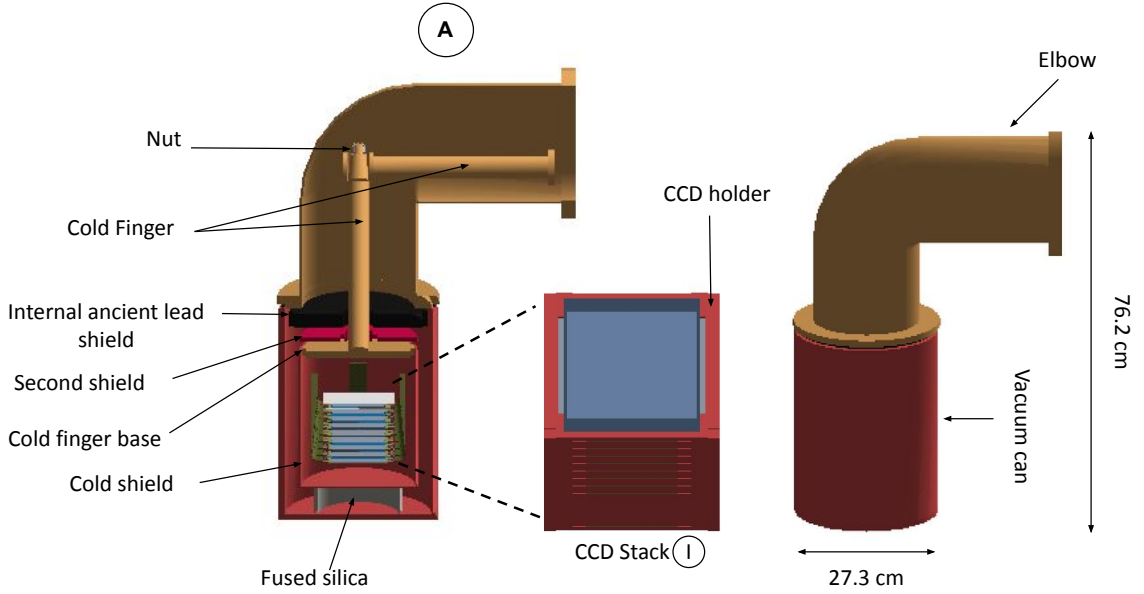
Figure 5.4 – Cryostat design A. The red components are made of EFC, the yellow ones of OFHC, and the black ones of lead. The nut is assumed to be made of copper. The ancient lead shield, the vertical finger base, and the second shield are 2.5 cm, 1.27 cm, and 6.35 mm thick, respectively. The CCD sensitive and not sensitive parts are represented in light and dark blue, respectively.

3 or 6 millions events are generated. This number varies component per component depending on the number of events observed in the CCDs and it is increased if necessary to accumulate enough statistics (e.g, for ^{210}Bi simulations). For the fused silica component, an activity of 1 ppt is assumed for ^{232}Th and ^{238}U (assuming secular equilibrium for the whole chains).

This section, devoted to the design A, focuses on the contribution to the background of the cold finger and the internal shield, whose thickness and material are optimized.

Cooling system: Cold Finger. As already mentioned, the cold finger ensures the thermal contact to cool down the CCD stack to the desired temperature. It is composed
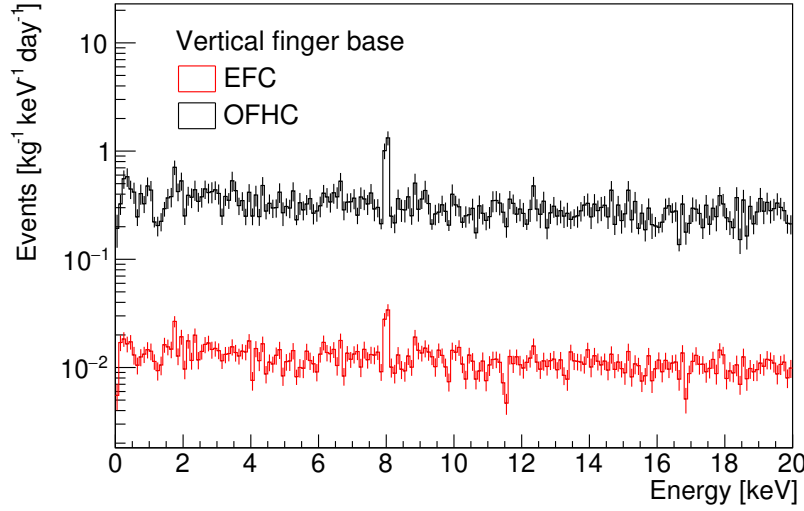
Figure 5.5 – Cluster energy spectra obtained for the vertical finger base made of OFHC or EFC. Considering the whole vertical finger, 300k events were simulated for each isotope, exception made for ^{210}Bi and ^{210}Pb. For ^{210}Bi and ^{210}Pb 3 million events were generated.

by three parts: an horizontal one (called horizontal finger), a vertical one (called vertical finger), and a base that is positioned above the CCD stack. The whole finger is initially considered made of OFHC. The horizontal contribution is negligible (0.001 d.r.u), while the vertical finger and base ones are 0.015 d.r.u and 0.35 d.r.u, respectively. In particular, considering the finger base, 30% of the rate is due to ^{210}Bi and 21% to cosmogenic isotopes. This result highlights the necessity to have the base made of a more radio-pure type of copper, i.e., EFC. By making it in EFC, the background rate is about 26 times lower (0.013 d.r.u, 71% of which is due to the contribution of the cosmogenic isotopes[4]). This motivated the change of the base material from OFHC to EFC, which is thus considered as the reference material for this component for all future designs. A comparison between the cluster energy spectra obtained for a vertical finger base made of OFHC or EFC is shown in Figure 5.5.

Internal shield. An internal shield, as also mentioned before, is needed to screen the CCD stack from the cryostat components made of not radio-pure materials, like the elbow or the cold finger. The shield is initially considered to be made of ancient lead, due to its high density and purity. Two thickness options are investigated: 25 and 50 mm. The

---

4. Note that for the OFHC and EFC components the assumed exposure time to cosmic rays is different, i.e., 3 months and 10 days, respectively.

corresponding lead shield spectra are shown in Figure 5.6.

(a)

(b)
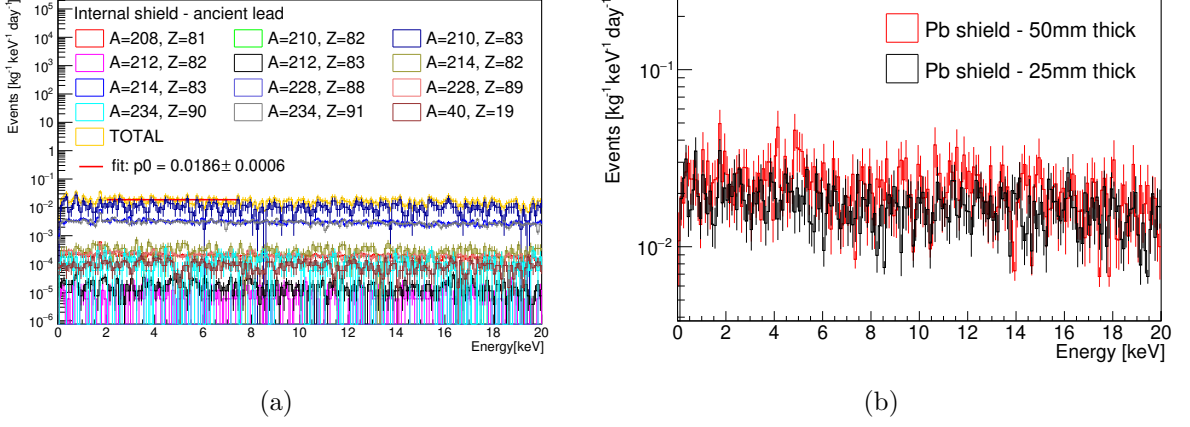
Figure 5.6 – (a): Cluster energy spectrum obtained for an internal shield made of ancient lead which is 25 mm thick. (b): Comparison between the spectra obtained for an ancient lead shield thickness of 25 mm or 50 mm. For each isotope, except for ^{210}Bi, 6 million events were simulated. For ^{210}Bi 300 million events were generated.

With a thickness of 25 mm the total background rate (considering all the design components) is about 0.195 d.r.u. The major contributors are the components closer to the CCD stack: the CCD holder (0.058 d.r.u), the vacuum can (0.040 d.r.u), and the cold shield (0.031 d.r.u). Apart from these components, those which have the higher impact on the total background budget are the internal shield (0.019 d.r.u), the vertical finger (0.015), and the elbow (0.014 d.r.u). The total background spectrum is shown in Figure 5.7 (a).

In an attempt to reduce the vertical finger and elbow contributions, the internal lead thickness is increased to 50 mm. Simulations are ran only for the shield itself and the components above it [5] (i.e., the vertical finger and the elbow), exception made for the horizontal finger and nut, being their contribution negligible. By changing the internal shield thickness from 25 mm to 50 mm, the lead shield contribution increases by 1.3 times (0.023 d.r.u), while the elbow and vertical finger background rates decrease. In particular, the elbow rate is reduced by about 2.3 times (reaching 0.06 d.r.u). A minimal variation in the total background budget (1.1 times lower, 0.190 d.r.u) is instead observed. This is expected since most of the components and in particular those that mostly contribute to

5. The contribution of the components below the internal shield does not change in case of an increased lead shield thickness. The background rate associated to these components is assumed to be the same in the case of a lead shield thickness of 50 or 25 mm.

Figure 5.7 – Contribution to the background of the different detector components for a cryostat design A with an internal shield made of ancient lead and which is 25 mm (a) or 50 mm (b) thick. The base of the vertical finger is considered to be in EFC and its contribution is included in the vertical finger one. The horizontal finger and the nut are not included in the plot in b, being their contribution negligible. The total background rates are 0.195 d.r.u (a) and 0.190 d.r.u (b).

the background are situated below the internal shield (and therefore their contribution is not affected by an increased lead shield thickness). The total background spectrum obtained by using 50 mm of thickness for the ancient lead shield is shown in Figure 5.7 (b), including all the detector components (above and below the internal shield).

Considering the non-negligible contribution to the background of the ancient lead disk, the possibility of making the internal shield in EFC is investigated. The study described before, carried out by varying the lead shield thickness, is repeated by changing the material to EFC. The difference with respect to the corresponding lead options is minimal, with a background improvement of a factor 1.1 in the best case (50 mm of thickness). These results are summarized in Figure 5.8. Although the total background rate is basically unchanged, the EFC shield has the advantage of a lower contribution to the total background budget. Its rate is about $5.1 \cdot 10^{-3}$ d.r.u ($8.4 \cdot 10^{-3}$ d.r.u) for a thickness of 25 (50) mm (see Figure 5.9). On the other hand, the EFC shield is less effective in screening background events than a lead shield with the same thickness. For example, the background rate of the elbow with the 25 mm thick EFC shield is about twice the one obtained with the lead shield of equal thickness. Figure 5.10 (a) shows a comparison between the cluster energy spectra obtained for the elbow with different internal shield
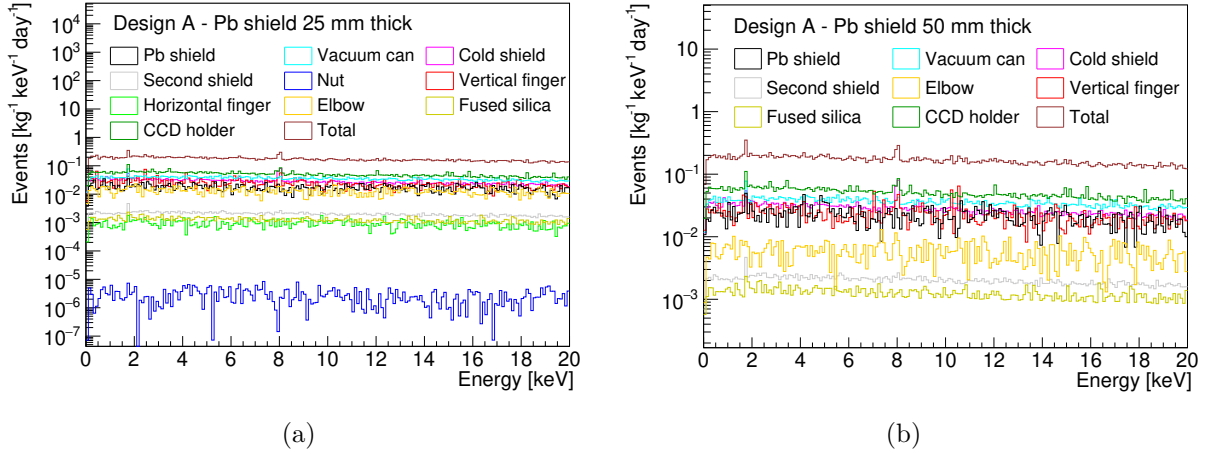
(a)
(b)
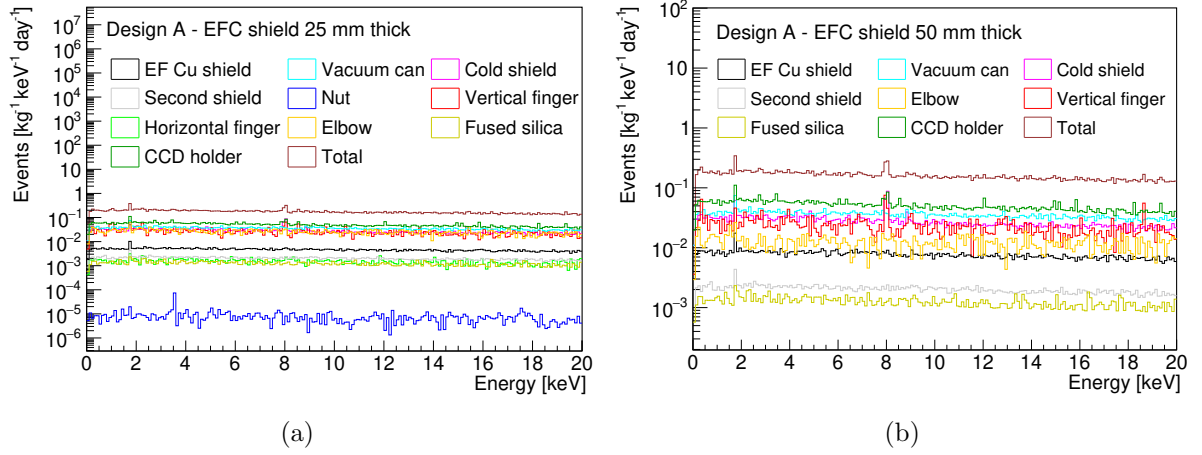
Figure 5.8 – Contribution to the background of the different detector components for a cryostat design A with an internal shield made of EFC and which is 25 mm (a) or 50 mm (b) thick. The total background rates are 0.195 d.r.u (a) and 0.180 d.r.u (b). The base of the vertical finger is considered to be in EFC and its contribution is included in the vertical finger one. The horizontal finger and the nut are not included in the plot in b, being their contribution negligible.

(a)
(b)
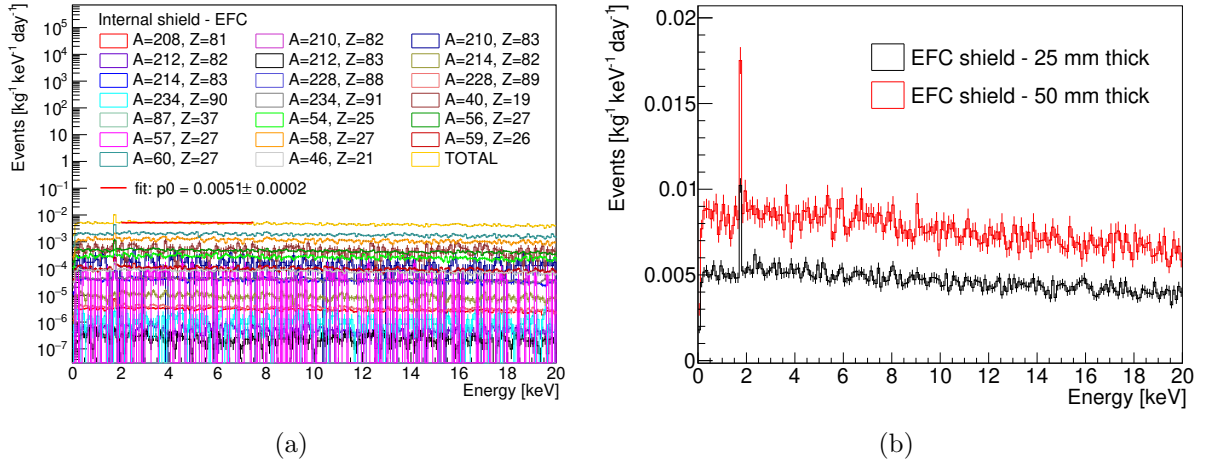
Figure 5.9 – (a): Cluster energy spectra obtained for an internal shield made of EFC which is 25 mm thick. (b): Comparison between the spectra obtained for an EFC shield which is 25 mm or 50 mm thick. For each isotope, except for ^{210}Bi, 6 millions events were simulated. For ^{210}Bi, $1.5 \cdot 10^8$ events were generated.

configurations. The case without any internal shield is also included. It is worth noting that compatible rates are reached for the elbow using 25 mm of lead and 50 mm of EFC.

(a)

(b)
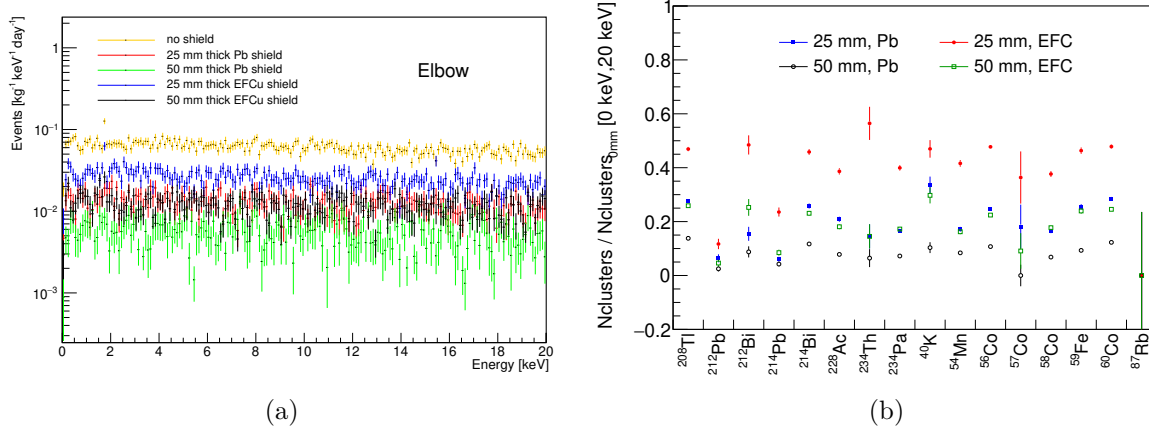
Figure 5.10 – (a): Elbow energy spectrum obtained considering different internal shield configurations: any internal shield, an internal shield made of ancient lead or EFC, 25 mm or 50 mm thick. (b): Ratio between the number of clusters obtained for simulations with and without an internal shield for each isotope. Only clusters with energy between 0 and 20 keV are considered. For each isotope 3 millions events are simulated. The errors on the y axis are calculated using the method suggested in [147]. ^{210}Pb,^{210}Bi, and ^{228}Ra ratios are not shown since no events are observed (in any configuration).

To better visualize the impact on the background of the different internal shield options outlined before, the total number of clusters observed for each isotope is normalized to the case without any shielding. The obtained results are shown in Figure 5.10 (b).

In view of the small gain in terms of background expected by employing an EFC shield instead of a lead one, its high cost and long production time, and the higher stopping power of lead, it was decided to use an internal shield made of archaeological lead. The different results obtained in this section are summarized in Table 5.3.

Design A - background estimation				
internal shield material	Pb		EFC	
internal shield thickness [mm]	25	50	25	50
total background rate [d.r.u]	0.195	0.190	0.195	0.180

Table 5.3 – Summary of the background rates associated to the different internal shield configurations in design A. The vertical finger base is assumed to be made of EFC.

Design B and C

Capitalizing on the simulation results obtained previously for the design A, a new design (B) is proposed (Figure 5.11, left). A 5 cm thick lead internal shield is considered
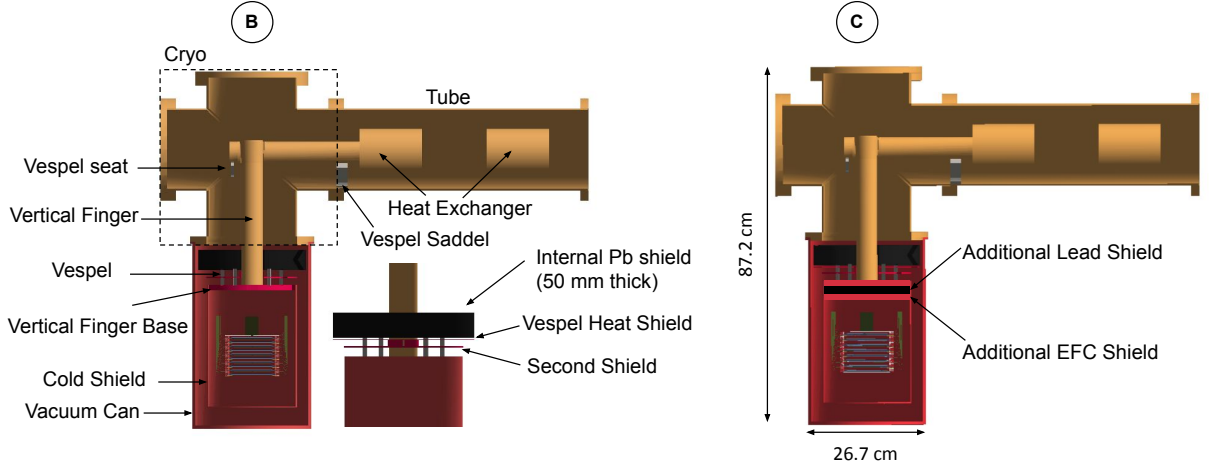
Figure 5.11 – Left: cryostat design B. The red components are made of EFC, the yellow ones in OFHC. The CCD stack I is used. Right: Cryostat design C. The dimensions are the same of the design B. With respect to the latter, two additional shields are introduced below the vertical finger base, one made of EFC (1 cm thick) and the other of lead (2 cm thick).

and a heat exchanger is introduced to optimize the cooling system performance. The total background rate for the new design B is about 0.173 d.r.u, its major contributors being the copper CCD holder (33% of the total rate, 0.06 d.r.u), the vacuum can (19.7%, 0.034 d.r.u), and the vertical cold finger (9.8%, 0.017 d.r.u). For the components made of Vespel [6], the following activities are used: 90.72 decays/kg/day for ^{238}U, 1.03 decays/kg/day for ^{232}Th, 936 decays/kg/day for ^{40}K, from the Majorana Demonstrator Radioassay Program [131].

In design C, shown in Figure 5.11 (right), two additional internal shields are introduced and the cooling system is further optimized. This section focuses on these modifications and discusses the associated background estimates.

---

6. Vespel is a high-performance polyimide-based thermoplastic material produced by DuPont™. It can withstands wide temperature ranges and it has excellent mechanical and insulation (electrical and thermal) properties.

133

Internal shields. In order to decrease the contribution of the cold vertical finger, additional shields are introduced below the vertical finger base (design C), as shown in Figure 5.11 (right). The two additional components are made of EFC and lead with a thickness of 1 cm and 2 cm, respectively. The EFC additional shield is positioned below the lead one in order to reduce the contribution of the latter. In this way, the rate of the vertical finger and its base decreases by about a factor 12 ($1.4 \cdot 10^{-3}$ d.r.u) and 15 ($6.7 \cdot 10^{-4}$d.r.u), respectively. Considering the whole design C, the total background rate slightly decreases (with respect to design B) to 0.169 d.r.u. The additional lead shield is one of the major contributors (15.4% of the total rate, 0.026 d.r.u), after the CCD holder and the vacuum can. Figure 5.12 reports the pie charts summarizing the component contributions to the background for the designs B and C.
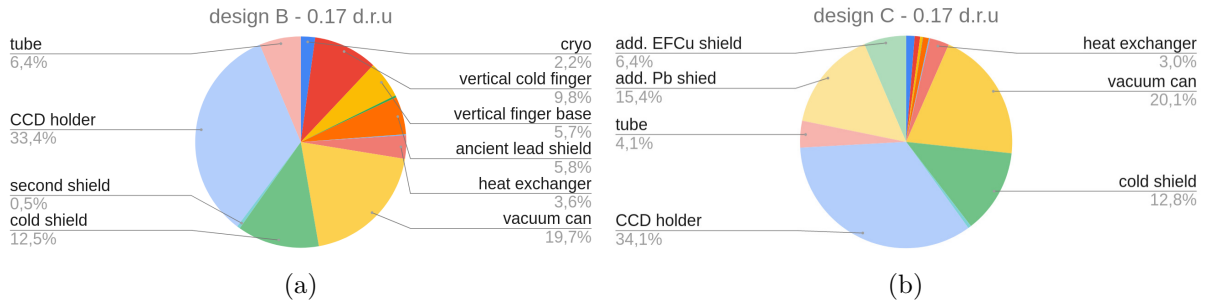
Figure 5.12 – (a): Contributions to the background of the different detector components for the cryostat design B. The total background rate is 0.173 d.r.u. (b): Contributions to the background of the different detector components for the cryostat design C. The total background rate is 0.169 d.r.u.

After the introduction of the additional lead shield, in order to minimize the amount of lead, the internal lead shield thickness (discussed for the design A) is re-optimized. A minimal increase in the total background (about 1.02 times higher) is observed by reducing to 2.5 cm the internal shield thickness (and therefore decreasing the total effective lead thickness which shields the CCD stack from 7 to 4.5 cm). In particular, the internal shield itself shows compatible background rates in both thickness cases ($1.5 \cdot 10^{-3}$ d.r.u.). In fact, considering a 50 mm thick shield, most of the events producing a cluster are actually originated from the lowest 25 mm of lead (those closest to the vertical finger base). For the following designs, an internal shield thickness of 25 mm is thus adopted.

Cooling system: Heat exchanger. An important change between the design A and the designs B and C concerns the cooling system and the introduction of the heat exchanger. In the design C context, the cooling system is further modified to ensure better performances. Figure 5.13 shows a comparison between the old (α) and new concept (β) of the cooling system in the design C. In the first case (α), the system consists of a
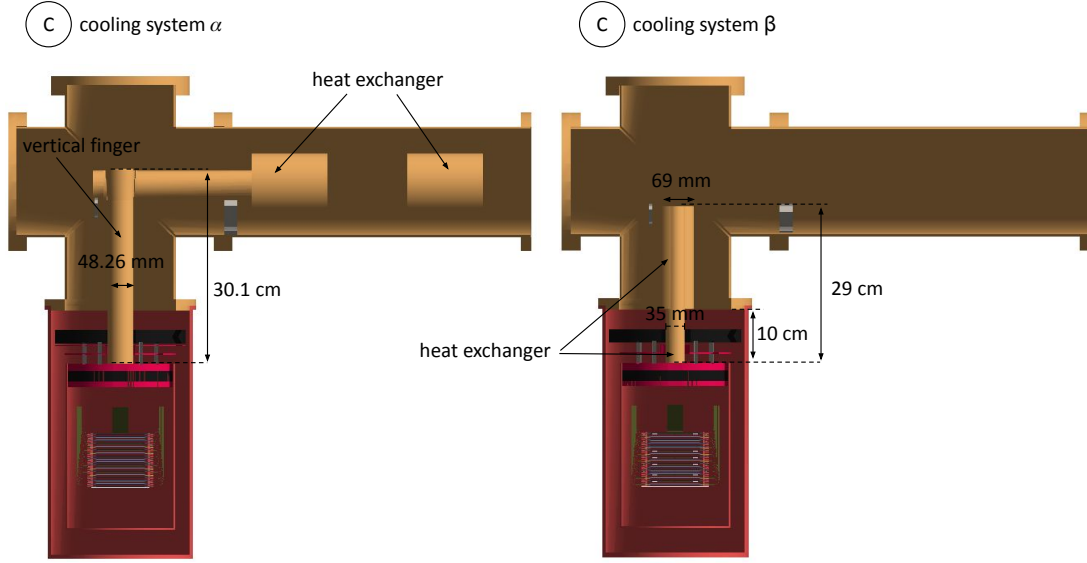
Figure 5.13 – Left: cryostat design C with the old cooling system, composed by a vertical finger and a heat exchanger, in horizontal position. Right: cryostat design C with the new cooling system composed by a new designed heat exchanger, vertically oriented. Note that the heat exchanger system includes also another component which is not shown, since it is expected to have a negligible contribution to the background, being positioned very far from the CCD stack.

horizontal heat exchanger and a vertical finger. In the latest version (β), the system is instead composed by only a new designed vertical heat exchanger. The impact on the background rate is evaluated. The rate associated to the new heat exchanger is about $1.4 \cdot 10^{-3}$ d.r.u, which is about 5 times lower than the one obtained for the old configuration ($1.7 \cdot 10^{-3}$ d.r.u from the vertical finger plus $5.4 \cdot 10^{-3}$ d.r.u from the horizontal heat exchanger). Although the new heat exchanger has a slightly higher mass (about 7 kg) than the vertical finger (about 6 kg), its background budget is lower. This is due to its shape. In fact, most of the events creating a cluster in the CCDs are generated in the region nearest to the vertical finger base, which in the new heat exchanger case is smaller

than in the system α case. Figure 5.14 shows the y-z positions of the generated events creating a cluster for the vertical finger and new heat exchanger simulations. The cooling system β ensures therefore a lower background rate with respect to the one obtained with the system α. For the following designs, the cooling system β is considered (with only minor modifications applied).

(a)   (b)
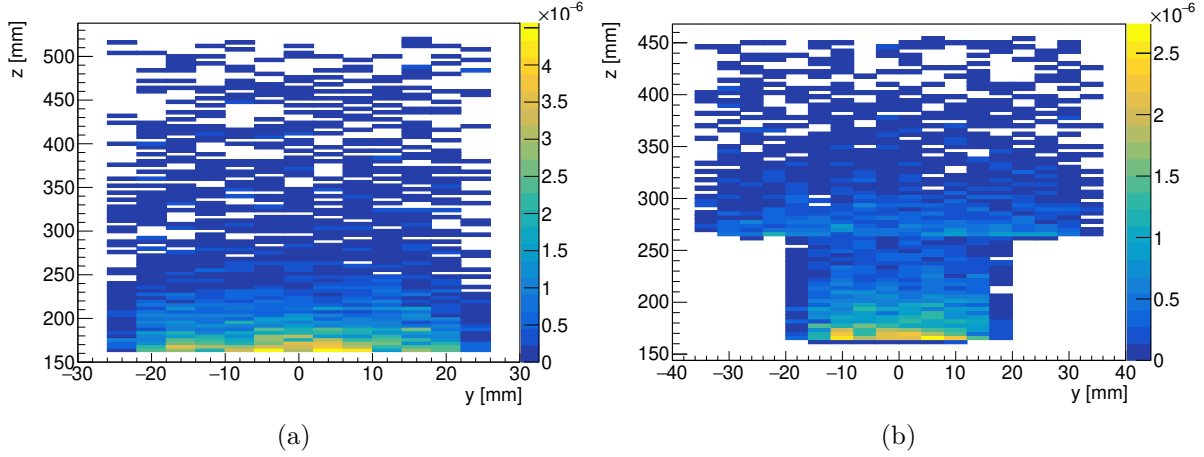
Figure 5.14 – Positions (y,z) of the generated events creating a cluster in the CCD, for the vertical finger (a) and the new heat exchanger (b). The color code indicates the number of clusters normalized to total number of simulated events.

The different results obtained in this section are summarized in Table 5.4.

Designs B and C - background estimation				
	design B	design C		
cooling system	α	α	α	β
internal shield thickness [mm]	50	50	25	25
total rate [d.r.u]	0.173	0.169	0.173	0.166

Table 5.4 – Background rate associated to the design B and the different configurations of design C.

Design E and F

For the design C, the CCD holder is found to be one of the major contributors to the background (0.06 d.r.u). In order to minimize this contribution, a new CCD stack configuration (III) is adopted. This caused also modifications in other detector parts, bringing to the development of a new design (E), shown in Figure 5.15.
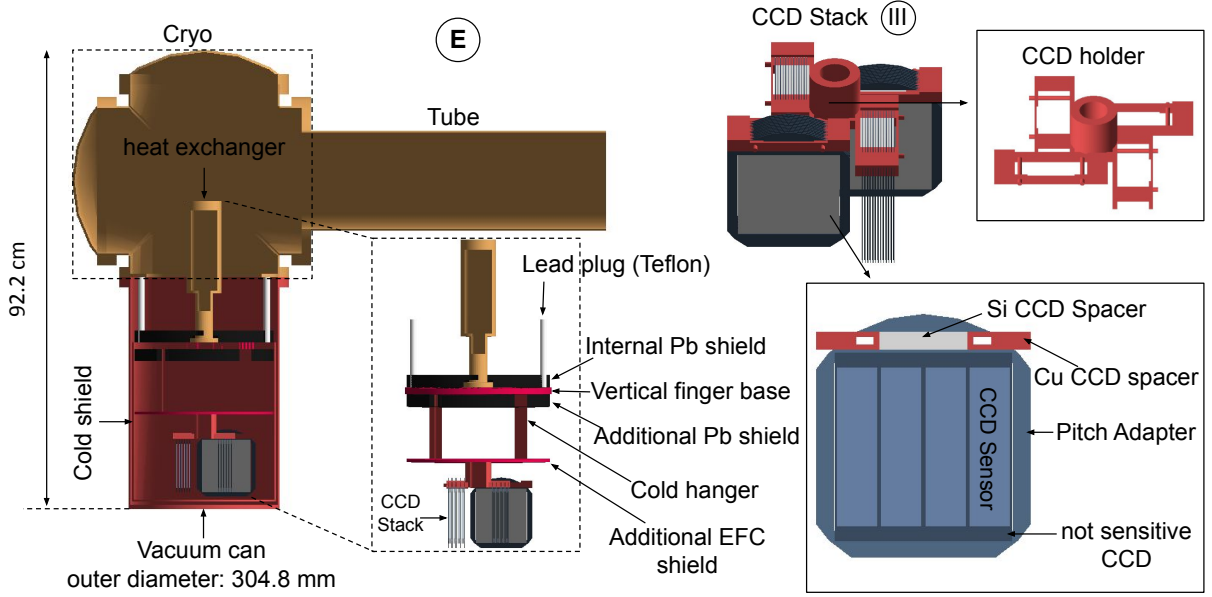
Figure 5.15 – Cryostat design E. The red components are made of EFC, the yellow ones in OFHC. The internal lead shield thickness is equal to 25 mm. With respect to design C, the additional lead shield thickness is increased to 2.5 cm and the additional EFC shield decreased to 6 mm.

In the new configuration, a set of 4 CCDs (1.5k pixels × 6k pixels) is glued on top of a silicon support, called pitch adapter. The pitch adapters are then held vertically by an EFC support (CCD holder) and are placed following a spiral arrangement. To ensure adequate distance between the pitch adapters, EFC and silicon spacers are used. In this way the amount of copper around the CCDs and the associated background rate is reduced. In fact, the contributions of the EFC CCD holder and spacers are $5.8 \cdot 10^{-3}$ d.r.u and $8.1 \cdot 10^{-3}$ d.r.u, respectively. Their sum is about 4.3 times lower than the CCD holder rate in the cryostat design C. Furthermore, this new CCD configuration also helps to decrease the rate of the components above the stack.

The cryostat design E has an associated background rate of 0.13 d.r.u. The major contributors are the cold shield (33.6%), the vacuum can (26.8%), and the additional lead shield (15.7% of the total rate), as shown in Figure 5.16.

The design is further optimized, obtaining a new version F. The space between the additional lead and EFC shields is reduced (by about 7.6 cm) to lower the cables contribu-

(a)   (b)

Figure 5.16 – Background rate for the cryostat design E and CCD stack design III. The total rate is 0.13 d.r.u. (a): Pie chart summarizing the contribution of the different components. (b): Total cluster energy spectrum. The red line is the result of the fit to a constant used to estimate the background rate between 2 and 7.5 keV. The CCD spacer refers only to the one made of EFC.
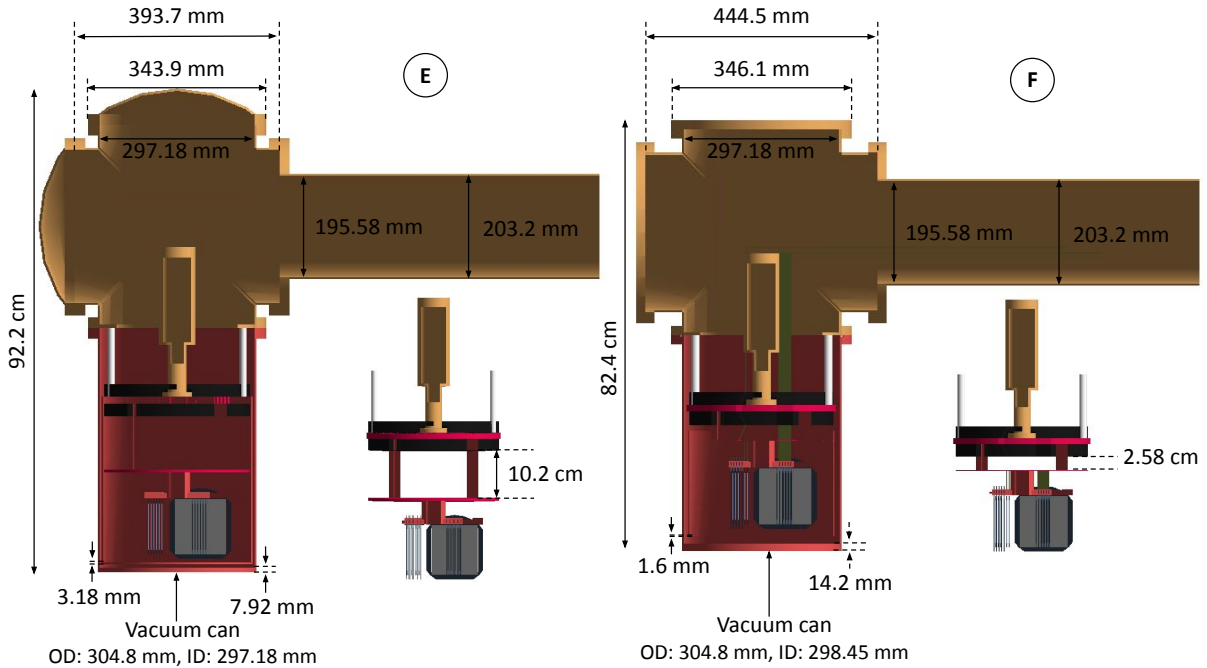
Figure 5.17 – Comparison between the cryostat designs E (left) and F (right). The outer (OD) and internal (ID) diameters are indicated. The red components are made of EFC, the yellow ones in OFHC.

tion, which is discussed in the Section 5.1.2. Furthermore, the thickness of the additional EFC shield is decreased to 3.18 mm to reduce the amount of EFC to be produced and the thickness of the vacuum can base is doubled (reaching 14 mm) to ensure adequate stiffness under vacuum. These modifications cause an increase of the background up to 0.15 d.r.u, which is balanced by the decrease of the background associated to the cables. Figure 5.17 shows a comparison between the designs E and F. The individual component
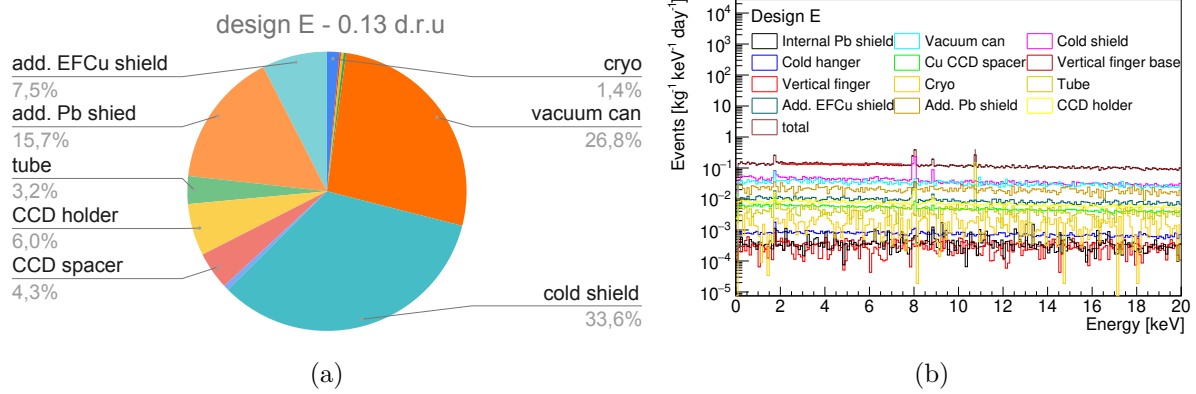

(a)

(b)
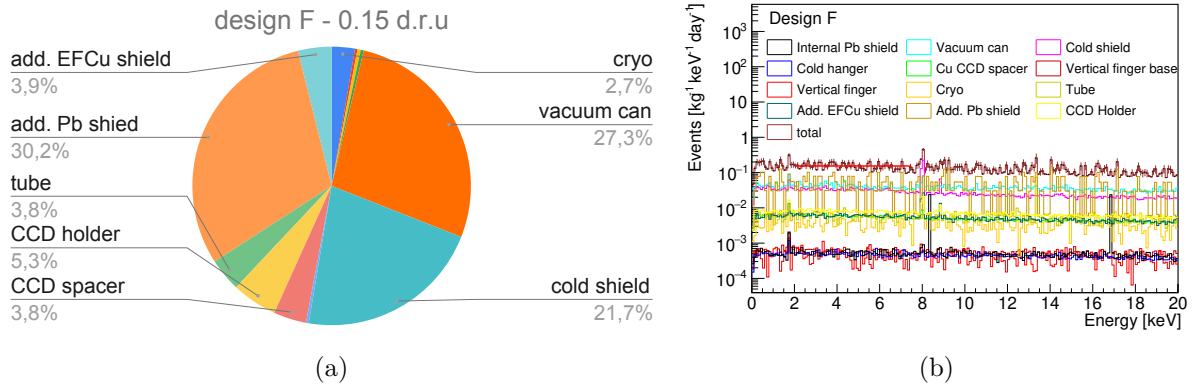
Figure 5.18 – Background rate for the cryostat design F and CCD stack design III. The total background rate is about 0.15 d.r.u. (a): Pie chart summarizing the contribution of the different components. (b): Total cluster energy spectrum. The red line is the result of the fit to a constant used to estimate the background rate between 2 and 7.5 keV.

contributions for the design F are shown in Figure 5.18, the major ones being the additional lead shield, the vacuum can, and the cold shield. For the additional lead shield, the isotopes with the highest rates are ^{210}Bi (85% of the volume rate) and ^{214}Bi (11% of the volume rate). For the vacuum can, instead, the major volume rate contributors are ^{57}Co (33%) and ^{60}Co (19%). The spectra associated to the vacuum can and the additional lead shield are shown in Figure 5.19.

In the following, the contribution to the background of the cosmogenic isotopes in the EFC components is discussed. The contributions of the additional shields, the vertical finger base and the vacuum can base are also treated in details. In particular, the impact of having the vacuum can and the vertical finger base made of OFHC is explored. The study carried out to optimize the additional EFC shield thickness is also reported.

Cosmogenic isotopes. As discussed in Section 3.3.3, the cosmogenic isotopes play an important role in the background budget. Although the components close to the CCDs
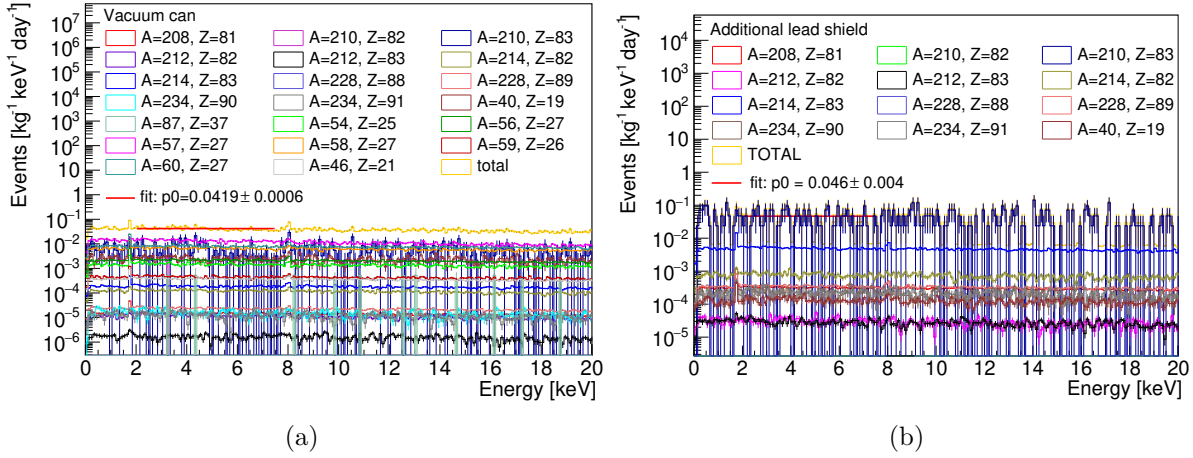
Figure 5.19 – Energy spectra for the vacuum (a) and the additional lead shield (b). For the vacuum can and the additional lead shield, 6 millions events were simulated for each isotope. Simulations were performed using the cryostat design F and CCD stack design III. The red line on the spectra is the result of the fit to a constant (p0) used to estimate the background rate between 2 and 7.5 keV. The major contributors for the vacuum can are ^{57}Co (33% of the rate), ^{60}Co (19%), and ^{58}Co (16%). The ones for the additional shield are ^{210}Bi (85%), ^{214}Bi (11%), and ^{214}Pb (1.7%).

are made of EFC, the exposure time to cosmic rays may increase significantly the expected background. Considering an exposure time of 10 days, a cooling time of 6 months, and a running time of the experiment of 1 year, the cosmogenic contribution from all the EFC components in the design F is of about 0.063 d.r.u (Figure 5.20, b). Keeping the other parameters fixed, the rate decreases by a factor 10 with an exposure time of 1 day, while it increases by a factor 2.5 without cooling time. The major contributors to the cosmogenic background are the vacuum can (52% of the total cosmogenic rate) and the cold shield (26%). The evolution of the vacuum copper can rate as a function of the exposure and cooling times is also shown in Figure 5.20 (a). For an exposure time of 10 days and a cooling time of 0 days, the vacuum can background rate is about 0.1 d.r.u, 3 times higher than the one obtained with a cooling time of 6 months. If the exposure time is increased to 15 days, in order to recover the same rate obtained with T_{exp}= 10 days and T_{cool}= 6 months, about 295 days of cooling time are needed. This study helped to set a reference limit on the exposure (cooling) time of the EFC components that is 10 days [7] (6 months).

---

7. A shorter exposure time would be very difficult to achieve, considering the time needed to ship the raw material (if produced in the USA) and manufacture the final components.

(a)   (b)
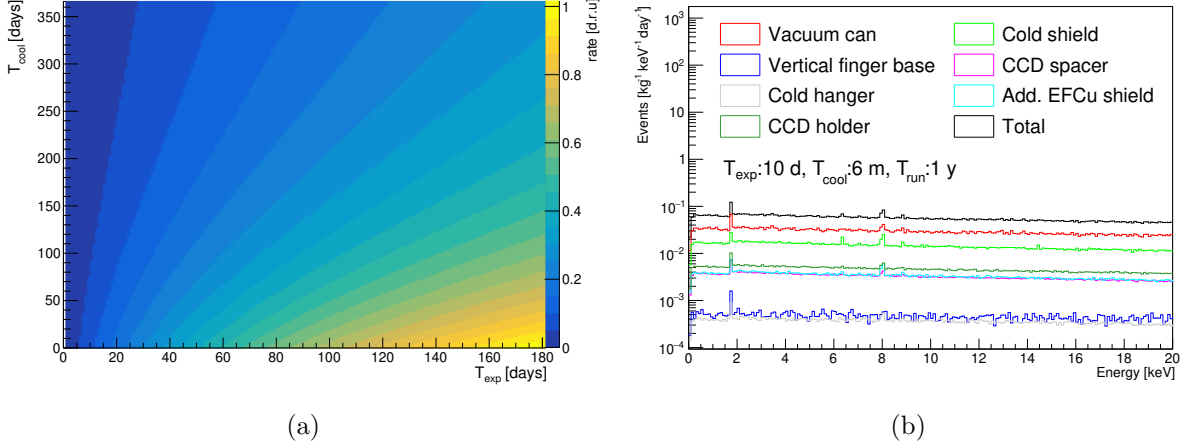
Figure 5.20 – (a): Evolution of the vacuum copper can cosmogenic rate as a function of the exposure and cooling time. The run time is 1 year. (b): contributions of the cosmogenic isotopes in the different EFC components, for an exposure time of 10 days, a cooling time of 6 months, and a running time of 1 year. The cryostat design F is considered in both plots.

Additional internal shields. Since the additional lead shield is one of the major contributors to the background, the effect of increasing the thickness of the underlying additional EFC shield is studied. By doubling the thickness of the EFC shield (2×3.18 mm), the sum of the contributions of the additional shields is 0.045 d.r.u, which is 1.16 times lower with respect to the standard configuration. By increasing the thickness to 10 mm and 15 mm the sum is in both cases 1.7 times lower. The two thickness options show the same rate due to the fact that the decreased additional lead shield rate is balanced by the increased EFC shield contribution dominated by the cosmogenic component. These results are summarized in Table 5.5.

Add. EFC shield thickness [mm]	Add. Pb shield rate [d.r.u]	Add. EFC shield rate [d.r.u]	total [d.r.u]
3.18	0.046	0.006	0.052
6.36	0.035	0.010	0.045
10	0.019	0.012	0.031
15	0.015	0.016	0.031

Table 5.5 – Additional shields background rate for different EFC shield thicknesses.

Vertical finger base. In order to reduce the amount of EFC needed (due to its high cost and long production time), the impact on the background of having the vertical finger base made of OFHC is investigated. The rate associated to the OFHC finger base is 0.0085 d.r.u, which is 0.008 d.r.u higher than the EFC case. This small difference is due to the presence of the additional lead and EFC shields (not present in designs A and B) that screen the base contribution.

Vacuum copper can base. As already mentioned before, the thickness of the vacuum can base is increased to 14 mm. However, producing such a thick EFC component is problematic. Therefore, the possibility of having the base of the vacuum can in OFHC is explored. The base background rate increases by 20 times, reaching 0.4 d.r.u. In order to screen its contribution it is necessary to add shields above it. Different shielding

shield thickness	OFHC vacuum can base rate [d.r.u]	EFC base shield rate [d.r.u]	Pb base shield rate [d.r.u]	total rate [d.r.u]
Pb: 0 mm, EFC: 0 mm	0.4	-	-	0.4
Pb: 0 mm, EFC: 2 cm	0.097	n.c.	-	>0.097
Pb: 7.5 mm, EFC: 2 cm	0.037	0.029	0.021	0.087
Pb: 7.5 mm, EFC: 1 cm	0.046	0.018	0.041	0.11
Pb: 7.5 mm, EFC: 5 mm	0.055	0.012	0.06	0.13

Table 5.6 – Background rate associated to the OFHC vacuum can base and its shields for different shielding configurations. "n.c." stands for not calculated. The "n.c." contribution is not evaluated given the already too high OFHC base rate.

configurations are studied, using only an EFC shield or an EFC shield on top of a lead one. Different thicknesses are selected for the shields. In order to host them the vacuum can height is increased by 15 mm (in case of a total base shielding thickness higher than 13 mm). Note that, unlike the case of the vacuum can base, the EFC shield does not have to be made of a single piece but it can be composed by many thin layers. Therefore, its thickness does not represent a limitation for its production. The results obtained for the different shielding setups are summarized in Table 5.6. The lower background rate is ensured by employing a 7.5 mm thick lead shield and a 20 mm thick EFC shield. In this

case, the vacuum can base contribution decreases to 0.037 d.r.u. It is worth noting that an EFC shield alone with a thickness of 20 mm would not be enough to properly shield the base contribution. Considering the whole cryostat design, the lowest background shielding configuration leads to a total rate of 0.22 d.r.u, 0.066 d.r.u higher than the rate for the standard configuration F.

The results presented in this section for the designs E and F are summarized in Table 5.7.

Design E and F - background rate [d.r.u]					
design E	design F				
	standard	OFHC v. f. b.	a. EFC s. - tx2	OFHC v. c. b.	
				no shields:	shields[†] :
0.13	0.15	standard + 0.008	standard - 0.007	standard + 0.39	standard + 0.066

Table 5.7 – Background rate associated to the design E and the different configurations of the design F. "OFHC v. f. b.": OFHC vertical finger base. "a. EFC s. - tx2": additional EFC shield with a thickness that is 2 times the one in the standard case (2×3.18 mm). "OFHC v. c. b.": OFHC vacuum can base. ([†]): the thicknesses of the lead and EFC can base shields are 7.5 mm and 2 cm, respectively.

5.1.2 Cable simulations

Due to their proximity to the CCDs, the choice of the cables is crucial for the background control. Three different types of cables are considered: 5-layers kapton cables (used also in DAMIC), 2-layers kapton cables, and Axon cables. The kapton cables are characterized by layers of kapton and copper. The number of layers in the cable type refers to the number of copper layers. The fraction of mass of copper in the 5-layers (2-layers) kapton cables is about 70% (60%). The Axon cables instead were designed specifically for DAMIC-M by a french company called Axon. Each of them consists in a 17-ways connector and 17 pico-coaxial cables. The activities used to evaluate the cable background rates are reported in Table 5.8. The 2-layers kapton cables show lower ^{232}Th and ^{238}U activities with respect to the 5-layers ones. Note that, since the ^{40}K and ^{87}Rb activities were not provided by Axon, these isotopes are not simulated in the Axon cable case.

For each CCD stack design, different types of cables are simulated. The associated results are reported in the following sections.

Isotope	Kapton (5-layers) [decays/day/kg]	Kapton (2-layers) [decays/day/kg]	Axon connector [decays/day]	Pico-coaxial [decays/day/m]
^{210}Pb	420†	1182†	0.05 †	0.008†
^{232}Th	280 ± 40	42.5	0.18*	0.02*
^{226}Ra	420 ± 490	1182†	0.05†	0.008†
^{238}U	5000 ± 490	1182	0.05*	0.008*
^{40}K	2480 ± 170	2480†		
^{87}Rb	86.4†	86.4†		

Table 5.8 – Cable activities per isotope and material used for simulations. The kapton cables (5-layers) were measured by the DAMIC collaboration [78]. The Axon and kapton cables (2-layers) activities were provided by the material suppliers. Note that the activities reported for the Axon connectors and pico-coaxial cables refer to only 1 component (1 connector or 1 pico-coaxial cable). (†): in absence of measurements, the ^{87}Rb activity was assumed to be 1 mBq/kg, the activity of ^{226}Ra was assumed equal to that of ^{238}U, the one of ^{210}Pb equal to that of ^{226}Ra and the one of ^{40}K for the 2-layers kapton cables equal to that of the 5-layers kapton cables. (*): measurement with unknown precision.

CCD stack design I

The possibility to use the 5-layers kapton cables and the Axon ones was explored for the cryostat design C (with a 25 mm thick internal lead shield) and the CCD stack design I (see Section 5.1.1), as shown in Figure 5.21. Each CCD features 2 kapton cables or 6 Axon cables (6 Axon connectors and 102 pico-coaxial cables). The cables can be divided in two parts, the one in contact with the CCD ("on CCD") and the outgoing one, which run across the cryostat away from the CCD stack. In the Axon case, the connector represents the "on CCD" part, while the pico-coaxial cables the outgoing part.

The activities of the cosmogenic isotopes are evaluated considering only the percentage of copper mass in the cables and assuming an exposure time of 3 months, a cooling time of 6 months, and a running time of 1 year.

For the "on CCD" and outgoing kapton cable parts a background rate of 1.3 and 1.8 d.r.u is obtained, respectively. In both cases, the cosmogenic isotopes contribution is negligible, being only the 0.6% of the rates. The background spectra obtained for the 5-layers kapton cables are shown in Figure 5.22.
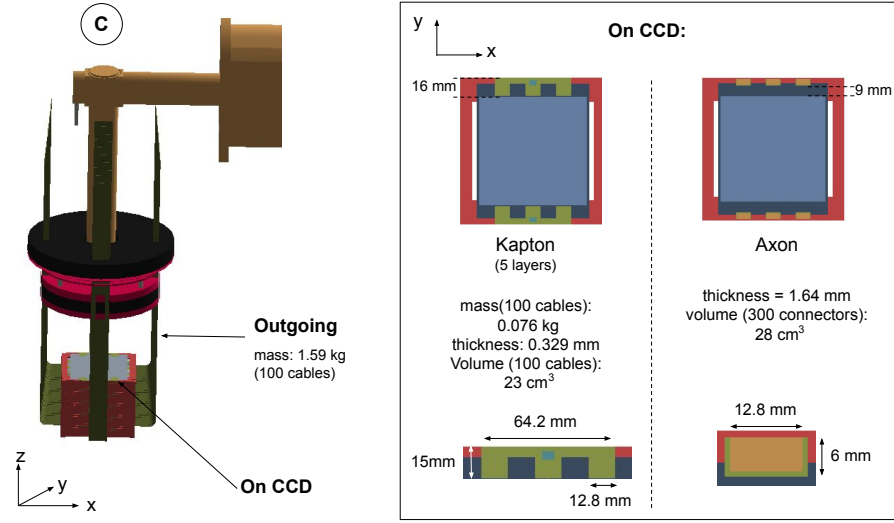
Figure 5.21 – Simulated geometry for the kapton (5-layers) and axon cables. Each CCD features 2 (6) kapton cables (Axon connectors). Simulations were performed using the cryostat design C and CCD stack design I. The CCD sensitive part and not sensitive part are represented in light and dark blue respectively. The top dead layer is not shown. The outgoing kapton cables are 0.5 m long, 30 mm wide, and 0.329 mm thick.
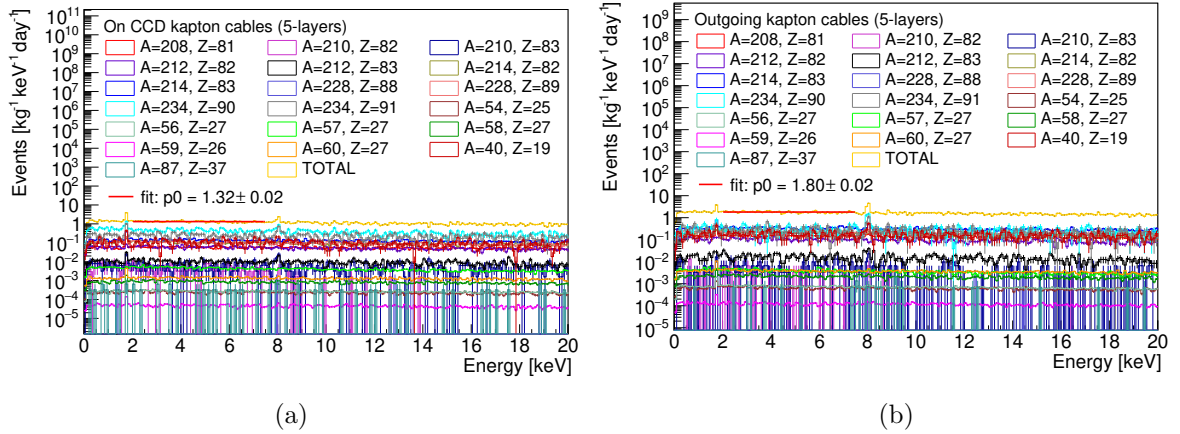
Figure 5.22 – Energy spectra for the "on CCD" (a) and the outgoing (b) kapton cables (5-layers). For the "on CCD" (outgoing) cables, 0.3 (3) millions events were simulated for each isotope. Simulations were performed using the cryostat design C and CCD stack design I. The red line on the spectra is the result of the fit to a constant (p0) used to estimate the background rate between 2 and 7.5 keV.

Most of the events that produce a cluster in a CCD come from the portion of the out-going cables below the additional EFC shield. In particular, 95% of the background rate is due to events generated below the shield, as shown in Figure 5.23. Therefore, reducing the space between the CCD stack and the additional copper shield helps decreasing the outgoing cable contribution to the background.
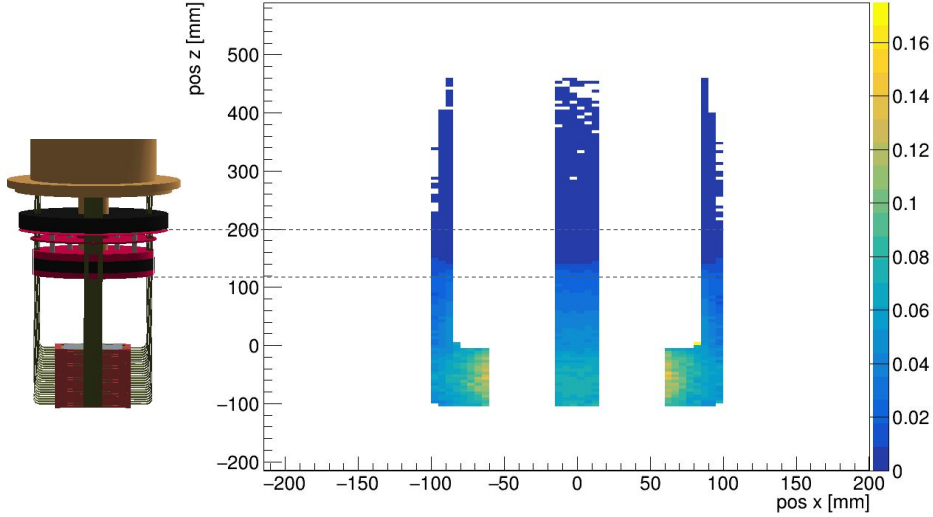
Figure 5.23 – Spatial distribution of the events generating a cluster, for the outgoing kapton cable (5-layers) simulations (cryostat design C, CCD stack I). The number of the events per bin (indicated by the color code) is normalized to the corresponding bin value of the generated events spatial distribution.

Considering the simulations performed for the "on CCD" part of the kapton cables, the spatial distribution of clusters in the CCDs is shown in Figure 5.24. All the clusters in the whole energy range are considered. The distribution is clearly not uniform and the contribution of the "cable fingers" are visible, both on the y- and x-axis. This is due to the fact that, in the case of the CCD stack I, each CCD is rotated by 90 degrees with respect to the previous one. A detailed study of this cluster spatial distribution is reported in the Appendix (Section D), where the possibility of applying a fiducial cut in the x and y directions is also discussed.

For the Axon proposed solution, since the ensemble of the 51 pico-coaxial cables would have roughly the same size of the outgoing kapton cables, their contribution is estimated by re-scaling the results of the kapton cable simulations using the Axon cable activities and mass. This leads to a background rate of 0.083 d.r.u for the pico-coaxial cables.
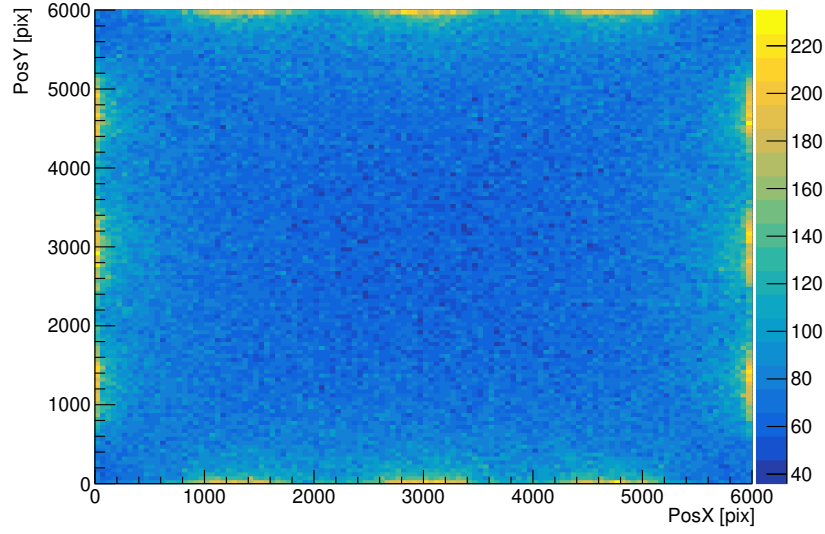
Figure 5.24 – Spatial distribution of clusters detected in the CCDs for the ("on CCD") 5-layers kapton cable simulations (CCD stack I). The color code indicates the number of entries per bin. The x (y) coordinate of a cluster is calculated as the energy-weighted average of the x (y) positions of the pixels inside the cluster. The global reference frame is considered.

For the connectors, a dedicated simulation is performed, using the proper geometry and materials. A background rate of 0.5 d.r.u is obtained. Thus, the Axon solution contributes to the background budget with a total of 0.58 d.r.u, which compares with the 2.8 d.r.u of the 5-layers kapton cables[8]. Therefore, the Axon option ensures the lowest background rate. The spectra obtained for the connectors and the pico-coaxial cables are shown in Figure 5.25.

The position of the cables on the CCD influences the background budget. The configuration of the "on CCD" parts of the cables is changed in order to study the impact on the background rate. The applied modifications are summarized in Figure 5.26.

Pushing the kapton cables 2 cm away from the CCD with respect to their original simulated position (see Figure 5.26, left) reduces by 5 times their "on CCD" contribution, as shown in Figure 5.27 (a). Figure 5.27 (b) shows the spatial distribution of clusters with the kapton cables in this new position. The excess of events on the borders is less visible than for the standard case (see Figure 5.24). Therefore, a fiducial cut can be avoided,

---

8. For a fair comparison, in the case of the kapton cables, the contributions of ^{40}K and ^{87}Rb ($\sim$0.1 and $\sim$0.2 for the "on CCD" and outgoing parts, respectively) should be removed since they are not included in the Axon cable simulations.

(a)   (b)
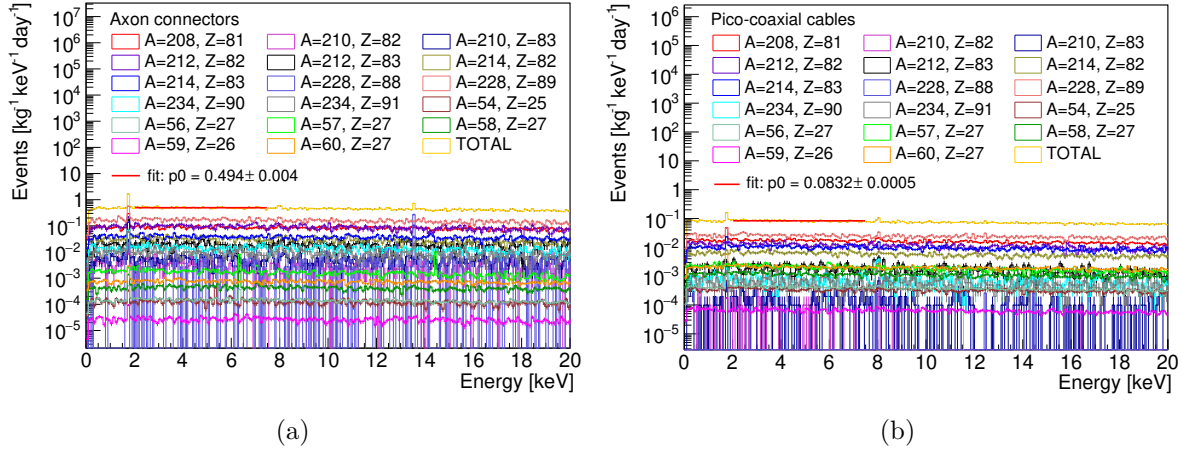
Figure 5.25 – Energy spectra for the Axon connectors (a) and the pico-coaxial cables (b). For the connectors (pico-coaxial cables) 0.3 (3) millions events were simulated for each isotope. The pico-coaxial cable spectrum is obtained from the kapton cable simulations by re-scaling for the proper activities and mass. Simulations were performed using the cryostat design C and CCD stack design I. The red line on the spectra is the result of the fit to a constant (p0) used to estimate the background rate between 2 and 7.5 keV.
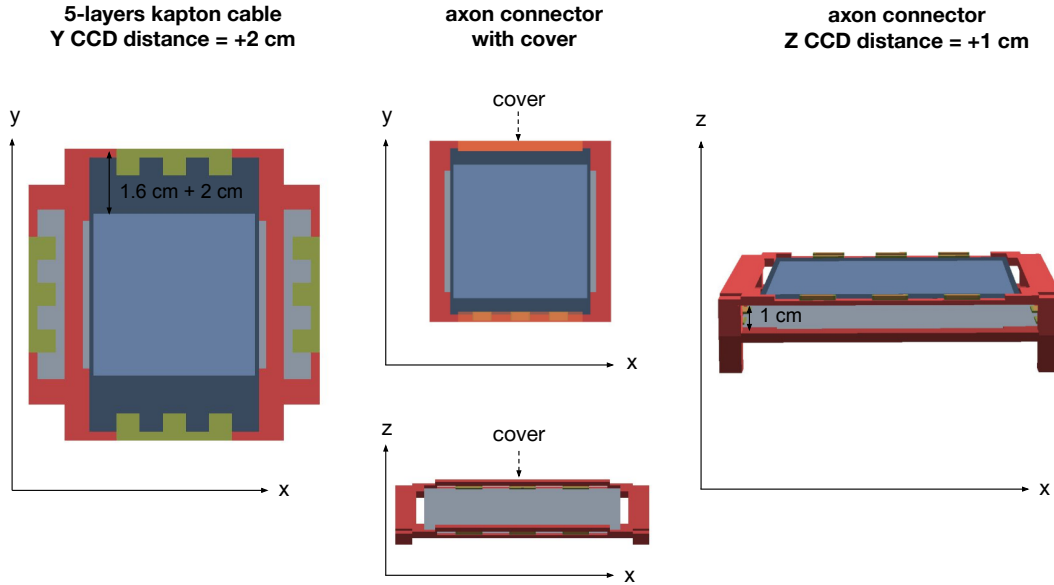
Figure 5.26 – Investigated modified geometries for the kapton (5-layers) and Axon cables. The CCD sensitive part and not sensitive part are represented in light and dark blue respectively.

(a) (b)
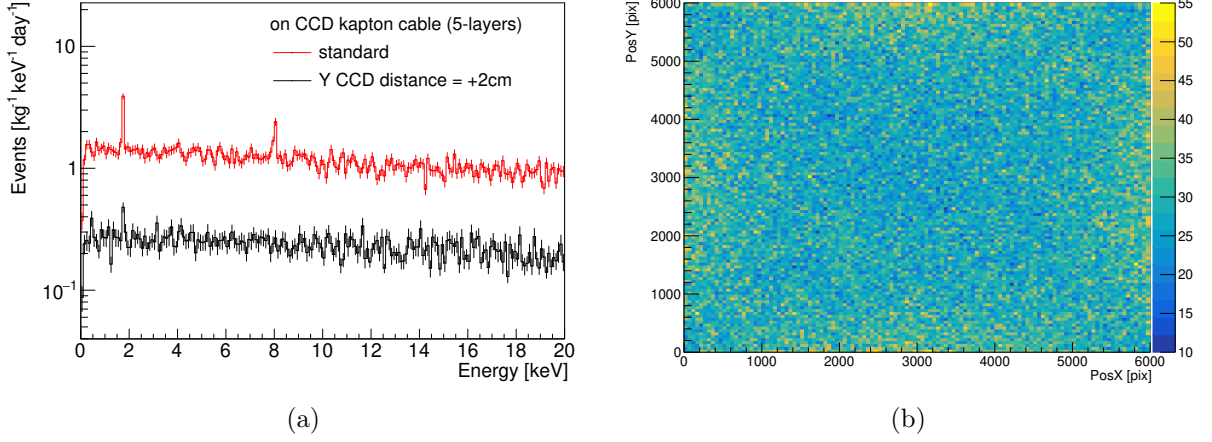
Figure 5.27 – (a): Kapton cable ("on CCD") energy spectra for different distances from the CCDs: the standard position (red) and 2 cm away from it (black). The CCD stack I is considered. (b): Spatial distribution of clusters in the CCDs for the 5-layers kapton cable simulations (CCD stack I), with cables 2 cm away from their standard position. The color code indicates the number of entries per bin. The x (y) coordinate of a cluster is calculated as the energy-weighted average of the x (y) positions of the pixels belonging to the cluster.

with a gain in exposure.

Increasing the distance on the z-axis between the CCDs (see Figure 5.26, right) also helps to reduce the cable contribution. In particular, increasing by 5 mm (1 cm) the separation on the z-axis between consecutive CCDs (set to 3.3 mm for the Axon case and to 2 mm for the kapton cable case), the axon connector contribution decreases by about 1.2 (1.6) times.

In order to screen the emissions of the isotopes inside the Axon connectors, a layer of copper (2 mm thick) is added on top of the them (see Figure 5.26, center). This further increases the CCD separation by 2 mm. In this case the connector rate decreases by about 1.2 times. This small variation in the rate is due to the range of the emissions of the isotopes in the "on CCD" parts. This can be verified by looking at the distribution of the distance d, expressed in number of CCDs, between a cluster and the generated event:

$$d = |\text{CCDID}_{\text{cluster}} - \text{CCDID}_{\text{genevt}}|, \tag{5.3}$$

where the $\text{CCDID}_{\text{genevt}}$ is evaluated considering the ID of the CCD[9] to which the cable or

---

9. The IDs of the CCDs are consecutive integer numbers which increase for decreasing z positions.

(a) (b)
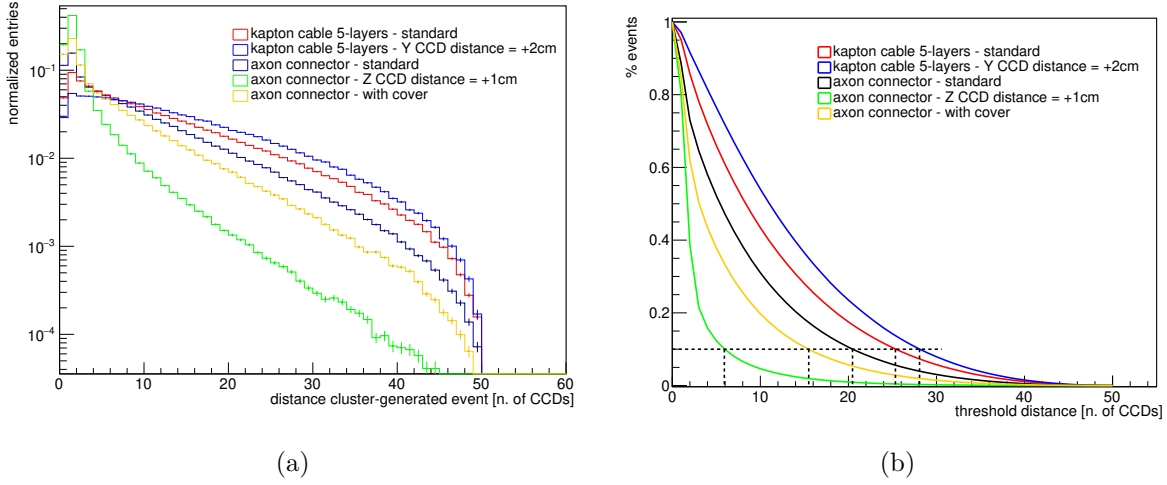
Figure 5.28 – (a): Distribution of the distance d (in terms of number of CCDs) between a cluster and the corresponding generated event (see text). The peak at $d{=}1$ is due to the higher probability to detect a cluster in the CCD right above and below the one of generation. (b): Fraction of events obtained by integrating the distributions in (a) for d greater than a given threshold and then normalizing for the integral in the whole d range.

the connector (where a given event is simulated) is attached. The d distributions for the different investigated cable configurations are shown in Figure 5.28 (a). Figure 5.28 (b) gives the integrated and normalized distributions against a threshold distance. The dashed lines indicate the distance $d_{0.1}$ corresponding to a percentage of events equal to 0.1. For the "on CCD" kapton cable and axon connector simulations in the standard configuration, $d_{0.1}$ is $\sim$25 CCDs and 20 CCDs, respectively. This means that, in 90% of the cases, a generated event is able to produce a cluster up to a distance equal to $d_{0.1}$. The difference between the kapton cable and axon connector cases can be explained as a geometry effect because of the different dimensions and positions of the two components. Considering an axon connector with a separation between CCDs increased by 1 cm, $d_{0.1}$ is reduced to 6. In the axon connector case with a copper cover, $d_{0.1}\sim$15. Instead, for the kapton cable simulations with increased Y distance (+2 cm) from the CCD, $d_{0.1}$ is $\sim$28. Therefore, if the separation (on the z-axis) between CCDs is increased, the d distribution tends to be more peaked at low d values, while if the Y distance between the CCD and the cables is increased, the distribution is spread over greater d values. Considering only the clusters with energy less than 20 keV, the d distributions shows the same behaviour and about the same results are obtained for $d_{0.1}$.

CCD stack design II

In order to reduce the cable contribution (as well as the CCD holder one, as discussed in Section 5.1.1), a new CCD stack design is proposed, i.e., the CCD stack II. The simulated geometry is shown in Figure 5.29. Cables are simulated only up to the additional EFC shield. In fact, this is the cable part that mostly contributes to the background, as observed for the CCD stack I.
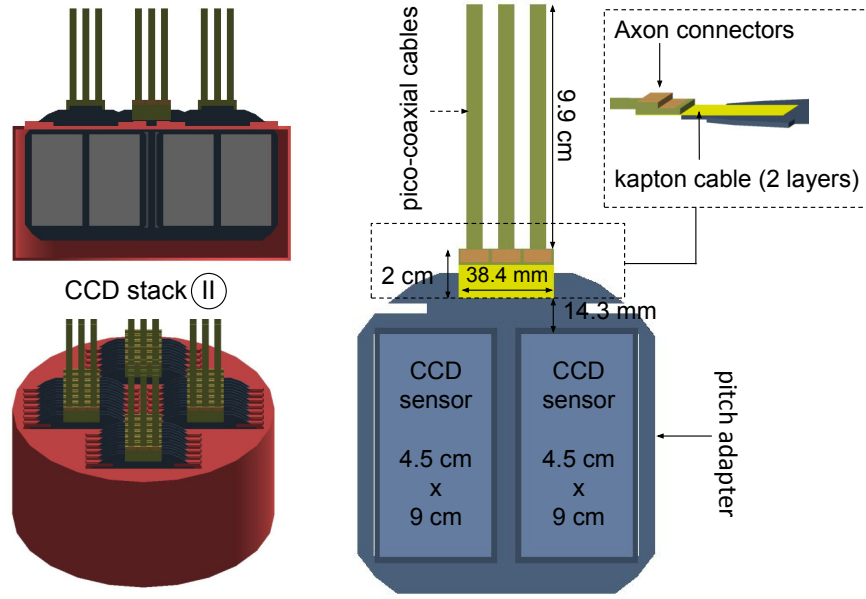
Figure 5.29 – Simulated design using a 2-layers kapton cable, 3 Axon connectors, and 51 pico-coaxial cables. The 2-layers kapton cable is 0.189 mm thick. Each pico-coaxial cable is 0.4 mm thick and wide. 17 pico-coaxial cables are attached to each Axon connector. The CCD sensitive part and not sensitive part are represented in light and dark blue, respectively. The bottom dead layer is shown in gray in the top left image. The simulations are performed using the cryostat design D and CCD stack design II.

In the CCD stack II, the CCDs are supported by silicon pitch adapters that are held vertically thanks to specific slots on top of a copper cylinder (which plays the role of the cold shield described in Section 5.1.1). With this new design, the cable is positioned only on one side of the CCD and not on both sides as for the CCD stack I. Given the difficulties faced in interfacing the Axon connectors to the pitch adapters and the prior experience of the DAMIC-M collaboration with kapton cables, a hybrid solution was proposed. This consists in a cable composed by a short 2-layers kapton cable to which 3 Axon connectors and 51 pico-coxial cables are attached. The pico-coaxial cables are

simulated using the proper material and dimensions. The ^{40}K and ^{87}Rb contributions are included in the kapton cable budgets. The activities of the cosmogenic isotopes are evaluated by considering only the percentage of copper mass in the components and assuming an exposure time of 3 months, a cooling time of 6 months, and a running time of 1 year. This cable configuration has an associated total background rate (the sum of the kapton and Axon cables) equal to 0.24 d.r.u, with 41% due to the kapton cables, 54% due to the Axon connectors, and 5% due to the pico-coaxial cables. The corresponding energy spectra are shown in Figure 5.30.

(a)

(b)

(c)
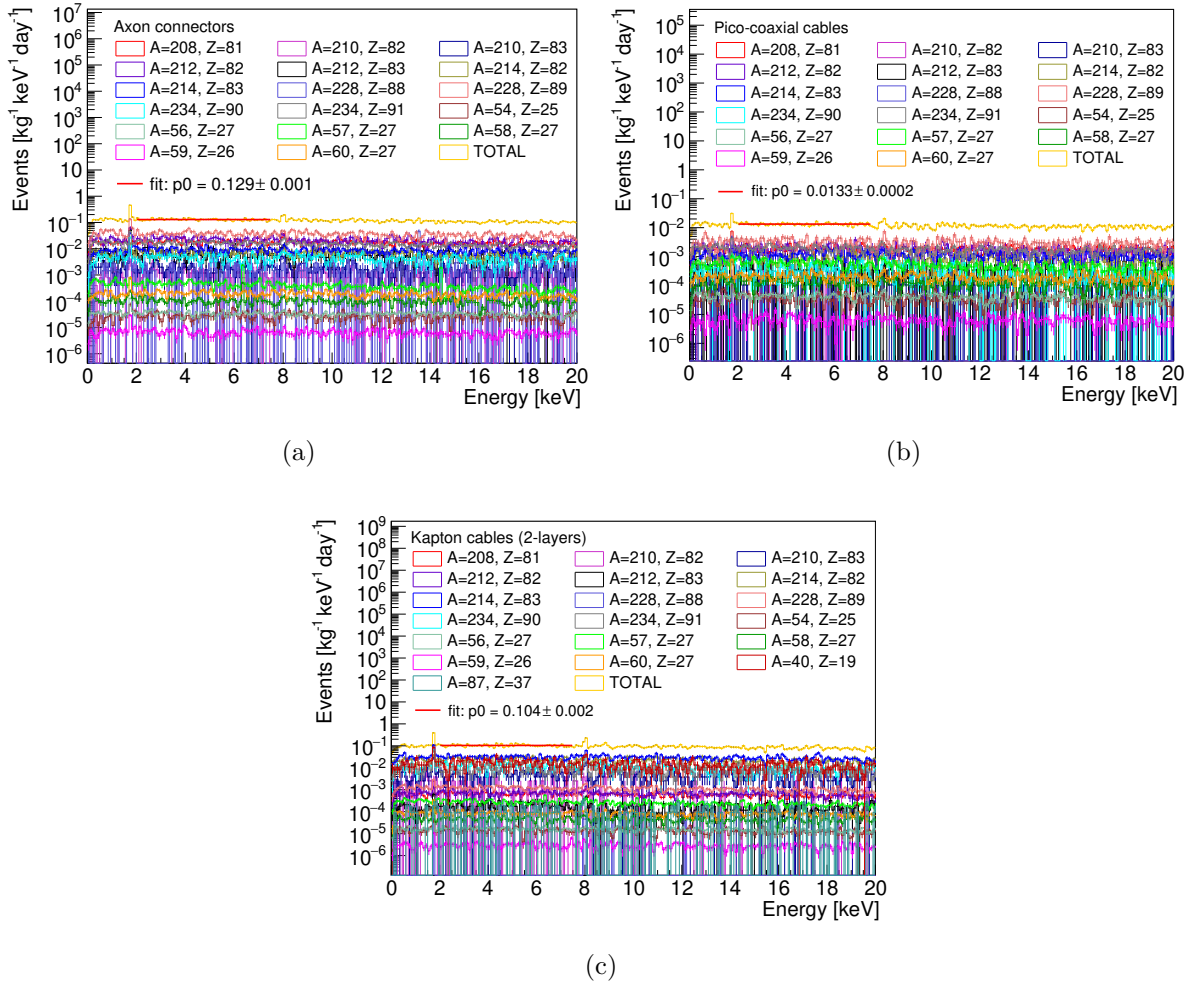
Figure 5.30 – Energy spectra associated with the cable configuration (axon connectors, pico-coaxial cables, and kapton cables) shown in Figure 5.29 (CCD stack design II). For each isotope, 300k events were simulated. The red line on the spectra is the result of the fit to a constant (p0) used to estimate the background rate between 2 and 7.5 keV.

To study the corresponding impact on the background, the length of the kapton cables and the pico-coaxial cables is changed, by maintaining the total length of the cable system (pico-coaxial and kapton cables) constant to 11.9 cm. By increasing the kapton cable length to 8 cm, and so decreasing to 3.9 cm the one of the pico-coaxial cables, the rate rises to 0.36 d.r.u, 83% coming from the kapton cable. The remaining 16% and 1% of the rate are due to the connectors and the pico-coaxial cables, respectively. Excluding the kapton cables from the design and shifting the Axon connector closer to the CCD by 4 mm leads to a total background of about 0.15 d.r.u, 93% of which is due to the connectors. A cable system made only of Axon cables ensures a lower background with respect to a system with an additional kapton cable. However, compatible background budgets can be achieved assuming an ^{238}U contamination 10 times lower for the 2-layers kapton cable. This activity is expected to be feasible by the producer and dedicated assays will confirm this hypothesis. Under this assumption, the kapton cable rate decreases to 0.03 d.r.u (0.08 d.r.u) for a length equal to 2 cm (8 cm). It is worth noting that the ^{40}K activity of the 2-layers kapton cable is set equal to the one for the 5-layers type, in absence of any other measurement. The ^{40}K is one of the major contributors to the background for the 2-layers kapton cable (about 17% of the background rate, assuming the standard ^{238}U contamination). Due to difficulties and uncertainties in the interface between the Axon connectors and the pitch adapters or the kapton cables, it was preferred to employ only a 2-layers kapton cable.

CCD stack design III

In order to optimize the space occupied by the CCD stack II, a more compact design is adopted (CCD stack III). Figure 5.31 shows the new CCD stack inside the cryostat (design E). The 2-layers kapton cables are also visible. A similar cable configuration is used for the design F.

The contribution to the background of the 2-layers kapton cables is estimated for the designs E and F. The cosmogenic isotopes are not taken into account since their contribution is negligible, being about the 0.4% of the kapton cable rate shown in Figure 5.30. This percentage grows to 1.5% if a 10 times lower ^{238}U contamination is considered.

For the cryostat design E, the cables (outgoing and "on CCD") have a background contribution equal to 0.18 d.r.u, 44% of which due to the outgoing component. The "on CCD" contribution (0.1 d.r.u) is equivalent to the one obtained for the 2-layers kapton cable shown in Figure 5.29. The spatial distribution of the clusters for the "on CCD"
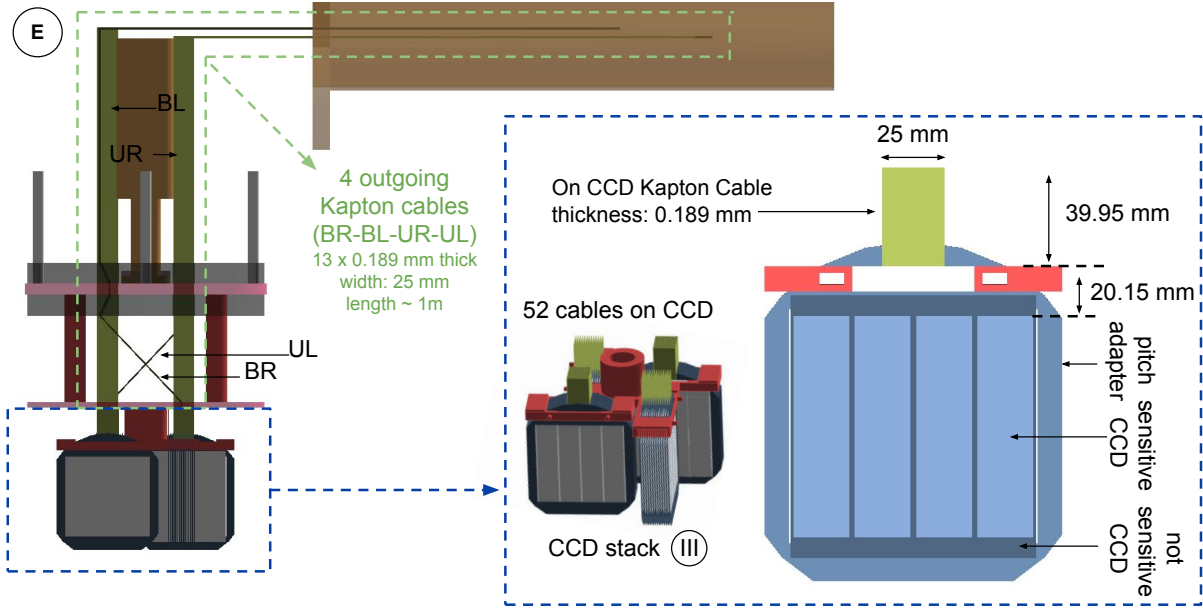
Figure 5.31 – Simulated designs using 2-layers kapton cables (green). The cryostat design E and the CCD stack design III are considered.

simulations is also studied and it is discussed in Section D. Summing up the contribution of the cables to the rate obtained for the design E, a total background rate of 0.3 d.r.u is achieved.

For the cryostat design F, the outgoing cables contribution decreases to 0.05 d.r.u, 1.6 times smaller than to the obtained rate for the cryostat design E. This is mostly due to the reduced cable length before entering in the EFC and lead shields. In fact, the distance between the additional lead and EFC shields is decreased by about 7.6 cm. The energy spectra obtained for the "on CCD" and outgoing parts of the cable are shown in Figure 5.32. The major contributors to the background are ^{214}Pb and ^{214}Bi. Summing up the contribution of the cables to the rate obtained for the design F (standard design), a total background rate of 0.3 d.r.u is achieved. The rate is equal to that found for the cryostat design E. The cables are the major contributors, having an associated background rate that is 48% of the total (15.6% for the outgoing parts and 32.3% for the "on CCD" parts).

(a)   (b)
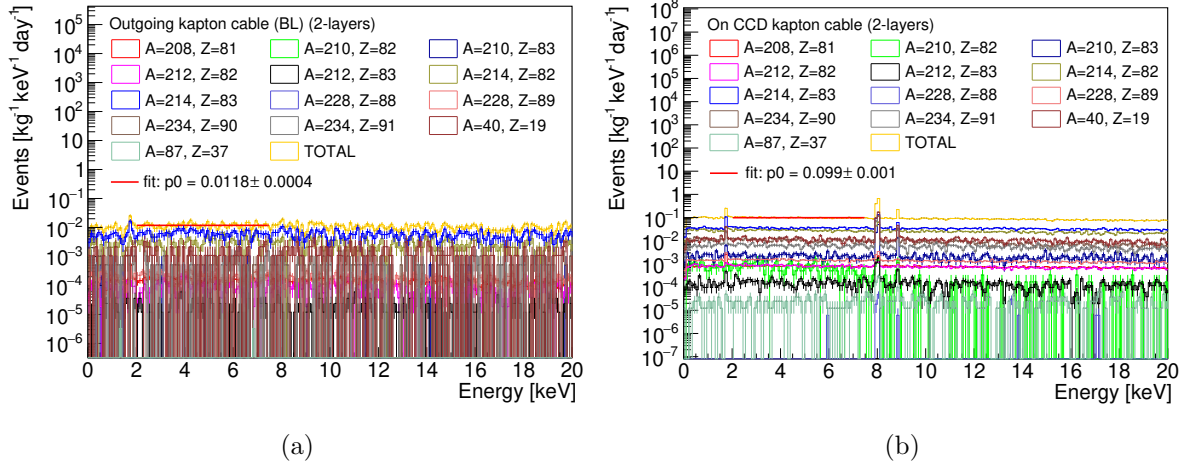
Figure 5.32 – Energy spectra for one outgoing 2-layers kapton cable (a) and all the "on CCD" parts (b). Simulations were performed using the cryostat design F and CCD stack design III. The red line on the spectra is the result of the fit to a constant (p0) used to estimate the background rate between 2 and 7.5 keV. For the outgoing ("on CCD") cable simulations, 6 (3) milions events were simulated for each isotope.

5.1.3   External lead shield simulations

An external lead shield is simulated surrounding the detector. At the time these simulations were done, the shield had not yet been designed. Therefore, simulations were performed with a simplified geometry, in order to provide an estimation of the possible external shield contribution. The specific design of the shield is however crucial for the proper estimation of the external background (external γs, neutrons, and muons) which is not treated in this section.

Isotope	Standard lead	Ancient lead
^{232}Th	<0.4	0.2*
^{226}Ra	<17.6	**<2.0**
^{238}U	<1.1	<2.0
^{210}Pb	$(15.6\pm4.3)\cdot10^5$	2850*
^{40}K	<19	<0.5

Table 5.9 – Activities in decays/day/kg per isotope and material used for simulations. These activities were measured by the DAMIC collaboration. The bold activities are decreased by a factor 10 with respect to the measured value at SNOLAB, given the expected reasonable improvement in the material purity. (*): measurement with unknown precision.

155
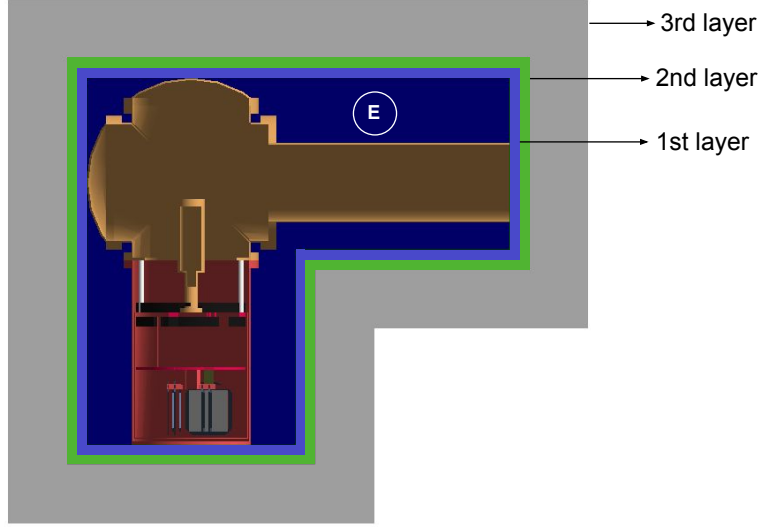
Figure 5.33 – Design of the external lead shield for the detector design E. The first, second, and third layers are shown in blue, green, and gray respectively. The same conceptual design is used for the design F.

Figure 5.33 shows a conceptual design of the external lead shield for the design E. The shield is 20 cm thick and, for convenience, is simulated divided into 3 different concentric layers. The two most internal ones (1st and 2nd layers) are made of ancient lead and are 2.5 cm thick each. The most external layer (3rd layer) is instead made of standard lead and it is 15 cm thick. The choice of these shield thicknesses relies on the DAMIC experience. Moreover, simulations on the Low Background Chamber (LBC) estimate that around 15 cm of lead are needed to shield from the external background at LSM [10].

The activities used to estimate the external shielding contribution are reported in Table 5.9.

In the design E, the total external shielding background is about 0.28 d.r.u, 93% (4%) of which due to the first (third) layer, as shown in Figure 5.34. The major contributors are ^{210}Bi and ^{214}Bi. Most of the events producing a cluster come from the most internal 5 cm of lead thickness and from the portion of shield surrounding and below the vacuum can, as shown in Figure 5.35. In particular, 14% of the events producing a cluster are from the part of the external shield below the vacuum can. Considering the whole detector setup E, including also the cable simulation results, the total background rate is about

---

10. The external background in LSM (especially for γs) has large uncertainties. Thus, data collected with the LBC will help in its understanding.
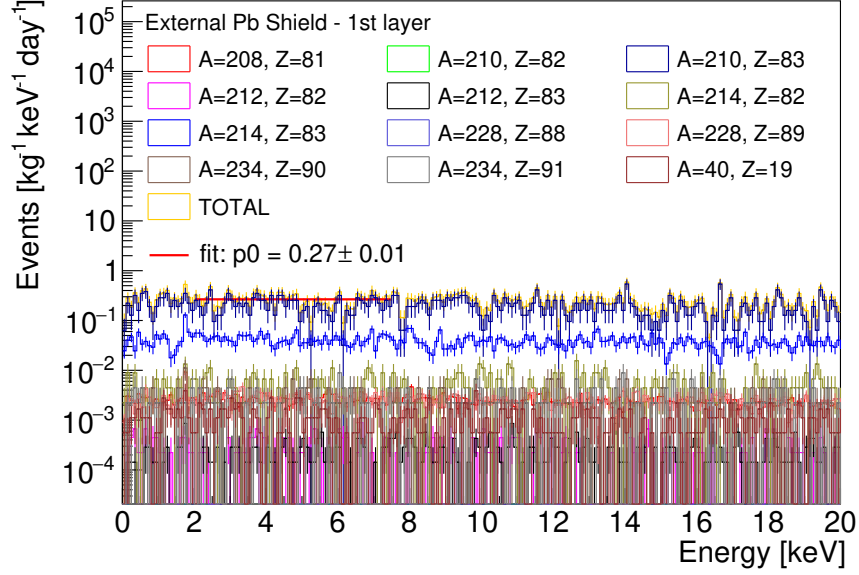
(a)
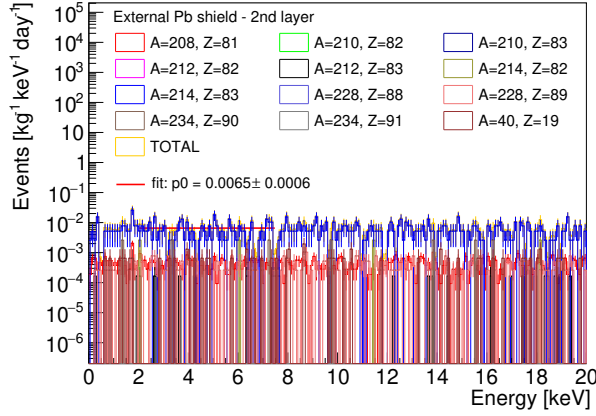
(b)
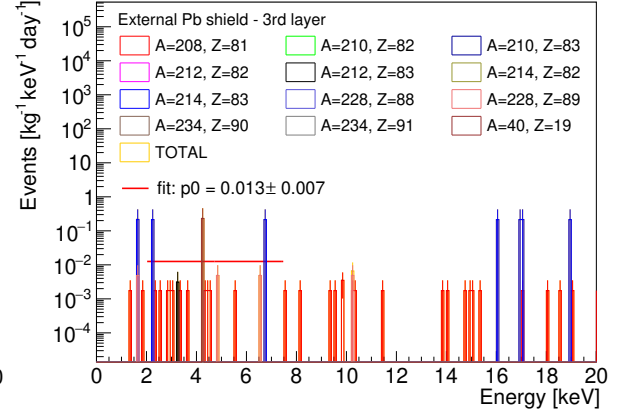
(c)

Figure 5.34 – (a): Cluster energy spectra obtained for the first (a), second (b), and third (c) layers of the external lead shield. The cryostat design E is considered. For each isotope, 12 millions events are generated, exception made for the ^{210}Bi. For the latter, $1.2 \cdot 10^9$ (24 millions) events are simulated for the first layer (second and third layers). The red line on the spectra is the result of the fit to a constant (p0) used to estimate the background rate between 2 and 7.5 keV.
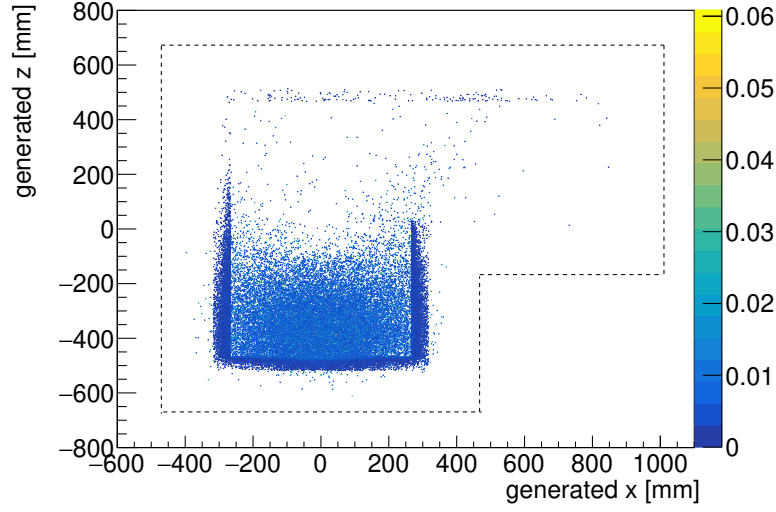
Figure 5.35 – Spatial distribution of the generated events producing a cluster for the external lead shield simulations (cryostat design E). The content of each bin is normalized to the corresponding bin value in the generated events distribution. The dashed line indicates the external perimeter of the shielding.

0.6 d.r.u, the external lead shield being the major contributor (47%).

In order to reduce the background budget, the possibility to increase the thickness of the lateral part of the vacuum can is explored. The shield rate decreases by a factor 1.2 and 1.9 by increasing the lateral can thickness, originally equal to 3.81 mm, by 3 and 5 times, respectively. On the other side, the rate due to the can increases by 0.03 d.r.u increasing its lateral thickness by 3 times [11]. The improvement in the total background rate would be minimal using a vacuum can only 3 times thicker. To have a background gain of about 0.1 d.r.u, it would be necessary to increase the can lateral thickness at least by 5 times.

The same external shield conceptual design of design E (see Figure 5.33) is used for design F. The total background due to the shield is about 0.3 d.r.u, 93% (5%) of which due to the first (third) layer (Figure 5.36). The results are very similar to those obtained for the design E. As observed previously, the major contributors are ^{210}Bi (77% of the rate) and ^{214}Bi (18%) and most of the events producing a cluster come from the most internal 5 cm of lead thickness. In particular, 12% of events producing a cluster are from the part of the external shield below the vacuum can (referred also as external shield base).

---

11. The contribution of the cosmogenic isotopes is included and it is equal to 0.024 d.r.u with $T_{exp} = 10$ days, $T_{cool} = 6$ months, and $T_{run} = 1$ year.
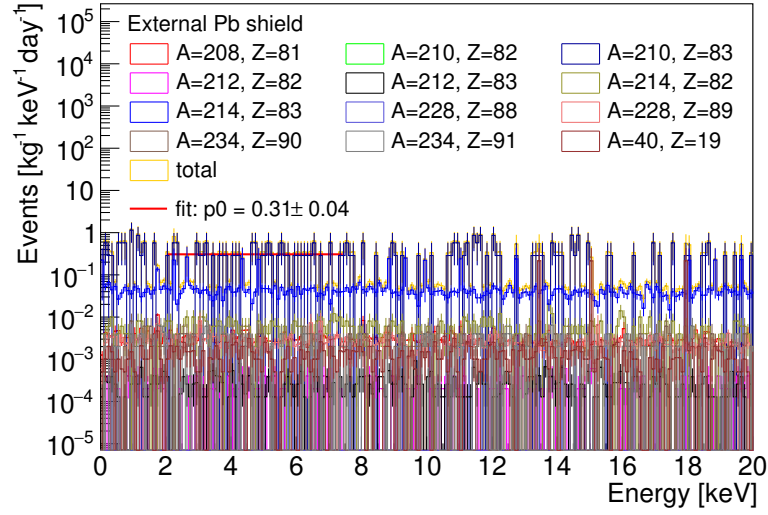
Figure 5.36 – Cluster energy spectrum obtained summing up the contributions of external lead shield layers. The cryostat design F is considered. For each isotope, 12 millions events are generated. The red line on the spectrum is the result of the fit to a constant (p0) used to estimate the background rate between 2 and 7.5 keV.

This contribution is slightly lower than the one observed for the cryostat E. This could be due to the increased (by about a factor 1.55) total thickness of the EF components between the external shield base and the CCD stack [12] and the decreased vacuum can lateral thickness (in the design F case, equal to 3.18 mm). The external shield rate is calculated assuming also the presence of the two additional vacuum can base shields in EFC (20 mm thick) and ancient lead (7.5 mm thick) discussed in Section 5.1.1. These were added to screen the CCD stack in case of a vacuum can base made of OFC, given the difficulty to produce it in EFC. The external shield contribution is unchanged (0.3 d.r.u), but the external shield base one decreases to 5%.

Considering the whole detector setup F (standard design, without the additional can base shields), including also the cable contribution, the total background rate is unaltered with respect to design E (about 0.6 d.r.u). Figure 5.37 summarizes the contribution of the detector components to the total background budget for the design F. Note that the activity assumed for ^{210}Pb and ^{210}Bi in the ancient lead is the one measured for DAMIC,

---

12. In fact, with respect to the previous cryostat design, the vacuum can base thickness is increased by 1.79 times (reaching 14.2 mm) and the cold shield thickness is decreased by 1.43 times (reaching 1.59 mm). The overall EFC thickness between the CCD stack and the external shield base is therefore increased by a factor 1.55.
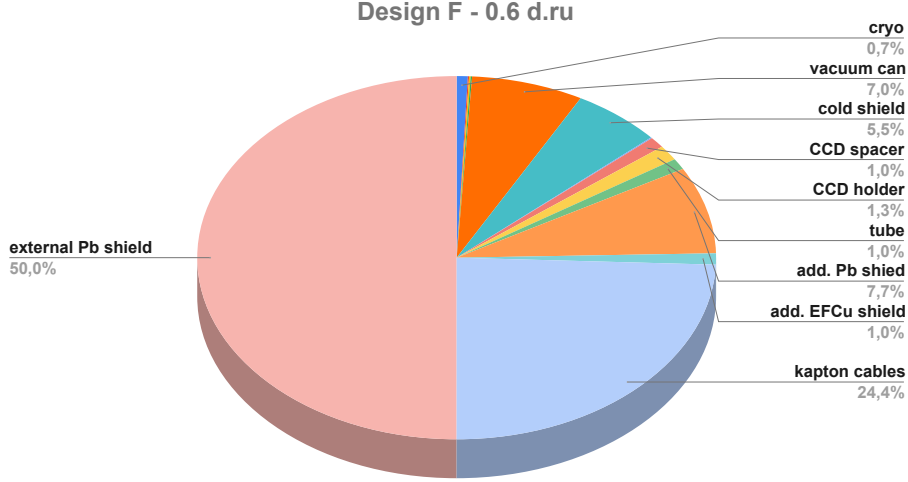
Figure 5.37 – Pie chart summarizing the contributions of the different components for the cryostat design F (standard) and CCD stack design III. The kapton cables and the external shield contributions are included. The total background rate is about 0.6 d.r.u.

which used lead recovered from a Spanish galleon. Instead, the ancient lead that DAMIC-M will use is from the Roman age and it is thus expected to have a lower ^{210}Pb and ^{210}Bi contamination. Consequently, this will reduce the contribution to the background of the ancient lead components. It is also worth mentioning that the possibility of using the external shielding of the Edelweiss experiment [148] is being evaluated. This would imply a modification of the detector design and would require further simulations.

5.1.4 Pitch adapter and surface background simulations

The pitch adapter constitutes a silicon support for CCDs. On top of it electrical traces will carry the signals from the CCD to the cable and vice-versa. Its design is assessed via simulations. In particular, two designs are investigated for the CCD stack III and are shown in Figure 5.38.

The design with holes (Figure 5.38, right) would be advantageous because the pitch adapter (assuming it contains radioactive contaminants) would contribute less to the background level than in the case of a design without holes (Figure 5.38, left). However, a pitch adapter without holes would help in screening the CCDs from background events, for example those coming from their surface or bulk. Therefore, the choice of the pitch adapter design is driven by the interplay between these two effects. Note that the design with holes is the standard one, considered for all the other detector simulations.
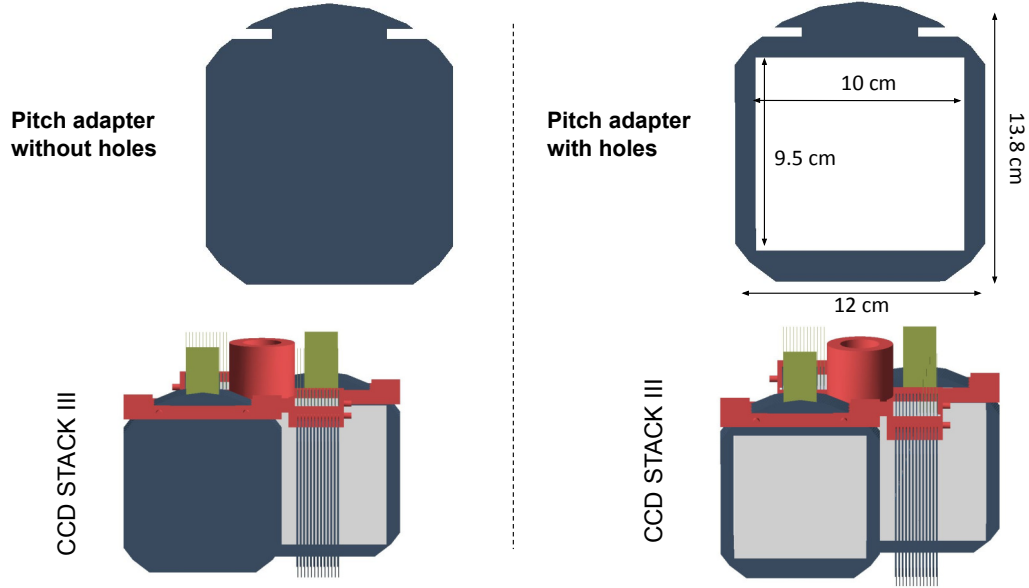
Figure 5.38 – Pitch adapter designs (with holes on the right, without holes on the left) for the CCD stack III. The pitch adapter thickness is equal to 0.68 mm. The top and bottom dead layers of CCDs are shown in gray. Each pitch adapter supports 4 CCDs.

The major contaminants are considered for the pitch adapters and the CCDs: bulk contamination by ^{22}Na and ^{32}Si and surface contamination by ^{210}Pb (see Section 3.3). Tritium, which is also an important source of background, is not simulated since it has a negligible impact on this study. Indeed, given the mean β energy of about 6 keV (Q-value = 18.6 keV), the emissions of tritium in the pitch adapter (CCD) bulks are not expected to reach the sensitive area of the (other) devices.

^{22}Na, ^{32}Si, and ^{32}P are simulated with a uniform distribution in the CCD and pitch adapter bulk. ^{210}Pb and ^{210}Bi are instead simulated on the CCD and pitch adapter surfaces with a distribution following the complementary error function (Erfc) defined in equation 4.1 with characteristic maximum depth M_d= 100 nm (see Section 3.3.2).

The same activities are assumed for the pitch adapters and the CCDs since they will be fabricated from the same silicon wafers. ^{22}Na activity is calculated via equation 3.13 considering a production rate of 49.6 decays/kg/day, as measured in [116], and an exposure time to cosmic rays of 3 months, a cooling time underground of 6 months, and a running time of DAMIC-M of 1 year. ^{32}Si and its daughter ^{32}P are assumed to have an activity equal to 12.96 decays/kg/day, as measured in DAMIC [78]. An activity of 0.7 decays/day/m^2 is assumed for the surface ^{210}Pb and ^{210}Bi, since a reduction of a factor

100 is expected with respect to the DAMIC case [78].

Considering all these contributions, the background rate associated to CCDs and pitch adapters for the two different pitch adapter designs are calculated.

As expected, the background rate from the CCD surface in case of a pitch adapter with holes is higher, almost a factor 2, than in the other case. A negligible improvement is instead observed for CCD bulk contributions (only a factor 1.1). The total rate from CCD simulations is about 0.24 (0.21) d.r.u for the pitch adapter configuration with (without) holes.

For the pitch adapter simulations, a substantial difference is observed between the background rates obtained with the two designs. For both bulk and surface simulations, a pitch adapter with holes ensures a background rate about 5 times lower than in the other case. The total pitch adapter contribution for a design with (without) holes is equal to 0.012 (0.06) d.r.u.

The results just reported for the CCD and pitch adapter simulations are summarized in Table 5.10.

Pitch adapter designs - background rates [d.r.u]				
	with holes		w/o holes	
	CCD	pitch adapter	CCD	pitch adapter
surface	0.02	0.002	0.01	0.01
^{22}Na	0.02	0.005	0.02	0.02
^{32}Si and ^{32}P	0.20	0.005	0.18	0.03
total	0.24	0.012	0.21	0.06

Table 5.10 – Background rate (in d.r.u) associated to the bulk and surface contamination of CCDs and pitch adapters.

The effect of having a pitch adapter without holes on the contribution of the other components of the design was also tested, without observing any significant improvement.

Summing up the CCD and pitch adapter contributions, the total background rate in case of a pitch adapter with holes is equal to about 0.25 d.r.u. A pitch adapter design without holes would instead bring to a slightly higher rate (0.27 d.r.u). This difference is due to the bulk contamination (about 92% of the rates), while the surface one is roughly the same in both configurations. Since ^{32}Si and ^{32}P contamination is intrinsic, only a variation in the ^{22}Na and surface activities would change these results. The only case in which the pitch adapter configuration without holes would be more advantageous than the other is for a measured CCD surface contamination higher than the one assumed here.
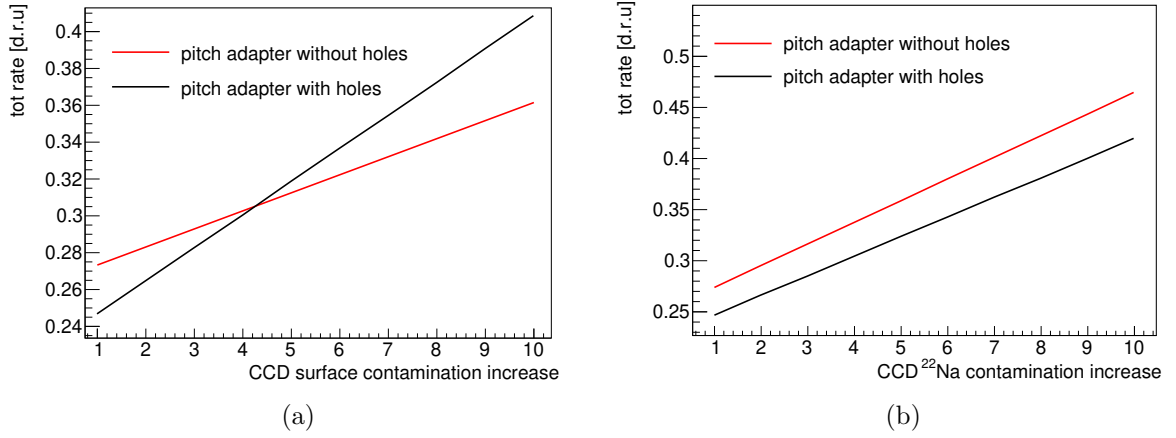
Figure 5.39 – Background rate evolution in case of an increased CCD surface (a) or ^{22}Na (b) contamination with respect to the level assumed. The rate is obtained by summing the bulk and surface contribution of the CCDs and the pitch adapters. Two different designs are considered for the latter, with and without holes.

In particular, a contamination at least ~4.3 times larger would be needed. Increasing the ^{22}Na contamination in CCDs or decreasing the one in the pitch adapter would not turn the tables. Figure 5.39 shows the evolution of the total background rate for a pitch adapter with and without holes in case of an increased CCD surface or ^{22}Na contamination. These results also highlight the importance of limiting the exposure time to cosmic rays and to radon of the silicon components. Note that in Figure 5.39 up to a factor 10 increase is considered for both CCD surface or ^{22}Na contamination. This is a very extreme situation (especially for ^{22}Na) and is reported only for illustrative purposes.

$$* * *$$

This chapter demonstrates the fundamental role played by simulations in identifying the major contributors to the background and in driving the DAMIC-M detector conception. The results discussed in the previous sections are summarized in Table 5.11. Simulations found the use of 5-layers kapton cables as done for DAMIC unfeasible for the DAMIC-M background goal. This result pushed the R&D for lower background cables. From the simulation results, the external shielding is the major contributor to the background. This suggests the importance of carefully designing this component. Furthermore, simulations highlight the importance of limiting the exposure time of the EFC

	Cryostat	Cables		External shielding	CCD and Pitch adapter p.a. with holes (w/o holes)
Background rate [d.r.u]					
		Kapton	Axon		
Design A	0.19	-	-	-	-
Design B	0.17	-	-	-	-
Design C	0.17	3.11 (5l)	0.57	-	-
Design D	-	0.10 (2l)	0.14	-	-
Design E	0.13	0.18 (2l)		0.28	-
Design F	0.15	0.15 (2l)		0.31	0.25 (0.27)

Table 5.11 – Background rates obtained for the different evaluated designs. In the case of the cables, the contribution of the cosmogenic isotopes is not included, being it negligible. "Axon" refers to the sum of the contributions of the Axon connectors and the pico-coaxial cables, provided by the Axon company. Design A: design with a EFC vertical finger base and a lead internal shield (50 mm thick). Design B and C: design with a lead internal shield (50 mm thick). For the design C, the cooling system β is considered. Design D: design with 1 kapton cable (2 cm long), 3 axon connectors and 51 pico-coaxial cables (9.9 cm long). Designs E and F: standard designs. (5l): 5-layers kapton cable. (2l): 2-layers kapton cable. (-): not evaluated contribution. "p.a.": Pitch adapter.

components to cosmic rays and a reference (and reasonable) limit of 10 days was set. Controlling the exposure time to cosmic rays and to air (and thus to radon) of the silicon components is also crucial, as stressed by simulation outcomes. An exposure time of 3 months to cosmic rays and a surface contamination 100 times lower with respect to DAMIC allow to reach a sufficiently low background level for DAMIC-M.

The detector design is still not finalized. Further optimization is needed also in view of the possibility to use the Edelweiss experiment external shielding. However, major improvements have been done and a great effort is being paid to finalize the detector design and reach the desired background rate.

COMPTON SCATTERING MEASUREMENT

Ionization signals from small-angle Compton scattering of environmental γ-rays are an important source of background for DAMIC-M, as already mentioned in Chapter 3. In fact the flux of environmental γ-rays is generally orders of magnitude higher than the one of fast neutrons and the associated Compton spectrum extends down to the energies of interest for the DM search, i.e., between 1 e$^-$ and 1000 e$^-$. A complete understanding and characterization of the low-energy part of the Compton spectrum is therefore necessary to proper distinguish a potential dark matter signal. Furthermore, Skipper CCDs, thanks to their sub-electron resolution, have the capability to resolve characteristic spectral features at the very low end of the spectrum associated with the atomic structure of the silicon target. This chapter is devoted to the measurements carried out by the DAMIC-M collaboration to model the Compton spectrum by means of a skipper CCD [127], with a focus in the energy range below 150 eV. The author of this thesis was directly involved in this measurement, in particular in the analysis, event selection, and modelling.

Note: This chapter is based on [127], of which I am one of the authors. Copyright rests with the American Physical Society.

6.1 Compton scattering and RIA approximation

The Compton (incoherent) scattering [149] describes the interaction between an incident photon and an atomic shell electron to which is trasferred a part of the initial photon energy. This process results in a recoiling electron and a deflected photon, whose energy and direction can be obtained by conservation of the system momentum and energy. In silicon, the Compton scattering is the predominant type of interaction for photons with energies between 60 keV and 15 MeV (Figure 6.1). Assuming a free electron at rest, the
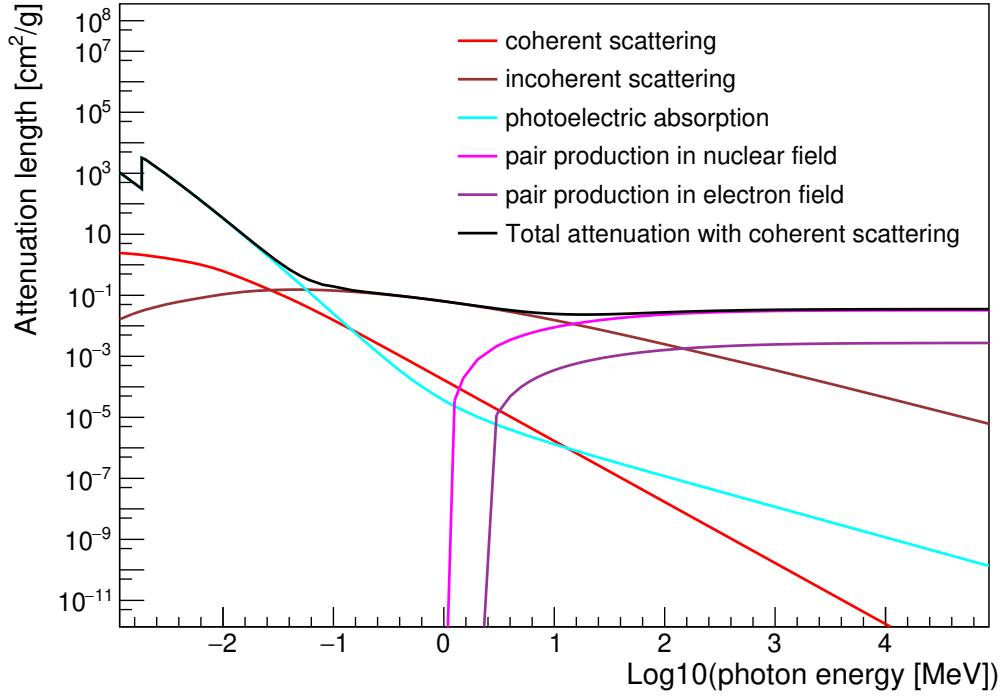
Figure 6.1 – Cross sections of silicon interaction processes taken from NIST XCOM database.

interaction cross-section is described by the well-known Klein-Nishina (KN) formula [150]:

$$\frac{d\sigma_{KN}}{d\Omega} = \frac{1}{2}r_0^2\left(\frac{x'_\gamma}{x_\gamma}\right)^2\left(\frac{x'_\gamma}{x_\gamma} + \frac{x_\gamma}{x'_\gamma} - sin^2\theta\right),\tag{6.1}$$

where $x_\gamma = \frac{E_\gamma}{mc^2}$, $x'_\gamma = \frac{E'_\gamma}{mc^2}$, m is the electron mass, r_0 its classical radius, θ the scattering angle of the photon, and E_γ and E'_γ are respectively the initial and final energy of the photon. The energy of the scattered electron can be thus derived as:

$$E = (E_\gamma - E'_\gamma) = E_\gamma\left(\frac{x_\gamma(1 - cos\theta)}{1 + x_\gamma(1 - cos\theta)}\right),\tag{6.2}$$

assuming that all the energy deposited in the target is absorbed by the electron. The energy E is characterized by a continuum distribution from zero to the so-called Compton edge, which corresponds to the case when the photon backscatters ($\theta = \pi$). However,

when the electron motion and binding energies become a significant fraction of the incident photon energy, the electron can no more be considered as free and at rest. Therefore, to properly describe the interaction, it is necessary to introduce the following correction to the KN formula [151]:

$$\frac{d\sigma}{d\Omega} = \frac{d\sigma_{KN}}{d\Omega} S(E_\gamma, \theta, Z), \tag{6.3}$$

where the incoherent-scattering function $S(E_\gamma, \theta, Z)$ depends on the target atomic number Z and on the quantum numbers n and l of the scattered electron.

The Relativistic Impulse Approximation (RIA) of Ribberfors and Berggren [151] provides a simple form for $S(E_\gamma, \theta, Z)$. Under the assumption that the energy transferred to electrons is much larger than the binding energy, the RIA model treats the scattering as in the case of free electrons but considering also the momentum distribution of the target before collision. This dependence is encoded in the $J(p_z)$ Compton profile, where p_z is the projection of the initial electron momentum on the photon scattering vector. The Compton profile brings to distortions of the E spectrum expected from the KN formula, e.g., the broadening of the Compton line[1]. Tabulated data for $J_{nl}(p_z)$ can be found in literature for different elements [152]. At relatively low-energy and momentum transfers, i.e., less than the electron mass, where the relativistic effects are less important, the RIA Compton double-differential cross section can be expressed in the following way [151]:

$$\left.\frac{d^2\sigma_{IA}}{dE \cdot d\Omega}\right|_{nl} = r_0^2 \frac{m}{2q} J_{nl}(p_z) \left(\frac{E^2}{E_\gamma^2} + (1 - \frac{E}{E_\gamma})(1 + cos^2\theta) \right), \tag{6.4}$$

where q is the module of the photon scattering vector and E is the energy deposited in the target[2]. By following this approach it is possible to split the cross section into the contributions coming from the individual atomic shells. Since a photon, in order to free an electron, must transfer to it at least an energy equal to the binding energy of the shell (E_{nl}), then it follows that $\left.\frac{d\sigma_{IA}}{dE \cdot d\Omega}\right|_{nl} = 0$ if $E < E_{nl}$. This gives rise to a step in the E spectrum in correspondance to E_{nl}, whose height is directly proportional to the number of electrons in the shell. At $E = E_{nl}$ the scattered electron has negligible kinetic energy and the photon is likely to escape after a single scatter, especially in a thin

---

1. In the free-electron approximation, the double differential cross section $\frac{d^2\sigma}{dE'_\gamma \cdot d\Omega}$ spectrum for a given photon scattering angle is an isolated line located at the Compton energy E'_γ calculated via equation 6.2, which is known as "Compton line".

2. The kinetic energy of the scattered electron can be retrieved by subtracting to E the binding energy of the electron shell.

detector as a CCD. Therefore, the deposited energy comes from the refilling of the atomic vacancy by the emission of secondary products like Auger electrons and fluorescence X-rays [153]. The continuum of freed electron energies gives instead rise to a slope structure between steps which is approximately constant. Figure 6.2 shows the computed electron low energy spectrum obtained under the RIA approximation for the Compton scattering of a 59.5 keV photon in silicon. The binding energies of the different atomic shells in silicon are reported in Table 6.1.
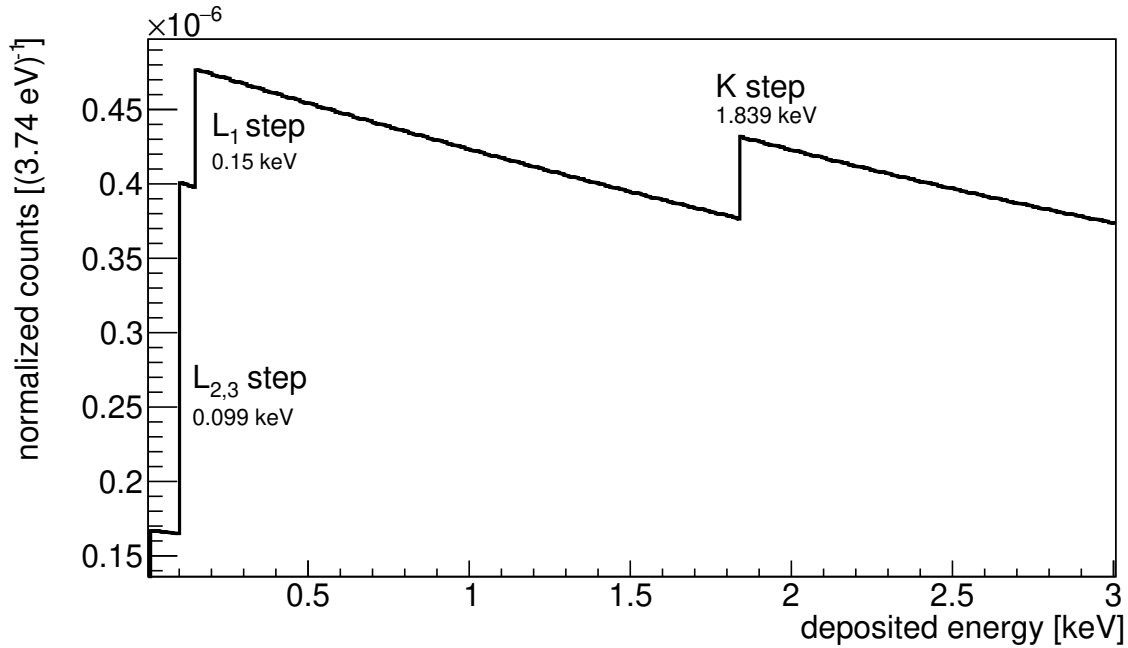
Figure 6.2 – Computed electron low energy spectrum obtained under the RIA approximation for Compton scattering of a 59.5 keV photon in silicon. The spectrum is obtained by calculating the cross section associated to a given photon deposited energy. The spectrum is normalized to the total number of entries of the histogram.

The free electron approximation may not be adequate when the energy transfer is comparable to the electron binding and kinetic energies [154]. In this case, it is more appropriate to compute $S_{nl}(E_\gamma, \theta, Z)$ with *ab initio* calculations, as possible with the FEFF code [155, 156]. FEFF performs a full quantum mechanical treatment to sum over all transition probabilities from the initial state to all possible atomic final states in the target material. The code was primarily developed (and has been extensively validated) for X-ray absorption spectroscopy (XAS)[157] but includes the option to calculate a

Atomic Shell	n	l	Binding energy [eV]	Number of e$^-$
K	1	0	1839	2
L$_1$	2	0	150	2
L$_{2,3}$	2	1	99.3	6
Valence	3	-	1.12	4

Table 6.1 – Quantum numbers, binding energies and number of hosted electrons of the different silicon atomic shells.

$S_{nl}(E_\gamma, \theta, Z)$ for non-resonant inelastic X-ray scattering (NRIXS)[3] [158].

The capability of DAMIC CCDs to reliably resolve Compton spectral features down to the experiment threshold (60 eV) was demonstrated in [82]. In this measurement, the RIA model was found to describe reasonably well the data in the K-shell region. However, in the L-shell region, the spectrum was observed to be notably softer than the model prediction. Furthermore, it was not possible to distinguish between the L$_{2,3}$ and L$_1$ steps due to experimental resolution. By profiting of the sub-electron resolution of skipper CCDs, the DAMIC-M collaboration has recently provided a refined measurement of the Compton spectrum by 59.5 keV γ-rays scattering in silicon, with a focus on the L-shell region [127]. The resulting spectrum is compared with the prediction from RIA and FEFF. Details about this measurement are reported in the following sections.

6.2 Experimental setup

The experimental setup for the Compton scattering measurement, shown in Figure 6.3, is located in a clean room at the University of Chicago. The detector consists of a 1024×6176 pixel skipper CCD, developed at Lawrence Berkeley National Laboratory MicroSystems Lab [159] and fabricated by Teledyne DALSA as a DAMIC-M prototype. The CCD features a three-phase polysilicon gate structure with a buried p-channel, a pixel size of 15×15 μm^2, and a thickness of 675 μm. The bulk of the device is made of high-resistivity (10–20 kΩ cm) n-type silicon which can be fully depleted at substrate biases $\geq$40 V. For

---

3. The process referred to as "Compton scattering" is more commonly known as NRIXS in the X-ray community. The NRIXS double differential cross section is usually expressed as $\frac{d\sigma}{dEd\Omega} = \frac{d\sigma_{Th}}{d\Omega}S(q,E)$, where the $\frac{d\sigma_{Th}}{d\Omega}$ is the Thomson scattering cross section (non-relativistic limit of the Klein Nishina formula) equal to $r_0^2 \frac{(1+\cos^2(\theta))}{2}(1 - \frac{E}{E_\gamma})$ for unpolarized radiation [158]. $S_{nl}(q,E)$ is called "dynamic structure factor". The variables are the same defined for equation 6.4.
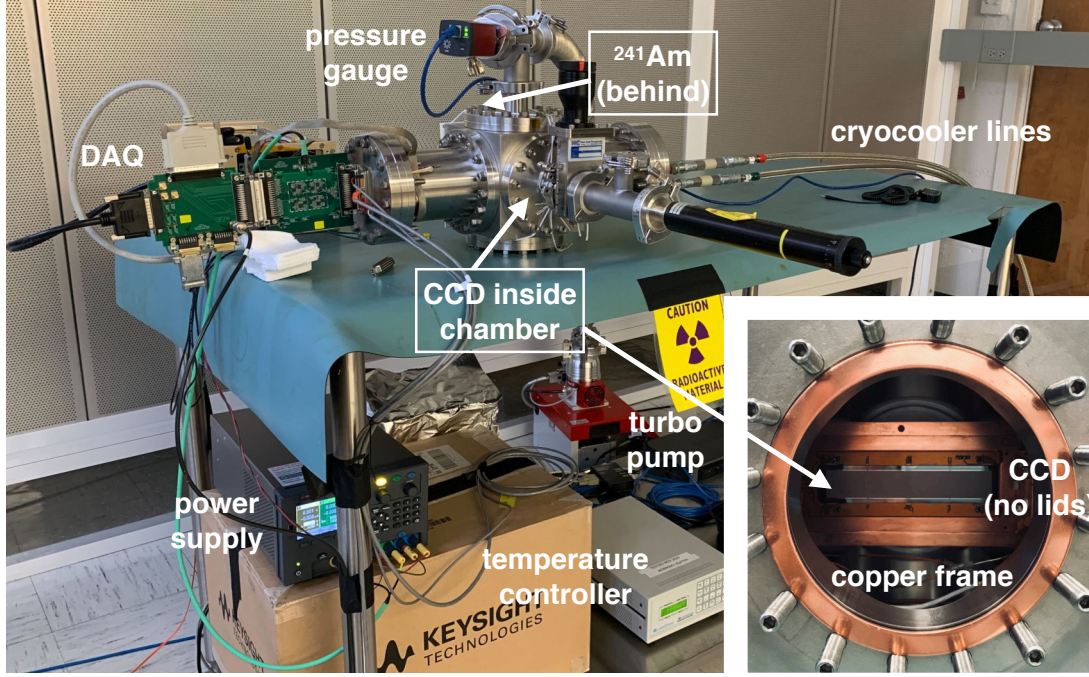
Figure 6.3 – Experimental setup used for the Compton scattering measurement. The 1k×6k Skipper CCD is held by a copper frame, as shown in the inset (lids not pictured), inside of the vacuum chamber. Components required for operation, e.g. the turbo pump, cryocooler, and electronics, interface with the chamber via flanges. The ^{241}Am source is positioned behind the chamber, centered with the CCD plane.

this measurement, the silicon bulk is fully depleted by a 95 V external bias, which also limits the lateral diffusion of charge carriers. The voltage biases, clocks, and video signals needed for the CCD operation are supplied via a kapton flex cable wirebonded to the device. The CCD is controlled and read out by commercial CCD electronics (Astronomical Research Cameras, Inc.). The CCD is housed in a copper frame within a stainless-steel vacuum chamber which is held at 10^{-7} mbar and cooled to 126 K. Thin aluminum lids are placed on both the front and backside of the copper frame to shield the CCD from IR photons generated by the warm chamber walls. The dark current rate is thus reduced by an order of magnitude. A slow control system controls and monitors the operation of the various instruments .

An ^{241}Am source (59.54 keV γ-ray) is mounted on the chamber illuminating the backside of the CCD. A 1.3 cm aluminum block is placed between the source and the CCD to suppress the weak γ-ray emissions between ~10-35 keV. Details about an ^{241}Am isotope are reported in Table 6.2. This particular source was chosen since it provides an

intense γ-ray line at a relatively low energy (59.54 keV) where the Compton scattering is the dominant type of interaction. In fact, the low energy of the emission results in a Compton spectrum more compressed towards the energy range of interest (below 2.5 keV and down to the L-shell region). Furthermore, low energy γ-rays are preferred since they induce shorter-range electron recoils. Therefore, the probability for an electron to escape the CCD without depositing its full energy is minimized, as well as the probability for a degraded-energy electron raised from the surfaces surrounding the device to reach the CCD. However, the γ-ray line cannot be too low (e.g., 26 keV), since the photoelectric absorption would dominate, making impossible to observe the Compton spectrum.

Half life	γ-ray energy [keV]	Intensity [%]
432.6(6) y	59.5409(1)	35.92(17)
	26.3446(2)	2.31(8)
	33.1963(3)	0.1215(28)

Table 6.2 – The half life, the energies and the intensities of the γ-ray lines of an ^{241}Am isotope. The emissions with intensity lower than 0.1% are not reported. The values are provided from the Nucléide-Lara library.

6.3 Data taking

Data are collected in an automated way and on a run-by-run basis. A run is a set of images, each image being a 2-D array of pixels. An example of image acquired with the Compton setup is shown in Figure 6.4.

The image acquisition cycle consists of three phases:
— *cleaning*: the entire CCD is cleaned in order to remove all the possible residual charges and to guarantee that all the images have the same exposure;
— *exposure*: the charges produced in the silicon bulk are accumulated and held in the pixels;
— *readout*: the collected charges are transferred vertically row by row (via "vertical clocks") into the serial register, and then horizontally (via "horizontal clocks"), to the readout node. Pixel binning can be used to sum the charge of several pixels before being readout. A n×m binning corresponds to summing the charge of n pixels in the horizontal direction and m pixels in the vertical direction. The charge in each pixel is then read multiple times (Non Destructive Charge Measurements,
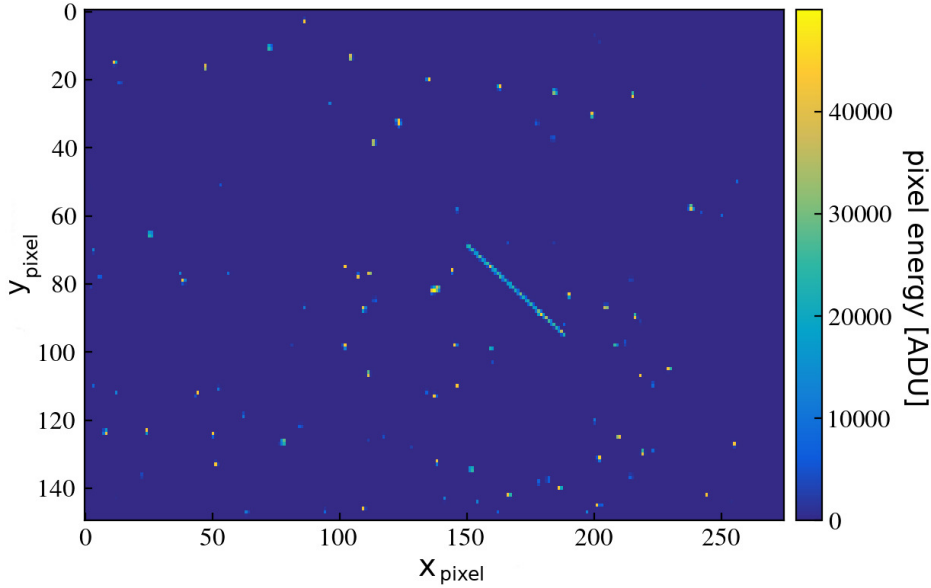
Figure 6.4 – Example of image acquired for the Compton scattering measurement. The image belongs to the source data set (see text). A muon track is visible as a straight line.

NDCMs) by a skipper amplifier. The final pixel charge is the average of all the different skipper measurements. Since the measurements are uncorrelated, the pixel readout noise scales as $1/\sqrt{\text{NDCMs}}$, as shown in Figure 6.5.

Data are acquired with two different configurations of the horizontal clocks:

— *standard* configuration: the amplitude of the horizontal clocks is equal to 3.5 V and the corresponding clock timing is equal to 0.24 μs. 30% (68 %) of the source (background) images are collected with this configuration. The horizontal clock parameters are then optimized to limit the observed asymmetry in the cluster topology (see Section 6.6.1);

— *optimized* configuration: this configuration allows to reduce the asymmetries in the cluster topology observed with the standard configuration. The amplitude of the horizontal clocks are increased from 3.5 V to 4.5 V, and the corresponding clock timing is enhanced from 0.24 to 0.4 μs.

Both standard and optimized configuration data are used for the final analysis, being the resulting cluster energy spectra compatible within each other. Further details are provided in Section 6.6.1.

Within a given run, different types of images are acquired by changing the size, the number of NDCMs (or N_{skips}), and the pixel binning, depending on the image scope. Full
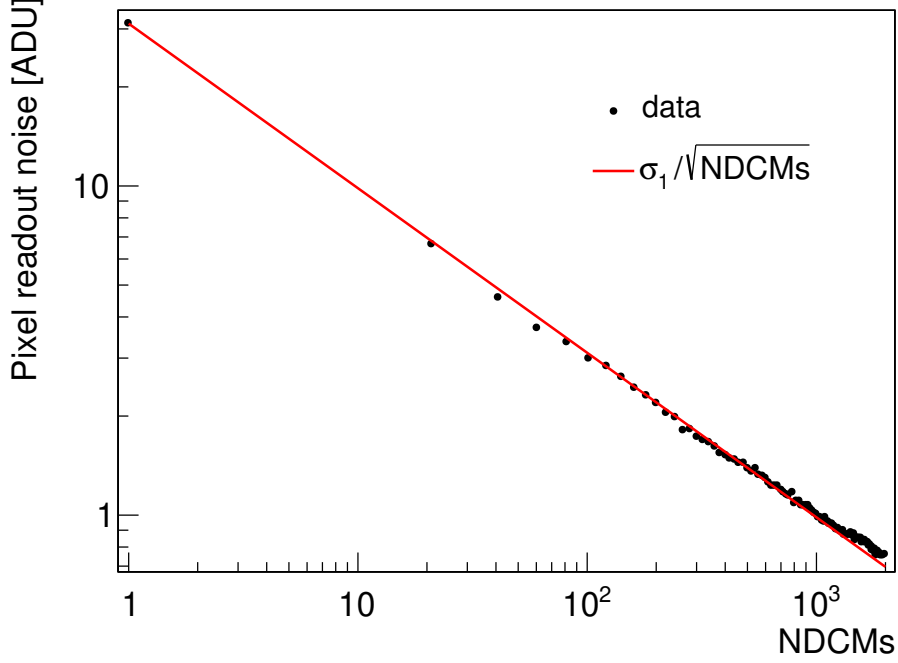
Figure 6.5 – Readout noise in ADU as a function of the number of skipper measurements (NDCMs). σ_1 refers to the readout noise obtained with NDCMs=1. The readout noise is calculated from the overscan region (see Section 6.4.1). Note that 1 electron charge corresponds approximately to 5.2 ADU.

CCD images with no binning and N_{skips}=1 are taken to monitor the overall quality of the device, including stability of defects (hot pixels and columns) over its entire active area. Images with N_{skips}=2000 are taken to calibrate the energy response and measure the dark current of the CCD with optimal resolution. For the Compton analysis data set, the image acquisition parameters are optimized to ensure good resolution while minimizing pile-up events which could potentially bias the measured spectrum. To reduce the impact of dark current, the acquisition is restricted to only 600 rows (each image corresponds to 1/10 of the CCD active area) with a very short exposure time (3 s). A 4×4 binning is used to reduce the contribution of the readout noise to the charge measurement (but at the expense of a worsened spatial resolution). A 4×4 binning allows also to speed up the readout procedure and thus to decrease the level of dark current. Every pixel is readout with N_{skips}= 64, further reducing the readout noise. The resulting image contains 150×256 binned rows and columns of active region, 15 binned columns of overscan, and

173
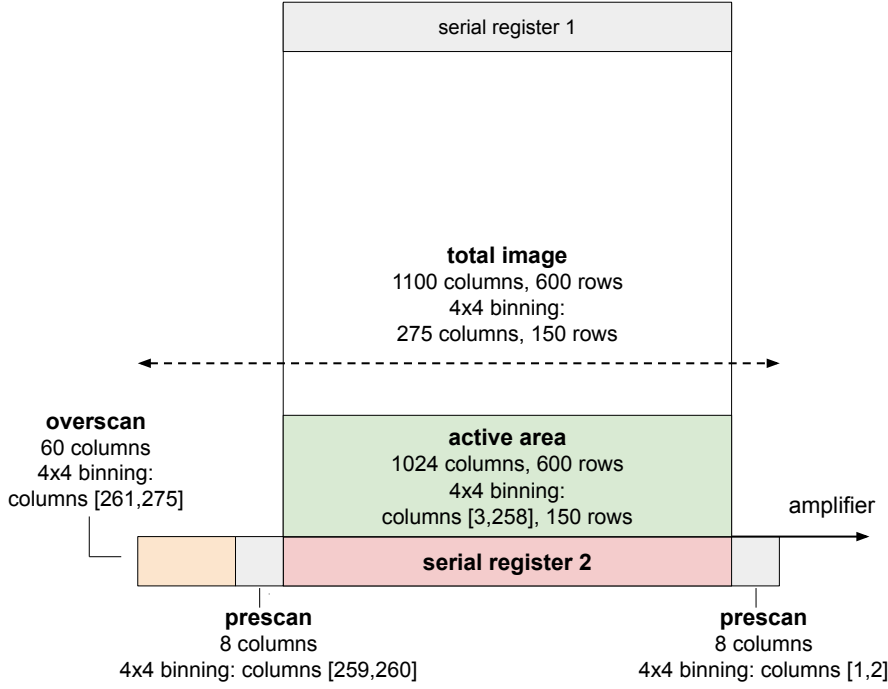
Figure 6.6 – Schematics of the CCD structure and image dimensions for the Compton measurement. Only the serial register 2 is used for the data taking.

4 binned columns of prescan (immediately after and before the active region) with a readout time of 37 seconds per image. The prescan consists of 8 unbinned physical pixels (2 binned columns) in front of the amplifier. The overscan instead is made of active region pixels that are read for a second time after the readout of a complete row. Also the prescan pixels are read for a second time before the overscan, resulting in 2 additional binned columns in the image size. These overscan additional pixels along the serial register do not contain charges and are thus used to determine the pedestal baseline row-by-row. From now on, while referring to runs with binning, the word "pixel" will be used instead of "bin", the word "row" ("column") instead of "binned row" ("binned columns"). For example, considering 4×4 binning data, the term "pixel" will be used to refer to a 4 pixel $\times$ 4 pixel bin. A schematics of the CCD structure and image dimensions is reported in Figure 6.6.

A background data set is taken removing the ^{241}Am source and using the same parameters of the Compton analysis data. Another data set, referred as serial register data set, is acquired with the ^{241}Am source in place and the vertical clocks moving the charge in the opposite direction with respect to the readout serial register. This allowed to study

the background in the serial register (see Section 6.6 for details). The serial register data set is acquired only with the *optimized* configuration. Table 6.3 summarizes the main data sets together with the relevant CCD operating parameters.

Source	Binning [row×col]	Image size [row×col]	N_{skips}	Charge direction	Images	Exposure [days]	Type
^{241}Am	1×1	6200×1024	1	sr	909	1.3	diagnostic
	16×4	60×275	2000	sr	909	5.9	calibration
	4×4	150×275	64	sr	242663	113.5	source
	4×4	150×275	64	aa	16789	7.9	serial register
None	4×4	150×275	64	sr	103106	48.2	background

Table 6.3 – Summary of the data sets used in the analysis. The image size includes the 15 overscan columns and 4 prescan columns. The charge direction parameter represents the direction in which charge is moved, either towards the readout serial register (sr) or in the opposite direction, away into the active area of the CCD (aa).

Data were collected for several months and their quality was continuously monitored. For each run, an automatic data analysis report was generated, providing information about the pedestal baselines, dark current level, calibration constants, readout noise and single electron resolution. This allowed to track in an accurate way the CCD performance and stability. All monitored parameters show a good stability, with less than 1% of the data rejected due to occasional spurious noise sources in the laboratory. Further information concerning the image processing is provided in the next section.

6.4 Image processing, calibration, and event reconstruction

The WADERS code, described in Chapter 4 for the simulation framework, is used to process the images acquired for the Compton measurement. WADERS takes care of all the passages needed for the analysis and can be configured via a json file. The raw images are provided in a FITS file format. The code is then used to compress a set of single skip measurements into a single image using a statistical function which can be set by the user. In the Compton measurement case, the statistical function is the mean. WADERS is then employed to subtract the pedestal value (row by row, column by column, using the overscan or active region) and to clusterize charged pixels. The code is also used

to monitor the quality of data. Among the monitoring elements there are: the median and MAD (Median Absolute Deviation) of the pixel charges in the active and overscan regions calculated per row or columns, the mean pedestal and readout noise value in an image, the presence of pixels above a given threshold (hot pixels), and the dark current rate value per image.

In this section all the steps followed for the data analysis are described.

6.4.1 Pedestal and readout noise estimation
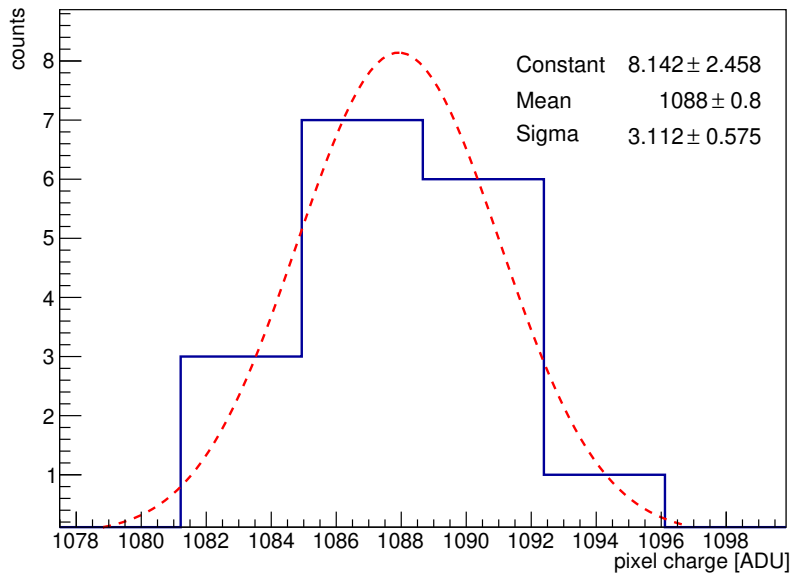
Figure 6.7 – Pixel charge distribution obtain for one overscan row. The Gaussian fit is shown in red. The fit outputs (constant, mean, sigma) are reported in the top right of the plot.

The image processing starts with the determination of the pedestal value, being the DC offset introduced by the electronics chain[4]. The pedestal is evaluated by a Gaussian fit of the pixel charge distribution for each overscan row. In fact, the overscan pixels, being exposed for a small period of time, are expected to have a charge distribution compatible with a gaussian distribution centered in the pedestal value and with a standard deviation equal to the readout noise. An example of Gaussian fit for an overscan row is shown in Figure 6.7.

---

4. In other words, the pedestal is the value in ADU corresponding to 0 signals.

Horizontal clusters can be observed in the overscan region, due to ionizing particles hitting the serial register (or a close-by region) during the reading of individual rows. These horizontal clusters are commonly present when operating a CCD at a surface laboratory in presence of cosmic rays and natural radiation. Their number increases significantly with an ^{241}Am source, due to the increased flux of incident radiation. It is necessary to mask pixels from horizontal clusters to not bias the pedestal estimation. To do so, first the median (m_{ovs}) of the pixel charges in the overscan is calculated, together with the median absolute deviation (MAD). Pixels with $q_{pix} - m_{ovs} > 10 \cdot MAD$ are not included in the Gaussian fit.

The pedestal value (the mean of the Gaussian, μ_{ovs}^{row}) is then subtracted row by row in the active area. The median of all the standard deviations obtained per row is calculated (σ_{ovs}) and it is used later on for the clusterization process. Figure 6.8 shows the evolution of the median per run of the σ_{ovs} (a) and μ_{ovs} (b) parameters. The latter is the median of the μ_{ovs}^{row} values in a given image.

6.4.2 Data quality

Bad images mask

Anomalous images are excluded from the analysis to ensure good data quality. Bad images are spotted by looking for a shifting baseline and a high noise in the overscan region.

To identify a shifting baseline, the overscan region of an image (after pedestal subtraction) is divided in 25 partitions[5]. For each partition the median and standard deviation of the pixel charges is calculated. The most frequent standard deviation value (σ_{mode}) is then identified between all the values obtained. The deviation between the median pixel charge obtained for a given partition and the following one is calculated. If it is bigger than $0.75 \cdot \sigma_{mode}$[6], then a baseline shift is tagged and the image is excluded from the analysis. In the same overscan region, if no horizontal clusters are present, the standard deviation of all the pixel charges is calculated. If it is higher than a given threshold (set to 4 ADU[7]), then the image is discarded from the analysis. An horizontal cluster

---

5. The number of partitions was chosen after an optimization study. Its value can be changed by the user via json file.

6. $0.75 \cdot \sigma_{mode}$ was chosen as threshold after an optimization study. Its value can be changed by the user via json file.

7. A threshold of 4 ADU was found to be the optimal one after a dedicated study. Its value can be changed by the user via json file.
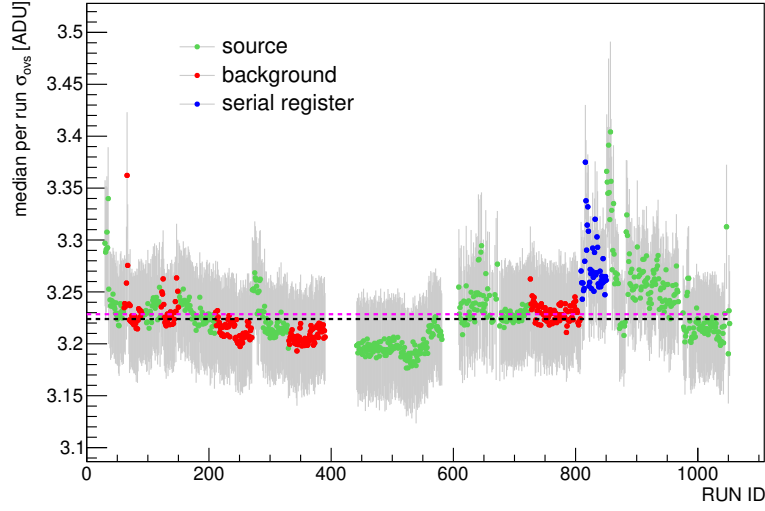
(a)
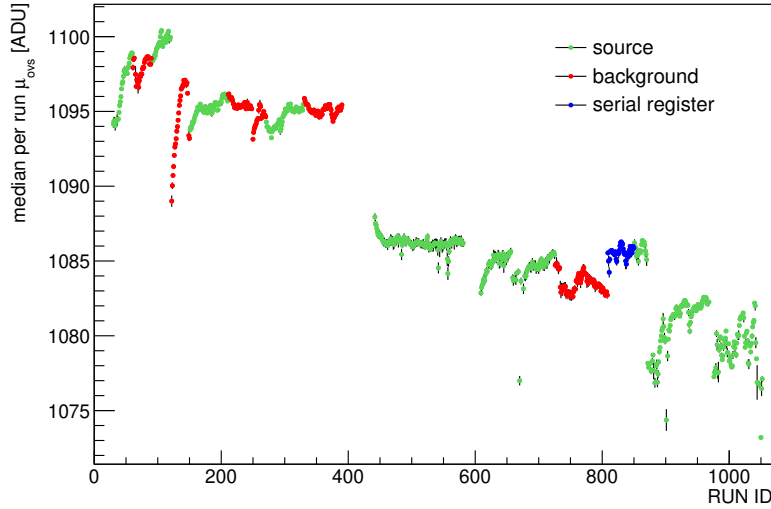
(b)

Figure 6.8 – (a): median per run of σ_{ovs} value. The gray lines indicate the MAD calculated for each run within all σ_{ovs} per image. The runs from the source, background, and serial register data sets are shown in green, red, and blue, respectively. The black and magenta dashed lines indicate the median and the mean, respectively, of all the points in the graph. (b): median per run of pedestal μ_{ovs} value. μ_{ovs} is calculated for each image as the median of the $\mu_{\mathrm{ovs}}^{\mathrm{row}}$ values .The black lines indicate the MAD calculated for each run within all μ_{ovs} per image. The runs from the source, background, and serial register data sets are shown in green, red, and blue, respectively.

is identified if at least 3 pixels in the same row show a charge 10 times higher than an effective sigma (σ_{eff}). This σ_{eff} is calculated as the minimum between the average of the standard deviations found per row and the standard deviation determined considering the whole overscan region. All the procedures described before were validated and optimized on data. Different thresholds were tested. The ones bringing to a noticeable improvement of the energy spectrum (in terms of cleanness), while keeping the statistics high, were selected for the final analysis. All these quality cuts are applied automatically by the software used to process the data.

Hot pixels mask

Hot pixels, columns, and rows are identified by looking for pixels which shows a higher charge than expected. In particular, a pixel is considered as "hot" if it has a charge higher than $\text{thr}_{\text{hot}} = (\text{m}_{\text{ovs}} + 3 \cdot \text{MAD})$ in 50% of the images of a given run. A column or row is considered hot as well if made of 30% hot pixels. These hot pixels, columns, and rows are not considered for the analysis.

Dark current estimation

The 2000 skips images are used to estimate and monitor the dark current level. For each run, one 2000 skips image is acquired. The charge distribution of pixels in the active area is characterized by a series of consecutive Gaussian peaks ($\mathcal{G}$) with standard deviation equal to σ_0, the readout noise. The k-th peak is centered in $(k-1)$ e$^-$. The first peaks are the result of the convolution with a Poisson distribution ($\mathcal{P}$) with average λ, associated to the dark current induced charges. A fit is thus perfomed on the first two peaks to estimate the dark current rate ($\lambda[\text{ADU/pixel/image}]$), as well as the gain ($g[\text{ADU/e}^-]$) and the readout noise ($\sigma[\text{ADU}]$):

$$\mathcal{N} \sum_{n=0}^{k-\text{peaks}} \left[\mathcal{P}\left(\frac{\lambda}{g}\right) \circledast \mathcal{G}\left(n - \frac{\mu_0}{g}, \frac{\sigma}{g}\right) \right], \tag{6.5}$$

where $\mathcal{N}$ is the normalization and g represents the conversion constant between ADU and e$^-$. The latter corresponds to the distance between the centers of the 0 and 1 electron peaks (considering the charge distribution in ADU units). An example of pixel charge distribution is shown in Figure 6.9, together with the associated dark current fit. Figure 6.10 shows the evolution over the different runs of the gain (a) and dark current rate (b).
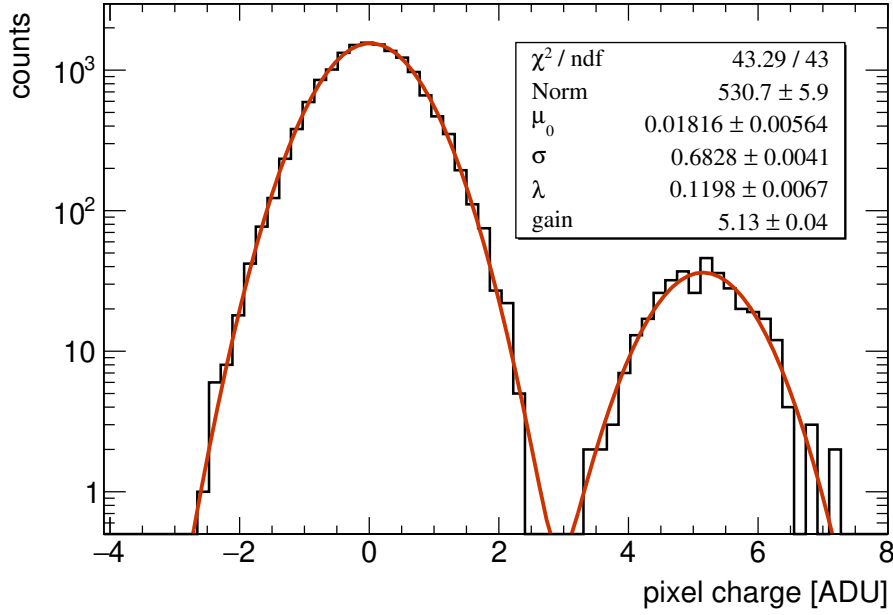
Figure 6.9 – Pixel charge distribution for a 2000 skips background image, after pedestal subtraction. The distribution is fitted using equation 6.5. The red line indicates the fit result.

The dark current level for source runs (λ_{DC}^{SRC}=0.36 ADU/pixel/image) is found higher than the one for background runs (λ_{DC}^{BKG}=0.11 ADU/pixel/image). This suggests the existence of an additional source of noise in the source runs, which is not present in the background ones (see Section 6.6.2)

It can be noticed that some runs show an anomalous level of dark current. These runs show a deviation from the median higher than 3×MAD (considering different median and MAD values for source and background runs). Their removal from the analysis does not produce any significant change in the energy spectra with respect to the ones obtained with all the runs. Therefore, it was decided to not discard them to have more statistics.

6.4.3 Electronic transient effect

The pixel charge is expected to have a flat distribution over the columns of the active area. However, the first 25 columns show a median pixel charge value higher than the one observed for the other columns. This is caused by a transient response of the readout amplifier which features an exponential behaviour with approximately the same decay
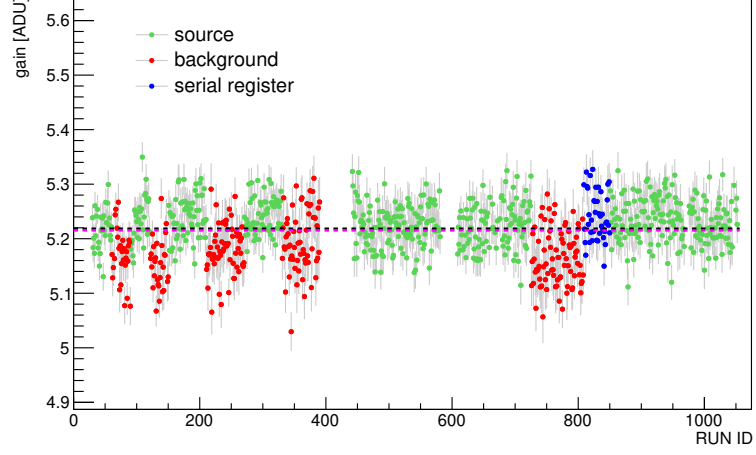
(a)
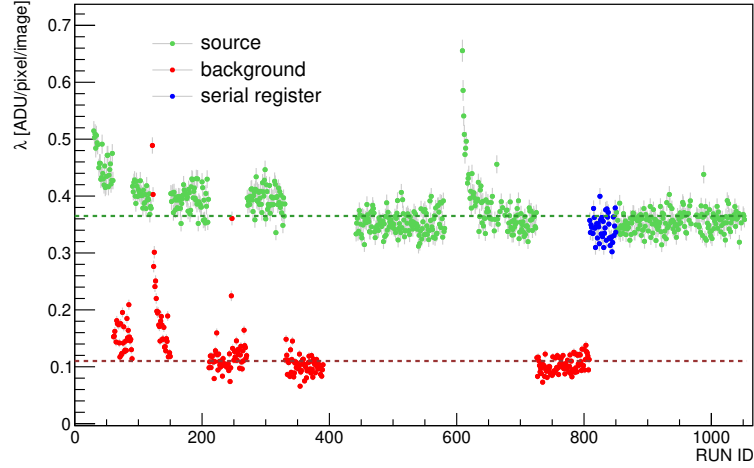
(b)

Figure 6.10 – (a): Gain value per run. The gray lines indicate the error associated to fitted parameter. The runs from the source, background, and serial register data sets are shown in green, red, and blue, respectively. The black and magenta dashed lines indicate the median and the mean, respectively, of all the points in the graph. (b): Dark current value per run. The gray lines indicate the error associated to the fitted parameter. The runs from the source, background, and serial register data sets are shown in green, red, and blue, respectively. The dashed lines indicate the median of the dark current values for the source and background runs, respectively equal to 0.36 ADU/pixel/image (MAD = 0.02) and 0.11 ADU/pixel/image (MAD = 0.01). Note the exponential behaviour of the dark current (starting at run 122 and run 609), whose value is positively correlated with the decreasing temperature of the setup. The chamber in fact was warmed up and then cooled down again.

constant for all the runs ($\mu = -0.12\pm0.03$). This effect is thus modelled by an exponential fit performed for the first 50 columns. The median of the pixel charges m_i is determined for the i-th column in the active area. The median of the m_i values with $i \geq 50$ is calculated (M) and then subtracted to the m_i values with $i < 50$. An exponential fit is performed on the $[m_{i<50} - M]$ values as a function of the column i: $y_{i<50} = A \exp(-\mu \cdot i)$. The obtained $y_{i<50}$ value is then subtracted to the pixel charges in the corresponding i-th column. A flat pixel charge distribution over all the columns is thus retrieved. This correction is applied after the pedestal subtraction process.

Figures 6.11 show the median of the μ parameters obtained for all the images in a given run.
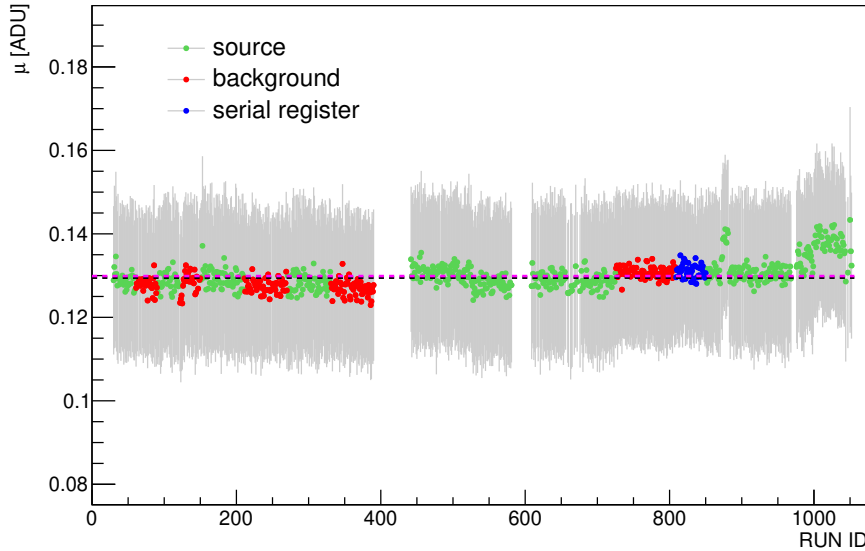
Figure 6.11 – Median of the μ values per run. The gray lines indicate the MAD calculated for each run μ sample. The runs from the source, background, and serial register data sets are shown in green, red, and blue, respectively.

6.4.4 Calibration

A self calibration is performed to determine the proper conversion between ADU and number of electrons. To this end, the $N_{skips} = 2000$ images are used (after pedestal subtraction), characterized by a resolution a factor $\sqrt{64}/\sqrt{2000}$ better than $N_{skips} = 64$ images. The total pixel charge distribution obtained from this set of images shows 550
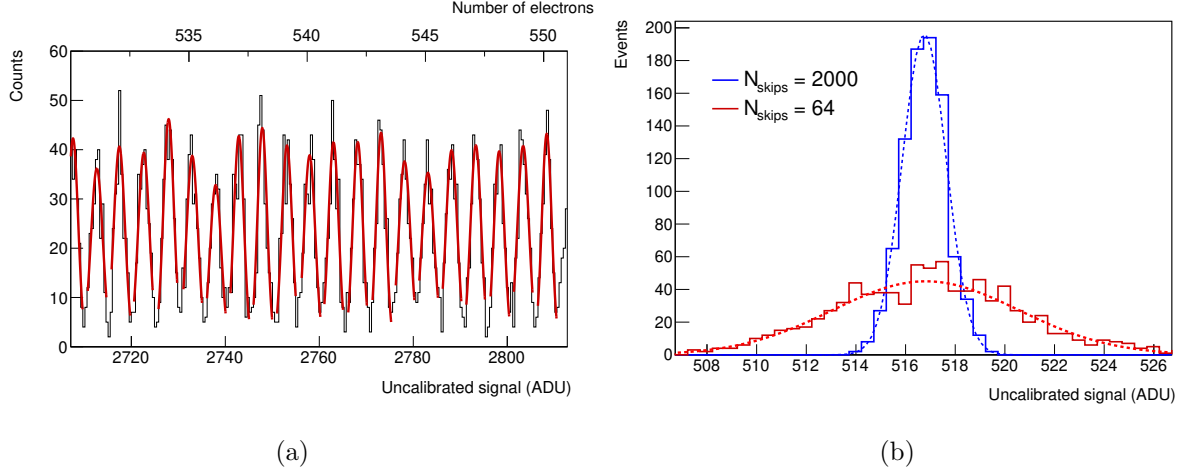
Figure 6.12 – (a): Pixel charge distribution with single-electron resolution ($N_{skips} = 2000$) showing individual peaks from 530 electrons (about 2.0 keV) up to 550 electrons (about 2.1 keV). To calibrate the energy scale, the mean in ADU units of the k-th peak is associated to a number of $k - 1$ electrons. (b): Pixel charge distribution with $N_{skips} = 2000$ (blue) and $N_{skips} = 64$ (red) corresponding to a charge of 100 electrons. The pixels entering the two distributions are the same, but, in the $N_{skips}= 64$ case, their charge is calculated using only the first 64 out of the 2000 NCDMs.

consecutive peaks resolved with good statistics (Figure 6.12, a).

For each peak, the charge of the associated pixels is recalculated using only the first 64 out of the 2000 NDCMs, as shown in Figure 6.12 (b). A new 64 skips charge distribution is thus obtained and it is fitted with a Gaussian. The mean, expressed in ADU units, of the k-th peak is associated to a number of $k - 1$ electrons. A two degree polynomial is used to describe the conversion function between ADU and electrons:

$$E_{pix}[e^-] = \left(-0.040 + 0.193 \cdot q_{64} + 1.033 \cdot 10^{-6} q_{64}^2\right),\tag{6.6}$$

where q_{64} is the charge in ADU obtained with $N_{skips} = 64$. A very consistent result is obtained using the $N_{skips} = 2000$ peaks, which deviates slightly in the constant and squared terms of the equation 6.6 (20% and 6% respectively)[8]. The calibration function together with the corresponding residuals are shown in Figure 6.13 (a). As a comparison, the residuals obtained using a linear calibration function are also shown in Figure 6.13 (b). Using a linear calibration would lead to a worse fit to data, showing a deviation from the measured charge up to about 2 electrons.

---

8. This deviation would lead to a mismatch of about 0.12 electrons at 2500 ADU.
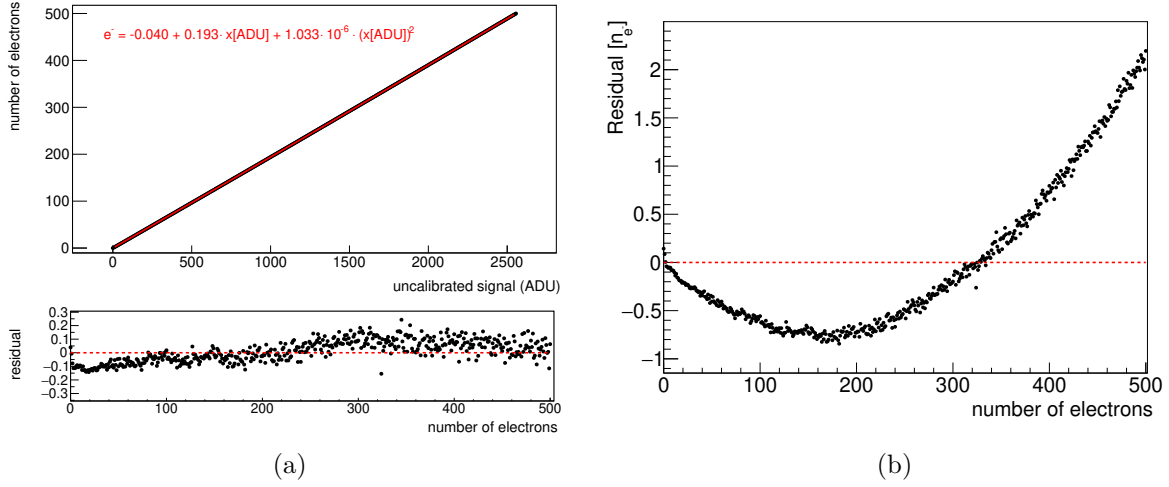
Figure 6.13 – (a): Number of electrons (n_{e^-}) as a function of the mean charge value (in ADU) for $N_{skips} = 64$. The red line is the result of the fit obtained using a two degree polynomial. The corresponding residuals ($n_{e^-}^{measured} - n_{e^-}^{fit}$) are shown in the bottom panel. (b): Residuals ($n_{e^-}^{measured} - n_{e^-}^{fit}$) obtained using a linear fitting function. The fit results in a conversion formula equal to: $y[e^-] = -0.143 + 0.195 \cdot x[\text{ADU}]$.

To finally convert a charge from electron units to eV, the average energy to create an electron–hole pair (ϵ_{eh}) is used:

$$E_{pix}[\text{eV}] = \text{E}_{\text{pix}}[\text{e}^-] \cdot \epsilon_{\text{e}-\text{h}}. \tag{6.7}$$

For this work, ϵ_{eh} is assumed to be 3.74 eV, being the expected at 126 K [79]. The calibration is applied at the pixel level, prior the clusterization and after the electronic transient effect correction.

6.4.5 Clusterization and event selection

A clusterization algorithm is run to collect all contiguous charged pixels in a cluster. Only pixels with charge higher than $3.6\sigma_{\text{ovs}}$ are considered (see Section 6.4.1 for σ_{ovs} calculation). For the final analysis, only clusters with at least one pixel with charge $> 4.6\sigma_{\text{ovs}}$ are selected. These thresholds limit to $< 5\%$ the fraction of fake clusters made by pixels with zero charge which still pass the selection due to the charge resolution.

Defects in the CCD array result in warm columns (x-axis) and warm rows (y-axis), which are identified for source and background runs. These don't meet the criteria to be
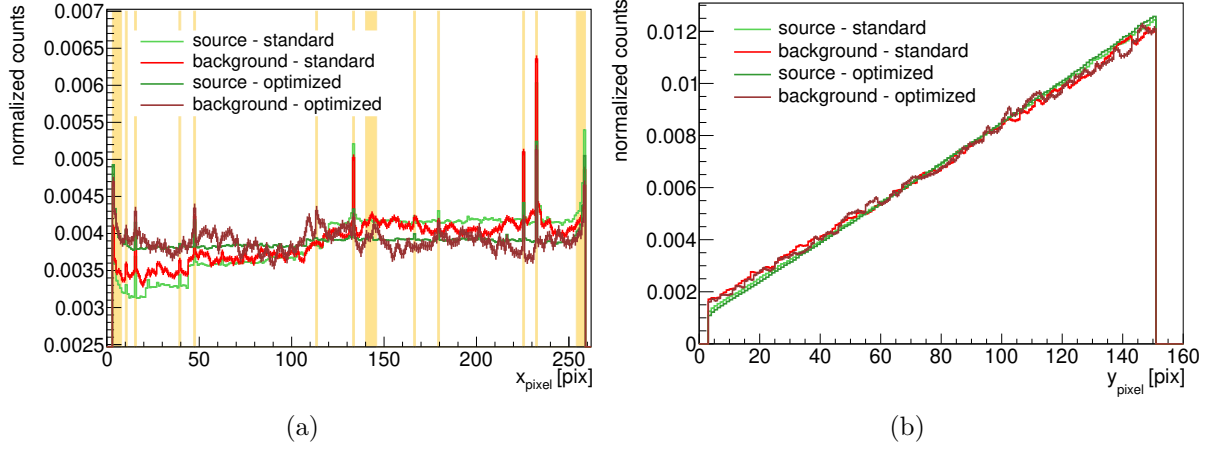
Figure 6.14 – (a): x_{pixel} distributions, normalized by their own area. The orange bands indicate the warm columns selected. Data from standard and optimized runs are shown separately since they feature different distribution shapes. (b): y_{pixel} distributions, normalized by their own area.

considered hot, therefore they are not identified by the initial mask (see Section 6.4.2). Warm columns and rows are selected by looking at the cluster pixel position with a frequency higher than expected[9]. In fact, pixels are supposed to be distributed in a uniform way over all the columns. It is worth reminding that the pixel row distribution is linear as a function of the row number. During the readout process, rows farther from the amplifier experience a longer exposure time than the nearer ones. All the clusters (in background, source, and serial register runs) with at least 1 pixel at one of these warm columns or rows are excluded from the analysis. The pixel x (x_{pixel}) and y (y_{pixel}) distributions are shown in Figure 6.14. 19 warm columns are identified: $x_{pixel} \leq 7$, $x_{pixel} = 10$, $x_{pixel} = 15$, $x_{pixel} = 39$, $x_{pixel} = 47$, $x_{pixel} = 133$, $x_{pixel} = 166$, $x_{pixel} = 179$, $x_{pixel} = 225$, $x_{pixel} = 232$, $x_{pixel} \geq 254$. An excess of low energy clusters (energy below 70 eV) is localized on the active area edges and at specific columns (Figure 6.15). Therefore, also the first 3 and last 2 rows are excluded from the analysis ($y_{pixel} \leq 3$ and $y_{pixel} \geq 149$), together with columns at $140 \leq x_{pixel} \leq 145$ and $x_{pixel} = 113$. Note that the first 2 rows are excluded from the analysis by the initial hot mask.

---

9. For example, considering the spatial distribution of pixels inside clusters, the warm columns have on average from ~2% up to ~40% more counts per image than a standard column.
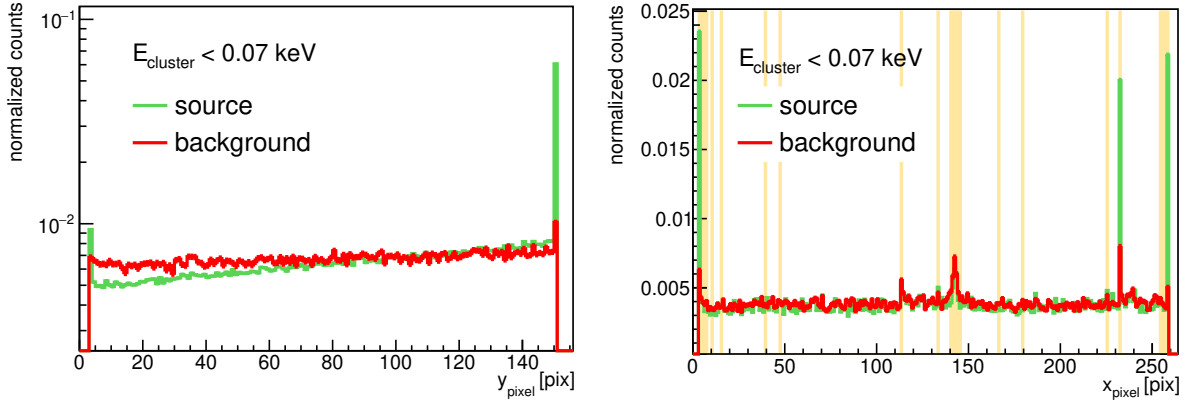
Figure 6.15 – y_{pixel} (left) and x_{pixel} (right) distributions, normalized by its own area. The orange bands indicate the selected warm columns.

6.5 Simulations

Geant4 simulations were run by the DAMIC-M collaboration to validate the data analysis methods, determine the reconstruction efficiency and interpret the results. The implemented setup geometry is shown in Figure 6.16. The Livermore low-energy electromagnetic models are used for the simulations.
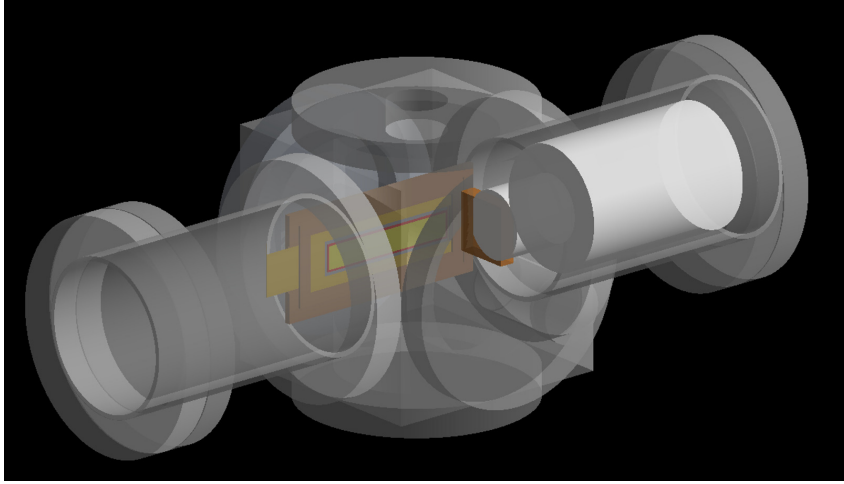
Figure 6.16 – Visualization of the calibration chamber as constructed in the Geant4 simulation framework. The CCD is shown in yellow, the silicon plate is shown in red, the kapton cable in orange, and the copper plate in brown. The aluminum shielding was excluded for the sake of clarity.

Geant4 provides the energy E_{dep} deposited by particle interactions in the silicon bulk

of the CCD as well as its location (x-y-z). WADERS (described in Section 4.2) is then used to convert the energy into number of electrons, apply the Fano factor smearing and diffusion process. The "advanced" approach, described in Section 4.2.1, is used to calculate the number of electron-hole pairs produced by a given energy deposit. The charges are then laterally diffused according to the parameters measured in the same CCD with cosmic ray tracks [10], following the procedure described in [78] (see also Section 2.2.3) and using 1×1 binned images to maximize the spatial resolution. The following parameters are obtained: A = 349 ($\pm$ 56) μm^2, B = 6.22 $\cdot 10^{-4}$ ($\pm$ 0.49 $\cdot 10^{-4}$) μm^{-1}, α_0= 0.975, $\alpha/\sigma_{xy}(z = z_{\rm D}, {\rm E} = 0)$= 0.0113 keV^{-1} (see equation 4.9). The α_0 and α parameters take into account the energy dependence of the diffusion process. They are obtained by fitting to a linear function the maximum observed spread of cosmic ray clusters as a function of energy (in 1 keV slices from 3 to 18 keV). The measured mean value of the maximum diffusion (at the back of the CCD) is equal to 13.44 ± 0.03 μm.

(a)   (b)
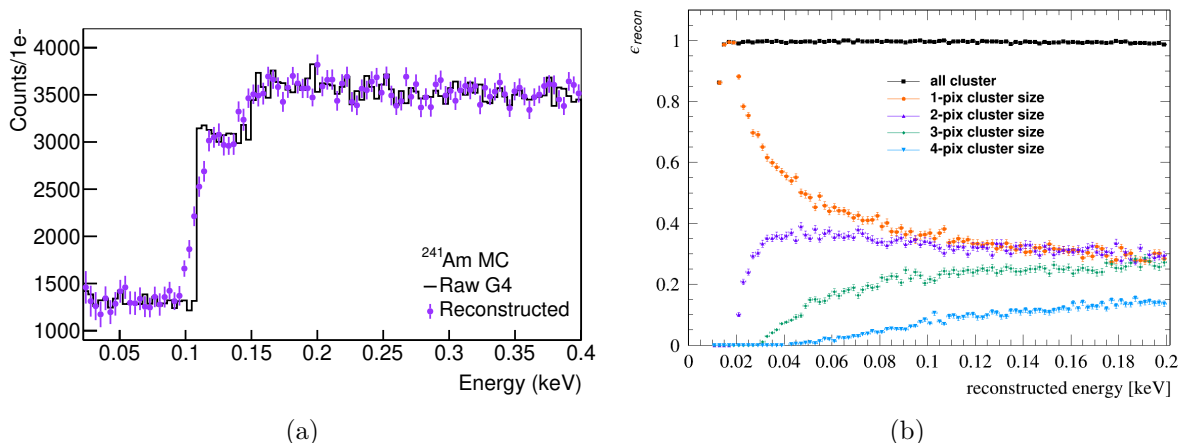
Figure 6.17 – (a): Reconstructed low-energy spectrum from the Monte Carlo simulation of the Compton scattering experiment (purple). The spectrum reproduces the expected features of the Relativistic Impulse Approximation model implemented in Geant4 (black, generator level spectrum). The smearing in the reconstructed spectrum comes from the Fano resolution and pixel readout noise. (b): Reconstruction efficiency for simulated events with energy between 0 and 200 eV and cluster sizes between 1 and 4 pixels.

In simulations, the average energy to produce an electron-hole pair ($\epsilon_{\rm eh}$) is assumed to

---

10. Being the cosmic rays minimum ionizing particles (MIPs), their tracks follow a straight line with a relatively constant energy deposition per unit length. Cosmic ray tracks show a large (narrow) area of diffusion where the MIP crosses the back (the front) of the CCD. By fitting the width of the MIPs that penetrate the CCD as a function of depth, diffusion parameters can be retrieved.

be 3.74 eV, as for real data. The Fano factor (F) is set to 0.128 as measured in [82]. Other measurements at similar temperatures observed a value near $F = 0.118$ [81, 160], however this has a negligible impact on the smeared spectrum. The simulated clusters are then pasted onto images from the serial register data set ("blanks") to properly include the pixel readout noise, the dark current and the presence of other tracks. In fact, serial register data are found to have the major contribution at low energies (see Section 6.6.2). The number of simulated clusters pasted per image and their spatial distribution is chosen to reproduce the rate of events for source data. Going farther from the amplifier, the rows experience an increasing exposure. Therefore, clusters are pasted into blank images accounting for this row dependence. Blanks images in ADU units are converted in e^- units using the calibration of equation 6.6. The final image, after having pasted simulated clusters, is then converted again in ADU using a constant gain (5.18 ADU/e^-). This simulation process results in a set of images which closely resembles the source data and can be processed through the same analysis chain used for real data. The reconstructed energy spectrum from simulated images is shown in Figure 6.17 (a) between 20 eV and 0.3 keV. The spectrum matches the expected features of the RIA model implemented in Geant4, indicating that clusters are reconstructed with high efficiency and accuracy.

The reconstruction efficiency is estimated via a dedicated Monte Carlo simulation. This efficiency measures both the fraction of clusters with a given size and energy and how accurately specific energies are reconstructed. Point-like energy deposits from a uniform energy and spatial distribution are generated, diffused and pasted onto images from the background data set. The same reconstruction process used for real data is then applied. The efficiency is quantified as:

$$\epsilon_{total}(E) = \sum_i \epsilon_i(E) = \sum_i \frac{N_i^{reconstructed}(E)}{N_i^{simulated}(E)} \tag{6.8}$$

where $N_i(E)$ is the number of clusters made of i pixels with a given energy (E) and ϵ_i is the related reconstruction efficiency. The reconstruction efficiency is determined to be near 100% down to 15 eV, as shown in Figure 6.17(b).

6.6   Data analysis

6.6.1   Optimization of the CCD operating parameters

As mentioned in Section 6.3, data are collected with two different configurations, standard and optimized. In the source runs acquired with the standard CCD parameters, the cluster topology changes while moving along the columns (x-axis). In particular, 3 different zones are identified:

— 1st zone: x < 43,

— 2nd zone: 45 < x < 118,

— 3rd zone: x > 120,

where the clusters show (from the 1st to the 3rd zone):

— an increasing mean number of pixels,

— an increasing mean size on the x-axis (DX) [11],

— a decreasing mean pixel charge,

— an increasing asymmetry on the x-axis with respect the maximum pixel charge (A_x).

This effect is less visible in the background data.
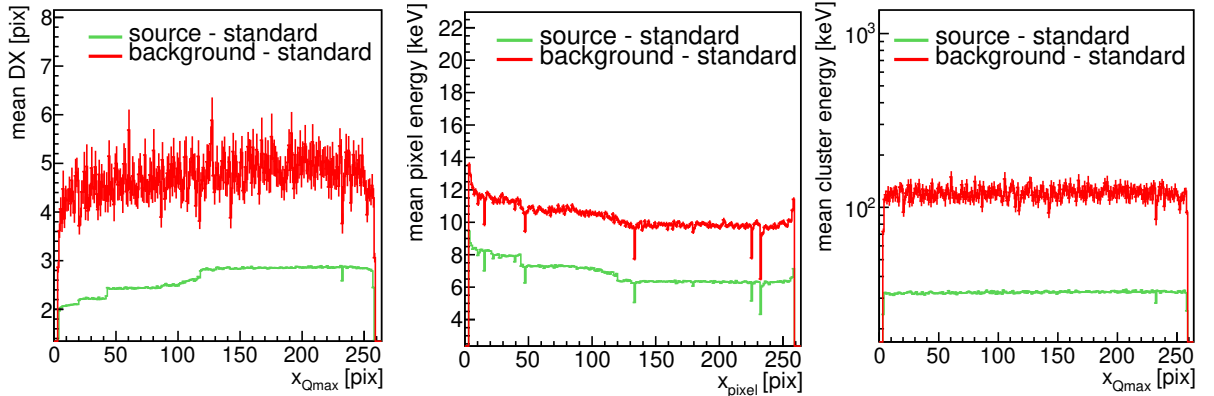
Figure 6.18 – Left: Mean DX as a function of x_{Qmax} for all standard source and background runs. Center: Mean pixel energy as a function of x_{pixel} for all standard source and background runs. The hot columns are visible as dips in the distributions. Right: Mean cluster energy as a function of x_{Qmax}.The hot columns are visible as dips in the distributions.

This anomalous phenomenon is investigated in order to understand the impact on

---

11. The variable DX is calculated as $x_{pixel}^{max} - x_{pixel}^{min} + 1$, where x_{pixel}^{min} and x_{pixel}^{max} are the extreme x positions of the pixels in the cluster.

the cluster energy spectrum, especially at low energies. Figure 6.18 (Left) shows the mean DX distribution as a function of the x position of the maximum charge pixel in a cluster (x_{Qmax}) for all background and source standard runs. In Figure 6.18 (Center), the mean pixel energy distribution as a function of x_{pixel} (x position of a pixel in a cluster) is reported. In both Figures 6.18 (Left) and (Center), the "zone" effect is clearly visible for source data, while it is less evident for background data. Figure 6.18 (Right) shows instead the mean cluster energy distribution as a function of x_{Qmax}, which is constant over all the x_{Qmax} range for source and background runs. This means that, as moving farther from the amplifier, from the 1st to the 3rd zone, clusters are longer and longer (on the x axis) and their energy is distributed over more and more pixels, which individually carry less and less energy.

(a)   (b)   (c)
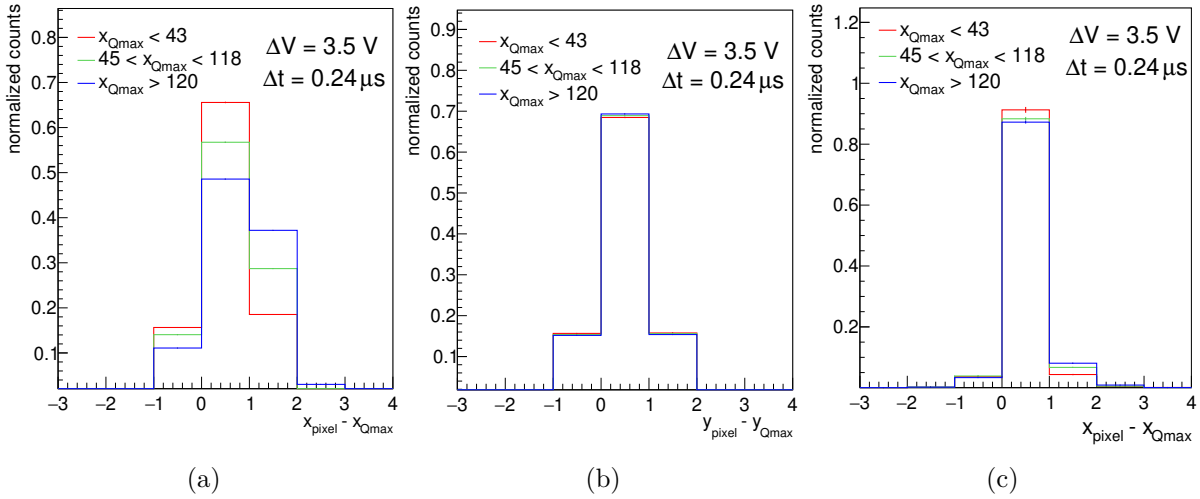
Figure 6.19 – (a): a_x (in pixel units) distribution for all standard source runs. $\Delta_{\mathcal{I}_x}$ = -0.030 (1st zone), -0.15 (2nd zone), -0.29 (3rd zone). A compatible distribution can be observed also using only 1 source run. (b): a_y distribution for all standard source runs. $\Delta_{\mathcal{I}_y}$ = -0.0010 (1st zone), -0.0024 (2nd zone), -0.0021 (3rd zone). (c): a_x distribution for all standard background runs. $\Delta_{\mathcal{I}^x}$ = -0.011 (1st zone), -0.032 (2nd zone), -0.055 (3rd zone). The histograms are normalized to their area. Only clusters with energy less than 3 keV are considered. Clusters with at least 1 pixel at one warm column or row are excluded.

The cluster asymmetry on the x-axis (A_x) is also studied and is calculated from the distribution of the a_x variable defined as:

$$a_x = x_{pixel} - x_{Qmax}. \tag{6.9}$$

This distribution is expected to be symmetric from simulations. The A_x value is then calculated as:

$$A_x = |\Delta_{\mathcal{I}_x}| = |\mathcal{I}_l - \mathcal{I}_r|, \tag{6.10}$$

where $\mathcal{I}_l$ is the integral to the left and $\mathcal{I}_r$ the integral to the right of the a_x distribution (excluding the bin containing $a_x = 0$). If the a_x distribution is symmetric, then $\Delta_{\mathcal{I}_x}$ is expected to be close to zero. Instead, if the pixels inside the cluster are more distributed after (before) the pixel with maximum energy, $\Delta_{\mathcal{I}_x}$ takes negative (positive) values.

Source and background data show a decreasing value of $\Delta_{\mathcal{I}_x}$ while moving from the 1st zone to the 3rd one, as reported in Figure 6.19 (a and c). Therefore clusters feature a longer and longer tail after the pixel with maximum energy as moving farther from the amplifier. On the contrary, the a_y distributions obtained for the same set of source runs are symmetric, as shown in 6.19 (b).
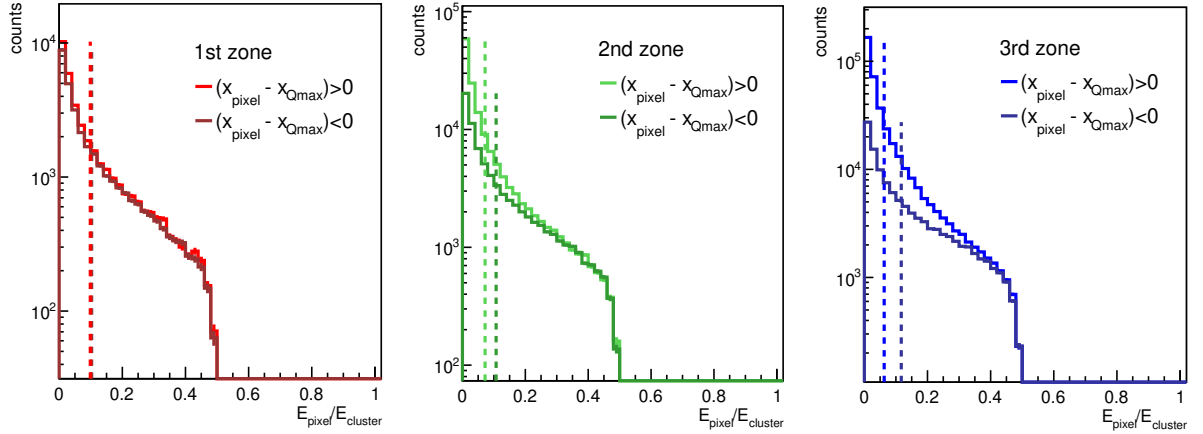
Figure 6.20 – $E_{pixel}/E_{cluster}$ distribution of pixels with $a_x > 0$ and $a_x < 0$, for the 3 different zones. All source standard runs are considered. The dashed lines indicate the mean value for each distribution. The clusters with DY = 1 (horizontal and single pixel clusters) are excluded.

The spatial distribution of energy inside a cluster is also investigated, in particular by looking at the fraction of energy ($E_{pixel}/E_{cluster}$) brought by pixels with $a_x > 0$ and $a_x < 0$. Figure 6.20 shows the distributions of the $E_{pixel}/E_{cluster}$ variable for the 3 different zones. In the 1st zone, the pixels with $a_x > 0$ carry on average the same fraction of energy than the pixels with $a_x < 0$. As moving farther from the amplifier, in the 2nd and 3rd zones, the average $E_{pixel}/E_{cluster}$ value for pixels with $a_x > 0$ is smaller and smaller with respect to the one for pixels with $a_x < 0$.

(a)   (b)   (c)
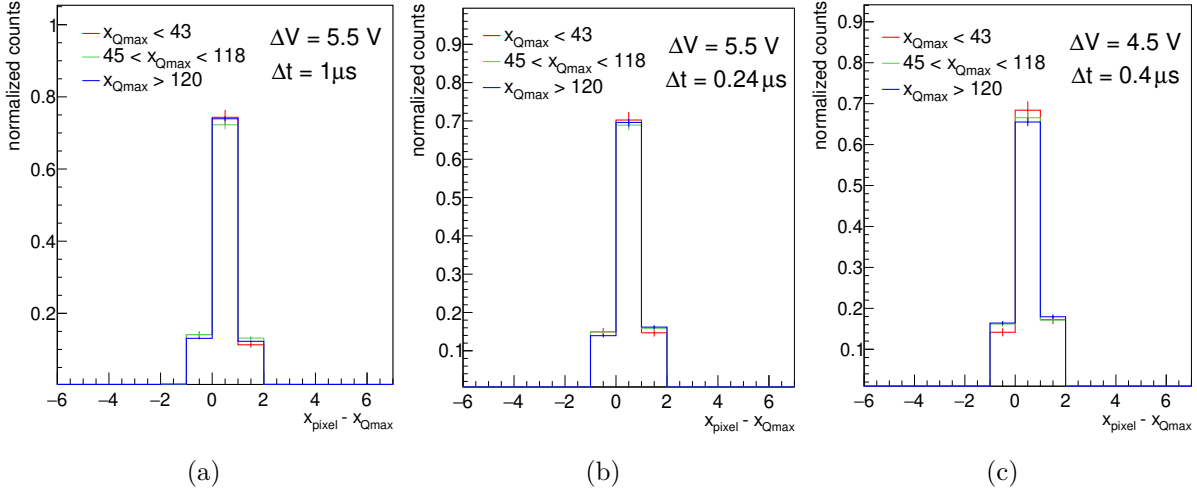
Figure 6.21 – a_x (in pixel units) distribution for the source runs with different CCD parameters (400 images for each set of parameters). The histograms are normalized to their area. (a): $\Delta_{\mathcal{I}^x}$ =0.030 (1st zone),0.0092 (2nd zone), 0.0088 (3rd zone) . (b): $\Delta_{\mathcal{I}^x}$ = 0.0026 (1st zone), -0.010 (2nd zone), -0.023 (3rd zone) . (c): $\Delta_{\mathcal{I}^x}$ = -0.033 (1st zone), -0.0098 (2nd zone), -0.016 (3rd zone). Only clusters with energy less than 3 keV are considered. Clusters with at least 1 pixel at one warm column or row are excluded.

This zone effect arises while moving the charge along the serial register. It is therefore possible to minimize it by changing (increasing) some of the horizontal clock parameters: the amplitude (ΔV) and the time width (Δt). To find the optimal serial clock parameters, different value are assessed. Three test runs (each made of 400 images) are acquired with 3 different sets of ΔV and Δt values: ΔV = 5.5 V and Δt = 1 μs , ΔV = 5.5 V and Δt = 0.24 μs, ΔV = 4.5 V and Δt = 0.4 μs. As shown in Figures 6.21 and 6.22, by increasing the ΔV and time width, the zone effect is reduced. In particular, Figure 6.21 reports the a_x distributions obtained for the test runs. Figure 6.22 (a) shows the associated $\Delta_{\mathcal{I}^x}$ values and compares them with the ones obtained for standard runs. It can be observed how the asymmetry of the a_x distributions is drastically reduced for test runs. A comparison between the mean pixel energy distributions as a function of x_{pixel} obtained for all standard source and test runs can be found in Figure 6.22 (b).

As optimal horizontal clocks parameters ΔV = 4.5 V and Δt = 0.4 μs are selected. In fact, using ΔV = 5.5 V triggers the appearance of warm columns between $x_{pixel} = 153$ and $x_{pixel} = 157$, as also visible in Figure 6.22 (b). Further background and source images are acquired with the optimized configuration, achieving a total exposure time of 80.1
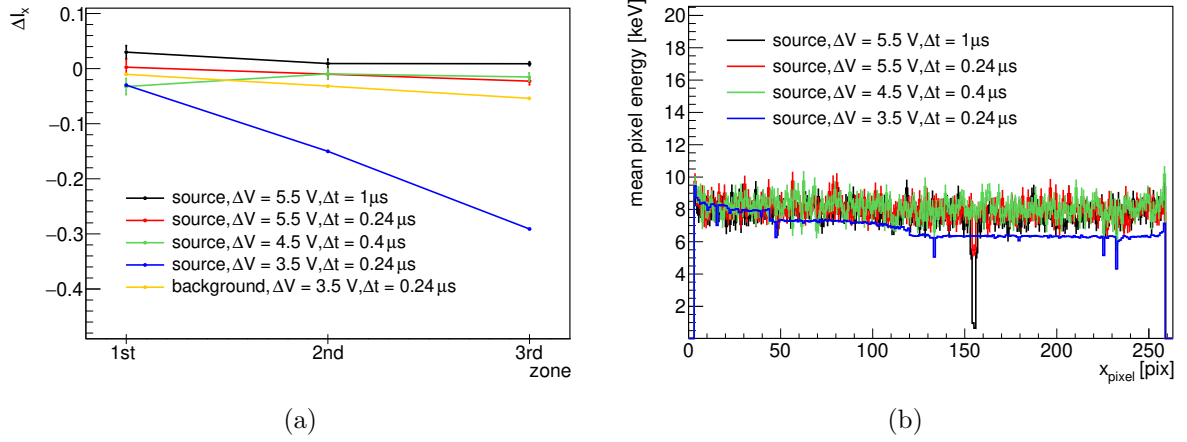
Figure 6.22 – (a): $\Delta_{\mathcal{I}^x}$ values as a function of zone obtained for the 3 test runs and for all the standard source and background runs. Also by using only 1 source run, a statistically significant difference between the 2nd and 3rd zone $\Delta_{\mathcal{I}^x}$ values for source and test runs is observed. (b): mean pixel energy as a function of x_{pixel} for all standard source and test runs. The hot columns are visible as dips in the distributions.

days (15.5 days) for source (background) runs. Figure 6.23 shows a comparison between the mean DX and pixel energy distributions as a function of columns obtained with the standard and optimized configurations, confirming the attenuation of the zone effect in the new runs case.

Finally, the cluster energy spectra obtained for standard and new optimized runs are compared within each other. The two distributions are found to be compatible, as shown in Figure 6.24. Therefore both the data sets are used for the analysis.

6.6.2 Compton spectrum measurement

By applying the analysis procedure described in the previous sections, cluster energy spectra are derived from the source, background, and serial register data.

The distributions are shown in Figure 6.25 for energies up to around 18 keV. Higher energies are affected by saturation effects in the electronics, which is optimized for single-electron resolution and low energy measurement. The spectra corresponding to background and serial register data are normalized to the exposure time of the ^{241}Am source data. Characteristic features of the Compton scattering of the 59.54 keV γ-ray in silicon, as the Compton edge at 11.2 keV and the K-shell step at 1.8 keV, are visible in the measured spectrum. The γ-ray lines between 10 keV and 24 keV usually observed with ^{241}Am

(a)   (b)
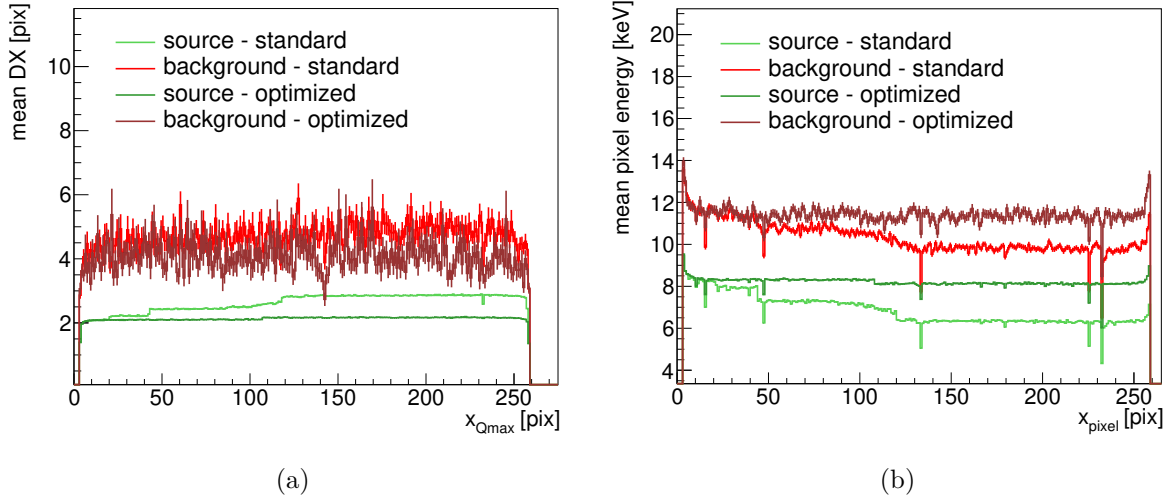
Figure 6.23 – (a): mean DX as a function of x_{Qmax} for all standard and optimized ($\Delta V = 4.5$ V, $\Delta t = 0.4$ μs) runs. (b): mean pixel energy as a function of x_{pixel} for all standard and optimized runs. The hot columns are visible as deeps in the distributions.

(a)   (b)
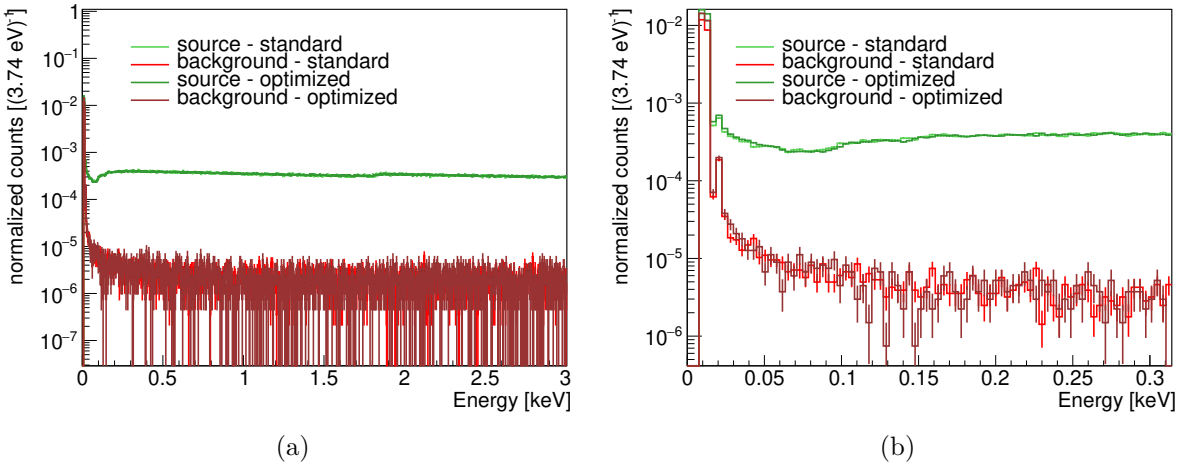
Figure 6.24 – (a): Cluster energy spectra obtained for standard and optimized runs. (b): Zoom at low energies of the cluster energy spectra obtained for standard and optimized runs. The spectra are normalized to the corresponding exposure time.

are not present since they are blocked by the aluminium shield in front of the source (as described in Section 6.2).

The background contribution is very small above $\approx$1 keV, while rises in the L-shell region. However, the background only spectrum is not enough to fully explain the increase
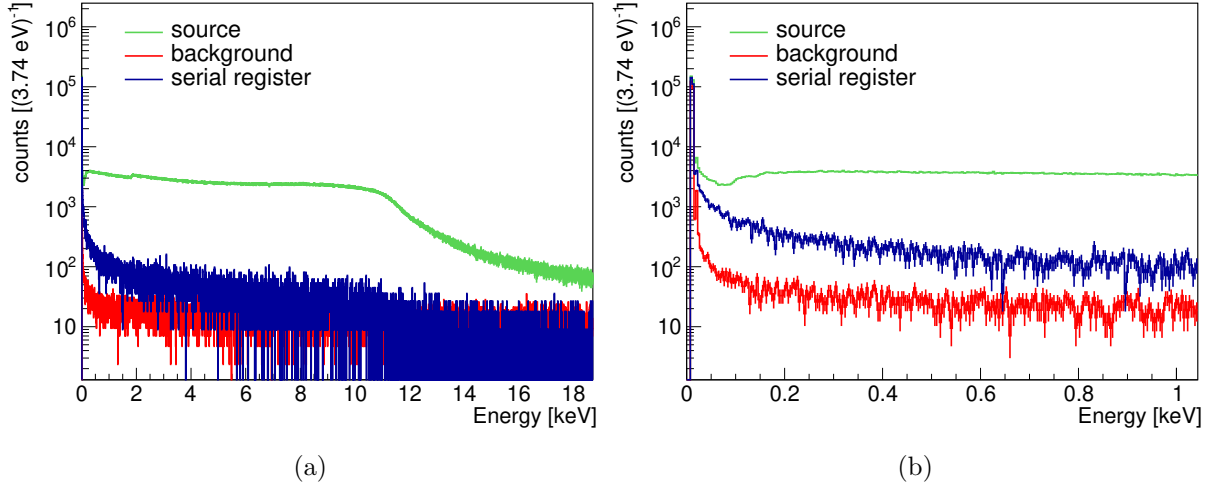
Figure 6.25 – (a): Cluster energy spectra obtained for source, background and serial register data. The background and serial register spectra are normalized to the exposure time of the source data set. (b): Zoom at low energies of the cluster energy spectra obtained for source, background and serial register data.

of events in the low energy part of the source spectrum. An extra source of background is present in source data: the so-called "horizontal clusters" from the serial register, already mentioned in Section 6.4.1. These events are caused by particles (cosmic rays, natural radiation, gammas from ^{241}Am) hitting the serial register and generating charge. As the rows are read out, the clusters are reconstructed as horizontal tracks in the CCD active area. If the particle energy is not fully deposited, the resulting horizontal cluster contains only a few pixels and cannot be distinguished (by its topology) from real low energy events. The number of horizontal clusters is directly proportional to the incident particle flux. Therefore, background data features a lower number of horizontal clusters with respect to data acquired in presence of the ^{241}Am source. This also explains the mismatch in the dark current level between source and background data (Figure 6.10, b). To characterize the serial register events, images are taken with the source in place and with vertical clocks moving the charge from the CCD active area towards the serial register opposite to the one used for readout (serial register data set). This operating mode results in images containing only clusters originating in the serial register. The image processing confirmed that the rate of horizontal clusters with the ^{241}Am source is a factor of ten higher than the rate of clusters measured in the standard background runs. To increase the statistics of the serial register data set, clusters in the overscan of the

source images are also considered. In fact, clusters in this region are also originated by the interaction of particles in the serial register (or nearby areas). The exposure time of the serial register data sets is therefore increased of about 4.8 days (with respect the time reported in Table 6.3) [12]. Serial register data spectrum is also shown in Figure 6.25. The same analysis procedure used for source and background data set is applied. Only two hot columns are identified for overscan data (columns 261 and 275), showing an excess of 1 pixel clusters. Clusters with at least one pixel at one hot column or one of the hot rows identified for the source and background data sets, are excluded from the overscan (serial register) data sets.

(a) (b)
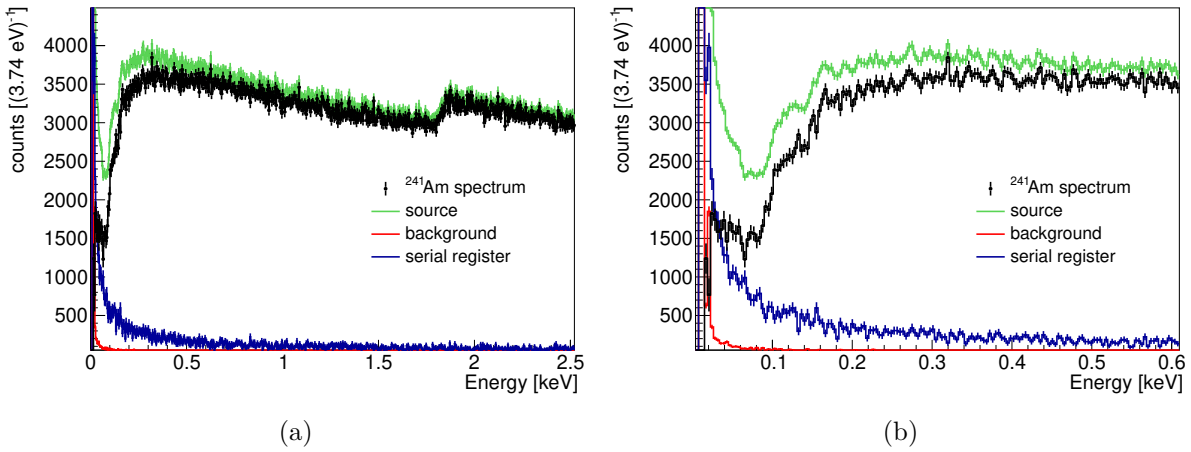
Figure 6.26 – (a): The subtracted ^{241}Am Compton spectrum (black). To illustrate the measurement components, the normalized spectra used in the subtraction are shown: ^{241}Am source (green), ^{241}Am serial register (blue), and background (red). (b): zoom at low energies of the subtracted ^{241}Am Compton spectrum and the subtraction components.

Two methods are developed to clean the source spectrum from background (standard background and serial register events) contributions. In the first method, a bin-by-bin subtraction of the serial register and standard background spectra from the ^{241}Am source spectrum is performed. The subtracted spectra are normalized to the exposure time of the source data. This approach accounts for both the increased rate of horizontal clusters due to the source (serial register background) and background clusters in the CCD active

---

12. This exposure time is calculated taking into account the overscan area (150 rows, 15 columns) and the identified hot columns and rows: $t_{overscan} = t_{image} \cdot (15 - Nx_{hot}^{overscan})/(256 - Nx_{hot}^{active})$. The t_{image} value indicates the full exposure time of the images from which the overscan portion is extracted. Nx_{hot}^{active} and $Nx_{hot}^{overscan}$ are the number of hot columns in the active and overscan region. The same hot rows found in the active region are excluded from the overscan data.

area from cosmic rays and radiogenic sources in the apparatus (standard background). The ^{241}Am spectrum after the bin-by-bin subtraction method is shown in Figure 6.26. In
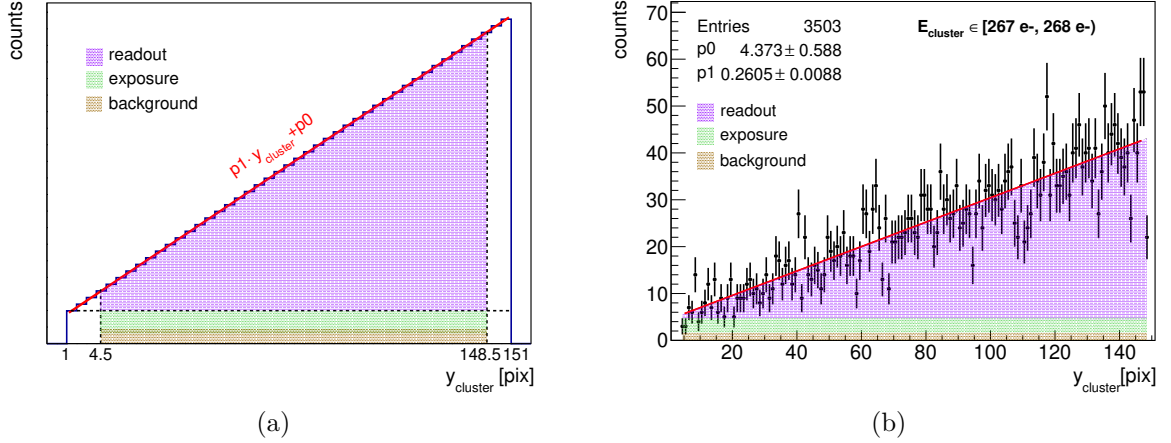
Figure 6.27 – (a): Schematic illustration of the data-driven subtraction approach. The row (y_{cluster}) distribution is fitted with a linear function (counts = p1 · y_{cluster} + p0). The y_{cluster} is calculated as the energy weighted average of the y positions of the pixels in a cluster. The area of the trapezium (purple) is taken as an estimate of the signal. The small rectangle right below (green) accounts for 3 s exposure before the readout. The brown rectangle represents the subtracted background. (b): Number of reconstructed clusters with energy in the example interval [267 e^-, 268 e^-) as a function of row (y_{cluster}) in the CCD. The red line indicates the linear fit. Note that the histogram (bin width = 1) is filled for $4 \leq y_{\text{cluster}} \leq 148$ since all the clusters with at least one pixel at one warm row are excluded from the analysis.

the second method, a data-driven approach uses only the ^{241}Am source data to estimate the background and select only Compton scattered events. The approach is illustrated in Figure 6.27. Due to the sequential readout of the CCD, the effective exposure time of a row increases linearly with its readout order. Therefore, the number of clusters produced by Compton scattering in the active area increases as a function of row position in the image. On the contrary, the number of horizontal clusters remains constant since the exposure time in the serial register is the same for all rows. It is thus possible to evaluate the signal by performing a linear fit of the number of clusters as a function of row. The estimated signal is represented by the area of the trapezium (purple) illustrated in Figure 6.27. A small correction ($\approx$16%) is applied to take into account that the CCD is exposed for 3 s, during which clusters accumulate uniformly over the rows (while the readout process lasts about 37 s). This procedure is repeated for each energy bin, with

197

a size of 3.74 eV (1 e$^-$). The final ^{241}Am spectrum is shown in Figure 6.28 and it is
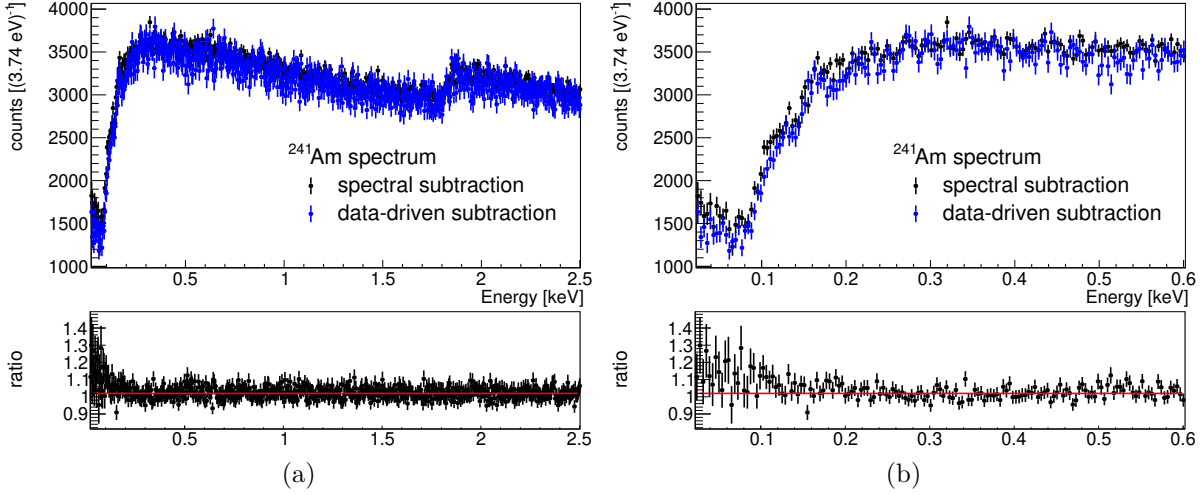
Figure 6.28 – (a): Comparison of the ^{241}Am spectra obtained via the spectral subtraction (black) and the data driven subtraction (blue) methods. The two spectra are not normalized to each other. The ratio between the two distributions (counts$_{spectral}$/counts$_{data-driven}$) is shown in the bottom panel. The red line is the result of the fit to a constant (p0) between 0.025 and 2.5 keV: p0 = 1.020 ± 0.002. (b): zoom at low energies of the two spectra.

compared with the one obtained with the first method. The two spectra are in agreement and show similar features. It should be noted that the spectra are not normalized to each other. Their agreement in the absolute rate indicates that the same amount of signal is recovered by both methods. This is demonstrated by the (bin-by-bin) ratio between the two spectra which is constant and close to one over the whole energy range (see bottom panels of Figure 6.28), exception made for energies < 0.1 keV. In fact, at low energies, the data-driven method is able to clean more properly the spectrum than the other approach. However, the uncertainties on data are lower in the spectral subtraction case. The second approach is also applied to the serial register background data set, verifying that the rate of horizontal clusters does not depend on the row number.

6.6.3 Comparison with theoretical models

The accurate estimate of the contribution to the background of low energy events from Compton scattering of radiogenic γ-rays is crucial for DAMIC-M as well as for the other future direct detection experiments with energy thresholds of $\sim$10 eV [54, 161–163].

Usually these experiments rely on Monte Carlo packages as Geant4 [138] and MCNP [164] to model the background spectrum. Both simulation codes use the RIA model to describe Compton scattering. The measured spectra (obtained from both the spectral and data-driven subtraction methods) are used to test the validity of the RIA model, and thus the appropriateness of these Monte Carlo simulations, in an unexplored energy range, down to 23 eV. It is worth reminding that the assumptions of the RIA model are not valid for energy transfers close to the electron binding energy and its predictions may not be inaccurate near the silicon steps.
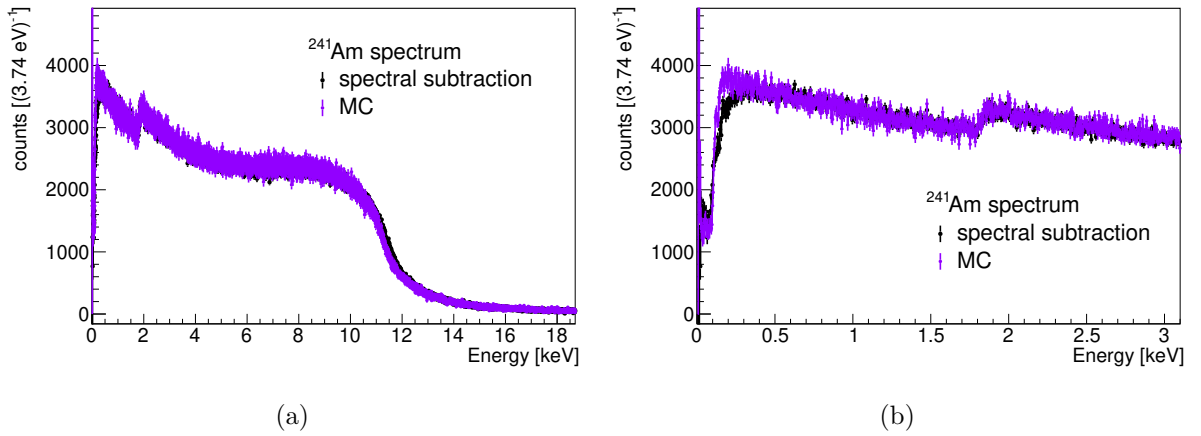
Figure 6.29 – (a): Measured (subtracted) ^{241}Am source spectrum (black). The normalized spectra from the Monte Carlo simulation is also shown (purple). In particular, the simulation spectrum is normalized to the area of the ^{241}Am source data between 1.5 keV and 3.0 keV (b): Zoom at low energies of the spectra.

The subtracted ^{241}Am spectrum is compared with the one obtained from Monte Carlo simulation (Figure 6.29), which incorporates both the RIA model and the detector response (Section 6.5). The Monte Carlo spectrum is obtained by subtracting to the energy distribution obtained from clusters pasted on blanks the one from the blanks only. A slight mismatch above the Compton edge is observed, due to limitations in extrapolating the calibration curve, which is measured only up to 2.1 keV, being the electronics optimized for the L-shell region (Section 6.4.4), to higher energies.

In alignment with the previous result in [82], the measured spectrum is in a good agreement with the Monte Carlo at the K-shell, as shown in Figure 6.29 (b). In particular, the K-shell step and slopes of the spectrum before and after the K-shell energy are reproduced. The simulated Geant4 Compton spectrum is in agreement with data
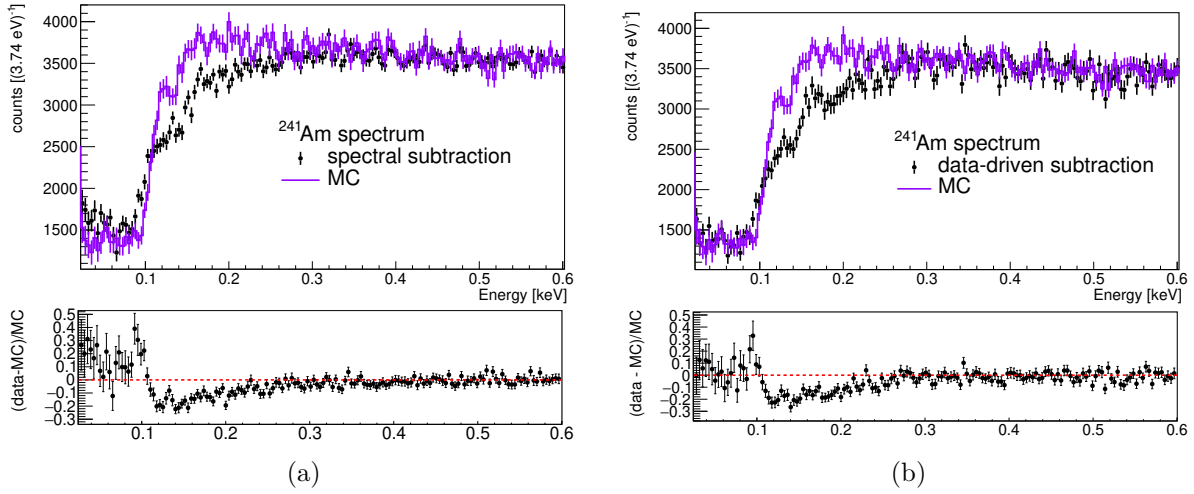
Figure 6.30 – Measured (subtracted) ^{241}Am source spectrum (black) obtained with the spectral subtaction (a) and data-driven method (b). The normalized spectra from the Monte Carlo simulation is also shown (purple). The simulated spectrum is normalized to the area of the ^{241}Am source data between 1.0 keV and 3.0 keV. The fractional residuals are shown in the bottom panel.

down to about 0.5 keV. However, the simulated and measured energy distributions differ notably in the L-shell region, as shown in Figure 6.30 (a). In particular, a softening is observed below 0.5 keV, confirming what previously measured in [82]. The two steps ($L_{2,3}$ and L_1) features, predicted by the RIA model, seem to be reproduced by data but with a softer shape. A plateau can be observed below the $L_{2,3}$ energy (99.2 eV) corresponding to Compton scattering with only valence electrons. Its measured amplitude is consistent with the expectation of scaling by the number of electrons available in the shell, although the height of the plateau is slightly overestimated with respect to the MC prediction. This discrepancy is attenuated in the case of the spectrum obtained with the data-driven method (Figure 6.30, b). Overall the Geant4 Monte Carlo overestimates the measured spectra by up to about 25% below 0.5 keV and in the L-shell region, as shown in Figure 6.30.

The measured spectra are then compared with *ab initio* calculations from the FEFF code (see Section 6.1). The FEFF predictions are obtained by computing the corresponding $S_{nl}(q, E)$ (see Equation 6.3) in discrete steps of $q(\cos\theta)$ and E and summing over all scattering angles. The code used is FEFF10 with configuration and silicon crystal structure from the Materials Project [165] (Materials Id mp-149). Further details about the

computation are reported in [127]. It is worth noting that the FEFF code was initially run with a configuration (`Corehole Rpa`) which uses an approximation similar to that in the Bethe-Salpeter equation (BSE) [166] to treat the interaction of the photoelectron with the vacated core-hole. This resulted in an L-step that was too sharp with respect to data. The configuration was thus changed (`Corehole none`) for the L-shell to neglect the core-hole interaction, providing a much better match to the data. This is consistent with previous NRIXS measurements in silicon, where the omission in the calculation of the core-hole interaction with the photoelectron was observed to better match the spectrum in the extended energy region [167, 168]. For a realistic comparison of the FEFF model, the spectrum is convoluted with the detector response of the silicon CCD, considering the experimental energy resolution (σ_E). The latter is calculated as:

$$
\begin{aligned}
\sigma_E^2 &= \sigma_F^2 + \sigma_C^2, \\
\sigma_F^2 &= \mathrm{F} \cdot \mathrm{E} \cdot \epsilon_{\mathrm{eh}}, \\
\sigma_C^2 &= \mathrm{N_{pix}} \cdot \sigma_{\mathrm{pix}}^2,
\end{aligned}
\tag{6.11}
$$

where F is the Fano factor, E the cluster energy, ϵ_{eh} the mean energy per electron-hole pair, N_{pix} the number of pixels in a cluster, σ_{pix} the single pixel readout noise. To smear the FEFF spectrum, $\sigma_C = 0.9$ e$^-$ and F = 0.128 are assumed [13].

The FEFF spectrum before and after applying the detector resolution is shown in Figure 6.31. The FEFF prediction is compared with the measured Compton spectrum in Figure 6.32 and shows a good agreement with the data over the entire energy range. In particular, FEFF reproduces the L-shell features to better than 10% (down to 0.1 keV), where a softening of the spectrum is observed and the RIA model fails. The spectral subtraction spectrum overestimates the number of events in the plateau region (below 0.1 keV) up to 35% from the FEFF prediction, as visible in the bottom panel of Figure 6.32 (b). This disagreement reduces to 25% in the case of the spectrum obtained with the data-driven method.

To have further insight into the measured spectrum features, data are fitted between 0.025 keV and 3.0 keV with an empirical function. The fitting function consists of a series of Erfc functions centered at the different shell step locations and with a correction to

---

13. The σ_C value is obtained from data, averaging the mean cluster readout noise (σ_C) at the L-shell (about 0.8 e$^-$) and K-shell (about 1 e$^-$). A $\sigma_{pix} = 0.6$ e$^-$ is assumed. This value is calculated by using the calibration equation to trasform the median of the σ_{ovs} values (Figure 6.8) in electron units. Using an energy dependent σ_C does not change in a significant way the shape of the spectrum, being the σ_C factor negligible with respect to the Fano factor one (σ_F).
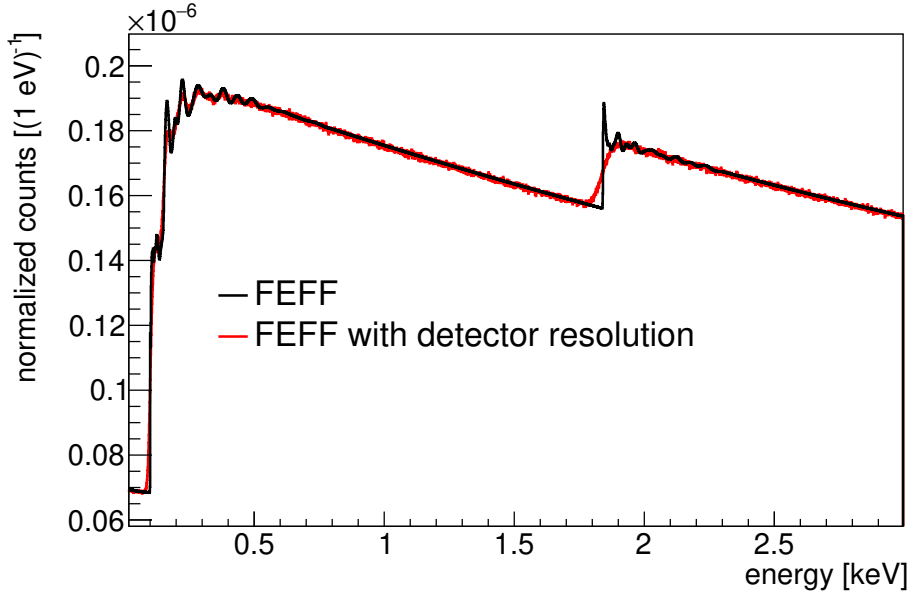
Figure 6.31 – The normalized FEFF spectrum before and after the dectector resolution smearing.

(a)   (b)
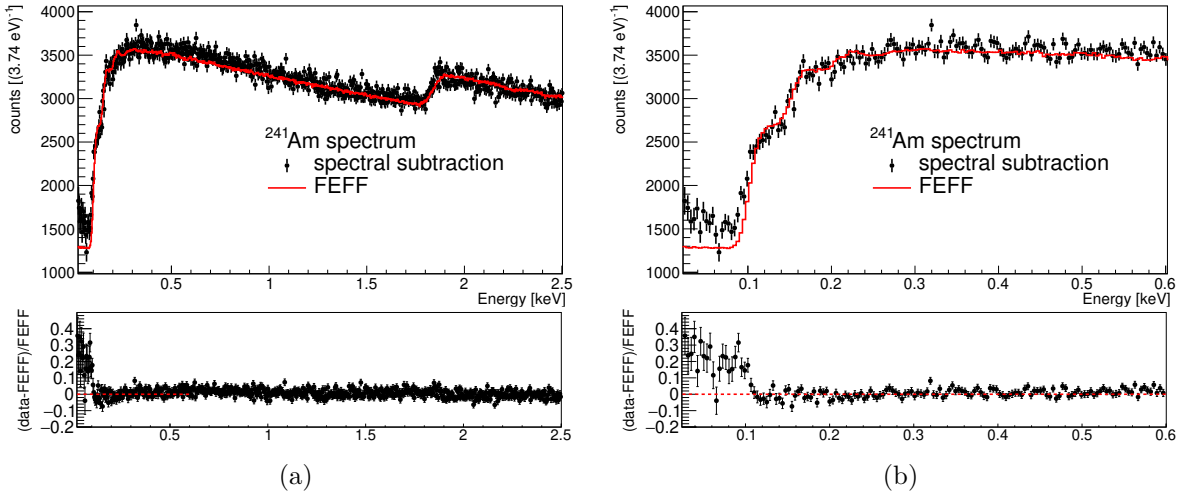
Figure 6.32 – (a): The measured ^{241}Am spectrum (black), obtained with the spectral subtraction method and the normalized FEFF spectrum (red). In particular, the FEFF spectrum is normalized to the area of the ^{241}Am spectrum between 1.0 keV and 2.5 keV. The fractional residuals are shown in the bottom panel. (b) Zoom at low energies of the spectra in (a).

take into account the slopes between the steps:

$$f(x) = h_0 + f_{L2,3}(x) + f_{L1}(x) + f_K(x) + f_{soft}(x), \tag{6.12}$$

where h_0 is the height before the $L_{2,3}$ step and $f_{L2,3}(x)$, $f_{L1}(x)$, $f_K(x)$, and $f_{soft}(x)$ describe the spectrum in the $L_{2,3}$, L_1, K step and softening regions, respectively. The latter are defined as:

$$
\begin{aligned}
f_{L2,3}(x) &= \frac{(N_{L2,3} + s \cdot x)}{2} \mathrm{Erfc}\left(\frac{-\mathrm{x} + \mathrm{L}_{2,3}}{\sqrt{2}\sigma_{\mathrm{L}2,3}}\right), \\
f_{L1}(x) &= \frac{N_{L1}}{2} \mathrm{Erfc}\left(\frac{-\mathrm{x} + \mathrm{L}_1}{\sqrt{2}\sigma_{\mathrm{L}1}}\right), \\
f_K(x) &= \frac{(N_K + s_{corr} \cdot x)}{2} \mathrm{Erfc}\left(\frac{-\mathrm{x} + \mathrm{K}}{(\sqrt{2}\sigma_{\mathrm{K}}}\right), \\
f_{soft}(x) &= \frac{N_{soft}}{2} \mathrm{Erfc}\left(\frac{-\mathrm{x} + \mathrm{step}_{\mathrm{soft}}}{\sqrt{2}\sigma_{\mathrm{soft}}}\right),
\end{aligned}
\tag{6.13}
$$

where N_{L1}, $N_{L2,3}$, and N_K are the normalization parameters, while s and $s + s_{corr}$ are the slopes before and after the K step, respectively. Finally, $\sigma_{L2,3}$, σ_{L1}, σ_K describe the Gaussian spread around the step locations. Equation 6.12 (with $f_{soft}(x)$=0) is tested on the RIA model expectation [14] and MC simulations, showing a relative difference less than 1% and 10% respectively. The function in equation 6.12 is then tested on the FEFF spectrum. The fitting function agrees with the FEFF spectrum within less than 2%. These results confirm the goodness of the fitting function to properly describe data.

Equation 6.12 is then used to fit the measured spectrum obtained with the spectral subtraction method. All the parameters are left free. The results of the best fit is shown in Figure 6.33, together with the corresponding residuals to demonstrate the goodness of the fit.

The heights of the steps are expected to be proportional to the number of electrons enclosed in the corresponding shells. This hypothesis is tested on data, also in the L-shell region where the softening of the spectrum is observed. The height of the K-step can be obtained from the measured spectrum fit as $h_K = N_k + N_{soft} + N_{L1} + N_{L2,3} + h_0$ and can be compared with the height before the step ($h_K^* = N_{soft} + N_{L1} + N_{L2,3} + h_0$). The ratio h_K/h_K^* is equal to 1.06±0.08 and is compatible with the expected value 1.17 (14e$^-$/12e$^-$).

---

14. The RIA spectrum is obtained by convolving the distribution in Figure 6.2 with the detector resolution, as done in the FEFF case.
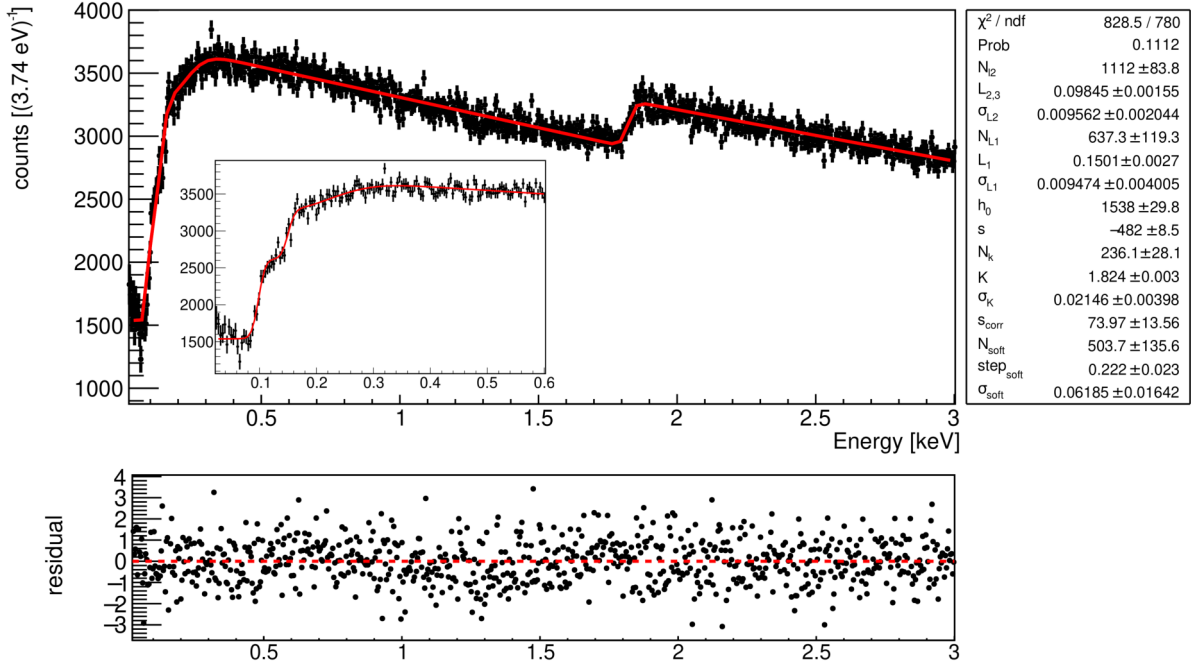
Figure 6.33 – Result of the fit (red) of the measured ^{241}Am spectrum (black) with equation 6.12. The ^{241}Am spectrum is obtained with the spectral subtraction method. The inset shows a zoom at low energies (L-shell energies). The residuals (the bin-by-bin difference between the two spectra and the fitting function, normalized to the data error) are shown in the bottom panel.

The L shell heights are calculated as: $h_{L2,3} = N_{L2,3} + h_0$ and $h_{L1} = N_{L1} + N_{L2,3} + h_0$. The ratio $h_{L1}/h_{L2,3} = 1.24 \pm 0.07$ is compatible with the expected value of 1.2 ($12e^-/10e^-$). A compatible result is obtained by fitting the FEFF spectrum (using the same data fitting function, in the same energy range). The $h_{L2,3}/h_0$ value (1.72 ± 0.07) is lower than expected ($10e^-/4e^- = 2.5$) due to the softening of data. Furthermore, it deviates from the FEFF spectrum value (equal to 2.1) by about 5σ [15]. This is due to the higher height of the plateau. For the same reason, the $(h_{L1} + N_{soft})/h_0$ ratio (2.46 ± 0.14) is not compatible within 3σ with the expected value ($12e^-/4e^- = 3$, the same retrieved also from the FEFF spectrum).

In the case of the data-driven method, the ratios between the heights of the steps are calculated following the same procedure described above. All the results (for the height ratio) are compatible with the ones derived for the spectral subtraction spectrum, exception made for the $(h_{L1} + N_{soft})/h_0$ (1.92 ± 0.07) and $h_{L2,3}/h_0$ (2.73 ± 0.12) values,

---

15. In this case, σ means the parameter error.

which in this case are compatible with the FEFF ones. In fact, the data-driven spectrum shows a lower plateau level. This stresses once again the capability of the data-driven method to clean more properly data at low energies than the spectral subtraction method, although with higher uncertainties.

Considering the fit of the spectrum from the spectral subtraction method, the L_1 and $L_{2,3}$ steps are reconstructed at the expected values, within the parameter errors. The K step location, instead, is not compatible with the nominal value (about 5σ from the predicted value). The same happens considering the fit of the data-driven approach spectrum. To investigate the K step location discrepancy, the fit is repeated restricting the fitting range around the K step for both the measured spectra. The same procedure is applied to the FEFF spectrum as comparison. The results are shown in Figure 6.34 for different fitting ranges. In all the cases, the step value decreases by increasing the
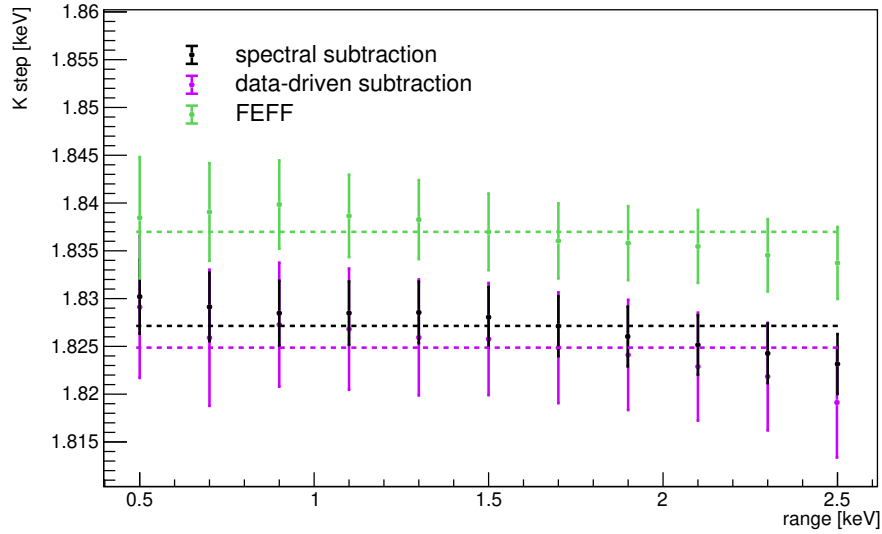
Figure 6.34 – K step locations obtained from the fit of the FEFF and measured spectra (derived with the spectral and data-driven subtraction approaches) around the step nominal position (1.839 keV). Different energy ranges are considered for the fit: $[1.6 - 0.1 \cdot i, 2.1 + 0.1 \cdot i]$ keV, with i takes value from 0 to 10. The x-axis in the plot indicates the difference between the extremes of the fitting range $(2.1 + 0.1 \cdot i - (1.6 - 0.1 \cdot i)$ keV). The FEFF spectrum is normalized to the measured one and its bin errors are set equal to those of measured data. The dashed lines indicate the mean value of the K step values. The calculated mean (m) and the root-mean-square deviation values are the following: $m_{\text{data}}^{\text{spectral−subtraction}} = 1.827 \pm 0.002$ keV, $m_{\text{data}}^{\text{data−driven}} = 1.825 \pm 0.003$ keV, $m_{\text{FEFF}} = 1.837 \pm 0.002$ keV.

205

fitting range, due to the slight change in the slopes before and after the step. For small fitting range values, the K step location is compatible with the nominal one, while the discrepancy grows for increasing ranges. For a given spectrum, the K step locations are compatible within each other and with the result obtained for the whole energy fit. The systematic lower value of the K-step with respect to the expectation suggests a small (less than 1%) systematic error in the calibration (either in the conversion from ADU to electrons or in the ϵ_{eh} value).
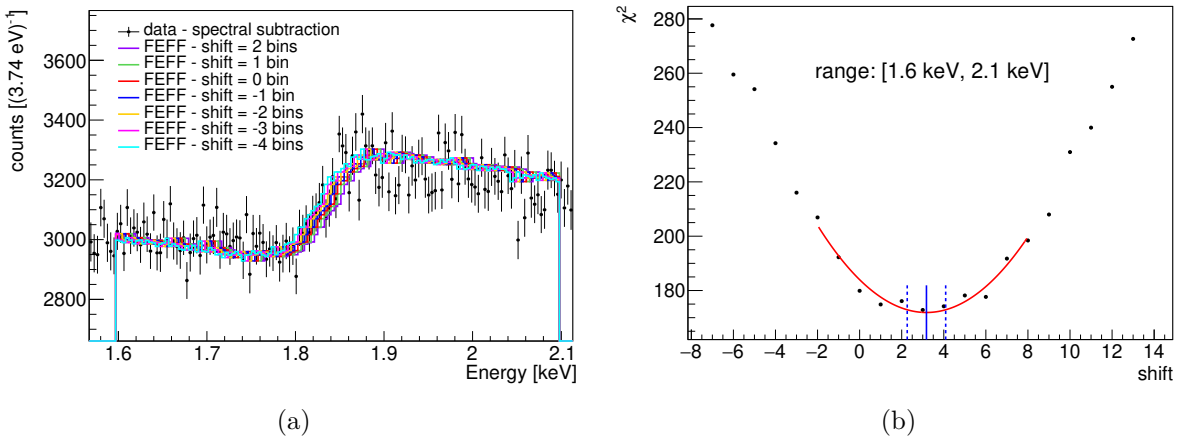
Figure 6.35 – (a): FEFF spectra (shown in different colours) shifted to the right and to the left of an integer number of bins. The measured spectrum (from the spectral subtraction approach) is shown as comparison. The FEFF spectrum is normalized to the data spectrum area in the fitting range. (b): χ^2 as a function of the shift of the FEFF spectrum, for a fitting range between 1.6 keV and 2.1 keV. The blue solid line indicates the shift corresponding to the minimum χ^2. The blue dashed lines instead point out the shift values corresponding to minimum χ^2 plus 1.

To cross-check the empirical function results, an alternative fitting method is developed to estimate the K step location, using the FEFF spectrum. The FEFF spectrum is first normalized to the area of the measured spectrum in energy range of interest. It is then shifted to the right and to the left of an integer number of bins (with width equal to 3.74 eV), as shown in Figure 6.35 (a). The χ^2 is calculated as: $\sum_i (y_i^{FEFF} - y_i^{data})^2 / (\sigma_i^{data})^2$ where i runs over the considered bins. The χ^2 is then plotted as a function of the shift and a parabola fit is performed around the minimum χ^2 value, as shown in Figure 6.35 (b). The shift ($\Delta(\chi^2_{min})$) corresponding to the minimum of the parabola is obtained together with the associated error, evaluated as $\Delta(\chi^2_{min} + 1) - \Delta(\chi^2_{min})$. Several energy ranges

are used for the fit. The results for the spectral subtraction spectrum [16] are shown in Figure 6.36. The mean and the root-mean-square deviation of all the values obtained with the different fitting ranges are taken as final result: -2.8 bins ± 1.1 bins (the sign minus indicates a shift of the FEFF spectrum to the left). Being each bin 3.74 eV wide, the shift between the FEFF and the measured spectrum minimizing the χ^2 is equal to -10.4 eV ± 4.1 eV. This corresponds to a K step location equal to 1.829 ± 0.004 keV (assuming a nominal value of 1.839 keV), in agreement with the empirical function fit result.
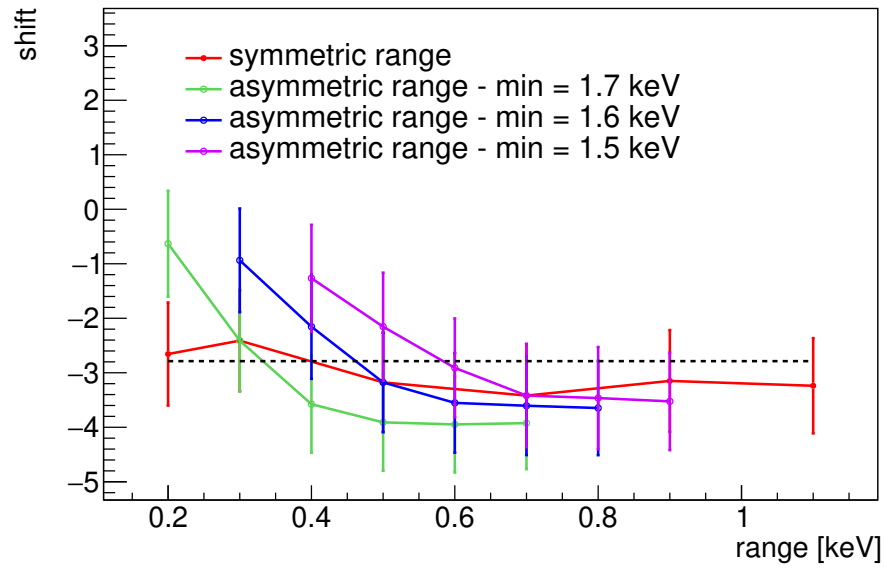
Figure 6.36 – Shift (in number of bins) of the FEFF spectrum corresponding to the minimum χ^2. The range is calculated as the difference between the fit extremes. The "symmetric range" values are obtained by performing the fit in a symmetric range around the K step: [1.75,1.95] keV, [1.7-i·0.1,2+i·0.1] keV, where i runs over 0 to 4. The "asymmetric ranges" values are instead obtained by keeping the fitting range minimum fixed (1.7 or 1.6 or 1.5 keV) and increasing the maximum (from 1.9 to 2.4 keV). The dashed line indicates the mean of all the shift values, equal to -2.8 bins. The root-mean-square deviation is instead equal to 1.1 bins. Each bin is 3.74 eV wide.

A similar procedure, by shifting the FEFF spectrum, could be applied at the L-shell energies but there are theoretical uncertainties in the *ab initio* calculations [169] and more statistics are required to validate the predicted structures.

---

16. This fitting method is applied only to the spectral subtraction spectrum, showing smaller uncertainties at the K step than the data-driven spectrum.

It has been proposed that energy loss mechanisms may vary with the deposited energy, resulting in an energy-dependent ϵ_{e-h} [170, 171]. To test this hypothesis, the mean energy per pair ϵ_{e-h} is retrieved from the fitted steps locations:

$$\epsilon_{e-h}(\mathrm{E_{step}[keV]}) = \frac{\mathrm{E_{step}^{expected}[keV]} \cdot (0.00374\,\mathrm{keV})}{\mathrm{E_{step}[keV]}}, \tag{6.14}$$

obtaining $\epsilon_{e-h}(\mathrm{L_{2,3}}) = 3.772 \pm 0.059$ eV, $\epsilon_{e-h}(\mathrm{L_1}) = 3.733 \pm 0.066$ eV, $\epsilon_{e-h}(\mathrm{K}) = 3.757 \pm 0.008$ eV, considering a fitting range equal to 0.5 keV, between 1.6 keV and 2.1 keV. The current errors don't allow to corroborate or reject the hypothesis of an energy-dependent ϵ_{e-h} value. A more precise measurement is needed. The possibility of measuring the Fano factor from the steps is also explored. However, being it strongly dependent on the detailed shape of the predicted spectrum, it is difficult to derive a meaningful value. Although further investigations are needed, it can be noticed that the σ_K, $\sigma_{L2,3}$, and σ_{L1} are compatible with an energy resolution (equation 6.11) calculated using F=0.128 and $\sigma_C = 0.8$ e$^-$ (1.0 e$^-$) for the L-shell (K-shell).

<p style="text-align:center">* * *</p>

The measurement and the analysis of the Compton spectrum highlight the necessity to have a more appropriate Compton scattering description at low energies (below 0.5 keV) than the one offered by the RIA approximation. This is pivotal to have a robust background estimation down to the eV-scale for DAMIC-M. In fact, to produce background models, the dark matter community relies heavily on Monte Carlo packages such as Geant4, which incorporates the relativistic impulse approximation model to describe the scattering physics. The measured spectrum is found in good agreement with predictions from *ab initio* calculations of Compton scattering with bound electrons using the FEFF code. However, additional statistics is required to confirm the robustness of the FEFF model predictions. A more precise measurement, as well as a solid theoretically motivated model for the spectrum shape, is also needed to have a meaningful measure of the Fano factor and of the ϵ_{e-h} and to investigate their energy dependence. To this end, the DAMIC-M collaboration plans to take additional measurements at different γ-ray energies using a ^{57}Co source ($E_\gamma = 122$ and 136 keV).

This measurement represents also a first test of the capabilities of a skipper CCD, which showed a good stability over the whole period of data taking. Furthermore, it

was pivotal to develop calibration and event reconstruction procedures optimized for sub-electron resolution. Skipper CCD capabilities will be further explored in a low background environment with the Low Background Chamber, described in Section 2.3.1.

CONCLUSION

The existence of Dark Matter (DM) is supported by overwhelming evidence. Despite the efforts of scientists, DM nature is still unknown. Among the most popular candidates there are the WIMPs and the Hidden Sector particles. In the past decade, direct detection experiments have done impressive improvements in terms of sensitivity to these candidates.

DAMIC-M is a near future direct detection experiment that aims at breaking new ground in the hidden sector particle search thanks to the use of skipper CCDs. To meet this goal, the background level has to be controlled to the sub d.r.u (events/kg/day/keV) level. This is a very challenging requirement that implies a careful and extensive optimization of the detector design and material selection. Furthermore, a complete understanding of the expected features of the background spectrum is required for the success of the DAMIC-M dark matter search. Therefore, precision measurements of one of the major expected source of background, the small-angle Compton scattered electrons, were carried out. This thesis focuses on the estimate of the background via simulations and its characterization via the analysis of the Compton scattering measurement.

The DAMIC-M baseline design involves a vacuum cryostat housing the CCD stack. All the components nearest to the devices will be made of ultra-pure materials, e.g., electro-formed copper. Internal shield disks made of low background materials, i.e., electro-formed copper and ancient lead, will be then utilized to further screen the CCDs from the non radio-pure parts of the detector. An external lead shield 20 cm thick will protect the setup from environmental gamma-rays. The most internal 5 cm are assumed to be made of ancient lead.

In this thesis work, Geant4 based simulations were used to drive the detector conception. Thanks to them, the level of background corresponding to a given design was predicted and the possible strategies for its reduction were identified. The latest developed design has an estimated background level of about 0.6 d.r.u, excluding the contribution of the CCD themselves. This demonstrates that the background goal is within reach, although further optimization is still needed. The simulations highlighted the importance of reducing the exposure time to cosmic rays of the EF components, finding a reference

limit of about 10 days followed by a cooling (storage) time underground of at least 6 months. An exposure time greater than the reference limit would require a longer period of time spent underground before data taking. For example, if the exposure time is increased to 15 days, a cooling time of about 295 days is needed to recover the level of background obtained in the reference case. Furthermore, the simulations found that the ancient lead components have a non-negligible impact on the background rate. Considering the latest assessed design, the ancient lead external shielding is the major contributor to the background, accounting for 50% of it. It is worth noting that for the external shielding a simplified geometry was used, since it has not yet been designed. The simulations highlighted also the necessity of developing more radio-pure background cables, being them one of the nearest components to the CCDs and one of the major contributors to the background budget. Using the same kapton cables of DAMIC would not be feasible for DAMIC-M from the background perspective. New low radioactivity flex cables will be produced for DAMIC-M by using radiopure copper-polyimide laminates and reducing background contributions during their fabrication. Controlling the exposure time to cosmic rays and to air (and thus to radon) of the CCDs and their close-by components is crucial to achieve the foreseen background goal. The simulations showed that, if the exposure time to cosmic rays of these components is kept below 3 months and their surface contamination is reduced by 100 times with respect to DAMIC, a sufficiently low background level for DAMIC-M is reached. Further modifications are being considered for the detector design in view of the possibility of using the Edelweiss external shielding.

A precise knowledge of the expected background spectrum is fundamental to be able to distinguish a potential dark matter signal. Ionization signals from small-angle Compton scattered electrons constitute a significant background for direct detection experiments like DAMIC-M that aim to detect dark matter through particle recoils down to the eV scale. Geant4 simulations are commonly exploited to estimate these backgrounds. The Monte Carlo package incorporates the relativistic impulse approximation (RIA) model to describe the scattering physics. However, the model assumptions are not valid in the small scattering angle regime. In fact, previous CCD measurements in silicon observed a softer spectrum than predicted below 0.25 keV. Therefore, the DAMIC-M collaboration carried out a precision measurement of Compton scattering on silicon atomic shell electrons down to 23 eV, exploiting the excellent energy resolution of a skipper CCD. The latter, developed as a prototype for the DAMIC-M experiment, was exposed to a ^{241}Am γ-ray source over several months. The author of this thesis contributed to the data analysis of this

measurement. The obtained spectrum is in good agreement with the expectation from the RIA down to 0.3 keV. At lower energies, the RIA model fails to reproduce properly the data, overestimating the measured spectrum up to 25%. The experimental data were instead found to be in much better agreement with predictions from *ab initio* calculations using the FEFF code. However, additional statistics and data are required to finally validate the FEFF model as reference for Compton scattering. In the context of this thesis work, a parametrization was derived for the spectrum, offering further insight into its features. This measurement was important not only because it highlighted the necessity to find a more proper model than the RIA one to describe Compton scattering events in the low energy regime, but also because it demonstrated the capability of the DAMIC-M skipper CCDs to detect with high efficiency and accuracy energy deposits of just a few ionization charges in the silicon bulk.

To conclude, the DAMIC-M collaboration is on its way toward installing and operating the DAMIC-M detector, which will help to shed light on the DM mystery. CCDs are being produced and tested, calibration measurements using radioactive sources are being performed, and the detector design is being carefully assessed and optimized. The DAMIC-M prototype, the Low Background Chamber, is finally operating at LSM. The author of this thesis also participated in its installation and assembly. The LBC has already provided very exciting first results despite the low total exposure ($\sim$115 g-days) and a background level more than 10 times bigger than the one that DAMIC-M will achieve. This gives confidence in the forthcoming search for dark matter particles with DAMIC-M.

DAMIC-M GEANT4 OUTPUT

Table A.1 – RunInfo tree content. This tree contains general information on the simulation setup. It contains 1 entry per run.

Branch	Type	Unit	Description
NEvt	int	-	number of events simulated
NCCD	int	-	number of CCD in the detector geometry
Seed	int	-	initial seed: -1 if based on the process time
concatedVolumeNames	string	-	list of volumes in geometry
volumeNameID	int	-	volume ID in the list
volumeMass	double	kg	mass of the volumes in the list
volumeDensity	double	g/cm^3	density of the volumes in the list
volumeVolume	double	cm^3	volume of volumes in the list
volumeSurface	double	cm^2	surface of the volumes in the list
primaryParticle	string	-	selected primary particles
primaryIon	string	-	primary ion A and Z (AaZz)
simulatedVolume	string	-	logical volume in which the primary particles were simulated

Table A.2 – EventOut tree content. This tree contains the information on the generated event. It is filled once per event and contain a number of entries equal to the total number of simulated events.

Branch	Type	Unit	Description
EventID	int	-	ID of the simulated event
pdg	int	-	pdg code of the primary particle
charge	int	-	charge of the primary particle
volid	int	-	volume ID of the generated particle
energy	double	eV	kinetic energy of the primary
momx	double	eV	x-coord of the primary particle momentum
momy	double	eV	y-coord of the primary particle momentum
momz	double	eV	z-coord of the primary particle momentum
posx	double	mm	absolute position x (in Geant4 coordinate system)
posy	double	mm	absolute position y (in Geant4 coordinate system)
posz	double	mm	absolute position z (in Geant4 coordinate system)
triggerTime	double	s	trigger time

Table A.3 – CCDOut tree content. This tree contains information on the energy deposits in the CCD sensitive region. For a given event, the tree is filled once per particle per pixel.

Branch	Type	Unit	Description
EventID	int	-	EventID
pdg	int	-	pdg code of the particle
trackid	int	-	trackID of the particle
parentid	int	-	trackID of the mother particle (0 in case of a primary)
CCDid	int	-	CCD ID
Edep	double	eV	total deposited energy in the pixel
posx	double	mm	energy-weighted average x-position per pixel (local position)
posy	double	mm	energy-weighted average y-position per pixel (local position)
posz	double	mm	energy-weighted average z-position per pixel (local position)
gposx	double	mm	energy-weighted average x-position per pixel (global position)
gposy	double	mm	energy-weighted average y-position per pixel (global position)
gposz	double	mm	energy-weighted average z-position per pixel (global position)
time	double	s	mean global time
localtime	double	s	mean local time (with respect to track time)

Table A.4 – TrackOut tree content. This tree contains information on each step of a particle in the sensitive volume.

Branch	Type	Unit	Description
EventID	int	-	event ID
pdg	int	-	pdg code of the particle
trackid	int	-	trackID of the particle
stepid	int	-	stepID of the particle
parentid	int	-	trackID of the mother particle (0 in case of a primary)
CCDid	int	-	CCD ID
volid	int	-	volume id
energy	double	eV	kinetic energy of the particle at the beginning of the step
deltaE	double	eV	energy difference (post - pre) in the step.
Edep	double	eV	deposited energy in the step
posx	double	mm	x-position (Geant4 coord system)
posy	double	mm	y-position (Geant4 coord system)
posz	double	mm	z-position (Geant4 coord system)
time	double	s	particle absolute time
startProcess	int	-	process ID (at preStep)
endProcess	int	-	process ID (at postStep)

Table A.5 – PartInfo tree content. This tree contains the information for each particle of a given event. The tree is filled once per event, with vectors of particle information.

Branch	Type	Unit	Description
EventID	int	-	event ID
pdg	int	-	pdg code of the particle
trackid	int	-	track ID of the particle
parentid	int	-	track ID of the mother particle (0 in case of a primary)
initialEkin	double	keV	kinetic energy of the particle at creation
firstVolID	int	-	Volume ID (at creation)
lastVolID	int	-	Volume ID (before being killed)
CreatorProcessID	int	-	ID of the creator process
LastProcessID	int	-	ID of the last process before being killed
posx	double	mm	x-position at creation (Geant4 coord system)
posy	double	mm	y-position at creation (Geant4 coord system)
posz	double	mm	z-position at creation (Geant4 coord system)

WADERS OUTPUT

Table B.1 – ClustersRec tree content. This tree contains cluster information. The tree is filled once per event, with vectors of cluster variables. To each vector of clusters, it is associated a vector of pixels. Pixel information (variables starting with "pixels_") is taken from the pixelizedEvent tree. Variables concerning the primary particle (those starting with "pp_") are from the EventOut tree.

Branch	Type	Unit	Description
event	int	-	event ID
Nclusters	int	-	number of clusters in a given event
DX	float	pixels	X width of the cluster (maxX-minX+1)
DY	float	pixels	Y width of the cluster (maxY-minY+1)
Energy	float	keV	total energy of the cluster
Npix	int	-	number of pixels of the cluster
PosX	float	pixels	energy-weighted average pixels x positions
PosY	float	pixels	energy-weighted average pixels y positions
PosZ	float	mm	energy-weighted average pixels z positions
Qmax	float	keV	maximum pixel charge in a cluster
QmaxX	float	pixels	x position of the pixel with maximum charge
QmaxY	float	pixels	y position of the pixel with maximum charge
RMSX	float	pixels	root mean square of the x positions of pixels
RMSY	float	pixels	root mean square of the y positions of pixels
RMSZ	float	mm	root mean square of the z positions of pixels
STD_X	float	pixels	standard deviation of the pixel x positions
STD_XY	float	pixels	standard deviation of the pixel x-y positions
STD_Y	float	pixels	standard deviation of the pixel y positions
STD_Z	float	mm	standard deviation of the pixel z positions
ccd	int	-	CCD ID

cluster_id	int	-	cluster ID
img_time	float	-	mean pixels image time
maxX	float	pixels	maximum pixel x position
maxY	float	pixels	maximum pixel y position
maxZ	float	pixels	maximum pixel z position
meanTime	float	s	mean time of pixels r
meanX	float	pixels	mean pixels x-position
meanY	float	pixels	mean pixels y-position
meanZ	float	mm	mean pixels z-position
minTime	float	s	minimum pixel time
minX	float	pixels	minimum pixel x position
minY	float	pixels	minimum pixel y position
minZ	float	mm	minimum pixel z position
pixels_E	float	keV	energy of a pixel in a given cluster
pixels_img_time	float	-	pixel image time (pixels_time divided by the image duration)
pixels_std_time	s	mm	standard deviation of time per pixel
pixels_time	float	s	pixel time (energy-weighted average of time per pixel)
pixels_x	int	pixels	pixel x position
pixels_y	int	pixels	pixel y position
pixels_z	float	mm	pixel z position
pp_energy	float	eV	primary particle energy
pp_momx	float	-	primary particle x momentum
pp_momy	float	-	primary particle y momentum
pp_momz	float	-	primary particle z momentum
pp_posx	float	mm	primary particle x position
pp_posy	float	mm	primary particle y position
pp_posz	float	mm	primary particle z position
wSTD_X	float	pixels	energy weighted standard deviation of pixels_x
wSTD_Y	float	pixels	energy weighted standard deviation of pixels_y

wSTD_Z	float	mm	energy weighted standard deviation of pixels_z
wTime	float	s	energy weighted pixels_time average

Table B.2 – PixelizedEvent tree content. This tree contains pixel information. The tree is filled once per event and CCD, with vectors of pixel variables. This tree is created at the end of the pixelization process, after the diffusion and continuous readout processes (if applied).

Branch	Type	Unit	Description
event	int	-	event ID
Npix	int	-	number of pixels per CCD and event
ccd	int	-	CCD ID
pixels_Edep	float	keV	total energy deposited in a given pixel
pixels_time	float	s	energy-weighted average of time per pixel
pixels_x	int	pixels	pixel x position
pixels_y	int	pixels	pixel y position
pixels_z	float	mm	mean depth value per pixel
pixel_Neh	int	-	number of electron-hole pairs in each pixel
pixel_sigma_xy	float	μm	mean σ_{xy} used to diffuse the e-h pairs position
pp_energy	float	eV	primary particle energy (from EventOut tree)
pp_momx	float	-	primary particle x momentum (from EventOut tree)
pp_momy	float	-	primary particle y momentum (from EventOut tree)
pp_momz	float	-	primary particle z momentum (from EventOut tree)
pp_posx	float	mm	primary particle x position (from EventOut tree)
pp_posy	float	mm	primary particle y position (from EventOut tree)
pp_posz	float	mm	primary particle z position (from EventOut tree)

Table B.3 – geant4_config tree content. This tree contains information concerning the Geant4 simulation.

Branch	Type	Unit	Description
NCCDs	int	-	number of CCDs
Seed	int	-	seed number
ccd_density	float	g/cm^3	CCD density
ccd_mass	float	kg	total mass of CCDs
ccd_surface	float	cm ^{2}	total surface of CCDs
ccd_vol	float	cm ^{3}	total volume of CCDs
pp_gps	-	-	simulated primary particle
pp_ion	-	-	simulated primary particle A and Z
pp_vol_density	float	g/cm^3	density component where primary particles were simulated
pp_vol_mass	float	kg	mass component where primary particles are simulated
pp_vol_pvnames	-	-	name of the component where primary particles were simulated
pp_vol_surface	float	cm ^{2}	surface of the component where primary particles were simulated
pp_vol_volume	float	cm ^{3}	volume of the component where primary particles were simulated

Table B.4 – process_config tree content. Parameters used to configure WADERS processes. Each variable, except the global ones used in all the processes, is preceded by the name of the process of interest. In this table only the variables associated with the ClusterFinder and PixelizeSignal processes are listed.

Branch	Type	Unit	Description
ADC2e	float	ADU/e-	ADC units corresponding to 1e$^-$
ADC2eV	float	eV/ADU	eV corresponding to 1 ADU
e2eV	float	eV/e-	eV corresponding to 1 e$^-$
img_exp_time	float	s	image exposure rime

ClusterFinder_max_nearest _neighbor	int	-	N defined in Section 4.2.2
ClusterFinder_sequence_id	int	-	id of the process (processes applied in ascending order)
PixelizeSignal_N_pixels_in_x	int	-	number of pixels in x direction
PixelizeSignal_N_pixels_in_y	int	-	number of pixels in y direction
PixelizeSignal_pixel_size_in_x	-	-	pixel size in x direction
PixelizeSignal_pixel_size_in_y	-	-	pixel size in y direction
PixelizeSignal_sequence_id	int	-	id of the process (processes applied in ascending order)
PixelizeSignal_shift_pixel_in_x	int	-	shift of the pixels in x
PixelizeSignal_shift_pixel_in_y	int	-	shift of the pixels in y

REDUCTION OF THE CABLE INDUCED BACKGROUND

In Section 5.1.2 the cable contribution is discussed and is found to have a significant impact on the background rate. In this section, the spatial distribution of the clusters in the CCD originated by the emissions of the radioactive isotopes in the cables is studied in details. In particular, the possibility of applying fiducial cuts on the x-y cluster positions is explored.

CCD stack I. Different CCD stack designs and cable options were considered for DAMIC-M. In the so-called CCD stack I case, the use of two 5-layers kapton cables per CCD (6k pixels × 6k pixels) was evaluated, as shown in Figure 5.21 (for more details refer to Section 5.1.2). Simulations were performed dividing in two parts the cables, the "on CCD" part, the one closer to the CCDs, and the outgoing part. In this section the spatial distribution of clusters originated by the "on CCD" part of the kapton cables is discussed, since it features a not uniform distribution as shown in Figure C.1 (a). Given the presence of an over-density of events on the border of the CCD, it would be useful to calculate the dimension of the frame (enclosing the border events) to be cut in order to recover an uniform distribution. To this end, several Monte-Carlo toy simulations are performed in which spatial distributions are generated with an over-density of events in a given frame. An example is shown in Figure C.2 (left), where events were simulated such that the 83% of them are enclosed in a frame with width $\Delta XY = 1000$ pixels. The cumulative distribution (Figure C.2, right) is then calculated by evaluating the fraction of events within a frame with increasing ΔXY (from 50 pixels to 3000 pixels). The distribution is then compared with the one expected for events uniformly distributed over the CCD area. The point of maximum distance (y_{max}) between the two distributions is obtained for $\Delta XY_{max} = 1000$ pixels, which indicates the width of the frame enclosing the simulated over-density. The same procedure is repeated for the kapton cable simulations, obtaining

Figure C.1 – (a): Spatial distribution of clusters in the CCDs for the "on CCD" 5-layers kapton cable simulations (CCD stack I). The color code indicates the number of entries per bin. The x and y position are calculated considering the global reference frame. (b): Cumulative distribution of clusters (black) compared to the cumulative distribution obtained assuming an uniform spatial distribution (blue). The fraction of left surface, assuming to cut a frame with width ΔXY, as a function of ΔXY is also shown (red).

a $\Delta XY_{\mathrm{max}} = 650$ pixels (Figure C.1, b). The same result is obtained by considering only the clusters with energy < 20 keV. Assuming to cut a frame with a width of 650 pixels, the fraction of left CCD area would be equal to 0.6. This study therefore helps to determine the CCD region in x and y to cut (fiducial cut) to reduce the cables impact. However, it is worth reminding that in the continuous readout case, the y (row) resolution is completely degraded. Thus, a fiducial cut would only be applied in the x direction. Furthermore, by looking at the cumulative distribution it is possible to estimate the distance to which the cables need to be pushed away (in x and y direction) from the CCD in order to reduce the associated background rate. For example, by moving the cables 2 cm ($\sim$1333 pixels) away from the CCD, the number of clusters would approximately decrease by a factor equal to:

$$\frac{1}{1 - \epsilon(\Delta XY = 1333\,\mathrm{pix})} \sim 4, \tag{C.1}$$

where $\epsilon(\Delta XY)$ indicates the fraction of clusters enclosed in a frame with width equal to ΔXY. As discussed in Section 5.1.2, simulations show that, by pushing the kapton cables 2 cm away (on the y direction) from the CCD (with respect to their standard simulated positions), their "on CCD" contribution is reduced by 5 times. Figure C.3 shows the cluster spatial distribution and the corresponding cumulative distribution. A
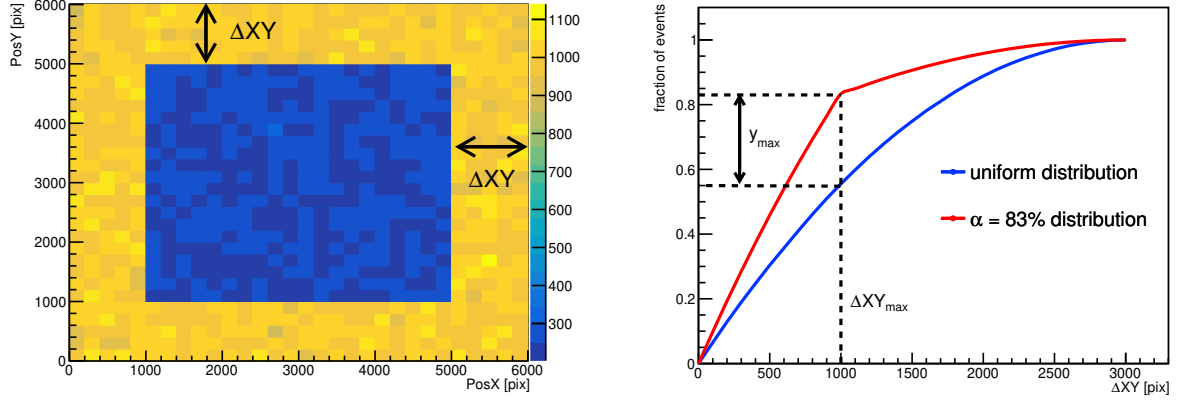
Figure C.2 – Left: spatial distribution of events obtained from a Toy Monte-Carlo simulation. The fraction of generated events (α) enclosed in a frame with $\Delta XY = 1000$ pixels is equal to 0.83. Right: cumulative distribution of events (red) compared to the cumulative distribution obtained assuming an uniform spatial distribution (blue). The point of maximum y distance (y_{max}) between the two distribution occurs at $\Delta XY_{max} = 1000$ pixels.

clear difference is visible with respect to the ones shown in Figure C.1. In fact, in this new configuration case the distributions are much closer to ones expected for a uniform distribution of events in the CCD.

CCD stack III. The same study performed for the CCD stack I is repeated for the CCD stack III (Figure 5.31). In this case, for each group of 4 CCDs (1.5k pixels × 6k pixels) an only one 2-layers kapton cables is considered (for more details see Section 5.1.2). The spatial distribution of the clusters (for all the isotopes and the whole energy range) is studied for the "on CCD" simulations and it is shown in Figure C.4 (a). A cumulative distribution is obtained by calculating the fraction of clusters with (6000 pixels - ΔY pixels) < PosY < 6000 pixels, with increasing values of ΔY (from 50 pixels to 6000 pixels). The distribution is shown in Figure C.4 (b) and it is compared with the one expected for clusters uniformly distributed over the CCD area. The point of maximum y distance (y_{max}) between the two distributions is obtained for $\Delta Y_{max} = 2450$ pixels, corresponding to a fraction of events equal to 0.57. Performing a fiducial cut at $\Delta Y_{max} = 2450$ pixels, that is cutting all clusters with PosY > (6000 pixels - ΔY pixels), reduces by 41% the CCD area. The same result is obtained considering only the clusters with energy below 20 keV. As already mentioned before, if the continuous readout is used, the y (row) resolution
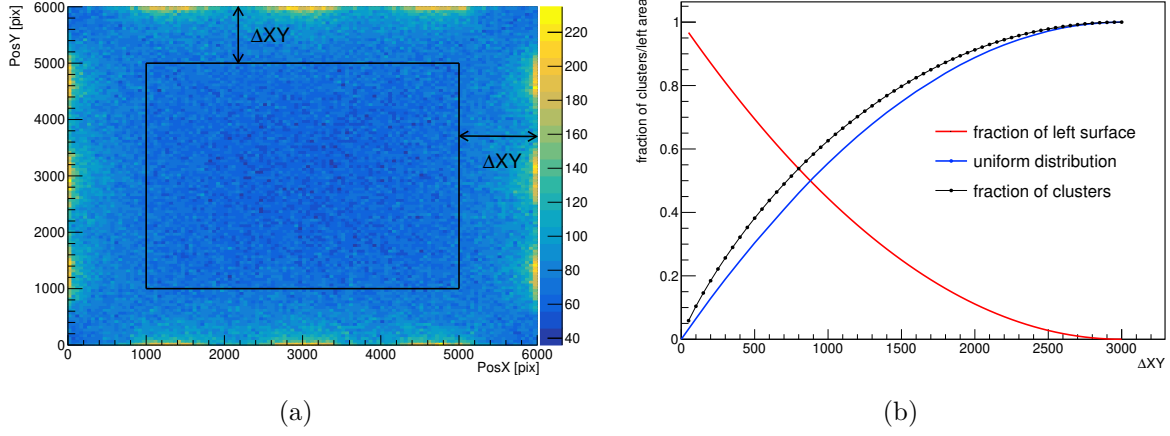
223
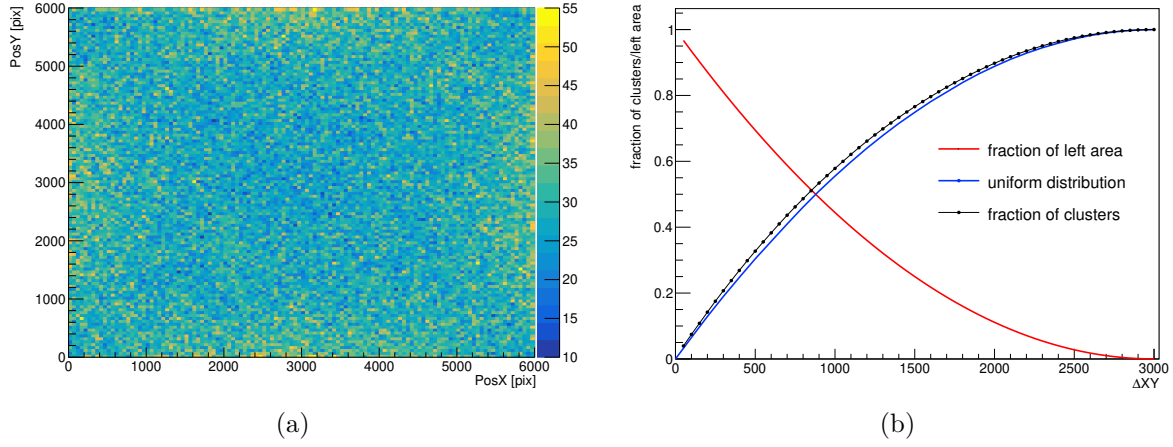
Figure C.3 – (a): Spatial distribution of clusters in the CCDs for the "On CCD" 5-layers kapton cable simulations (CCD stack I), with cables 2 cm away from their standard position. The color code indicates the number of entries per bin. The x and y position are calculated considering the global reference frame. (b): Cumulative distribution of clusters (black) compared to the cumulative distribution obtained assuming an uniform spatial distribution (blue). The fraction of left area, assuming to cut a frame with width ΔXY, as a function of ΔXY is also shown (red).

is completely degraded. Thus, a fiducial cut could not be applied in the y direction. However, it is possible to retrieve from the cumulative distribution an estimate of the distance to which the cables need to be moved away (in the y direction) from the CCD in order to reduce the associated background rate. For example, by moving the cables 1.5 cm (1000 pixels) away from the CCD, the number of clusters would approximately decrease by a factor equal to $\frac{1}{1-\epsilon(\Delta Y=1000\,\text{pix})} \sim 1.4$, where $\epsilon(\Delta Y)$ indicates the fraction of clusters enclosed in a frame with width equal to ΔY.

(a)	(b)
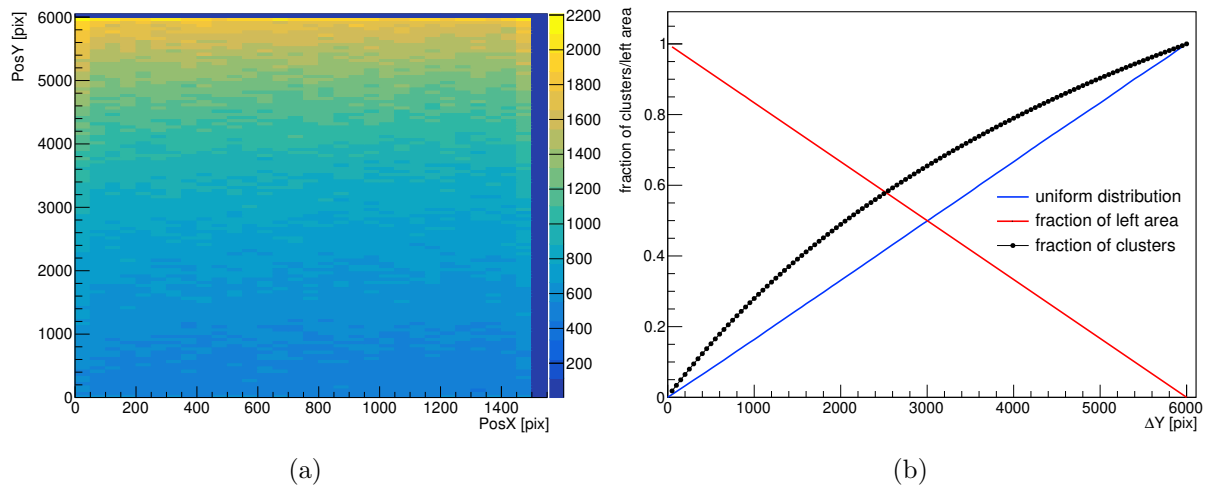
Figure C.4 – (a): Spatial distribution of the clusters for the "on CCD" 2-layers kapton cable simulations (CCD Stack III). The color code indicates the number of clusters in a given bin. (b): Cumulative distribution of clusters (black) compared to the cumulative distribution obtained assuming an uniform spatial distribution (blue). The fraction of left surface, assuming to cut a frame with width ΔY, as a function of ΔY is also shown (red).

RÉSUMÉ EN FRANÇAIS

La matière ordinaire ne constitue qu'une petite fraction (5%) de l'Univers, tandis que les 27% restants sont composés par un type de matière non identifiée, connue sous le nom de matière noire (MN). Même si la MN est cinq fois plus abondante que la matière ordinaire, sa nature reste un mystère. De nombreux candidats de MN ont été proposés au fil des années. Parmi les plus populaires, il existe les particules massives interagissant faiblement appelées WIMPs (pour *Weakly Interacting Massive Particle*), avec une gamme de masse allant de quelques GeV aux TeV. Pour explorer et confirmer la composition de la MN, il faudrait qu'elle puisse interagir avec la matière ordinaire autrement que via la gravité. Partant de l'hypothèse que cela soit possible, même s'il s'agirait d'un cas extrêmement rare, différentes approches ont été développées au cours des dernières décennies afin de capter un signal de MN. Parmi elles, la méthode de détection directe recherche des événements de collision de particules de MN avec des cibles souterraines de matière ordinaire. Compte tenu de l'absence d'observation d'un signal de WIMPs, dont l'espace de paramètres est de plus en plus restreint, la communauté scientifique a orienté ses recherches vers d'autres candidats, par exemple, ceux du secteur sombre. Le Chapitre 1 de cette thèse introduit la MN, les principales preuves de son existence et les candidats les plus populaires pour la décrire.

DAMIC-M (*Dark Matter In CCD at Modane*) est une expérience de détection directe qui vise à atteindre une sensibilité inégalée pour l'observation des particules de MN du secteur sombre, tout en poursuivant la recherche des WIMPs à faible masse. L'expérience sera installée en 2024 au sein du laboratoire souterrain de Modane et possédera une cible constituée de dispositifs à couplage de charge (CCDs). Il s'agit de capteurs pixelisés à base de silicium, couramment utilisés dans le domaine astronomique. Les CCDs sont capables de collecter les charges créées par les interactions de particules ayant lieu dans leur volume de silicium. En raison du faible niveau de courant d'obscurité (*dark current*) et du bruit de lecture induit sur les mesures de charge, ces dispositifs peuvent détecter de petits signaux d'ionisation (de seulement quelques électrons), provenant du recul de noyaux ou

d'électrons, suite à la diffusion de particules de MN de faible masse. La faible masse du noyau de silicium assure une bonne sensibilité aux reculs nucléaires des WIMPs dans une plage des masses comprises entre 1 et 10 GeV, tandis que la bande interdite du silicium ($\sim$1.1 eV) fournit une sensibilité aux interactions de MN du secteur sombre avec les électrons. De plus, l'excellente résolution spatiale des CCDs permet de caractériser et de rejeter les événements de bruit de fond provenant de sources radiogéniques. L'utilisation de ces capteurs dans la recherche de la MN a été initiée par l'expérience DAMIC au SNOLAB. DAMIC-M présente plusieurs nouveautés par rapport à son prédécesseur. La masse du détecteur sera augmentée d'un facteur d'environ 17, en utilisant $\sim$200 CCDs, atteignant une masse d'environ 0.7 kg. Le niveau du bruit de fond atteindra une fraction de d.r.u (*differential rate unit*, exprimé en événements/keV/kg/jour) contre environ les 10 d.r.u atteint par DAMIC. En outre, une nouvelle technologie de CCDs, basée sur des amplificateurs de type skipper, permettra d'atteindre un niveau de bruit de lecture sous-électronique. Ainsi, dans le Chapitre 2, on retrouve une description du fonctionnement de capteurs CCDs, en se focalisant sur leur utilisation dans les expériences de MN comme DAMIC et DAMIC-M.

Cette thèse s'insère dans le contexte de recherche de la MN avec l'expérience DAMIC-M. Elle se concentre principalement sur l'estimation du bruit de fond via des simulations et la caractérisation de ce dernier via des mesures expérimentales spécifiques.

L'objectif de l'expérience DAMIC-M de diminuer le bruit de fond a amené à une vaste campagne de recherche qui vise à améliorer la technologie et la conception même du détecteur. Des simulations sont utilisées afin d'optimiser la conception du détecteur et pour guider les ingénieurs dans la sélection et la manipulation des matériaux. L'auteure de cette thèse a été principalement impliquée dans cette tâche. La chaîne de simulation repose sur un code en Geant4 et sur un code en Python. Ceux-ci ont été développés par la collaboration DAMIC-M et une partie de cette thèse a été consacrée à leur amélioration et optimisation. Le code en Geant4 a été employé pour simuler les interactions des particules traversant le détecteur. Le code en Python, appelé WADERS (*softWAre for Dark matter ExpeRiments with Skippers*), a été développé pour imiter la réponse des CCDs. Pour chaque design de détecteur évalué, une chaîne de simulation complète a été effectuée. Les isotopes sont simulés dans le volume ou à la surface des composants du détecteur et le niveau du bruit de fond associé est obtenu en considérant leurs activités radioactives. Les simulations présentées dans ce travail de thèse ont permis d'identifier les principales sources de bruit et d'établir une limite pour le temps d'exposition des

composants du détecteur aux rayons cosmiques. Le dernier modèle développé atteint un niveau de fond estimé à environ 0.6 d.r.u, excluant la contribution des CCDs eux-mêmes. Cela démontre que l'objectif de base est à portée de main, bien que d'autres optimisations sont encore nécessaires. Les principales sources de bruit proviennent du blindage extérieur en plomb (qui cause environ 50% du bruit global) et par les câbles (qui eux sont à environ 25% du bruit global). Les simulations ont également mis en évidence l'importance de réduire le temps d'exposition aux rayons cosmiques des composants de cuivre électroformé, en identifiant une limite de référence d'environ 10 jours, suivie d'un temps de refroidissement souterrain (stockage) d'au moins 6 mois. Les types de bruit de fond les plus importants pour l'expérience DAMIC-M et les principales stratégies pour leur atténuation sont résumés dans le Chapitre 3, tandis que le Chapitre 4 décrit les codes de simulation et leurs caractéristiques. Enfin, dans le Chapitre 5, un aperçu de tous les designs de détecteurs évalués et des principaux résultats de simulation sont reportés.

Il est essentiel d'acquérir une connaissance complète de toutes les sources de bruit de fond possibles pour la recherche de la MN. Les électrons diffusés par effet Compton par les rayons gamma environnementaux représentent une source importante de bruit de fond pour DAMIC-M, puisque leur spectre s'étend jusqu'à la région d'intérêt énergétique allant de l'eV au keV. Par conséquent, une mesure de précision du spectre Compton a été effectuée avec un détecteur CCD de pré-production de DAMIC-M, exposé à des rayons gamma de 60 keV provenant d'une source de ^{241}Am. Grâce à l'affichage de l'amplificateur skipper, le spectre a été mesuré jusqu'à la valeur minimale de 23 eV. L'excellente résolution énergétique du capteur CCD de type skipper a permis de sonder des caractéristiques spectrales qui ne pouvaient pas être observées précédemment avec l'utilisation d'un CCD standard de DAMIC. L'auteure de ce manuscrit a contribué à l'analyse des données recueillies avec le CCD de pré-production de DAMIC-M. Une paramétrisation du spectre Compton a également été obtenue dans ce contexte de travail de thèse. Une description détaillée de la mesure de diffusion Compton est fournie dans le Chapitre 6.

Cette thèse souligne le rôle crucial des simulations pour l'optimisation de la conception du détecteur et l'atténuation du bruit de fond. Elle démontre également l'excellente capacité des CCD skipper à détecter avec une efficacité et une précision élevées les dépôts d'énergie de quelques charges d'ionisation dans le volume de silicium. Cette propriété a été exploitée pour caractériser, dans une gamme d'énergie jusqu'alors inexplorée, le bruit de fond dû aux électrons diffusés Compton. En conclusion, ce travail montre que l'expérience DAMIC-M peut atteindre les exigences nécessaires pour éclairer le mystère de la MN.

BIBLIOGRAPHY

[1] H. Poincaré, « La voie lactée et la théorie des gaz », *Bulletin de la société astronomique de France*, vol. 20, pp. 153–165, 1906.

[2] L. W. T. Kelvin, *Baltimore lectures on molecular dynamics and the wave theory of light*. CUP Archive, 1904.

[3] F. Zwicky, « On the Masses of Nebulae and of Clusters of Nebulae », *The Astrophysical Journal*, vol. 86, p. 217, Oct. 1937. DOI: 10.1086/143864.

[4] F. Zwicky, « Die Rotverschiebung von extragalaktischen Nebeln », *Helvetica Physica Acta*, vol. 6, pp. 110–127, Jan. 1933.

[5] V. C. Rubin and J. Ford W. Kent, « Rotation of the Andromeda Nebula from a Spectroscopic Survey of Emission Regions », *The Astrophysical Journal*, vol. 159, p. 379, Feb. 1970. DOI: 10.1086/150317.

[6] V. C. Rubin, J. Ford W. K., and N. Thonnard, « Rotational properties of 21 SC galaxies with a large range of luminosities and radii, from NGC 4605 (R=4kpc) to UGC 2885 (R=122kpc). », *The Astrophysical Journal*, vol. 238, pp. 471–487, Jun. 1980. DOI: 10.1086/158003.

[7] M. Thomson, *Modern Particle Physics*. Cambridge University Press, 2013. DOI: 10.1017/CBO9781139525367.

[8] Planck Collaboration *et al.*, « Planck 2018 results - vi. cosmological parameters », *A&A*, vol. 641, A6, 2020. DOI: 10.1051/0004-6361/201833910. [Online]. Available: https://doi.org/10.1051/0004-6361/201833910.

[9] S. Dodelson, *Modern cosmology*. Elsevier, 2003.

[10] C. Bennett *et al.*, « Four-year cobe dmr cosmic microwave background observations: maps and basic results », *Astrophysical Journal - ASTROPHYS J*, vol. 464, Jun. 1996. DOI: 10.1086/310075.

[11] G. Hinshaw *et al.*, « Nine-year wilkinson microwave anisotropy probe (wmap) observations: cosmological parameter results », *The Astrophysical Journal Supplement Series*, vol. 208, Dec. 2012. DOI: 10.1088/0067-0049/208/2/19.

[12] D. Clowe *et al.*, « A direct empirical proof of the existence of dark matter », *Astrophys. J. Lett.*, vol. 648, pp. L109–L113, 2006. DOI: `10.1086/508162`. arXiv: `astro-ph/0608407`.

[13] M. Bartelmann and P. Schneider, « Weak gravitational lensing », *Physics Reports*, vol. 340, *4*, pp. 291–472, 2001, ISSN: 0370-1573. DOI: `https://doi.org/10.1016/S0370-1573(00)00082-X`. [Online]. Available: `https://www.sciencedirect.com/science/article/pii/S037015730000082X`.

[14] G. Bertone and D. Hooper, « History of dark matter », *Rev. Mod. Phys.*, vol. 90, *4*, p. 045 002, 2018. DOI: `10.1103/RevModPhys.90.045002`. arXiv: `1605.04909 [astro-ph.CO]`.

[15] T. Lin, « Dark matter models and direct detection », *PoS*, vol. 333, p. 009, 2019. DOI: `10.22323/1.333.0009`. arXiv: `1904.07915 [hep-ph]`.

[16] A. Boyarsky *et al.*, « Sterile neutrino dark matter », *Progress in Particle and Nuclear Physics*, vol. 104, pp. 1–45, 2019, ISSN: 0146-6410. DOI: `https://doi.org/10.1016/j.ppnp.2018.07.004`. [Online]. Available: `https://www.sciencedirect.com/science/article/pii/S0146641018300711`.

[17] A. Boveia and C. Doglioni, « Dark Matter Searches at Colliders », *Ann. Rev. Nucl. Part. Sci.*, vol. 68, pp. 429–459, 2018. DOI: `10.1146/annurev-nucl-101917-021008`. arXiv: `1810.12238 [hep-ex]`.

[18] M. Milgrom, « A modification of the Newtonian dynamics as a possible alternative to the hidden mass hypothesis. », *The Astrophysical Journal*, vol. 270, pp. 365–370, Jul. 1983. DOI: `10.1086/161130`.

[19] J. D. Bekenstein, « Relativistic gravitation theory for the MOND paradigm », *Phys. Rev. D*, vol. 70, p. 083 509, 2004, [Erratum: Phys.Rev.D 71, 069901 (2005)]. DOI: `10.1103/PhysRevD.70.083509`. arXiv: `astro-ph/0403694`.

[20] G. Jungman, M. Kamionkowski, and K. Griest, « Supersymmetric dark matter », *Physics Reports*, vol. 267, *5*, pp. 195–373, 1996, ISSN: 0370-1573. DOI: `https://doi.org/10.1016/0370-1573(95)00058-5`. [Online]. Available: `https://www.sciencedirect.com/science/article/pii/0370157395000585`.

[21] M. Fabbrichesi, E. Gabrielli, and G. Lanfranchi, « The Dark Photon », May 2020. DOI: `10.1007/978-3-030-62519-1`. arXiv: `2005.01515 [hep-ph]`.

[22] R. Essig, J. Mardon, and T. Volansky, « Direct Detection of Sub-GeV Dark Matter », *Phys. Rev. D*, vol. 85, p. 076 007, 2012. DOI: `10.1103/PhysRevD.85.076007`. arXiv: `1108.5383 [hep-ph]`.

[23] R. Essig *et al.*, « Working Group Report: New Light Weakly Coupled Particles », *in Community Summer Study 2013: Snowmass on the Mississippi*, Oct. 2013. arXiv: `1311.0029 [hep-ph]`.

[24] R. D. Peccei and H. R. Quinn, « Cp conservation in the presence of pseudoparticles », *Phys. Rev. Lett.*, vol. 38, pp. 1440–1443, 25 1977. DOI: `10.1103/PhysRevLett.38.1440`. [Online]. Available: `https://link.aps.org/doi/10.1103/PhysRevLett.38.1440`.

[25] J. E. Kim and G. Carosi, « Axions and the Strong CP Problem », *Rev. Mod. Phys.*, vol. 82, pp. 557–602, 2010, [Erratum: Rev.Mod.Phys. 91, 049902 (2019)]. DOI: `10.1103/RevModPhys.82.557`. arXiv: `0807.3125 [hep-ph]`.

[26] R. T. Co, L. J. Hall, and K. Harigaya, « Axion Kinetic Misalignment Mechanism », *Phys. Rev. Lett.*, vol. 124, *25*, p. 251 802, 2020. DOI: `10.1103/PhysRevLett.124.251802`. arXiv: `1910.14152 [hep-ph]`.

[27] B. Carr and F. Kühnel, « Primordial black holes as dark matter: recent developments », *Annual Review of Nuclear and Particle Science*, vol. 70, *1*, pp. 355–394, 2020. DOI: `10.1146/annurev-nucl-050520-125911`. eprint: `https://doi.org/10.1146/annurev-nucl-050520-125911`. [Online]. Available: `https://doi.org/10.1146/annurev-nucl-050520-125911`.

[28] T. M. Undagoitia and L. Rauch, « Dark matter direct-detection experiments », *Journal of Physics G: Nuclear and Particle Physics*, vol. 43, *1*, p. 013 001, 2015, ISSN: 1361-6471. DOI: `10.1088/0954-3899/43/1/013001`. [Online]. Available: `http://dx.doi.org/10.1088/0954-3899/43/1/013001`.

[29] S. Hoof, A. Geringer-Sameth, and R. Trotta, « A Global Analysis of Dark Matter Signals from 27 Dwarf Spheroidal Galaxies using 11 Years of Fermi-LAT Observations », *JCAP*, vol. 02, p. 012, 2020. DOI: `10.1088/1475-7516/2020/02/012`. arXiv: `1812.06986 [astro-ph.CO]`.

[30] V. A. Acciari *et al.*, « Combined searches for dark matter in dwarf spheroidal galaxies observed with the MAGIC telescopes, including new data from Coma

Berenices and Draco », *Phys. Dark Univ.*, vol. 35, p. 100 912, 2022. DOI: `10.1016/j.dark.2021.100912`. arXiv: `2111.15009 [astro-ph.HE]`.

[31]   L. Rinchiuso, « Latest results on dark matter searches with H.E.S.S », *EPJ Web Conf.*, vol. 209, M. De Vincenzi, A. Capone, and A. Morselli, Eds., p. 01 023, 2019. DOI: `10.1051/epjconf/201920901023`. arXiv: `1901.05299 [astro-ph.HE]`.

[32]   B. Zitzer, « The VERITAS Dark Matter Program », *PoS*, vol. ICRC2017, p. 904, 2018. DOI: `10.22323/1.301.0904`. arXiv: `1708.07447 [astro-ph.HE]`.

[33]   J. W. Foster *et al.*, « Deep Search for Decaying Dark Matter with XMM-Newton Blank-Sky Observations », *Phys. Rev. Lett.*, vol. 127, *5*, p. 051 101, 2021. DOI: `10.1103/PhysRevLett.127.051101`. arXiv: `2102.02207 [astro-ph.CO]`.

[34]   F. Hofmann and C. Wegg, « 7.1 keV sterile neutrino dark matter constraints from a deep Chandra X-ray observation of the Galactic bulge Limiting Window », *Astron. Astrophys.*, vol. 625, p. L7, 2019. DOI: `10.1051/0004-6361/201935561`. arXiv: `1905.00916 [astro-ph.HE]`.

[35]   R. Abbasi *et al.*, « Indirect search for dark matter in the Galactic Centre with IceCube », *in 37th International Cosmic Ray Conference*, Jul. 2021. arXiv: `2107.11224 [astro-ph.HE]`.

[36]   A. Albert *et al.*, « Search for dark matter towards the galactic centre with 11 years of antares data », *Phys.Lett.*, vol. B805, p. 135 439, 2020. arXiv: `1912.05296 [astro-ph.HE]`.

[37]   K. F. and, « Dark matter searches with the super-kamiokande detector », *Journal of Physics: Conference Series*, vol. 888, p. 012 210, 2017. DOI: `10.1088/1742-6596/888/1/012210`. [Online]. Available: `https://doi.org/10.1088/1742-6596/888/1/012210`.

[38]   F. Calore *et al.*, « AMS-02 antiprotons and dark matter: Trimmed hints and robust bounds », *SciPost Phys.*, vol. 12, *5*, p. 163, 2022. DOI: `10.21468/SciPostPhys.12.5.163`. arXiv: `2202.03076 [hep-ph]`.

[39]   P. Picozza and R. Sparvoli, « Dark matter search in space », *Nuclear Instruments and Methods in Physics Research Section A: Accelerators, Spectrometers, Detectors and Associated Equipment*, vol. 720, pp. 45–48, 2013, Selected papers from the 2nd International Conference Frontiers in Diagnostic Technologies (ICFDT2),

ISSN: 0168-9002. DOI: https://doi.org/10.1016/j.nima.2012.12.038. [Online]. Available: https://www.sciencedirect.com/science/article/pii/S0168900212015719.

[40] A. Albert *et al.*, « Searching for Dark Matter Annihilation in Recently Discovered Milky Way Satellites with Fermi-LAT », *Astrophys. J.*, vol. 834, *2*, p. 110, 2017. DOI: 10.3847/1538-4357/834/2/110. arXiv: 1611.03184 [astro-ph.HE].

[41] R. Bernabei *et al.*, « Final model independent result of DAMA/LIBRA-phase1 », *Eur. Phys. J. C*, vol. 73, p. 2648, 2013. DOI: 10.1140/epjc/s10052-013-2648-7. arXiv: 1308.5109 [astro-ph.GA].

[42] J. Amaré *et al.*, « Performance of ANAIS-112 experiment after the first year of data taking », *Eur. Phys. J. C*, vol. 79, *3*, p. 228, 2019. DOI: 10.1140/epjc/s10052-019-6697-4. arXiv: 1812.01472 [astro-ph.IM].

[43] G. Adhikari *et al.*, « Initial Performance of the COSINE-100 Experiment », *Eur. Phys. J. C*, vol. 78, *2*, p. 107, 2018. DOI: 10.1140/epjc/s10052-018-5590-x. arXiv: 1710.05299 [physics.ins-det].

[44] R. Agnese *et al.*, « Search for low-mass dark matter with cdmslite using a profile likelihood fit », *Phys. Rev. D*, vol. 99, p. 062001, 6 2019. DOI: 10.1103/PhysRevD.99.062001. [Online]. Available: https://link.aps.org/doi/10.1103/PhysRevD.99.062001.

[45] E. Armengaud *et al.*, « Searching for low-mass dark matter particles with a massive ge bolometer operated above ground », *Physical Review D*, vol. 99, *8*, 2019, ISSN: 2470-0029. DOI: 10.1103/physrevd.99.082003. [Online]. Available: http://dx.doi.org/10.1103/PhysRevD.99.082003.

[46] A. Abdelhameed *et al.*, « First results from the cresst-iii low-mass dark matter program », *Physical Review D*, vol. 100, *10*, 2019, ISSN: 2470-0029. DOI: 10.1103/physrevd.100.102002. [Online]. Available: http://dx.doi.org/10.1103/PhysRevD.100.102002.

[47] E. Aprile *et al.*, « Dark matter search results from a one ton-year exposure of xenon1t », *Phys. Rev. Lett.*, vol. 121, p. 111302, 11 2018. DOI: 10.1103/PhysRevLett.121.111302. [Online]. Available: https://link.aps.org/doi/10.1103/PhysRevLett.121.111302.

[48] J. Aalbers *et al.*, « First Dark Matter Search Results from the LUX-ZEPLIN (LZ) Experiment », Jul. 2022. arXiv: `2207.03764 [hep-ex]`.

[49] X. Cui *et al.*, « Dark Matter Results From 54-Ton-Day Exposure of PandaX-II Experiment », *Phys. Rev. Lett.*, vol. 119, *18*, p. 181 302, 2017. DOI: `10.1103/ PhysRevLett.119.181302`. arXiv: `1708.06917 [astro-ph.CO]`.

[50] Q. Arnaud *et al.*, « First results from the news-g direct dark matter search experiment at the lsm », *Astroparticle Physics*, vol. 97, pp. 54–62, 2018, ISSN: 0927-6505. DOI: `https://doi.org/10.1016/j.astropartphys.2017.10.009`. [Online]. Available: `https://www.sciencedirect.com/science/article/pii/ S0927650517301871`.

[51] E. Daw *et al.*, « The DRIFT Directional Dark Matter Experiments », *EAS Publ. Ser.*, vol. 53, F. Mayet and D. Santos, Eds., pp. 11–18, 2012. DOI: `10.1051/eas/ 1253002`. arXiv: `1110.0222 [physics.ins-det]`.

[52] C. Amole *et al.*, « Dark Matter Search Results from the Complete Exposure of the PICO-60 C_3F_8 Bubble Chamber », *Phys. Rev. D*, vol. 100, *2*, p. 022 001, 2019. DOI: `10.1103/PhysRevD.100.022001`. arXiv: `1902.04031 [astro-ph.CO]`.

[53] A. Aguilar-Arevalo *et al.*, « Results on low-mass weakly interacting massive particles from a 11 kg-day target exposure of DAMIC at SNOLAB », *Phys. Rev. Lett.*, vol. 125, p. 241 803, 2020. DOI: `10.1103/PhysRevLett.125.241803`. arXiv: `2007.15622 [astro-ph.CO]`.

[54] L. Barak *et al.*, « SENSEI: Direct-Detection Results on sub-GeV Dark Matter from a New Skipper-CCD », *Phys. Rev. Lett.*, vol. 125, *17*, p. 171 802, 2020. DOI: `10.1103/PhysRevLett.125.171802`. arXiv: `2004.11378 [astro-ph.CO]`.

[55] D. Baxter *et al.*, « Recommended conventions for reporting results from direct dark matter searches », *Eur. Phys. J. C*, vol. 81, *10*, p. 907, 2021. DOI: `10.1140/epjc/ s10052-021-09655-y`. arXiv: `2105.00599 [hep-ex]`.

[56] K. Freese, M. Lisanti, and C. Savage, « Colloquium: Annual modulation of dark matter », *Rev. Mod. Phys.*, vol. 85, pp. 1561–1581, 2013. DOI: `10.1103/RevModPhys. 85.1561`. arXiv: `1209.3339 [astro-ph.CO]`.

[57] J. Amare *et al.*, « Annual Modulation Results from Three Years Exposure of ANAIS-112 », *Phys. Rev. D*, vol. 103, *10*, p. 102 005, 2021. DOI: `10.1103/PhysRevD. 103.102005`. arXiv: `2103.01175 [astro-ph.IM]`.

[58] F. Ruppin, J. Billard, E. Figueroa-Feliciano, and L. Strigari, « Complementarity of dark matter detectors in light of the neutrino background », *Phys. Rev. D*, vol. 90, p. 083 510, 8 2014. DOI: `10.1103/PhysRevD.90.083510`. [Online]. Available: `http://link.aps.org/doi/10.1103/PhysRevD.90.083510`.

[59] L. Hehn *et al.*, « Improved EDELWEISS-III sensitivity for low-mass WIMPs using a profile likelihood approach », *Eur. Phys. J. C*, vol. 76, *10*, p. 548, 2016. DOI: `10.1140/epjc/s10052-016-4388-y`. arXiv: `1607.03367 [astro-ph.CO]`.

[60] P. Agnes *et al.*, « Darkside-50 532-day dark matter search with low-radioactivity argon », *Physical Review D*, vol. 98, *10*, 2018, ISSN: 2470-0029. DOI: `10.1103/physrevd.98.102006`. [Online]. Available: `http://dx.doi.org/10.1103/PhysRevD.98.102006`.

[61] P. Agnes *et al.*, « Low-mass dark matter search with the darkside-50 experiment », *Phys. Rev. Lett.*, vol. 121, p. 081 307, 8 2018. DOI: `10.1103/PhysRevLett.121.081307`. [Online]. Available: `https://link.aps.org/doi/10.1103/PhysRevLett.121.081307`.

[62] E. Aprile *et al.*, « Light dark matter search with ionization signals in xenon1t », *Physical Review Letters*, vol. 123, *25*, 2019, ISSN: 1079-7114. DOI: `10.1103/physrevlett.123.251801`. [Online]. Available: `http://dx.doi.org/10.1103/PhysRevLett.123.251801`.

[63] D. S. Akerib *et al.*, « Results from a search for dark matter in the complete lux exposure », *Phys. Rev. Lett.*, vol. 118, p. 021 303, 2 2017. DOI: `10.1103/PhysRevLett.118.021303`. [Online]. Available: `http://link.aps.org/doi/10.1103/PhysRevLett.118.021303`.

[64] M. Ibe, W. Nakano, Y. Shoji, and K. Suzuki, « Migdal Effect in Dark Matter Direct Detection Experiments », *JHEP*, vol. 03, p. 194, 2018. DOI: `10.1007/JHEP03(2018)194`. arXiv: `1707.07258 [hep-ph]`.

[65] S. Knapen, J. Kozaczuk, and T. Lin, « Migdal Effect in Semiconductors », *Phys. Rev. Lett.*, vol. 127, *8*, p. 081 805, 2021. DOI: `10.1103/PhysRevLett.127.081805`. arXiv: `2011.09496 [hep-ph]`.

[66] R. Essig *et al.*, « Direct Detection of sub-GeV Dark Matter with Semiconductor Targets », *JHEP*, vol. 05, p. 046, 2016. DOI: `10.1007/JHEP05(2016)046`. arXiv: `1509.01598 [hep-ph]`.

[67] R. Essig *et al.*, « Snowmass2021 Cosmic Frontier: The landscape of low-threshold dark matter direct detection in the next decade », *in 2022 Snowmass Summer Study*, Mar. 2022. arXiv: `2203.08297` `[hep-ph]`.

[68] H. An, M. Pospelov, J. Pradler, and A. Ritz, « Direct Detection Constraints on Dark Photon Dark Matter », *Phys. Lett. B*, vol. 747, pp. 331–338, 2015. DOI: `10.1016/j.physletb.2015.06.018`. arXiv: `1412.8378` `[hep-ph]`.

[69] Y. Hochberg, T. Lin, and K. M. Zurek, « Absorption of light dark matter in semi-conductors », *Phys. Rev. D*, vol. 95, *2*, p. 023 013, 2017. DOI: `10.1103/PhysRevD.95.023013`. arXiv: `1608.01994` `[hep-ph]`.

[70] A. Aguilar-Arevalo *et al.*, « First Direct-Detection Constraints on eV-Scale Hidden-Photon Dark Matter with DAMIC at SNOLAB », *Phys. Rev. Lett.*, vol. 118, *14*, p. 141 803, 2017. DOI: `10.1103/PhysRevLett.118.141803`. arXiv: `1611.03066` `[astro-ph.CO]`.

[71] J. Tiffenberg *et al.*, « Single-electron and single-photon sensitivity with a silicon skipper ccd », *Phys. Rev. Lett.*, vol. 119, p. 131 802, 13 2017. DOI: `10.1103/PhysRevLett.119.131802`. [Online]. Available: `https://link.aps.org/doi/10.1103/PhysRevLett.119.131802`.

[72] W. S. Boyle and G. E. Smith, « Charge coupled semiconductor devices », *The Bell System Technical Journal*, vol. 49, *4*, pp. 587–593, 1970. DOI: `10.1002/j.1538-7305.1970.tb01790.x`.

[73] G. F. Amelio, M. F. Tompsett, and G. E. Smith, « Experimental verification of the charge coupled device concept », *The Bell System Technical Journal*, vol. 49, *4*, pp. 593–600, 1970. DOI: `10.1002/j.1538-7305.1970.tb01791.x`.

[74] N. W. Ashcroft and N. D. Mermin, *Solid State Physics*. Holt-Saunders, 1976.

[75] B. J. Van Zeghbroeck, *Principles of semiconductor devices*, 2011.

[76] Y. Varshni, « Temperature dependence of the energy gap in semiconductors », *Physica*, vol. 34, *1*, pp. 149–154, 1967, ISSN: 0031-8914. DOI: `https://doi.org/10.1016/0031-8914(67)90062-6`. [Online]. Available: `https://www.sciencedirect.com/science/article/pii/0031891467900626`.

[77] S. Holland, « Fabrication of detectors and transistors on high-resistivity silicon »,
*Nuclear Instruments and Methods in Physics Research Section A: Accelerators,
Spectrometers, Detectors and Associated Equipment*, vol. 275, *3*, pp. 537–541, 1989,
ISSN: 0168-9002. DOI: `https://doi.org/10.1016/0168-9002(89)90741-9`.
[Online]. Available: `https://www.sciencedirect.com/science/article/pii/
0168900289907419`.

[78] A. Aguilar-Arevalo *et al.*, *Characterization of the background spectrum in damic
at snolab*, 2021. arXiv: `2110.13133 [hep-ex]`.

[79] K. Ramanathan and N. Kurinsky, « Ionization yield in silicon for eV-scale electron-
recoil processes », *Phys. Rev. D*, vol. 102, *6*, p. 063 026, 2020. DOI: `10.1103/
PhysRevD.102.063026`. arXiv: `2004.10709 [astro-ph.IM]`.

[80] K. Ramanathan, « Particles taking selfies: investigations into light dark matter
using silicon charge coupled devices », [Online]. Available: `http://knowledge.
uchicago.edu/record/2738`.

[81] D. Rodrigues *et al.*, « Absolute measurement of the fano factor using a skipper-
ccd », *Nuclear Instruments and Methods in Physics Research Section A: Acceler-
ators, Spectrometers, Detectors and Associated Equipment*, vol. 1010, p. 165 511,
2021, ISSN: 0168-9002. DOI: `https://doi.org/10.1016/j.nima.2021.165511`.
[Online]. Available: `https://www.sciencedirect.com/science/article/pii/
S0168900221004964`.

[82] K. Ramanathan *et al.*, « Measurement of low energy ionization signals from Comp-
ton scattering in a charge-coupled device dark matter detector », *Physical Review
D*, vol. 96, *4*, Aug. 2017, ISSN: 24700029. DOI: `10.1103/PhysRevD.96.042002`.

[83] S. Holland *et al.*, « Fully depleted, back-illuminated charge-coupled devices fabri-
cated on high-resistivity silicon », *IEEE Transactions on Electron Devices*, vol. 50,
1, pp. 225–238, 2003. DOI: `10.1109/TED.2002.806476`.

[84] A. Aguilar-Arevalo *et al.*, « Search for low-mass WIMPs in a 0.6 kg day exposure
of the DAMIC experiment at SNOLAB », *Phys. Rev. D*, vol. 94, *8*, p. 082 006,
2016. DOI: `10.1103/PhysRevD.94.082006`. arXiv: `1607.07410 [astro-ph.CO]`.

[85] J. Janesick, *Scientific Charge-coupled Devices* (Press Monographs). Society of Photo
Optical, 2001, ISBN: 9780819436986. [Online]. Available: `https://books.google.
fr/books?id=rkgBkbDie7kC`.

[86] A. Matalon, « Searching for light dark matter with damic at snolab and damic-m : investigations into radioactive backgrounds and silicon charge-coupled devices », Thèse de doctorat dirigée par Letessier-Selvon, Antoine et Privitera, Paolo Physique Sorbonne université 2021, Ph.D. dissertation, 2021. [Online]. Available: http://www.theses.fr/2021SORUS143.

[87] J. Janesick *et al.*, « New advancements in charge-coupled device technology: sub-electron noise and 4096 x 4096 pixel ccds », *in Other Conferences*, 1990.

[88] J. Estrada, J. Molina, and J. Blostein, « Plasma effect in Silicon Charge Coupled Devices (CCDs) », *Nucl. Instrum. Meth. A*, vol. 665, pp. 90–93, 2011. DOI: 10.1016/j.nima.2011.10.060. arXiv: 1105.3229 [physics.ins-det].

[89] A. Aguilar-Arevalo *et al.*, « Measurement of radioactive contamination in the high-resistivity silicon CCDs of the DAMIC experiment », *JINST*, vol. 10, *08*, P08014, 2015. DOI: 10.1088/1748-0221/10/08/P08014. arXiv: 1506.02562 [astro-ph.IM].

[90] R. Widenhorn *et al.*, « Temperature dependence of dark current in a ccd », *Proceedings of SPIE - The International Society for Optical Engineering*, vol. 4669, Apr. 2002. DOI: 10.1117/12.463446.

[91] A. E. Chavarria *et al.*, « DAMIC at SNOLAB », *Phys. Procedia*, vol. 61, F. Avignone and W. Haxton, Eds., pp. 21–33, 2015. DOI: 10.1016/j.phpro.2014.12.006. arXiv: 1407.0347 [physics.ins-det].

[92] A. Aguilar-Arevalo *et al.*, « Constraints on Light Dark Matter Particles Interacting with Electrons from DAMIC at SNOLAB », *Phys. Rev. Lett.*, vol. 123, *18*, p. 181 802, 2019. DOI: 10.1103/PhysRevLett.123.181802. arXiv: 1907.12628 [astro-ph.CO].

[93] E. Hoppe *et al.*, « Reduction of radioactive backgrounds in electroformed copper for ultra-sensitive radiation detectors », *Nuclear Instruments and Methods in Physics Research Section A Accelerators Spectrometers Detectors and Associated Equipment*, vol. 764, 116–121, Nov. 2014. DOI: 10.1016/j.nima.2014.06.082.

[94] A. E. Chavarria *et al.*, « Measurement of the ionization produced by sub-keV silicon nuclear recoils in a CCD dark matter detector », *Phys. Rev. D*, vol. 94, *8*, p. 082 007, 2016. DOI: 10.1103/PhysRevD.94.082007. arXiv: 1608.00957 [astro-ph.IM].

[95] J. Lindhard, V Nielsen, M Scharff, and P. Thomsen, « Integral equations governing radiation effects », *Mat. Fys. Medd. Dan. Vid. Selsk*, vol. 33, *10*, pp. 1–42, 1963.

[96] J. Ziegler, J. Biersack, and U. Littmark, *The Stopping and Range of Ions in Solids* (Stopping and ranges of ions in matter). Pergamon, 1985, ISBN: 9780080216034. [Online]. Available: `https://books.google.fr/books?id=xclwQgAACAAJ`.

[97] O. Abramoff *et al.*, « Sensei: direct-detection constraints on sub-gev dark matter from a shallow underground run using a prototype skipper ccd », *Phys. Rev. Lett.*, vol. 122, p. 161 801, 16 2019. DOI: `10.1103/PhysRevLett.122.161801`. [Online]. Available: `https://link.aps.org/doi/10.1103/PhysRevLett.122.161801`.

[98] T. Emken, R. Essig, C. Kouvaris, and M. Sholapurkar, « Direct Detection of Strongly Interacting Sub-GeV Dark Matter via Electron Recoils », *JCAP*, vol. 09, p. 070, 2019. DOI: `10.1088/1475-7516/2019/09/070`. arXiv: `1905.06348 [hep-ph]`.

[99] R. Agnese *et al.*, « First dark matter constraints from a supercdms single-charge sensitive detector », *Phys. Rev. Lett.*, vol. 121, p. 051 301, 5 2018. DOI: `10.1103/PhysRevLett.121.051301`. [Online]. Available: `https://link.aps.org/doi/10.1103/PhysRevLett.121.051301`.

[100] R. Essig, T. Volansky, and T.-T. Yu, « New constraints and prospects for sub-gev dark matter scattering off electrons in xenon », *Phys. Rev. D*, vol. 96, p. 043 017, 4 2017. DOI: `10.1103/PhysRevD.96.043017`. [Online]. Available: `https://link.aps.org/doi/10.1103/PhysRevD.96.043017`.

[101] I. M. Bloch *et al.*, « Searching for Dark Absorption with Direct Detection Experiments », *JHEP*, vol. 06, p. 087, 2017. DOI: `10.1007/JHEP06(2017)087`. arXiv: `1608.02123 [hep-ph]`.

[102] J. Suzuki, T. Horie, Y. Inoue, and M. Minowa, « Experimental Search for Hidden Photon CDM in the eV mass range with a Dish Antenna », *JCAP*, vol. 09, p. 042, 2015. DOI: `10.1088/1475-7516/2015/09/042`. arXiv: `1504.00118 [hep-ex]`.

[103] H. An, M. Pospelov, and J. Pradler, « New stellar constraints on dark photons », *Phys. Lett. B*, vol. 725, pp. 190–195, 2013. DOI: `10.1016/j.physletb.2013.07.008`. arXiv: `1302.3884 [hep-ph]`.

[104] R. Agnese *et al.*, « Silicon Detector Dark Matter Results from the Final Exposure of CDMS II », *Phys. Rev. Lett.*, vol. 111, *25*, p. 251301, 2013. DOI: `10.1103/PhysRevLett.111.251301`. arXiv: `1304.4279 [hep-ex]`.

[105] R. Arnold *et al.*, « Probing New Physics Models of Neutrinoless Double Beta Decay with SuperNEMO », *Eur. Phys. J. C*, vol. 70, pp. 927–943, 2010. DOI: `10.1140/epjc/s10052-010-1481-5`. arXiv: `1005.1241 [hep-ex]`.

[106] G. Papadopoulos, « Development and characterization of novel electronics for the search of dark matter for damic-m », Thèse de doctorat dirigée par Letessier-Selvon, Antoine et Gaior, Romain, Ph.D. dissertation, 2022.

[107] B. Schmidt *et al.*, « Muon-induced background in the EDELWEISS dark matter search », *Astropart. Phys.*, vol. 44, pp. 28–39, 2013. DOI: `10.1016/j.astropartphys.2013.01.014`. arXiv: `1302.7112 [astro-ph.CO]`.

[108] R. W. Leach and F. J. Low, « CCD and IR array controllers », *in Optical and IR Telescope Instrumentation and Detectors*, M. Iye and A. F. M. Moorwood, Eds., International Society for Optics and Photonics, vol. 4008, SPIE, 2000, pp. 337 – 343. DOI: `10.1117/12.395489`. [Online]. Available: `https://doi.org/10.1117/12.395489`.

[109] M. Traina, « Search for light dark matter and exploration of the hidden sector with the damic at snolab and damic-m charge-coupled devices », Thèse de doctorat dirigée par Letessier-Selvon, Antoine, Ph.D. dissertation, 2022.

[110] W.-M. Y. et al, « Review of particle physics », *Journal of Physics G: Nuclear and Particle Physics*, vol. 33, *1*, pp. 1–1232, 2006. DOI: `10.1088/0954-3899/33/1/001`. [Online]. Available: `https://doi.org/10.1088/0954-3899/33/1/001`.

[111] D.-M. Mei and A. Hime, « Muon-induced background study for underground laboratories », *Phys. Rev. D*, vol. 73, p. 053004, 5 2006. DOI: `10.1103/PhysRevD.73.053004`. [Online]. Available: `https://link.aps.org/doi/10.1103/PhysRevD.73.053004`.

[112] V. A. Kudryavtsev, L. Pandola, and V. Tomasello, « Neutron- and muon-induced background in underground physics experiments », *Eur. Phys. J. A*, vol. 36, pp. 171–180, 2008. DOI: `10.1140/epja/i2007-10539-6`. arXiv: `0802.3566 [astro-ph]`.

[113] C. Berger *et al.*, « Experimental study of muon bundles observed in the fréjus detector », *Phys. Rev. D*, vol. 40, pp. 2163–2171, 7 1989. DOI: `10.1103/PhysRevD.40.2163`. [Online]. Available: `https://link.aps.org/doi/10.1103/PhysRevD.40.2163`.

[114] O. M. Horn, « Simulations of the muon-induced neutron background of the EDELWEISS-II experiment for dark matter search », Other thesis, Jun. 2008.

[115] T. K. Gaisser, *Cosmic rays and particle physics.* 1990.

[116] R. Saldanha *et al.*, « Cosmogenic activation of silicon », *Phys. Rev. D*, vol. 102, p. 102 006, 10 2020. DOI: `10.1103/PhysRevD.102.102006`. [Online]. Available: `https://link.aps.org/doi/10.1103/PhysRevD.102.102006`.

[117] S. Cebrián, « Cosmogenic activation of materials », *Int. J. Mod. Phys. A*, vol. 32, *30*, p. 1 743 006, 2017. DOI: `10.1142/S0217751X17430060`. arXiv: `1708.07449 [nucl-ex]`.

[118] M. Gordon *et al.*, « Measurement of the flux and energy spectrum of cosmic-ray induced neutrons on the ground », *Nuclear Science, IEEE Transactions on*, vol. 51, pp. 3427 –3434, Jan. 2005. DOI: `10.1109/TNS.2004.839134`.

[119] I. S. Diggory, J. R. Hook, I. A. Jenkins, and K. E. Turver, « The momentum spectra of nuclear active particles in the cosmic radiation at sea level. 1. experimental data », *J. Phys. A*, vol. 7, pp. 741–764, 1974. DOI: `10.1088/0305-4470/7/6/010`.

[120] J. F. Ziegler and W. A. Lanford, « Effect of cosmic rays on computer memories », *Science*, vol. 206, *4420*, pp. 776–788, 1979. DOI: `10.1126/science.206.4420.776`. eprint: `https://www.science.org/doi/pdf/10.1126/science.206.4420.776`. [Online]. Available: `https://www.science.org/doi/abs/10.1126/science.206.4420.776`.

[121] J. F. Ziegler and W. A. Lanford, « The effect of sea level cosmic rays on electronic devices », *Journal of Applied Physics*, vol. 52, pp. 4305–4312, 1981.

[122] T. Sato, « Expacs: excel-based program for calculating atmospheric cosmic-ray spectrum user's manual », 2016.

[123] A. Malgin and O. Ryazhskaya, « Neutrons from muons underground », *Physics of Atomic Nuclei*, vol. 71, pp. 1769–1781, Oct. 2009. DOI: `10.1134/S1063778808100116`.

[124] N. Y. Agafonova and A. S. Malgin, « Universal formula for the muon-induced neutron yield », *Phys. Rev. D*, vol. 87, *11*, p. 113 013, 2013. DOI: `10.1103/PhysRevD.87.113013`. arXiv: `1304.0919 [nucl-ex]`.

[125] R. Lemrani *et al.*, « Low-energy neutron propagation in mcnpx and geant4 », *Nuclear Instruments and Methods in Physics Research Section A: Accelerators, Spectrometers, Detectors and Associated Equipment*, vol. 560, *2*, 454–459, 2006, ISSN: 0168-9002. DOI: `10.1016/j.nima.2005.12.238`. [Online]. Available: `http://dx.doi.org/10.1016/j.nima.2005.12.238`.

[126] S. Rozov *et al.*, « Monitoring of the thermal neutron flux in the lsm underground laboratory », *Bulletin of the Russian Academy of Sciences Physics*, vol. 74, pp. 464–466, Apr. 2012.

[127] D. Norcini *et al.*, « Precision measurement of compton scattering in silicon with a skipper ccd for dark matter detection », *Phys. Rev. D*, vol. 106, p. 092 001, 9 2022. DOI: `10.1103/PhysRevD.106.092001`. [Online]. Available: `https://link.aps.org/doi/10.1103/PhysRevD.106.092001`.

[128] G Heusser, « Low-radioactivity background techniques », *Annual Review of Nuclear and Particle Science*, vol. 45, *1*, pp. 543–590, 1995. DOI: `10.1146/annurev.ns.45.120195.002551`. eprint: `https://doi.org/10.1146/annurev.ns.45.120195.002551`. [Online]. Available: `https://doi.org/10.1146/annurev.ns.45.120195.002551`.

[129] P. Scovell *et al.*, « Low-background gamma spectroscopy at the boulby underground laboratory », *Astroparticle Physics*, vol. 97, 160–173, 2018, ISSN: 0927-6505. DOI: `10.1016/j.astropartphys.2017.11.006`. [Online]. Available: `http://dx.doi.org/10.1016/j.astropartphys.2017.11.006`.

[130] J. Dobson, C. Ghag, and L. Manenti, « Ultra-low background mass spectrometry for rare-event searches », *Nuclear Instruments and Methods in Physics Research Section A: Accelerators, Spectrometers, Detectors and Associated Equipment*, vol. 879, 25–30, 2018, ISSN: 0168-9002. DOI: `10.1016/j.nima.2017.10.014`. [Online]. Available: `http://dx.doi.org/10.1016/j.nima.2017.10.014`.

[131] N. Abgrall *et al.*, « The majorana demonstrator radioassay program », *Nuclear Instruments and Methods in Physics Research Section A: Accelerators, Spectrometers, Detectors and Associated Equipment*, vol. 828, pp. 22–36, 2016, ISSN: 0168-

9002. DOI: https://doi.org/10.1016/j.nima.2016.04.070. [Online]. Available: https://www.sciencedirect.com/science/article/pii/S0168900216302832.

[132] G. F. Moroni *et al.*, « Charge-collection efficiency in back-illuminated charge-coupled devices », *Phys. Rev. Applied*, vol. 15, p. 064 026, 6 2021. DOI: 10.1103/PhysRevApplied.15.064026. [Online]. Available: https://link.aps.org/doi/10.1103/PhysRevApplied.15.064026.

[133] R. Bunker *et al.*, « Evaluation and mitigation of trace ^{210}Pb contamination on copper surfaces », *Nucl. Instrum. Meth. A*, vol. 967, p. 163 870, 2020. DOI: 10.1016/j.nima.2020.163870. arXiv: 2003.06357 [physics.ins-det].

[134] M. Laubenstein and G. Heusser, « Cosmogenic radionuclides in metals as indicator for sea level exposure history », *Applied Radiation and Isotopes*, vol. 67, *5*, pp. 750–754, 2009, 5th International Conference on Radionuclide Metrology - Low-Level Radioactivity Measurement Techniques ICRM-LLRMT'08, ISSN: 0969-8043. DOI: https://doi.org/10.1016/j.apradiso.2009.01.029. [Online]. Available: https://www.sciencedirect.com/science/article/pii/S096980430900030X.

[135] A. Aguilar-Arevalo *et al.*, *The oscura experiment*, 2022. DOI: 10.48550/ARXIV.2202.10518. [Online]. Available: https://arxiv.org/abs/2202.10518.

[136] A. Aguilar-Arevalo *et al.*, « Measurement of the bulk radioactive contamination of detector-grade silicon with DAMIC at SNOLAB », *Journal of Instrumentation*, vol. 16, *06*, P06019, 2021. DOI: 10.1088/1748-0221/16/06/p06019. [Online]. Available: https://doi.org/10.1088/1748-0221/16/06/p06019.

[137] L. Pattavina *et al.*, « Radiopurity of an archaeological Roman lead cryogenic detector », *Eur. Phys. J. A*, vol. 55, *8*, p. 127, 2019. DOI: 10.1140/epja/i2019-12809-0. arXiv: 1904.04040 [physics.ins-det].

[138] S. Agostinelli *et al.*, « Geant4—a simulation toolkit », *Nuclear Instruments and Methods in Physics Research Section A: Accelerators, Spectrometers, Detectors and Associated Equipment*, vol. 506, *3*, pp. 250–303, 2003, ISSN: 0168-9002. DOI: https://doi.org/10.1016/S0168-9002(03)01368-8. [Online]. Available: https://www.sciencedirect.com/science/article/pii/S0168900203013688.

[139] J. Allison *et al.*, « Recent developments in geant4 », *Nuclear Instruments and Methods in Physics Research Section A: Accelerators, Spectrometers, Detectors and Associated Equipment*, vol. 835, pp. 186–225, 2016, ISSN: 0168-9002. DOI: https:

//doi.org/10.1016/j.nima.2016.06.125. [Online]. Available: `https://www.sciencedirect.com/science/article/pii/S0168900216306957`.

[140] D. Cullen, J. Hubbell, and L. Kissel, « Epdl97: the evaluated photon data library », vol. 6, Jan. 1997.

[141] S. T. Perkins *et al.*, « Tables and graphs of atomic subshell and relaxation data derived from the llnl evaluated atomic data library (eadl), z = 1–100 », DOI: `10.2172/10121422`. [Online]. Available: `https://www.osti.gov/biblio/10121422`.

[142] S. T. Perkins, D. E. Cullen, and S. M. Seltzer, « Tables and graphs of electron-interaction cross sections from 10 ev to 100 gev derived from the llnl evaluated electron data library (eedl), z = 1–100 », DOI: `10.2172/5691165`. [Online]. Available: `https://www.osti.gov/biblio/5691165`.

[143] M.V. Kossov, « Chiral-invariant phase space model - i. masses of hadrons », *Eur. Phys. J. A*, vol. 14, *3*, pp. 265–269, 2002. DOI: `10.1140/epja/i2001-10211-3`. [Online]. Available: `https://doi.org/10.1140/epja/i2001-10211-3`.

[144] B. Nilsson-Almqvist and E. Stenlund, « Interactions between hadrons and nuclei: the lund monte carlo - fritiof version 1.6 - », *Computer Physics Communications*, vol. 43, *3*, pp. 387–397, 1987, ISSN: 0010-4655. DOI: `https://doi.org/10.1016/0010-4655(87)90056-7`. [Online]. Available: `https://www.sciencedirect.com/science/article/pii/0010465587900567`.

[145] D. Wright and M. Kelsey, « The geant4 bertini cascade », *Nuclear Instruments and Methods in Physics Research Section A: Accelerators, Spectrometers, Detectors and Associated Equipment*, vol. 804, pp. 175–188, 2015, ISSN: 0168-9002. DOI: `https://doi.org/10.1016/j.nima.2015.09.058`. [Online]. Available: `https://www.sciencedirect.com/science/article/pii/S0168900215011134`.

[146] J. M. da Rocha, « Recherche de matière sombre légère avec des CCDs de l'expérience DAMIC à Snolab », Theses, Sorbonne Université, Nov. 2019. [Online]. Available: `https://tel.archives-ouvertes.fr/tel-03000897`.

[147] T. Ullrich and Z. Xu, « Treatment of errors in efficiency calculations », *arXiv: Data Analysis, Statistics and Probability*, 2007.

[148] H. M. Kluck, « Measurement of the cosmic-induced neutron yield at the Modane underground laboratory », Ph.D. dissertation, KIT, Karlsruhe, 2013. DOI: `10.5445/IR/1000039837`.

[149] A. H. Compton, « A quantum theory of the scattering of x-rays by light elements », *Phys. Rev.*, vol. 21, pp. 483–502, 5 1923. DOI: 10.1103/PhysRev.21.483. [Online]. Available: https://link.aps.org/doi/10.1103/PhysRev.21.483.

[150] N. Y. Klein O., « Über die streuung von strahlung durch freie elektronen nach der neuen relativistischen quantendynamik von dirac. », *Z. Physik*, vol. 52, 853–868, 1929. [Online]. Available: https://doi.org/10.1007/BF01366453.

[151] R. Ribberfors and K. F. Berggren, « Incoherent-x-ray-scattering functions and cross sections $(\frac{d\sigma}{d\Omega'})_{\text{incoh}}$ by means of a pocket calculator », *Phys. Rev. A*, vol. 26, pp. 3325–3333, 6 1982. DOI: 10.1103/PhysRevA.26.3325. [Online]. Available: https://link.aps.org/doi/10.1103/PhysRevA.26.3325.

[152] F. Biggs, L. Mendelsohn, and J. Mann, « Hartree-fock compton profiles for the elements », *Atomic Data and Nuclear Data Tables*, vol. 16, *3*, pp. 201–309, 1975, ISSN: 0092-640X. DOI: https://doi.org/10.1016/0092-640X(75)90030-3. [Online]. Available: https://www.sciencedirect.com/science/article/pii/0092640X75900303.

[153] D. Coster and R. D. L. Kronig, « New type of auger effect and its influence on the x-ray spectrum », *Physica*, vol. 2, *1*, pp. 13–24, 1935, ISSN: 0031-8914. DOI: https://doi.org/10.1016/S0031-8914(35)90060-X. [Online]. Available: https://www.sciencedirect.com/science/article/pii/S003189143590060X.

[154] R. Pratt *et al.*, « Limitations on the validity of impulse approximation in compton scattering », *Nuclear Instruments and Methods in Physics Research Section B: Beam Interactions with Materials and Atoms*, vol. 261, *1*, pp. 175–179, 2007, The Application of Accelerators in Research and Industry, ISSN: 0168-583X. DOI: https://doi.org/10.1016/j.nimb.2007.03.085. [Online]. Available: https://www.sciencedirect.com/science/article/pii/S0168583X0700599X.

[155] J. J. Kas *et al.*, « Advanced calculations of X-ray spectroscopies with *FEFF10* and Corvus », *Journal of Synchrotron Radiation*, vol. 28, *6*, pp. 1801–1810, 2021. DOI: 10.1107/S1600577521008614. [Online]. Available: https://doi.org/10.1107/S1600577521008614.

[156] *The FEFF Project*, https://feff.phys.washington.edu/feffproject-portal.html, Accessed: 2022-05-24.

[157] J. J. Rehr and R. C. Albers, « Theoretical approaches to x-ray absorption fine structure », *Rev. Mod. Phys.*, vol. 72, pp. 621–654, 3 2000. DOI: `10.1103/RevModPhys.72.621`. [Online]. Available: `https://link.aps.org/doi/10.1103/RevModPhys.72.621`.

[158] J. A. Soininen, A. L. Ankudinov, and J. J. Rehr, « Inelastic scattering from core electrons: a multiple scattering approach », *Phys. Rev. B*, vol. 72, p. 045 136, 4 2005. DOI: `10.1103/PhysRevB.72.045136`. [Online]. Available: `https://link.aps.org/doi/10.1103/PhysRevB.72.045136`.

[159] S. Holland, « An overview of CCD development at Lawrence Berkeley National Laboratory », *Exper. Astron.*, vol. 14, pp. 83–89, 2002. DOI: `10.1023/B:EXPA.0000004341.11906.bf`.

[160] B. Lowe and R. Sareen, « A measurement of the electron–hole pair creation energy and the fano factor in silicon for 5.9kev x-rays and their temperature dependence in the range 80–270k », *Nuclear Instruments and Methods in Physics Research Section A: Accelerators, Spectrometers, Detectors and Associated Equipment*, vol. 576, *2*, pp. 367–370, 2007, ISSN: 0168-9002. DOI: `https://doi.org/10.1016/j.nima.2007.03.020`. [Online]. Available: `https://www.sciencedirect.com/science/article/pii/S016890020700527X`.

[161] D. W. Amaral *et al.*, « Constraints on low-mass, relic dark matter candidates from a surface-operated SuperCDMS single-charge sensitive detector », *Phys. Rev. D*, vol. 102, *9*, p. 091 101, 2020. DOI: `10.1103/PhysRevD.102.091101`. arXiv: `2005.14067 [hep-ex]`.

[162] A. Aguilar-Arevalo *et al.*, « The Oscura Experiment », Feb. 2022. arXiv: `2202.10518 [astro-ph.IM]`.

[163] M. Mancuso *et al.*, « Searches for Light Dark Matter with the CRESST-III Experiment », *J. Low Temp. Phys.*, vol. 199, *1-2*, pp. 547–555, 2020. DOI: `10.1007/s10909-020-02343-3`.

[164] C. E. Werner, « MCNP Users Manual - Code Version 6.2 », *LA-UR-17-29981*, 2017.

[165] *Materials Project*, `https://materialsproject.org`, Accessed: 2022-05-24.

[166] J. Vinson and J. J. Rehr, « Ab initio bethe-salpeter calculations of the x-ray absorption spectra of transition metals at the *L*-shell edges », *Phys. Rev. B*, vol. 86, p. 195 135, 19 2012. DOI: `10.1103/PhysRevB.86.195135`. [Online]. Available: `https://link.aps.org/doi/10.1103/PhysRevB.86.195135`.

[167] H. Sternemann *et al.*, « Near-edge structure of nonresonant inelastic x-ray scattering from *L*-shell core levels studied by a real-space multiple-scattering approach », *Phys. Rev. B*, vol. 75, p. 075 118, 7 2007. DOI: `10.1103/PhysRevB.75.075118`. [Online]. Available: `https://link.aps.org/doi/10.1103/PhysRevB.75.075118`.

[168] H. Sternemann *et al.*, « An extraction algorithm for core-level excitations in nonresonant inelastic X-ray scattering spectra », *Journal of Synchrotron Radiation*, vol. 15, *2*, pp. 162–169, 2008. DOI: `10.1107/S0909049508001696`. [Online]. Available: `https://doi.org/10.1107/S0909049508001696`.

[169] *Private Communication, J.J. Kas, and J.J. Rehr.* 2022.

[170] G. Fraser *et al.*, « The x-ray energy response of silicon part a. theory », *Nuclear Instruments and Methods in Physics Research Section A: Accelerators, Spectrometers, Detectors and Associated Equipment*, vol. 350, *1*, pp. 368–378, 1994, ISSN: 0168-9002. DOI: `https://doi.org/10.1016/0168-9002(94)91185-1`. [Online]. Available: `https://www.sciencedirect.com/science/article/pii/0168900294911851`.

[171] F. Gao *et al.*, « Monte carlo method for simulating gamma-ray interaction with materials: a case study on si », *Nuclear Instruments and Methods in Physics Research. Section A, Accelerators, Spectrometers, Detectors and Associated Equipment, 579(1):292-296*, vol. 579, *1*, Aug. 2007. DOI: `10.1016/j.nima.2007.04.063`. [Online]. Available: `https://www.osti.gov/biblio/913319`.

[172] B. A. Smith, « Astronomical imaging applications for CCDs », *in Charge-Coupled Device Technology and Applications*, Jan. 1976, pp. 135–138.

[173] « Si-sio2 interface », *in CCD Image Sensors in Deep-Ultraviolet: Degradation Behavior and Damage Mechanisms*. Berlin, Heidelberg: Springer Berlin Heidelberg, 2005, pp. 81–91, ISBN: 978-3-540-27412-4. DOI: `10.1007/3-540-27412-X_6`. [Online]. Available: `https://doi.org/10.1007/3-540-27412-X_6`.

[174] W. Rhode *et al.*, « Limits on the flux of very high-energetic neutrinos with the Frejus detector », *Astropart. Phys.*, vol. 4, pp. 217–225, 1996. DOI: `10.1016/0927-6505(95)00038-0`.

[175] I. Waller and D. R. Hartree, « On the Intensity of Total Scattering of X-Rays », *Proceedings of the Royal Society of London Series A*, vol. 124, *793*, pp. 119–142, May 1929. DOI: `10.1098/rspa.1929.0101`.

[176] A. M. Botti *et al.*, « Constraints on the electron-hole pair creation energy and Fano factor below 150 eV from Compton scattering in a Skipper-CCD », Feb. 2022. arXiv: `2202.03924 [physics.ins-det]`.

[177] C. Sternemann *et al.*, « Correlation-induced double-plasmon excitation in simple metals studied by inelastic x-ray scattering », *Phys. Rev. Lett.*, vol. 95, p. 157 401, 15 2005. DOI: `10.1103/PhysRevLett.95.157401`. [Online]. Available: `https://link.aps.org/doi/10.1103/PhysRevLett.95.157401`.

[178] E. Klevak *et al.*, « Finite-temperature calculations of the compton profile of be, li, and si », *Phys. Rev. B*, vol. 94, p. 214 201, 21 2016. DOI: `10.1103/PhysRevB.94.214201`. [Online]. Available: `https://link.aps.org/doi/10.1103/PhysRevB.94.214201`.

[179] F. Scholze, H. Rabus, and G. Ulm, « Mean energy required to produce an electron-hole pair in silicon for photons of energies between 50 and 1500 ev », *Journal of Applied Physics*, vol. 84, p. 2926, 1998. DOI: `10.1063/1.368398`.

Titre : Recherche de matière noire légère avec l'expérience DAMIC-M

Mot clés : Matière noire, CCD, bruit de fond radioactif, DAMIC

Résumé : DAMIC-M (Dark Matter in CCDs at Modane) est une expérience en cours de développement qui aura pour objectif de détecter des particules de matière noire de faible masse grâce à l'interaction de ces dernières avec les atomes de silicium qui composent des capteurs photographiques CCDs. DAMIC à SNOLAB a été la première expérience à utiliser cette technologie pour la recherche de matière noire. Son successeur, DAMIC-M, aura une masse de détection 17 fois plus grande et utilisera une nouvelle technologie CCD (amplificateurs skipper) pour obtenir un bruit de lecture inférieur à un électron. Ces caractéristiques permettront à DAMIC-M d'atteindre une sensibilité inégalée aux candidats matière noire du «hidden sector» . Une telle sensibilité requiert un excellent contrôle du bruit de fond radiogénique, il doit en effet être contraint au niveau d'une fraction d'évènement par keV par kg-jour d'exposition. Pour répondre à cette exigence, des simulations Geant4 sont utilisées pour optimiser la conception du détecteur, piloter la sélection et la manipulation des matériaux et tester les techniques de rejet du bruit de fond. De plus, afin de caractériser le spèctre d'électrons diffusés par diffusion Compton, qui représentent une source dominante de bruit de fond à basse énergie, des mesures ont été réalisées avec des CCD skipper. Cette thèse se concentre sur les différentes configurations de détecteur testées, l'estimation du bruit de fond associé ainsi que sur les différentes stratégies mises en oeuvre pour la caractérisation et l'atténuation de celui-ci.

Title: Search for Light Dark Matter with the DAMIC-M experiment

Keywords: Dark matter, CCD, radioactive background, DAMIC

Abstract: DAMIC-M (Dark Matter in CCDs at Modane) is a near-future experiment that aims at searching for low-mass dark matter particles through their interactions with silicon atoms in the bulk of charge-coupled devices (CCDs). Pioneer in this technique was the DAMIC experiment at SNOLAB. Its successor, DAMIC-M, will have a detector mass 17 times larger and will employ a novel CCD technology (skipper amplifiers) to achieve sub-electron readout noise. Strengthened by these characteristics, DAMIC-M will reach unmatched sensitivity to the dark matter candidates of the so-called hidden sector. A challenging requirement is to control the radiogenic background down to the level of a fraction of events per keV per kg-day of target exposure. To meet this condition, Geant4 based simulations are being utilized to optimize the detector design, drive the material selection and handling, and test background rejection techniques. Furthermore, precise measurements were carried out with skipper CCDs to characterize the spectrum of Compton scattered electrons, which represent a dominant source of environmental background at low energy. This thesis focuses on the explored detector designs, the corresponding predicted background, and the strategies implemented for its mitigation and characterization.